

UNIVERSITY OF CAPE COAST

DESIGN AND FABRICATION OF AN ELECTRONIC INSTRUMENT FOR TESTING AND CHARACTERIZATION OF PHOTOMULTIPLIER TUBES TO IMPROVE THE IMAGE QUALITY OF LFOV SIEMENS GAMMA CAMERA

CLASS NO.

ACCESSION NO.

249428

CAT. CHECKED

FINAL CHECKED

BY

PAUL KWAMENA OBENG

Thesis submitted to the Department of Physics, School of Physical Sciences, University of Cape Coast in partial fulfilment of the requirement of the award of Doctor in Philosophy (PhD) Degree in Physics

August 2014

THE LIBRARY
UNIVERSITY OF CAPE COAST
CAPE COAST

DECLARATION**Candidate's Declaration**

I hereby declare that this thesis is the result of my own original work and that no part of it has been presented for another degree in this university or elsewhere.


.....

Date: 10/08/14

Paul Kwabena Obeng

(Candidate)

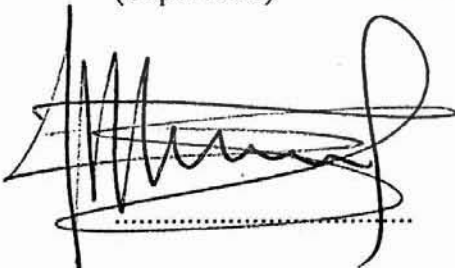
We hereby declare that the preparation and presentation of the thesis was supervised in accordance with the guidelines on supervision of thesis laid down by the University of Cape Coast.


.....

Date: 10/08/14

Prof. J. J. Fletcher

(Supervisor)


.....

Date: 29/7/14

Prof. S. Y. Mensah

(Co – supervisor)

ABSTRACT

A photomultiplier tube (PMT) electronic instrument was designed and fabricated. High voltage (-2000 V) and low voltage supplies (+8, ± 12 V) were also designed and constructed for the instrument. 40 PMTs were tested for voltage gains to determine whether they were good or bad using photoelectric effect principle. Good and bad PMTs were identified during the measurement of their gains. The dark currents of the PMTs were measured with a Keithy Electrometer and PMTs with high dark current ($I_{dc} \geq 1x \mu A$) were declared bad alongside the bad PMTs and were rejected.

PMTs that were identified as good during the testing were then sorted by their gains and arranged on the NaI (Tl) detector of the gamma camera. The PMT with the highest gain was placed at the centre, and PMTs with the lowest gains were placed at the outer circle (edge) of the detector. The power supplies and the signal processing boards of the gamma camera were then aligned (calibrated) to bring their offset voltage to zero (± 0.001 V) and the PMTs HV pots were adjusted to bring their individual energy to the same photo-peak (140 Kev of the ^{99m}Tc radionuclide).

Quality control pictures which were taken after alignment and fine-tuning the PMTs showed some high improvement of image quality. The central field of view (CFOV) Integral Uniformity was 1.64 %; and the Differential Uniformity was 1.13 %. The Useful field of view (UFOV) Integral and Differential Uniformities were 1.67 % and 1.26 %, respectively.

The results compared to NEMA showed that the Gamma camera uniformity and linearity were highly improved.



AKNOWLEDGEMENTS

I wish to express my sincere gratitude to my supervisors, Prof J. J. Fletcher and Prof. S. Y. Mensah for their guidance and supervision for the successful completion of this thesis.

I am most grateful to Prof Shilo Osae, Director of NNRI who assisted in divers ways and his encouragement to make this thesis a reality.

The Ghana Atomic Energy Commission (GAEC) and staff of DENIC now ESC are commended for allowing the use of their facility to carry out part of this project. The same thanks go to Dr. Kojo Wilson who is the head of the Labs, and the entire staff of the Nuclear Medicine Unit of the National Centre for Radiotherapy and Nuclear Medicine, for the use of the LFOV gamma camera where the rest of the project was carried out.

I am very grateful to gamma camera maintenance team, namely; Mr. E. K. Mornoh, Ms. Cynthia Ashong and Mr. Sarpei Addy for their technical support and suggestions which contributed immensely for the successful completion of this work.

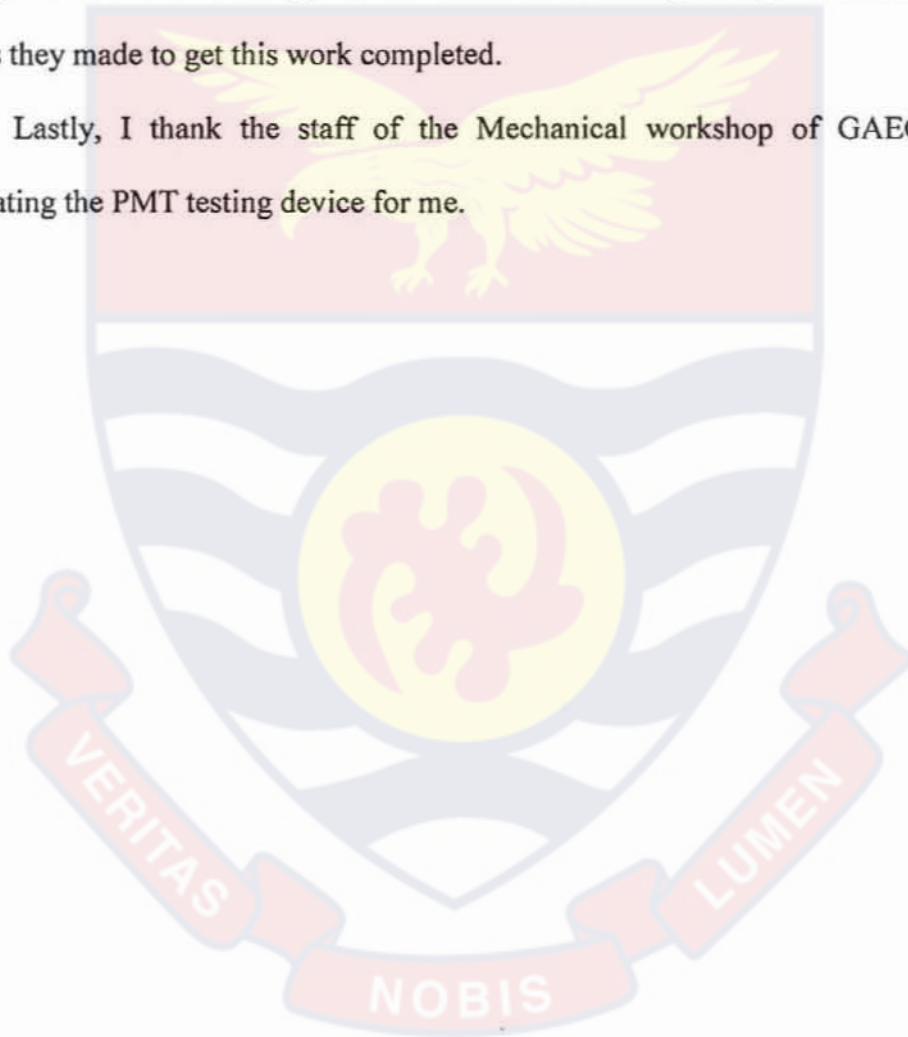
Prof. J. H. Amuasi and Prof A. K. Kyere who were the Medical Physicists who manned the gamma camera at the Nuclear Medicine Unit, at Korle Bu teaching hospital in Accra; through their efforts I was awarded a three months IAEA fellowship training on the maintenance and repairs of the LFOV gamma camera at MEDX Inc., USA, are sincerely thanked.

Much gratitude is extended to my nieces Mary Esi Nkansah and Irene Enimil for helping in typing the draft copies of this thesis, and I also thank my

MPhil. students Bans Frempong and Cynthia Ama Ashong, for their assistance in editing the captured data.

I also like to thank the Head of Physics Department, UCC, Dr. Alfred Owusu, and the entire lecturers and staff of the department, especially Dr. Jojo Eghan, and Dr. S. S. Sackey, for the words of encouragement, assistance, and efforts they made to get this work completed.

Lastly, I thank the staff of the Mechanical workshop of GAEC for fabricating the PMT testing device for me.



DEDICATION

To my wife Mrs. Joana Obeng and my children; Perez, Adu-Efah, Tessy Theresa and Afua Nhyira Obeng-Bosompem.



TABLE OF CONTENTS

	Page
DECLARATION	ii
ABSTRACT	iii
ACKNOWLEDGEMENTS	v
DEDICATION	vii
LIST OF TABLES	xvii
LIST OF FIGURES	xviii
LIST OF PLATES	xxix
LIST OF ABBREVIATIONS AND SYMBOLS	xxxii
CHAPTER	
ONE	
INTRODUCTION	1
Brief history	1
Background to the study	6
Statement of the Research problem	7
Purpose of the study	8
The Photomultiplier Tube (PMT)	9
Research objectives	11
Summary of objectives	13
Organisation of the rest of the study	14

TWO	LITERATURE REVIEW	15
	Overview	15
	Photomultiplier tube operation	16
	Gamma ray interaction with Matter	18
	Photoelectric absorption	18
	Compton scattering	20
	Pair production	21
	Photoemission from metals and semiconductors	22
	Negative electron affinity (NEA) photocathodes	26
	The Photocathode of a PMT	28
	Reflective and semi-transparent photocathodes (PCs)	30
	Photocathode Materials of PMTs	32
	Cs-I	32
	Infrared Ag-O-Cs (S-1)	33
	Sb-Cs	33
	Bialkali (Sb-Rb-Cs, Sb-K-Cs)	34
	High temperature bialkali (HTB)	34
	Extended green bialkali	34
	High temperature bialkali or low noise bialkali	34
	Visible: Na ₂ KSb:Cs(S-20)	35
	Ultraviolet: K ₂ CsSb	35
	Spectral response of the PMT	36
	Quantum efficiency and radiant sensitivity for the PMT	36

The window materials of PMTs	37
Borosilicate glass	37
UV-transmitting glass	37
Synthetic silica	37
The Dynodes (Electron multiplier) of PMTs	38
The linear-focused type	39
The venetian-blind type	39
The box or box and grid type	39
The circular cage type	40
The Microchannel plate (MCP) type dynode	41
The foil type	41
The anode of PMTs	41
The gain (Current amplification)	42
The Anode dark current of PMTs	43
Thermionic emission of electrons	44
Ionization of residual gases	44
Glass scintillation	44
Ohmic leakage	45
Field emission	45
The collection efficiency of PMTs	45
High voltage power supplies	47
Voltage-multiplier circuits	48
Voltage doubler circuit	49

Voltage tripler and quadrupler	50
The Cockcroft Walton high voltage supply	52
Cascade voltage multiplier with no load	52
Cascade voltage multiplier with load	55
PMT supply and circuits	56
Voltage Polarity	57
Rate of voltage application	58
Positive polarity	58
Negative polarity	59
Voltage dividers	60
Types of voltage distribution	60
Resistive dividers	61
Zener diode dividers	63
Decoupling	65
THREE THEORY OF PHOTOEMISSION AND	
GAMMA CAMERA	69
Overview	69
Hole-lifetimes	74
Photoemission studies of copper and silver: Theory	75
Steps of photoemission from solids	75
Probability of electron escape without inelastic scattering	76
Probability of electron escape after one inelastic scattering	80
Effect of elastic scattering	85

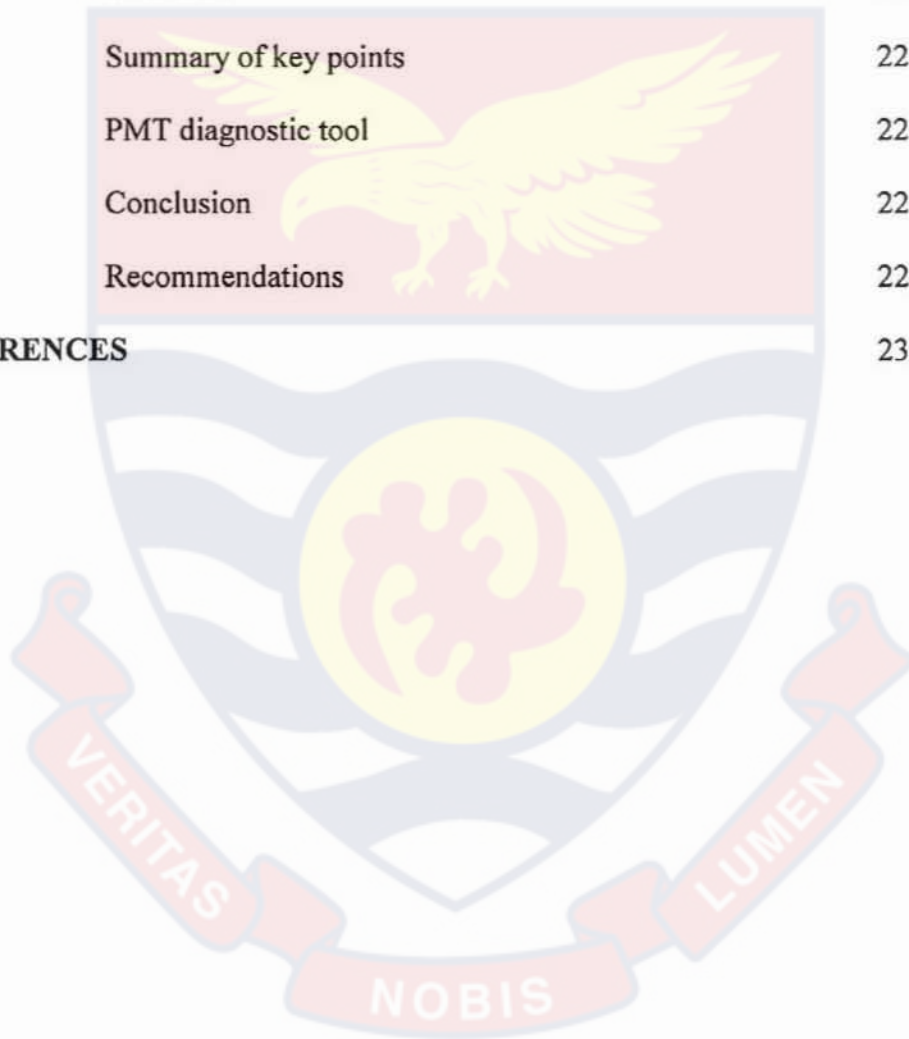
Relation of electron energy distribution to optical transition probabilities	86
Electron-electron scattering	89
Derivation of an expression for quantum efficiency	92
Gamma Camera	95
Basic components and gamma camera operation	96
Position determination "the anger logic"	98
The scintillation crystal	100
Light guide	103
Detector assembly	104
Collimators	106
General purpose low energy parallel collimator	107
High resolution collimator	108
High sensitivity collimator	108
The parallel multihole collimator	109
The diverging multihole collimator	110
Preventive maintenance	111
Quality control records	112
Gamma camera performance characteristics	113
Intrinsic spatial resolution	113
Energy resolution	116
Performance at high counting rates	117
Quality control and non-uniformity	120

	Basis of schemes for testing scintillation camera performance	121
FOUR	DESIGN AND FABRICATION OF PMT CASING, EXPERIMENTAL SET-UP AND PMT MEASUREMENTS	124
	Overview	124
	Design and fabrication of a PMT casing	124
	Material selection for the casing of the PMT instrument	125
	High voltage power design constraints	126
	Stray capacitance	126
	Leakage losses	126
	Voltage regulations of the designed high voltage supply	127
	Design of high voltage power and low voltage supplies circuit	128
	The operation of high voltage power supply circuit	129
	Operation of the oscillator section	129
	Operation of the multiplier section	130
	The operation of the low voltage power supply circuit	134
	The construction of the low voltage DC supply	134
	The construction of the High Voltage power supply circuit	135
	Experimental set-up	137
	The block diagram of the experimental setup	137

	Operation of the circuit	137
	PMT measurement	141
	The measurement of the dark current of a PMT	141
	Measurement of PMT voltage gain with and without the preamplifier connected	144
	Measurement of PMT gain with no preamp connected	144
	Measurement of PMT voltage gain with the preamplifier connected	145
	Plot of PMT Anode current versus High voltages	146
	Gamma camera board alignment	146
	Fine-tuning of PMTs	148
	Quality control position of the detector	149
FIVE	RESULTS AND DISCUSSION	151
	Overview	151
	Results	151
	PMT voltage gain with and without preamplifier connected	151
	Analysis of captured data	186
	Significance of the graphic data	187
	Identification of good PMTs	187
	Identification of bad PMTs	188
	PMT 8 output voltage	188

PMT 13 output voltage	189
PMT 21 output voltage	189
PMTs output gain with preamp connected	190
Repair of faulty preamps	191
Effect of PMT Anode current on high voltage	197
PMT dark current	198
Characterization and arrangement of PMTs on sodium iodide detector	201
Quality control pictures taken after alignment and fine-tuning	202
Discussions	210
Measurement of PMTs	211
High dark current on gamma camera performance	212
PMT output with preamp connected	213
Effect of characterization and sorting of PMTs	213
Quality control pictures obtained	214
Comparison of images between this work and NEMA standards (1994)	215
Image acquisition	221
Calculation of gamma camera integral and differential uniformity on quality control picture No 1	222
Comparison of images uniformities obtained in this work with modern gamma cameras	223

	Clinical studies image of a patient	225
SIX	SUMMARY, CONCLUSIONS AND RECOMMENDATIONS	227
	Overview	227
	Summary of key points	227
	PMT diagnostic tool	228
	Conclusion	228
	Recommendations	229
REFERENCES		230



LIST OF TABLES

Table 1	PMT gains with and without preamplifiers	184
Table 2	Preamplifier gains vs. PMT numbers after the preamps were repaired	193
Table 3	Effect of PMT anode current on high voltage	195
Table 4	Dark current of PMTs with HV fixed at 1200V	196
Table 5	Rearrangement of Table 4 by their gains for placement on the detector	200



LIST OF FIGURES

		Page
Figure 1	The schematic view of the working principle of the PMT	17
Figure 2	Simplified energy diagram	25
Figure 3	Simplified semiconductor energy model showing NEA	27
Figure 4	Types of photocathodes	30
Figure 5	Typical Spectral Response and Emission	38
Figure 6	The schematic view of the dynode (electron multipliers) (1) circular cage, (2) box-and-grid (3) linear focusing, (4) venetian blind, (5) foil and (6) MCP	40
Figure 7	Sample plot of gain vrs supply voltage	43
Figure 8	Typical collection efficiency on PMT as a function of cathode – to-first dynode	46
Figure 9	Half – wave voltage doubler	49
Figure 10	Half – wave voltage doubler operation showing each half – cycle of operation	50
Figure 11	A voltage quadrupler circuit	51
Figure 12	Cascade of the Cockcroft-Walton Circuit	53
Figure 13	Steady state potentials at the nodes of the circuit for zero load conditions	54
Figure 14	Loaded cascade circuit, showing voltage drop	55
Figure 15	PMT high voltage (HV) polarity	57
Figure 16	Network for decoupling the high-voltage switch-on	59

Figure 17	Voltage dividers	61
Figure 18	Inter-electrode voltage stabilization with zener diode	63
Figure 19	Dynode decoupling: (a) parallel (b) series	65
Figure 20	Scintillation camera incorporates collimator, scintillation crystal	96
Figure 21	The X-Y coordinate system of a scintillation camera	97
Figure 22	An example of a resistor network	100
Figure 23	Intrinsic total detection efficiency of gamma rays	101
Figure 24	Energy spectrum from a thin NaI (Tl) crystal	102
Figure 25	The spectral response of a bialkali PMT	103
Figure 26	The optimal arrangement of PMTs array on NaI(Tl)	104
Figure 27	The variation of spatial resolution R_s as function of R_i	107
Figure 28	The principle of a parallel multihole collimator	109
Figure 29	The principle of a diverging multihole collimator	110
Figure 30	Intrinsic spatial resolution of gamma camera as function of γ - ray energy	115
Figure 31	Intrinsic spatial resolution of gamma camera as function of crystal thickness	116
Figure 32	Energy resolution of a thin NaI(Tl) crystal at 150 keV using a point source of ^{99m}Tc	117
Figure 33	Single distorted output pulse from the amplifier	118
Figure 34	Illustrations of integral and differential non-uniformity	121
Figure 35	A block diagram of the casing for the PMT testing device	125

Figure 36	Factors that affect efficiency of high voltage power	127
Figure 37	A Schematic diagram of the high voltage supply of the PMT testing instrument	132
Figure 38	Designed low voltage (dc) power supply circuit using Target 3001 Schematic and PCB design Software V15	133
Figure 39	The block diagram of the experimental setup of the designed and fabricated PMT instrument	138
Figure 40	Position of detector and point source for quality control pictures	149
Figure 41a	PMT 1 Scope output showing the blue light output	153
Figure 41b	PMT 1: The graph showing the blue light output	153
Figure 41c	PMT 1: The graph showing measured frequency	154
Figure 42a	PMT 2: The PC scope captured waveforms	154
Figure 42b	PMT 2: The PC scope captured waveforms showing the preamp output marked 'A' and PMT2 output	155
Figure 43a	PMT 3: The PC scope captured waveforms showing the reference light marked A and PMT3 output	155
Figure 43b	PMT 3: The PC scope captured waveforms showing the preamp output marked A and PMT output	156
Figure 44a	PMT 4: The PC scope captured waveforms showing the PMT output marked 'A' and preamp output	156
Figure 44b	PMT4: The PC scope waveforms showing the PMT	

	output marked 'A' and preamp output	157
Figure 45a	PMT 5: Captured waveforms showing the reference light waveform 'A' and PMT output	157
Figure 45b	PMT 5: Captured waveforms showing the preamp output waveform 'A' and PMT output	158
Figure 46a	PMT 6: Captured waveforms showing the PMT output waveform 'A' and the reference light output	158
Figure 46b	PMT 6: Captured waveforms showing the Preamp output marked 'A' and PMT out	159
Figure 47a,	PMT 7: Captured waveforms showing the Preamp output marked 'A' and PMT out	159
Figure 47b,	PMT 7: Comparison between the measured frequency of the PMT output (31.82 kHz) and preamp output	160
Figure 48a	PMT 8: Picture of observed noise voltage waveform of PMT 8 output when the input ref light was off	160
Figure 48b	PMT 8: A picture of observed voltage waveform of PMT 8 output when the input reference light switched on	161
Figure 48c	PMT 8: A picture of observed voltage waveform of PMT 8 output when the input reference light was switched on	161
Figure 49a	PMT 9 PC scope captured waveforms showing reference light marked 'A' and PMT 9 output	162

Figure 49b	PMT 9: Captured waveforms showing PMT output voltage, marked 'A' and preamp output	162
Figure 50a	PMT 10: PC scope capture waveforms showing reference light marked 'A' and PMT output	163
Figure 50b	PMT 10: Captured waveforms showing PMT output voltage marked 'A' (blue) and preamp output (green)	163
Figure 51a	PMT 11: Captured waveforms of output voltage marked 'A' and the FFT, showing the harmonics of the PMT output marked 'C'	164
Figure 51b	PMT 11: Captured waveform of the reference light voltage marked 'A' and the preamp output voltage	164
Figure 52a	PMT 12: Captured waveforms of the reference light, marked 'A' and the PMT output.	165
Figure 52b	PMT 12: Captured waveforms of the PMT output, marked 'A' and the Preamp output.	165
Figure 53a	PMT 13: Captured waveforms showing the reference light voltage marked 'A' and the PMT output	166
Figure 53b	PMT 13: Captured waveforms showing the reference light voltage marked 'A' and 1 cycle of PMT13 output	166
Figure 54a	PMT 14: Captured waveforms showing the reference light voltage marked 'A' and PMT14 output	167
Figure 54b	PMT 14: Captured waveforms showing PMT 14 output voltage marked 'A' and Preamp output	167

Figure 55a	PMT 15: Captured waveforms showing the reference light output marked 'A' and PMT output	168
Figure 55b	PMT 15: Captured waveforms showing PMT output marked 'A' and Preamp output	168
Figure 56a	PMT 16: Captured waveforms showing the reference light marked 'A' and PMT output	169
Figure 56b	PMT 16: captured waveforms showing the PMT output light marked 'A' and Preamp out	169
Figure 57a	PMT 17: Capture waveforms showing the reference light marked 'A' and PMT output	170
Figure 57b	PMT 17: Captured waveforms showing the PMT output and Preamp output	170
Figure 58a	PMT 18: captured waveforms showing the reference light and PMT output	171
Figure 58b	PMT 18: captured waveforms showing the PMT output and Preamp output and Preamp output (green)	171
Figure 59a	PMT 19: captured waveforms showing the reference light (blue) and PMT output (green)	172
Figure 59b	PMT 19: Captured waveforms showing the PMT output is (green)	172
Figure 60a	PMT 20: Captured waveforms showing the reference light (blue) and the PMT output (green)	173
Figure 60b	PMT 20: Captured waveforms showing the PMT output	

	and Preamp output.	173
Figure 61a	PMT 21: Captured waveforms showing the PMT output (green) and reference light (blue)	174
Figure 61b	PMT 21: Captured waveform showing the PMT output and reference light	174
Figure 62a	PMT 22: Captured waveform showing the reference light voltage and PMT 22 output	175
Figure 62b	PMT 22: Captured waveforms showing PMT 22 output voltage and Preamp output	175
Figure 63a	PMT 23: Captured waveforms showing the reference light voltage and PMT 23 output	176
Figure 63b	PMT 23: Captured waveforms showing PMT 23 output voltage and Preamp output	176
Figure 64a	PMT 24: Captured waveforms showing the reference light voltage and PMT 24 output	177
Figure 64b	PMT 24: Captured waveforms showing PMT 24 output voltage and Preamp output	177
Figure 65a	PMT 25: Captured waveforms showing the ref light voltage and PMT 25output	178
Figure 65b	PMT 25: Captured waveforms showing the ref light output voltage and Preamp output	178
Figure 66a	PMT 26: Captured waveforms showing the reference light voltage and PMT 26 output	179

Figure 66b	PMT 26: Captured waveforms showing PMT 26 output voltage and Preamp output	179
Figure 67a	PMT 27: Captured waveforms showing reference light voltage and PMT 27 output	180
Figure 67b	PMT 27: Captured waveforms showing PMT 27 output voltage and Preamp output	180
Figure 68a	PMT 28: Captured waveforms showing the ref light voltage and PTM 28 output	181
Figure 68b	PMT 28: Captured waveforms showing PMT 28 output voltage and Preamp output	181
Figure 69a	PMT 29: Captured waveform showing the reference light voltage and PMT 29 output	182
Figure 69b	PMT 29: Captured waveforms showing PMT 29 output voltage and Preamp output	182
Figure 70a	PMT 30: Captured waveforms showing reference light voltage and PMT 30 output	183
Figure 70b	PMT 30: Captured waveforms showing PMT 30 output voltage and Preamp output	183
Figure 71	A bar chart showing the gain of PMTs with no Preamp connected	185
Figure 72	A bar chart showing the gains of PMTs with PMT8 output removed	185
Figure 73	A bar chart showing the gains of PMTs with Preamp	

	connected	191
Figure 74	A bar chart of the PMT numbers vrs. gain of the PMTs	194
Figure 75	PMT Anode current vrs. high voltage for 9 PMTs	197
Figure 76	PMT Anode current vrs. high voltage for 8 PMTs	198
Figure 77	PMTs dark currents at a fixed HV (-1200v)	199
Figure 78	Arrangement of PMTs on the sodium iodide detector	201
Figure 79	Quality control picture No. 1: This picture has the highest uniformity	202
Figure 80	Quality control picture No. 2: This picture has the 2 nd highest uniformity	203
Figure 81	Quality control picture No. 3: This picture has 3 rd highest uniformity	203
Figure 82	Quality control picture No. 4. This picture has accept uniformity	204
Figure 83	Quality control picture No. 5. Picture has a high uniformity flood image	204
Figure 84	Quality control picture No. 6 has a phantom bar with different width	205
Figure 85	Quality control picture No. 7 the Phantom bar is rotated 90°	205
Figure 86	Quality control picture No. 8 the Phantom Bar is rotated gain by 90°	206
Figure 87	Quality control picture No. 9. This picture has PLES	

	phantom bar on X-axis	206
Figure 88	Quality control picture No. 10. This picture has PLES phantom bar on Y-axis	207
Figure 89	Quality control picture No. 11. This picture has poor uniformity	207
Figure 90	Quality control picture No.12. This Picture has the worst uniformity	208
Figure 91	Report of one of the patients that was scanned with the Gamma camera after this work was completed	209
Figure 92	Another report of kidney studies after this work was completed	210
Figure 93	NEMA flood uniformity image, ^{99m}Tc 3 million counts	215
Figure 94	Flood uniformity image after tuning is compared with the NEMA standard image	216
Figure 95	NEMA standard showing examples of images with poor spatial linearity and resolution for ^{99m}Tc and ^{67}Ga radioisotopes	217
Figure 96	This work result showing Phantom bar with good linearity and spatial resolution as compared with the NEMA example	218
Figure 97	This work's result showing a four quadrant phantom bar pattern	218
Figure 98	NEMA qualitative spatial resolution and linearity	219

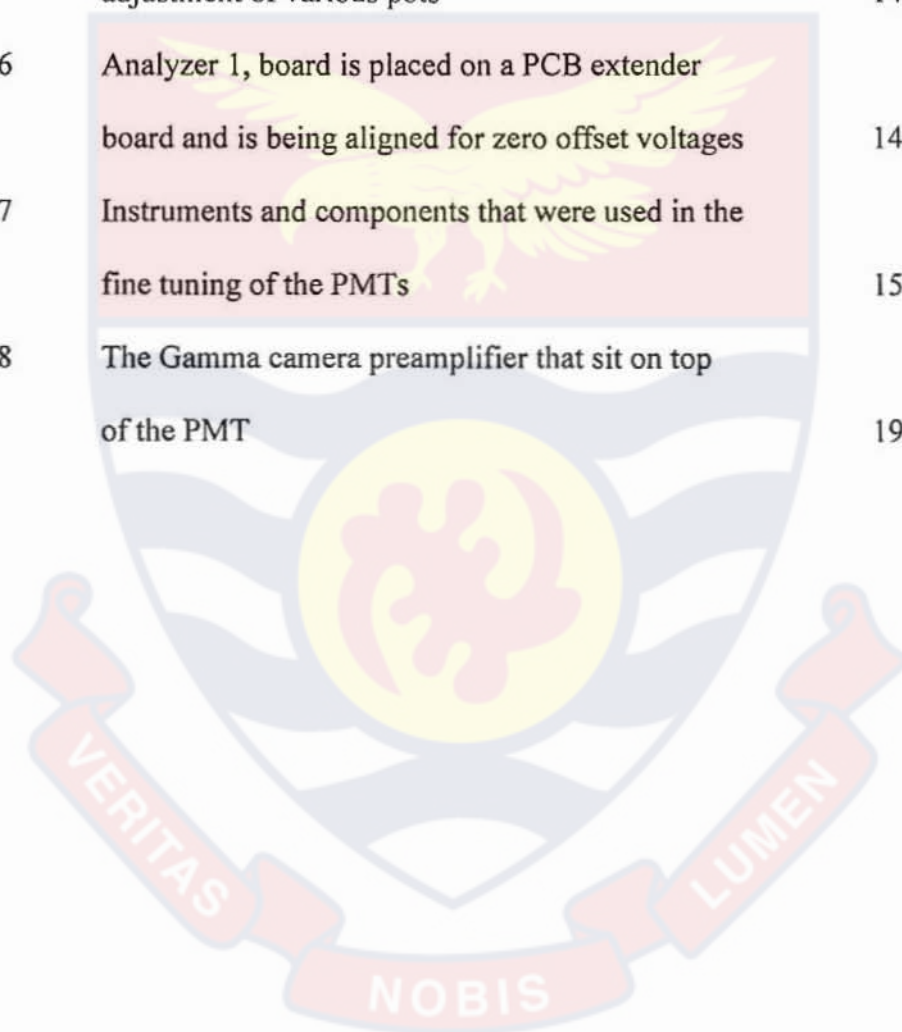
- Figure 99 Intrinsic image of the NEMA slit phantom pattern
using a distance point source of ^{99m}Tc 220
- Figure 100 Parallel lines Equal Spaces (PLES) linearity of the
image, and is compared with the NEMA 221
- Figure 101 A typical Kidney study analysis of the Gamma
camera after this work was completed 225



LIST OF PLATES

		Page
Plate 1	The LFOV Gamma Camera at the Korle Bu Teaching Hospital	95
Plate 2	Completed low voltage DC power supply (+5V, +12V and -12V) built on a PCB	135
Plate 3	Completed 17 Stage HV power supply built on a prototyping board	136
Plate 4	A BNC coaxial cable has tapped a voltage from one of the BNC sockets on the HV supply to the PMT under test in the testing instrument's chamber	136
Plate 5	Experimental Setup of Instruments used to measure low currents, low voltages and waveforms of the PMT under test	139
Plate 6	Fabricated instrument for testing and characterization of PMTs	140
Plate 7	Chamber of fabricated instrument for testing PMTs	140
Plate 8	Instrument for testing PMTs being closed for test to begin	140
Plate 9	Chamber of the PMT instrument showing low intensity blue LED	141
Plate 10	Chamber of the PMT instrument showing high intensity blue LED	141
Plate 11	The 40 PMTs that were tested in this work	142

Plate 12	One of the 40 PMTs that was tested in this work	143
Plate 13	Capture device	143
Plate 14	Two of the PMTs that were tested under this work	145
Plate 15	Alignment of detector power supply involved in the adjustment of various pots	147
Plate 16	Analyzer 1, board is placed on a PCB extender board and is being aligned for zero offset voltages	148
Plate 17	Instruments and components that were used in the fine tuning of the PMTs	150
Plate 18	The Gamma camera preamplifier that sit on top of the PMT	192



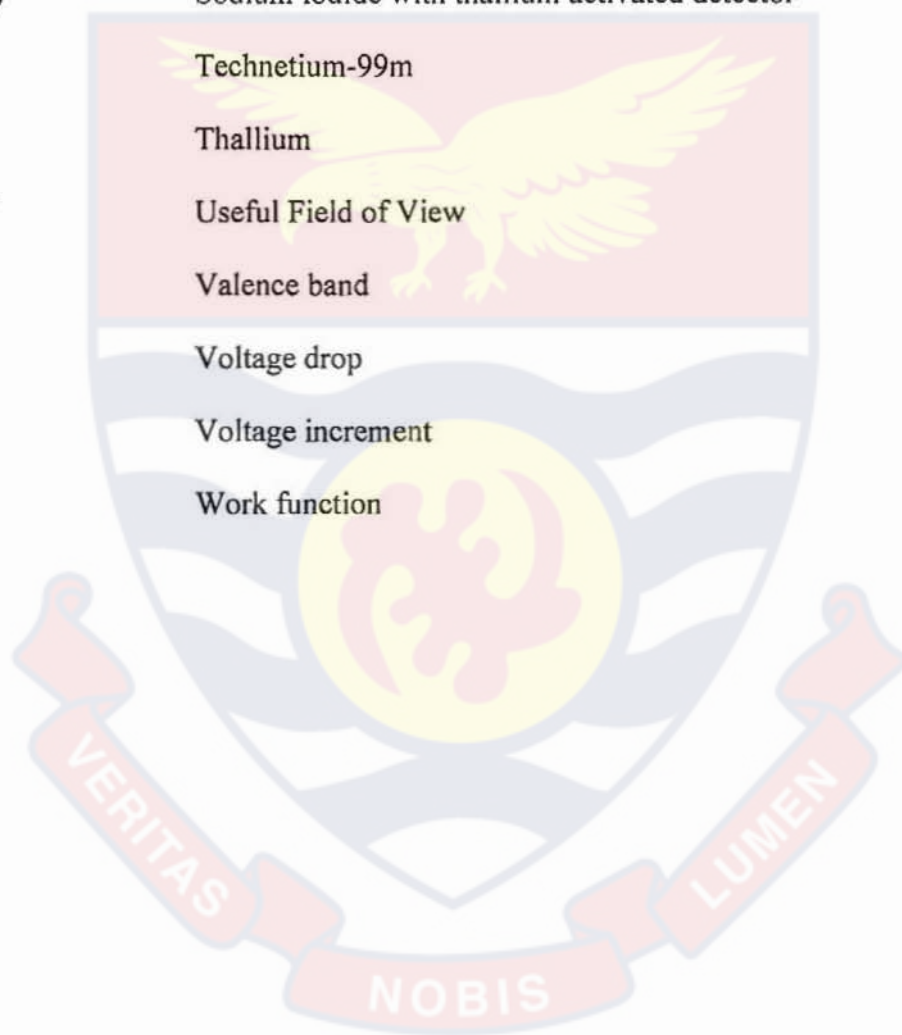
LIST OF ABBREVIATIONS AND SYMBOLS

α	Absorption coefficient
E_{absp}	Absorption efficiency
AC	Alternating current
ADCs	Analogue to digital converters
I_a	Anode current
ANTARES	Astronomy with a Neutrino Telescope and the Abyss Environmental Research
E_g	Band-gap energy
BLTH	Black Lion Teaching Hospital
E_b	Binding energy
BGO	Bismuth Germanate
CdTe	Cadmium Telluride
CZT	Cadmium Zinc Telluride
CdZnTe	Cadmium Zinc Telluride
CRO	Cathode ray oscilloscope
CFOV	Central field of view
^{57}Co	Cobalt-57
CMS-HF	Compact Muon Solenoid- Forward Calorimeter
CB	Conduction band
p	Crystal momentum
DA	Differential amplifier

DC	Direct current
E_A	Electron affinity
E_0	Energy of vacuum potential barrier
n	Equilibrium density of phonons in the metal
E_F	Fermi level
FOV	Field of view
FWHM	Full-Width at Half-Maximum
γ	Gamma
GAEC	Ghana Atomic Energy Commission
$G_1^+(E)$	Green's function
HPGe	High Purity Germanium
HTB	High Temperature Bialkali
HV	High Voltage
$h\nu$	Incident photon energy
IAEA	International Atomic Energy Agency
E_{int}	Intrinsic efficiency
R_i	Intrinsic resolutions
KNH	Kenyatta National Hospital
E_k	Kinetic energy
LFOV	Large Field of View
L	Length of a large box
LFT	Linear-Focused Type
LEED	Low Energy Electron Diffraction

MCP	Micro-Channel Plate type dynode
MiniBooNE	Mini Booster Neutrino Experiments
MTH	Mulago Teaching Hospital
NCRNM	National Centre for Radiotherapy and Nuclear Medicine
NEMA	National Electrical Manufactures Association
NEA	Negative Electron Affinity
I_p	Nominal divider current
PLES	Parallel Lines Equal Space
PC Scope	Personal Computer Oscilloscope
H_{sr}	Perturbation Harmiltonian
PC	Photocathode
E_{pe}	Photoemission threshold energy
$h\nu_0$	Photoemission threshold
PMT	Photomultiplier Tube
h	Planck's constant
PET	Positron Emission Tomography
Pot	Potentiometer
Preamp	Preamplifier
Δq_N	Pulse charge
PHA	Pulse height analyser
PHR	Pulse height Ratio
QE	Quantum Efficiency
RC	Resistor, Capacitor

R_s	Spatial resolution
c	Speed of light
SPECT	Single Photon Emission Computed Tomography
S/N	Signal to Noise Ratio
NaI(Tl)	Sodium iodide with thallium activated detector
^{99m}T	Technetium-99m
Tl	Thallium
UFOV	Useful Field of View
VB	Valence band
ΔV_0	Voltage drop
V_d	Voltage increment
Φ	Work function



CHAPTER ONE

INTRODUCTION

Brief history

The first moving-detector radioisotope imaging systems were based on the electromechanical rectilinear scanner, Cassen *et al* (1950, 1951), Mayneord and Newbery (1952), Mallard and Peachey (1959) with one or two detector heads. These automatic scanning devices allowed accurate transverse and longitudinal positioning of a scintillator crystal, which was equipped with a focused lead collimator to define the small area being imaged. The scintillator was usually a large-volume NaI(Tl) crystal, with thickness of 12.5 cm and 12.5 cm diameter. The collimator was a large, truncated lead cone with multiple holes in which the diameter of each hole tapers towards the focal point. Images were formed by attaching to the scanner a mechanical arm fitted with some form of recording stylus, such as a tapping pen, with a colour ribbon or a photo-recording system.

The rectilinear scanner has now become the 'steam train' of radioisotope imaging, and those in existence now are usually old commercial or home-made scanners kept going by enthusiasts (Flower *et al*, 1986). A direct extension of the rectilinear scanner was the development of linear scanners. In this case, the rectilinear motion was replaced by a single longitudinal scan with a laterally extended scanning head. The need to physically move the scanner necessitated long imaging times, ranging from 10 to 60 mins. Moreover, the extended time required to obtain a single image meant that this technology was not adaptable to dynamic studies, thus precluding many studies of organ

function. But rectilinear scanning demonstrated the potential for radionuclide imaging, and therefore a starting point for the field of nuclear medicine (Prekeges, 2011).

The limitations of the rectilinear scanner prompted development of the gamma camera by Anger (1958). Anger's stationary detector design using a large-diameter sodium iodide crystal that covered the patient revolutionized radionuclide imaging and enabled nuclear medicine to develop into function-oriented modality. The first Anger camera marketed for clinical use had 19 Photomultiplier tubes (PMTs). The intrinsic resolution for 140-keV gamma rays was approximately 10 mm. Significant improvement in resolution has been achieved by using thinner crystal (Chapman *et al*, 1979; Muehllehner, 1979), discrete section light guides, improved PMT technology (Engstrom, 1977; Persyk and Moi, 1978) and larger numbers of smaller diameter PMTs. Modern cameras use 37 to 91 PMTs with intrinsic resolution in the range of 3 to 4 mm Full- Width at Half Maximum (FWHM). In the case of intrinsic resolution lower energy does not mean better performance (Chapman *et al*, 1979). On the contrary, the lower the energy absorbed in the crystal, the less light produced in the scintillation process and Poisson noise in the PMT output increases, degrading the intrinsic resolution.

Despite being efficient and widely used instrument, the Anger camera or improved variants presented some limitations. In particular, Anger cameras exhibited degradation of the position resolution towards the edges of the camera, non-uniformity and various forms of image distortion. Due to the bulky and heavy design of the conventional Anger camera, it is often difficult to position it close to an organ as desired and to obtain the most suitable view. This

difficulty is enhanced by the existence of a dead zone of several centimetres (cm) at the edges of the camera, (Lopes and Chepel, 2004).

Anger cameras (Gruber *et al*, 2001) have therefore proven suboptimal in imaging tumours, due to their large size, thus preventing close access to desired imaging areas. The result is decreased sensitivity, a problem that could be lessened by compact camera design. Other small organ imaging applications, as well as applications involving surgical probes or the imaging of small animals, would also potentially benefit from compact gamma camera designs. The most common way to designing a compact gamma camera, is to replace the bulky PMTs with much more compact devices, either solid-state photo-detectors (Strobel, *et al*, 1997; Gruber *et al*, 1998; Part *et al*, 1998; Tornai *et al*, 1997) or solid-state radiation detectors such as CdZnTe which replaces the scintillator in addition to the PMTs (Buttler *et al*, 1998; Singh and Mumcuoglu, 1998). The major challenges in implementing these designs are to achieve a system that matches Anger camera performance, particularly with regard to energy resolution, reliability and cost. Silicon photodiode have traditionally suffered from excessive electronic noise, HgI₂ photodiodes typically experience reliability problems.

Modern technological advances however have led to recently produced photodiodes with acceptably high signal-to-noise characteristics even at room temperature. The most promising of these diodes are low noise, silicon PIN photodiodes (Holland, 1997) with extremely low leakage current (<5 pA/mm² at 50 V bias). Other photodiode technologies that have been under development and could potentially be used for compact camera designs are, silicon drift photodiodes (Avset, 1990), avalanche photodiodes (Gramsch, 1996) and photo-

detector materials such as HgI₂ (Iwanczyk, 1992) TlBr(I) (Olschner, 1992) or InI (Squillante *et al*, 1993). Two critical innovations that made compact gamma camera technologically feasible were the low noise Si PIN photodiodes (Holland, 1997) and the custom integrated circuit (IC) readout (Pedrali-Noy, 2001).

Oguwa K. *et al*, (2009) in their evaluation of an ultra-high resolution Single photon emission computed tomography (SPECT) system wrote that the intrinsic spatial resolution of a typical sodium Iodide NaI(Tl) scintillation detector used in SPECT system is around 3.8 mm full- width-at-half-maximum (FWHM) (Madson, 2007). This is mainly caused by the detection scheme of gamma-rays including a scintillator and PMTs. To cope with this resolution issue (Rowland, 2008), small animal SPECT systems with pinhole collimators have been proposed (McElroy, 2002; Beekman *et al*, 2005; Schramm *et al*, 2003; Lackas *et al*, 2005) and lack of the intrinsic spatial resolution of the scintillation detector was compensated for with the geometrical magnification effect of the pinhole collimator. Another way to improve the spatial resolution of the small animal SPECT system is utilization of pixelated detectors such as discrete NaI(Tl) or CsI(Tl) crystals (Weisenberger, 2003; Lage, 2007; Sun, 2007; MacDolnard, 2001; Beekman, 2004; Zeniya, 2006) or cadmium telluride (CdTe) or cadmium zinc telluride (CdZnTe) semiconductor detectors (Kastis, 2000; Kastis, 2002; Izaguirre, 2006; Kim, 2006; Mori, 2001; Kubo, 2005; Ogawa, 2006; Ogawa; 2007; Funk, 2003; Sun, 2005), which were used with a parallel-hole collimator or pinhole collimator.

Positron Emission Tomography (PET) made use of pairs of collinear photons emitted in the annihilation of a positron with an electron of the tissue,

and therefore was based on positron emitter radioisotopes. The potential of positron imaging and the value of eliminating the collimator was recognized by early developers of nuclear medicine instrumentation, long before transverse sections from data covering a large number of angles.

Brownell *et al*, (1969) developed a family of instruments over several decades that nicely demonstrated the evolution of PET first from dual planar detectors working in coincidence and providing longitudinal tomographic images, progressing from there to rotating detectors and using transverse reconstruction algorithms to obtain sections and finally to complete circular stationary detector arrangements, first with a single slice (Burnham *et al*, 1983) and subsequently using an increased number of transverse slices (Burnham *et al*, 1985). Anger (1966), also worked on positron imaging almost as soon as he developed the single photon Anger camera. His dual PET detector scanner was commercially available for a brief period by Nuclear Chicago Corporation, but early clinical data quickly pointed out the main relation with PET imaging: while the elimination of the collimator increased the photon flux hitting the detectors by more than an order of magnitude relative to single photon imaging, the fraction of event which were found in coincidence was of the order of 1%, therefore requiring a high singles count-rate capability to achieve an acceptable coincidence rate.

Early efforts to achieve transverse section images in nuclear medicine relied on iterative methods (Muehllehner and Wetzel 1971, Kuhl *et al*, 1973), but this changed rapidly with the introduction of X-ray computed tomography and the filtered back-projection technique. This allowed a series of PET scanners to be developed at a number of academic institutions (Ter-Pogossian

et al, 1978; Phelps *et al*, 1976; Burnham *et al*, 1985; Bohm *et al*, 1978; Senda *et al*, 1985; Cho, 1983; Derenzo *et al*, 1981; Wong *et al*, 1984), using first NaI(Tl) in a hexagonal arrangement(Phelps *et al*, 1976), a one-to-one crystal-to-photomultiplier tube (PMT) coupling and involving transverse scanning and wobbling motions, finally leading to the use of BGO in a circular arrangement operating in stationary mode (Thompson *et al*, 1979; Cho and Farughi, 1977).

Background to the Study

The International Atomic Energy Agency (IAEA) in the early nineties acquired some refurbished gamma cameras for some African countries (including Ghana) that had just introduced nuclear medicine in their respective countries but could not afford buying new cameras.

Adequate preparations were not made towards the rooms where the gamma camera were to be installed in terms of proper design of shielded rooms where electrical cables were properly laid to avoid electromagnetic interference on image acquisition. Some of the countries were not having any medical physicists to assist in the quality assurance and quality control of the camera.

Ghana however was fortunate to have two medical physicists who helped in the daily quality control of the camera.

I spent four months with MEDX Inc., USA in 1993, under the auspices of the IAEA, where I studied the maintenance, repairs and quality control of the refurbished LFOV Siemens gamma camera. Upon return from the training, I installed a similar type of camera in Kenyatta National Hospital (KNH), Nairobi, Kenya; on behalf of MEDX Inc., and for over ten years, I worked as

an IAEA gamma camera consultant (expert) where I fixed gamma cameras in Uganda, Kenya, and Ethiopia.

The gamma camera in Ghana was the only camera left that was being used for clinical studies, when other countries had packed their cameras because they did not have the competent engineers to repair them. For over ten years, the Ghanaian counterpart did not receive any electronic part or maintenance support from the IAEA, as other countries parked their camera due to lack of competent engineer to repair them. The maintenance group, of which I was the head, kept the camera in operation for over ten years.

Statement of the Research Problem

Medical Imaging manufacturers felt reluctant to send their service engineers to countries or places where only one of their products (e.g. Gamma or SPECT camera) was in operation and needed repairs. Manufactures would rather send their service engineers to places where many of their products (e.g., Gamma cameras) were installed and being operated and demand for their regular maintenance was very high. In such places, the service engineer provide 24 hours support to their customers.

In the light of this, developing countries was a matter of fact, lack maintenance culture because of a couple of reasons; Lack of money and lack of test instruments and maintenance technicians. As a result of this, hospital equipment e.g., gamma cameras often broke down and became “white elephant”. These equipments were often used for just a few years after purchase, and when they broke down Manufactures refuse to send in service engineers to repair them even when the equipment was under warranty.

However, if there was no money, a well-trained technician with the appropriate tools and instruments could be mandated to repair the equipment (gamma camera), gamma cameras life span in developing countries could be extended for some years.

Medical imaging manufacturers would not sell PMT testing instruments to their customers for the purpose of controlling their products in the market. Therefore designing and fabricating PMT testing instruments for various medical imaging centres in Ghana especially the Korle-Bu Teaching Hospital would enable local technicians to provide 24 hour maintenance support services to the centres, thereby replacing service engineers who should have offered such vital support services to the developing countries medical centres, but failed to do so because the developing countries could not afford to buy many of their products to qualify a service engineer to be stationed in that country.

Purpose of the Study

The purpose of the study was to design and fabricate a PMT testing instrument to be used as a diagnostic tool to assist local electronic technicians to provide maintenance support services to medical centres. Test instruments like multimeters and oscilloscopes can be bought in the open market but PMT testing instruments are not sold in the market and manufacturers of medical equipments are not willing to sell them to their customers. Upgrading the gamma camera every time the manufacturer upgrades their products to a newer version is not necessary when the camera is well maintained, and alternative parts could be bought from genuine suppliers when the manufacturer stops supplying spare parts to their customers.

The overall purpose of this study was therefore to design and fabricate an electronic instrument that can be used to repair and upgrade cameras in developing countries so as to extend their life span of gamma cameras when the manufacturer has stopped the supply of spare parts of such cameras.

Photomultiplier Tube (PMT)

A PMT converts light flux into electron flux, and then amplifies this generated current. This process starts with a photocathode, an electron-optical input system, an electron multiplier and an anode (Flyckt and Marmomier, 2002), all inside a vacuum tube. A PMT creates an electric charge in proportion to the amount of light energy that it receives. PMTs are fragile, expensive and very sensitive detectors that can easily be destroyed by collisions, explosions, or exposing them to too much light when biased.

For more than sixty years, photomultipliers have been used to detect low-energy photons in the ultra violet (UV) to visible range, high-energy photons (X-rays and γ -rays) and ionizing particles using scintillators.

Today, the PMT remains unequalled in light detection in all but a few specialized areas. The PMT's continuing superiority stems from three main features:

1. large sensing area
2. ultra-fast response and excellent timing performance
3. high gain and low noise

The last two give the photomultiplier an exceptionally high gain bandwidth (GB) product.

For detecting light from UV to visible wavelengths, the photomultiplier has so far successfully met the challenges of solid-state light detectors such as the silicon photodiode and the silicon avalanche photodiode. For detecting high-energy photons or ionizing particles, the photomultiplier remains widely preferred to solid state detectors.

To meet today's increasingly stringent demands in nuclear imaging, existing photomultiplier designs are constantly being refined. Moreover, for the analytical instruments and physics markets, completely new technologies have been developed such as the foil dynode (plus its derivative the metal dynode) that is the key to the low-crosstalk of modern multi-channel photomultipliers. And for large detectors for physics research, the mesh dynode has been developed for operation in multi-tesla axial fields. Recent developments include very large hemispherical photomultipliers with excellent time response for cosmic ray experiments, and ultra-fast tubes with a time jitter of less half a nanosecond.

PMTs are the most widespread vacuum electronic devices that are used for almost all kinds of experimental studies involving the detection of light in the areas of space research and archaeology, medicine and geology, biology and art, astronomy and metallurgy, chemistry and agriculture, etc.

Physics and astronomy-particle physics experiments are the most active users of PMTs. There are numerous experiments that tested the characteristics of PMTs used in high energy physics experiments. Two of such tests are reported in this thesis.

Barnhill, D. (2007), tested 4800 large PMTs that were used in the Cherenkov detectors at the Pierre Auger observatory. Before the PMTs were

deployed, each PMT was evaluated to check that various parameters, such as the linearity, dark noise, and gain fell within the specified range.

The MiniBooNE is an experiment at the Fermi lab designed to observe neutrino oscillations. A beam consisting primarily of muon neutrinos is directed at the detector filled with 800 tons of mineral oil and lined with 1,280 photomultiplier tubes. The test served to determine five characteristics about each PMT, these data were used to sort the tubes into five categories, from best to worst in timing and charge resolution (Brice, *et al*, 2006).

The above two experiments involve the measurement of very small signals from the outer space so stringent selection criteria were followed to ensure that the selected PMTs had very low dark currents and high gain among others to place them at the appropriate place on the detector.

Research Objectives

Gamma camera is a sophisticated diagnostic equipment that are used in hospitals or medical centres to scan patients for all types of tumours and cancers. Depending on the size of the camera head or the detector the PMTs may range from 9 to 91 arranged in a diagonal form in the detector assembly.

Since there were no test instruments available for PMTs, one had to do try and error to replace bad PMT which was very time consuming procedure. It took about forty minutes to open and close the detector assembly. Besides that, additional time was needed to locate and remove bad PMT, and put silicon grease on the new PMT for maximum light coupling between the PMT and Sodium Iodide (NaI(Tl)) detector before putting the new PMT on the NaI(Tl) detector.

Therefore, if an instrument for testing a PMT was available many cameras could be repaired and calibrated within a very short time.

Unlike other works (Barnhill, 2007), that tested new PMTS with various diameters for high energy physics and other applications; this work involved the testing of basic characteristics of old PMTs in a refurbished Siemens gamma camera which is situated at the nuclear medicine unit of the National Centre for Radiotherapy and Nuclear Medicine (NCRNM) of Korle-bu teaching hospital. The camera was manufactured in the late 70s, and has 37 PMTs installed in the (detector assembly) camera head.

The main objective of this work was to improve the image quality of the gamma camera by designing and fabricating a PMT electronic instrument that will facilitate the testing and characterization of PMTs in general and particularly the refurbished gamma camera at NCRNM, Korle Bu. The instrument will enable easy replacement of faulty PMTs during repairs and maintenance, since the state of the PMT that will be used to replace a damaged one will be known prior to replacement, there will be no more need for try and error method during maintenance of gamma cameras. After the characterization of PMTs by their gains and dark currents, the next stage was to rearrange the PMTs on the Sodium Iodide [NaI(Tl)] detector surface based on their new measured voltage gains. Then perform signal processor boards alignment in the detector assembly and console, and fine tuning of the PMTs (that is adjusting the PMTs High Voltage Pots to bring their individual energy to the same photopeak as the ^{99m}Tc isotope) of the camera and lastly perform quality control of the camera and compare the said pictures with others in terms of resolution

and differential and integral uniformities to determine the performance of the camera.

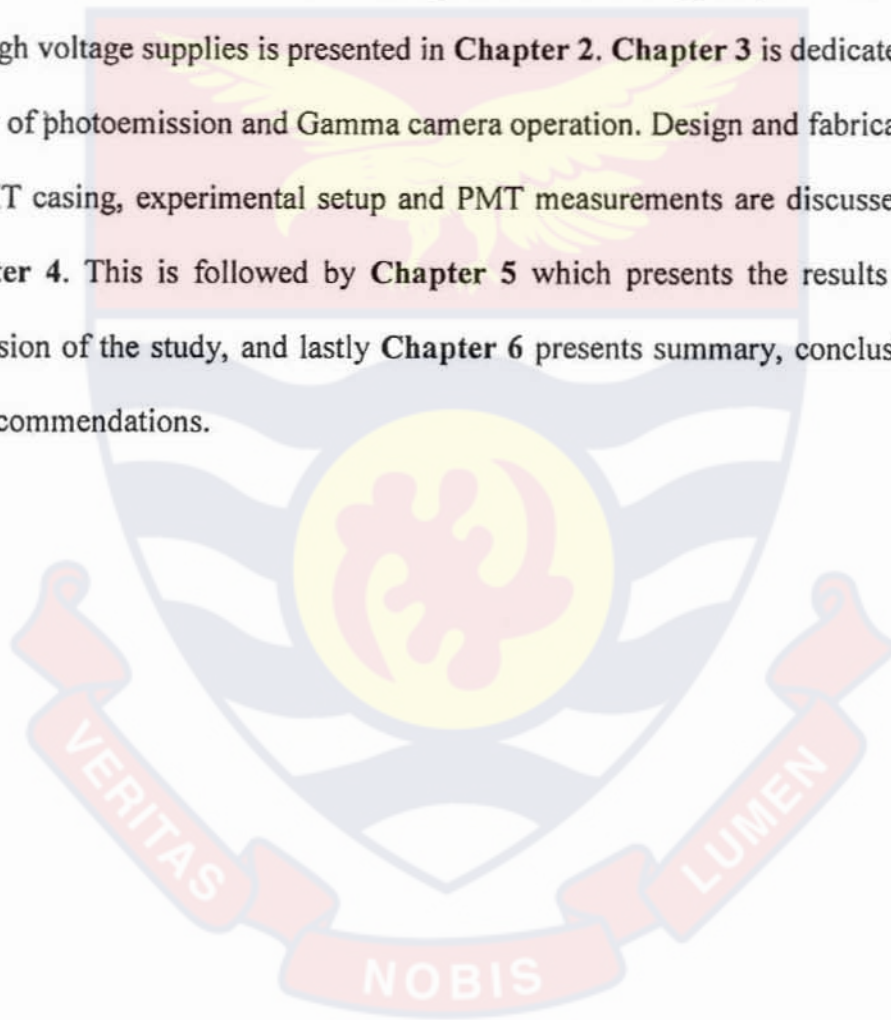
Summary of Objectives

1. Design and fabrication of PMT testing instrument and its accessories
 - I. Design and fabrication of the testing instrument's casing.
 - II. Design and construction of low and high voltage power supplies.
 - III. Design and construction of oscillator circuit
2. Characterization of forty PMTs by their:
 - I. Quantum efficiencies (voltage gain)
 - II. Dark currents and
 - III. Anode currents
3. Testing the voltage gains of each of the forty preamplifiers that sit on top of the PMT.
4. Placing of the tested PMTs on the NaI (TI) detector.
5. Perform processor boards alignment and fine tuning of the PMTs
6. Take quality control pictures of the gamma camera to check for integral and differential uniformity, and linearity of the camera.
7. Use the camera for clinical studies to confirm improvement in image quality.

Organisation of the Rest of the Study

The structure of this thesis proceeds from the basic principles of Photomultiplier operation to more practical aspect of testing PMTs quantum efficiency and arranging them properly on the NaI(Tl) detector to improve image quality of the gamma camera.

The literature review of PMT operation, cathode types, photoemission and high voltage supplies is presented in **Chapter 2**. **Chapter 3** is dedicated to theory of photoemission and Gamma camera operation. Design and fabrication of PMT casing, experimental setup and PMT measurements are discussed in **Chapter 4**. This is followed by **Chapter 5** which presents the results and discussion of the study, and lastly **Chapter 6** presents summary, conclusions and recommendations.



CHAPTER TWO

LITERATURE REVIEW

Overview

Photoelectric effect was first discovered by Hertz in 1887 through experiments by exposing negative electrode to ultraviolet radiation. In 1905, Einstein introduced the expression 'photon', when he explained the photoelectric effect (Einstein, 1905), which had already been discovered by Hertz, (1887) who showed that electric sparks occur more easily when electrodes are illuminated with ultraviolet light. Einstein's view of photon complementarity between light quanta and light waves was finally extended to the whole range of electromagnetic radiation by the discovery of the Compton effect (Compton, 1923), and by the detection of electron-positron annihilation (Blackett, *et al*, 1933). The human eye was used in former times by astronomers and by nuclear physicists as a photon detector. Geiger and Marsden (1913), counted with a microscope the scintillations released by alpha particles impinging on zinc sulphide. The advancement in the study of the photoelectric effect led to the production of the photocathode. The first compound photocathode made of Ag-O-Cs was discovered in 1929 by Koller (1930) and Campbell (1931). Since then various photocathode have been developed including bialkali photocathodes for visible region, multialkali with sensitivity extending into the near infrared region and alkali halide photocathode intended for ultraviolet detection.

The development of the photomultiplier is rooted in early studies of secondary electron emission. Photomultiplier tubes have been making rapid progress since development of photocathodes and secondary emission

multipliers. In 1902, Austin and Starke (Bruining, 1954) reported that the metal surfaces impacted by cathode rays emitted a larger number of electrons than were incident. Iams and Salzberg (1935), succeeded in producing a triode photomultiplier tube with a photocathode combined with a single-stage dynode mounted on the axis, and a collector grid surrounding the dynode. The tube had a gain of about eight. Because of its better frequency response the single-stage PMT was used for movie sound pickup. Zworykin *et al*, (1936) and Kubetsky (1937), achieved electron multiplication by secondary emissions from metal surfaces, because of a photomultiplier tube (PMT) having multiple dynode stages they developed. The dynode surfaces were of low work function and therefore liberated several electrons for each electron striking them (D'Ambrosio and Leutz, 2003).

Photomultiplier Tube (PMT) Operation

A Photomultiplier tube is a vacuum device consisting of an input window, a photocathode, and an electron multiplier sealed in an evacuated glass tube, which produces an output signal through the following process:

Light passing through the input window excites the electrons in the photocathode so that electrons are emitted into the vacuum (external photo electric effect). The photoelectrons are accelerated and focused by the focusing electrode onto the first dynode where electrons are multiplied by means of secondary emission. The secondary electrons emitted from the last dynode are finally collected by the anode.

A typical working principle of PMT is shown in Figure 2.1. Incident photons strike the photocathode and emit electrons with low energy because of

the photoelectric effect. These few electrons are accelerated and focused by the electric field towards a series of dynodes where extra electrons are produced. Each dynode has a higher positive voltage than the previous one. This showering effect generates 10^5 to 10^7 electrons for each photon hitting the first cathode depending on the series of dynodes and the accelerating voltage. At the end these electrons are accumulated at the anode where the level of the signal can be measured.

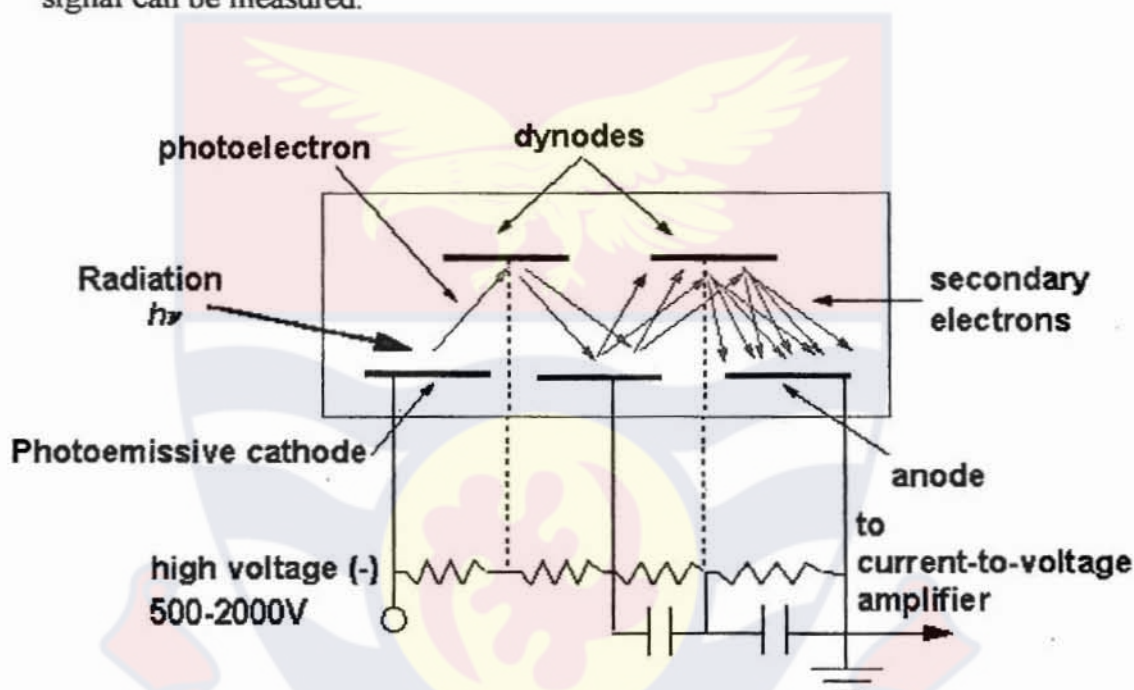


Figure 1: The schematic view of working principle of the PMT (PMT Design, <http://elchem.kaist.ac.kr/vt/chemed/optics/detector/pmt.htm>).

The head-on or end-on design, where light goes into the flat, circular top of the tube, is one of the well-known photomultiplier orientations and the side-on design, where light enters at a particular spot on the side of the tube, is the second important photomultiplier orientation. In addition, the transmission of the window material through which the light passes and the arrangement of the dynodes affect the performance of different photocathode materials. Various combinations of the dynode, window material,

and photocathode materials are used for making different kinds of photomultiplier models (Photomultiplier, <http://en.wikipedia.org/wiki/Photomultiplier>).

Gamma Ray Interactions with Matter

Of the various ways gamma rays can interact with matter, only three interaction mechanisms have real significance in gamma-ray spectroscopy namely: photoelectric absorption, Compton scattering, and pair production. Photoelectric absorption predominates for low-energy gamma rays (up to several hundred keV), pair production predominates for high-energy gamma rays (above 5-10 MeV), and Compton scattering is the most probable process over the range of energies between these two extremes (keV-MeV).

Photoelectric Absorption

In photoelectric absorption process, an incoming gamma-ray photon undergoes an interaction with an absorber atom in which the photon is absorbed and a photoelectron is produced from the electron shell of the absorber atom with kinetic energy given by the incident photon energy ($h\nu$) minus the binding energy of the electron in its original shell (E_b).

That is

$$E_{e^-} = h\nu - E_b \quad 2.1$$

The interaction is with the atom as a whole, and cannot take place with free electron. For typical gamma rays of sufficient energy, the photoelectron is most likely to emerge from the K shell, for which typical binding energies range from

a few keV for low atomic number (Z) material to tens of keV for materials with higher atomic number (Z).

Conservation of momentum requires that the atom recoils in this process, but its recoil energy is very small and usually can be neglected. In addition to the photoelectron, the interaction also creates an ionized absorber atom with a vacancy in one of its bond (K) shells. The vacancy that is created in the electron shell because of the photoelectric emission is quickly filled by electron rearrangement. In the process, the binding energy is liberated either in the form of a characteristic X-ray or Auger electron. Auger electrons have extremely short range because of their low energy. The characteristic X-rays may travel some distance before being reabsorbed through photoelectric interactions with less tightly bound electron shells of the absorber atoms. Thus, the effect of photoelectric absorption is the liberation of a photoelectron, which carries off most of the gamma-ray energy, together with one or more low energy electrons corresponding to absorption of the original binding energy of the photoelectron. If nothing escapes from the detector, then the sum of the kinetic energies of the electrons that are created must equal original energy of the gamma ray photon. Photoelectric absorption is therefore, an ideal process of measuring the energy of the original gamma ray. The above statement is correct if mono-energetic gamma rays are involved. Under these conditions, the differential distribution of electron kinetic energy for a series of photoelectric absorption events would be a simple delta function.

Compton Scattering

The interaction process of Compton scattering takes place between the incident gamma ray photon and an electron in the absorber material. It is most often the predominant interaction mechanism for gamma ray energies typical of radioisotope sources. In Compton scattering, the incoming gamma ray photon is deflected through an angle θ with respect to its original detection.

The photon transfer a portion of its energy to the electron (assumed to be initially at rest), which is known as a recoil electron. Because all angles of scattering are possible, the energy transferred to electron can vary from zero to a large fraction of the gamma ray energy. The expression, which relates to the energy transfer and scattering angle for any given interaction can be simply derived by writing simultaneous equation for the conservation.

It can be shown that, the energy of the scattered gamma ray $h\nu'$ in terms of its scattering angle θ is given by:

$$h\nu' = \frac{h\nu}{1 + (h\nu / m_0c^2)(1 - \cos \theta)} \quad 2.2$$

where m_0c^2 is the rest mass energy of the electron (0.511 MeV).

The kinetic energy of the recoil electron is therefore

$$E_{e^-} = h\nu - h\nu' = h\nu \left(\frac{(h\nu / m_0c^2)(1 - \cos \theta)}{1 + (h\nu / m_0c^2)(1 - \cos \theta)} \right) \quad 2.3$$

Two extreme cases can be identified:

For small scattering angles θ , where little energy is transferred.

1. One in which $C_{S_{11}O_3}$ in this case, Eqs. (2.2 and 2.3) predict that $h\nu' = h\nu$ and $E_{e^-} \cong 0$.

In this case the recoil Compton electron has very little energy and the scattered gamma ray has nearly the same energy as the incident gamma ray.

2. A head on collision in which $\theta = \pi$. In this extreme, the incident gamma ray is backscattered towards its direction of origin, whereas the electron recoils along the direction of incidence.

Pair Production

The third significant gamma ray interaction is the pair production. The process occurs in the intense electric field near the protons in the nuclei of the absorbing material and corresponds to the creation of an electron-positron pair at the point of complete disappearance of the incident gamma ray photon. Because an energy of $2m_0c^2$ is required to create electron-positron pair, a minimum gamma ray energy is required to make the process energetically possible.

All the excess energy carried in by the photon above the 1.02 MeV required to create the pair goes into kinetic energy shared by the positron and the electron. Because the positron will be subsequently annihilated after slowing down in the absorbing medium, two annihilation photons are produced as secondary products of the interaction. This annihilation radiation has important effect on the response of the gamma ray detector.

Photoemission from Metals and Semiconductors

Different methods of photon detection exist, but they all have in common that incident photons are converted into electrons via the photoeffect, which are subsequently recorded. Einstein explanation of photoemission of electrons from metallic surfaces is considered to be one of the first proofs of the quantized nature of light. The kinetic energy (E_k) of photoemitted electrons depends on the wavelength of the incident photon according to Eq. 2.1.

The number of emitted electrons is proportional to the number of incident photons. The average number of photoelectrons released per incident photon is designated the photoemissive material's Quantum Efficiency (QE). It depends on the properties of the irradiated material and on the energy or wavelength of the incident photons.

To explain the observed variation in QE for different materials by several orders of magnitude, it is useful to consider photoemission as a process involving three steps (Spicer, 1993), (1) absorption of a photon resulting in the transfer of energy from photon to electron, (2) motion of the electron towards the material-vacuum interface, and (3) escape of the electron over the potential barrier at the surface into the vacuum. This allows relating the photoemission characteristics of a material to parameters of the emitter, such as the optical absorption coefficient, electron scattering mechanisms in the bulk and the height of the potential barrier at the surface (Sommer, 1980).

Energy losses occur in each of these steps. In the first step, only the absorbed portion of the incident light is effective and thus losses by light transmission and reflection reduce the quantum efficiency. In the second step, the photoelectrons may lose energy by collision with other electrons (electron

scattering) or with the lattice (phonon scattering). In the last step, the potential barrier at the surface prevents the escape of some electrons.

Metals do not constitute efficient photoemitters. Metallic surfaces have a high reflectivity for photons and secondly excited electrons in the bulk rapidly lose their kinetic energy in collisions with the large number of free electrons in the metal through electron-electron scattering. Thus only electrons excited in the vicinity of the metal surface have a chance to escape as shown in Figure 2 (a). The average escape depth for photoelectrons is about $10 \pm 50 \text{ \AA}$, while the photons of visible and near UV spectral range can penetrate into the metal up to a depth of 100 \AA . Last, the surface barrier in metals is determined by the work function (in most metals it's above 2 eV). The process of photoemission in metals is schematically depicted in the energy diagrams of Figure 2 (a). The photoemission threshold in metals is given by the work function Φ , defined as:

$$E_{pe} = \Phi = E_0 - E_F = h\nu \quad 2.4$$

It is easy to define the threshold wavelength for photoemission in metals:

$$E_{pe} = h\nu_0 = \frac{hc}{\lambda} \quad 2.5$$

$$\lambda_{\max} = \frac{ch}{E_{pe}[\text{eV}]} = \frac{1236}{E_{pe}[\text{eV}]} [\text{nm}] \quad 2.6$$

where c is the speed of light and h is the Planck's constant.

The photoemission threshold for pure metals is between 2 eV and 6 eV. The boundaries of visible spectral range correspond to wavelengths between 380 nm and 780 nm, i.e. to photon energies between 1.6 - 3.25 eV. The majority of metals have the photoemission threshold $E_{pe} < 3.25 \text{ eV}$. The short –

wavelength photoemission threshold lies beyond the visible spectra, namely in the UV spectral range. Such metals are not sensitive to visible-light radiation. Among the variety of metals, only alkali and some alkali-earth metals have the photoemission threshold $E_{pe} < 3.25$ eV in the middle of the visible spectral range. Also there are no metals sensitive to radiation with a wavelength longer than 640 nm.

In a semiconductor an absorbed photon creates an electron-hole pair and excites the electron from the VB to the conduction band CB. The electron moves randomly in the conduction band and loses energy in the process. It has a relatively long range of motion as energy losses in semiconductors are dominated by electron – phonon scattering. Electron-electron scattering with considerably higher energy loss per event is strongly suppressed in semiconductors due to the small number of electrons in the conduction band. A photoelectron eventually arriving at the semiconductor surface is emitted into vacuum if it retained sufficient energy to overcome the potential barrier, the *electron affinity* (E_a), of the semiconductor. The average distance an excited electron can travel inside the semiconductor and still overcome the potential barrier is designated the *photoelectron escape length*.

A photon can generate an electron-hole pair if its energy $h\nu$ exceeds the band-gap energy E_g this photon can be absorbed and converted into free electron, i.e. raised from the valence band into the conduction band. Under this condition photo-conductivity (or *internal photo electric effect*) in the semiconductor is achieved. If the photon energy $h\nu$ is larger than the photoemission threshold E_{pe} ,

$$E_{pe} = E_G + E_A$$

2.7

namely the sum of gap energy and the electron affinity, photoelectron emission into vacuum (or external photoeffect) can occur.

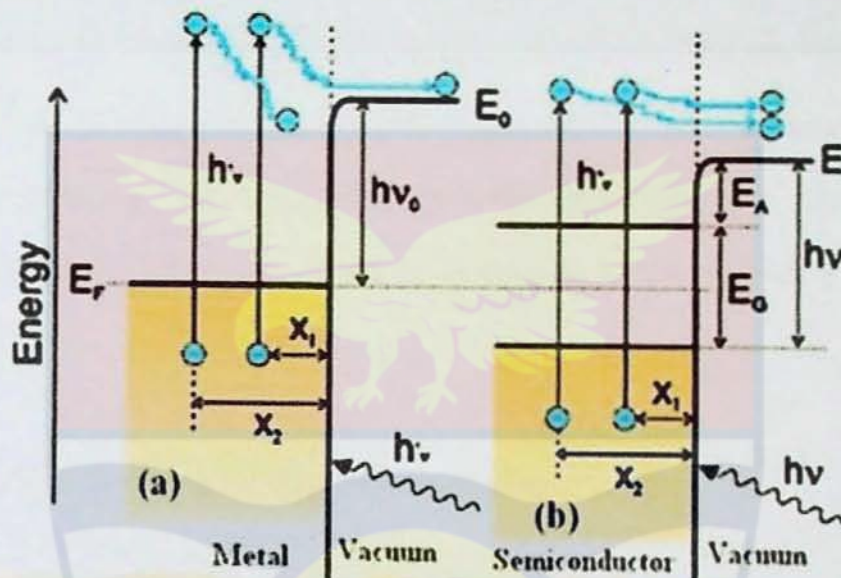


Figure 2: Simplified energy diagram for (a)-Metal and (b)- Semiconductor (Lyashenko, 2009).

Figure 2 is a simplified energy-bands diagram for a metal and a semiconductor both having the same photoemission threshold $h\nu_0$. An incident photon of energy $h\nu$ excites an electron at a distance x_1 or $x > x_1$ from the surface. In the semiconductor, the energy losses for excited electrons as they move to the surface are rather small.

The electrons excited at distances x_1 and x both have sufficient energy to escape into vacuum. In the metal, the excited electrons rapidly lose their kinetic energy in electron-electron collisions. Thus only electrons excited in the vicinity of the surface could escape into vacuum. Here E_F is the Fermi level, E_0 is the energy of vacuum potential barrier, E_g is the band gap of the

semiconductor and E_A is its electron affinity. For the PCs sensitive to visible light, this sum must therefore be less than 3.25 eV (less than 1.6 eV to cover the whole visible region up to 780 nm). This condition is fulfilled in some complex semiconductors has made modern PCs possible.

The Fermi level in Figure 2 (b) is drawn at halfway between valence band top and conduction band bottom assuming an intrinsic semiconductor. In a semiconductor the Fermi level determines the thermionic work function (hence the thermionic emission), which on diagram above corresponds to $E_{G/2} + E_A$.

Negative Electron Affinity (NEA) Photocathodes

By a deliberate modification of the semiconductor band-structure the electron affinity E_a can be reduced; moreover photocathodes having the vacuum level below the conduction band minimum can be manufactured, exhibiting negative electron affinity (NEA) (Spicer, 1993; Knoll, 2000). NEA photocathodes for the visible spectral range are obtained, for example, by covering a heavily p-doped semiconductor with a thin layer of CsO having a strong dipole moment and low electron affinity. The p-doping of the bulk in combination with the surface dipole causes strong band-bending at the interface, pulling the vacuum level below the conduction band minimum (Figure 3).

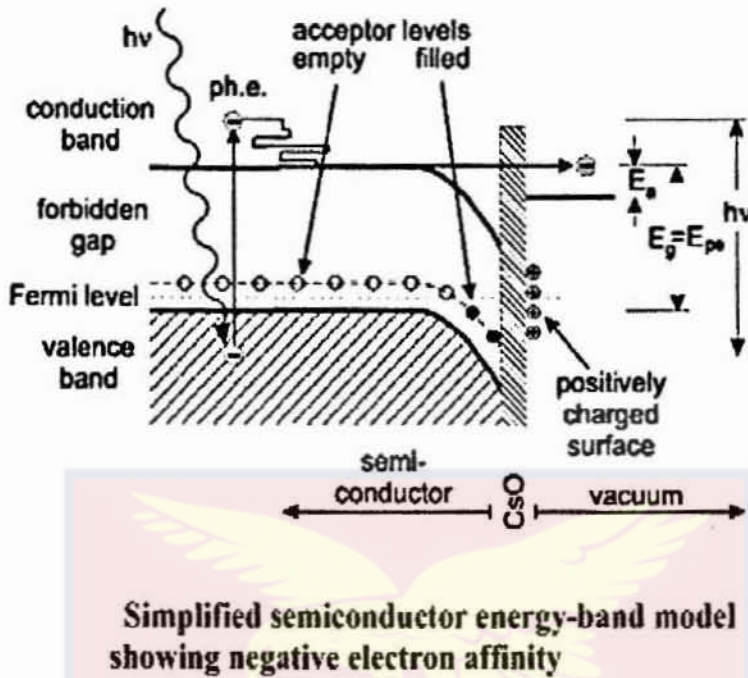


Figure 3: Simplified semiconductor energy model showing Negative electron affinity (Mormann, 2005)

The photoemission threshold of NEA photocathodes is determined by the band-gap energy $E_g = E_{pe}$ only. Photo-excited electrons in the bulk lose their energy in electron-phonon scattering processes and travel $\sim 100 \text{ \AA}$ until they reach the conduction band minimum. Electrons in the conduction band minimum can no longer lose small amounts of energy in electron-phonon interactions due to a lack of energetic states in the band gap. They continue to stay in the conduction band minimum for a long time and typically travel $10,000 \text{ \AA}$ before recombining with a hole.

In *standard* photocathodes the positive electron affinity prevents electrons in the conduction band minimum to contribute to the photoemission.

In NEA affinity photocathodes these electrons do contribute to the photoemission and high QE values (exceeding 50%) over a broad spectral range are observed. NEA is reported for many semiconductors, in particular III-V

semiconductors (GaAs-CsO) are widely used and commercially available (Arisaka, 2000; Bradbury *et al.*, 1997; Mirzoyan, *et al.*, 2000).

Furthermore, in ternary compounds, such as GaAsP, the band-gap may be tailored by varying the material composition, thus tuning the sensitivity range of the photocathode to the requirements (Mormann, 2005). Unfortunately, the fabrication of NEA photocathodes for the visible spectral range is difficult and complex, involving the epitaxial deposition of several layers of single crystal semiconductors. They retain their properties only in ultra-high vacuum conditions, restricting their use to small areas in well controlled and ultra-clean environments

Photocathode of the PMT

The basic radiation sensor of PMT is the photocathode which is located inside the vacuum envelope. Photoelectrons are emitted and directed by an appropriate electric field to an electrode or dynode within the envelope. The conversion efficiency for light to electrons, also known as quantum efficiency, is typically 1 to 3 photoelectrons per 10 incident photons (Simon *et al.*, 2003). A number of secondary electrons are emitted at this dynode for each impinging primary photoelectron. These secondary electrons in turn are directed to a second dynode and so on until a final gain of perhaps 10^6 is achieved. In order to achieve reasonable quantum efficiencies, the photocathode composition must be of low work function and of optimum thickness so that photon absorption is balanced with electron emission (D'Ambrosio and Leutz, 2003). Soon after Gorlich (1936), found that the mixture of cesium and antimony improved efficiency.

Much of the development work on photomultiplier tubes has been concerned with their physical configuration and the related electron optics. But a very important part of the development of photomultiplier tubes was related to the photocathode and secondary-emission surfaces and their processing. Radio Corporation of America (RCA) was very fortunate during the 1950's and 60's in having on its staff, probably the world's foremost photocathode expert, Sommer (1968). His treatise on photoemissive materials continues to provide a wealth of information to all photocathode process engineers (Burle Industries Inc, 1980). Very high secondary-emission yields have been reported (Mostovskii, *et al*, 1964; Ghosh and Varma 1978) for $\text{Na}_2\text{KSb:Cs}$, the multi-alkali photocathode (S-20 response). A very practical secondary emitter can be made from an oxidized silver-magnesium Alloy (Zworykin *et al* 1941; and Rappaport, 1954) containing approximately 2 % of magnesium. Although Silver-magnesium dynodes do not have as high a secondary-emission ratio as some of the materials mentioned earlier, the material is easily processed and is more stable at relatively high currents.

A material having characteristics very similar to those of silver-magnesium is an oxidized layer of copper-beryllium alloy (Allen, 1947; Tyutikov, 1963; and Sommer, 1958) in which the beryllium component is about 2 % of the alloy. Secondary emission is usually enhanced by the bake-out in cesium vapour. Because of the advantages in handling and the manufacturing cost, the copper-beryllium is largely taking the place of silver-magnesium in applications requiring low dark emission and stability at relatively high current densities.

Reflective and Semitransparent Photocathodes (PCs)

Photocathode in most of photo-sensors is usually a thin layer of semiconductor photo-sensitive material deposited either onto a transparent substrate or reflective (metal) substrate. One distinguishes reflective (or opaque) from semi-transparent (or transmissive) photocathodes according to their mode of operation. In reflective photocathodes, light incident on a thick photoemissive film and the electrons are emitted backwards (Figure 4 (a)), while in semitransparent photocathodes the photoemissive material deposited onto a transparent substrate is illuminated from the substrate side and the electrons are emitted in a forward direction (Figure 4 (b)).

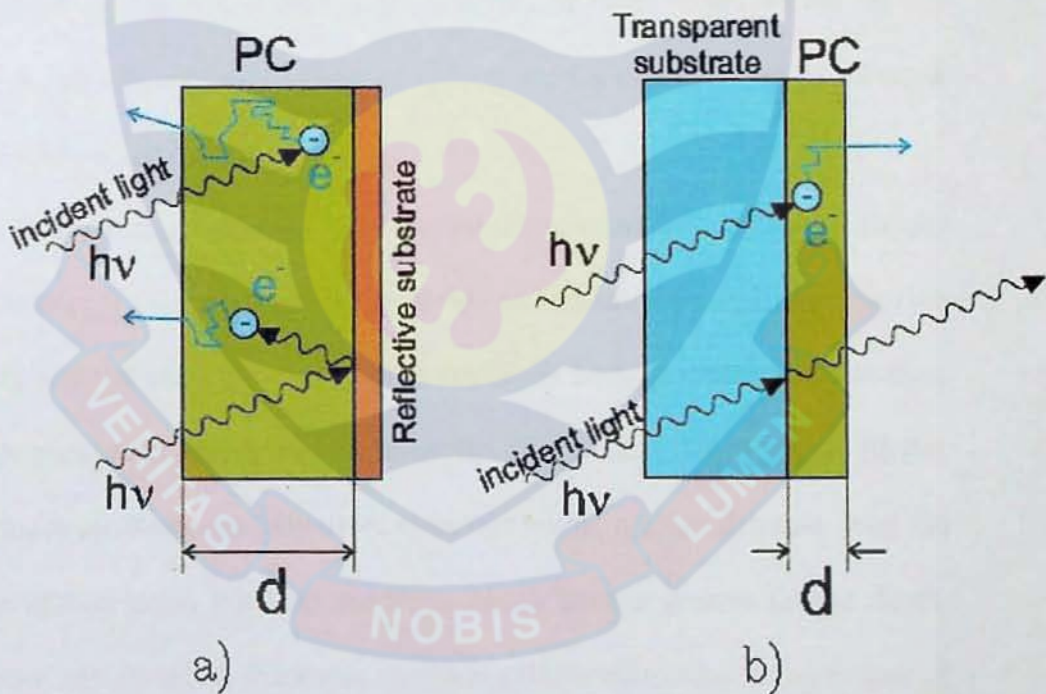


Figure 4 Types of Photocathodes (a)- Reflective (b)- Semitransparent (Lyashenko, 2009)

For semi-transparent PCs the thickness of the cathode film has a critical optimum value. If the thickness exceeds the escape depth of photoelectrons, the

sensitivity is unnecessarily reduced, because photoelectrons produced by light absorbed beyond the escape depth cannot be emitted into vacuum. On the other hand, if the thickness is much smaller than the escape depth the sensitivity may be reduced, since a fraction of the incident light is transmitted rather than absorbed.

For reflective PCs, the cathode thickness is less critical. If the cathode is deposited onto a reflective (usually metal) substrate, the incident light which was not absorbed in the cathode is reflected back by the substrate and could be absorbed when the light passes the PC for the second time (Figure 4 (b)). The reflective PCs exhibit higher QE values due to an efficient light absorption and are simpler in fabrication due to the absence of strict requirements on the thickness. However, the coupling of reflective PCs of large area to electron multipliers is more difficult.

The optimal thickness of a semi-transparent PC is not a unique characteristic for a particular PC material. In semiconductors the absorption constant and the photoelectron escape depth are both wavelength dependent; they increase with decreasing wavelength. This means that, light of shorter wavelength produces not only more electrons within a given distance from the surface of incidence, but also electrons which have a greater escape depth. Therefore, the optimum thickness represents the compromise between loss of light by transmission and loss of those electrons that cannot escape; it is wavelength dependent. As a result, the spectral response of a semi-transparent PC can be modified to a certain extent by using the optimum thickness for the spectral region in which maximum sensitivity is required. For instance, because of low light absorption near the threshold wavelength, increased PC thickness

tends to enhance long wavelength response at the expense of sensitivity in shorter wavelengths.

Photocathode Materials of PMTs

Most photocathodes (Hamamatsu Photonics, 2007) are made of compound semiconductor mostly consisting of alkali metals with low work function. There are about ten kinds of photocathodes which are currently in practical use. Each photocathode is available in transmission (semi-transparent) type and (or) in reflection (opaque) type with different device characteristics. Some of the photocathode materials commonly used in PMTs are as follows:

Cs-I

The Cs-I PMT is insensitive to solar radiation and therefore often called solar blind PMT. Its sensitivity falls sharply at wavelengths longer than 200 nm and it is exclusively used for vacuum ultraviolet detection. As window materials, MgF_2 crystals or synthetic silica are used because of high ultra violet transmittance.

Although Cs-I itself has high sensitivity to wavelengths shorter than 115 nm, the MgF_2 crystal used for the input window does not transmit wavelengths shorter than 115 nm. This means that the spectral response of a PMT using combination of Cs-I and MgF_2 covers a range from 115-200 nm.

Infrared Ag-O-Cs (S-1)

One of the first photocathodes available for practical applications was the Ag-O-Cs, or S-1, photocathode. The structure of the photocathode consists of silver particles distributed throughout a matrix of Cs_2O with a thin layer of $Cs_{11}O_3$ on its surface. The $Cs_{11}O_3$ lowers the electron affinity at the surface so that the Ag-O-Cs is a negative electron affinity surface with a work function of 1.55 eV (Bates, 1981).

In this configuration, quantum efficiency (QE) levels for the Ag-O-Cs peak in the infrared around 1%. This peak is due to resonance absorption in the silver particles. Additionally, the low quantum efficiency (QE) in the visible is due to reflection from the film of silver on the outer surface of the photocathode (Bates, 1981).

While 1 % quantum efficiency is low, Ag-O-Cs has historically been the top performing photocathode for the infrared region.

Sb-Cs

This type of photocathode material used PMT has sensitivity in the ultra violet to visible range, and is widely used in many applications. Because the resistance of the Sb-Cs photocathode (PC) is lower than that of the alkali PC described below, it is suited for applications where light intensity to be measured is relatively high so that a large current can flow in the cathode. It is also used where changes in the photocathode resistance due to cooling affects measurements. Sb-Cs is chiefly used in the reflection type photocathode.

Bialkali (Sb-Rb-Cs, Sb-K-Cs)

These have a spectral response range similar to the Sb-Cs photocathode, but have higher sensitivity and lower noise than Sb-Cs. The transmission mode bialkali photocathodes also have a favourable blue sensitivity for scintillator flashes from NaI(Tl) scintillators, thus are frequently used for radiation measurement using scintillation counting of most scintillators. Hence, it is mostly used for scintillator applications.

High Temperature Bialkali (HTB)

The HTB major application is oil well logging, and is useful at higher operating temperatures up to 175 °C. Moreover, it can perform with very low dark current at the room temperature.

Extended Green Bialkali

A variant of bialkali photocathode, has particularly high sensitivity in the green region. It fits for scintillating tile or fiber calorimeters with wavelength shifters and for CsI(Tl) scintillators. The spectral response range is defined by the materials of the photocathode and the window (Hamamatsu Photonics and Assemblies, 2005).

High temperature bialkali or low noise bialkali (Na-K-Sb)

This is particularly useful at higher operating temperatures since it can withstand up to 175 °C. A major application is in the oil well logging industry. At room temperatures, this photocathode operates with very low dark current,

making it ideal for use in photon counting applications (Hamamatsu Photonics and Assemblies, 2005).

Visible: Na₂KSb:Cs (S-20)

Sommer's most noteworthy contribution was the Na₂KSb:Cs, or S-20, photocathode. The Na₂KSb:Cs photocathode has a high sensitivity in the UV and visible that extends into the infrared, more than the earlier Cs₃Sb photocathode. The spectral response of Cs₃Sb was limited, barely extending through the visible. The Na₂KSb:Cs photocathode is also more stable at higher temperatures than Cs₃Sb and has a low dark emission rate. The success of Na₂KSb:Cs led the Radio Corporation of America (RCA) team to use the photocathode as a match to the NaI:Tl crystals used in scintillation counting (Burle Industries, Photomultiplier Handbook). Figure 3 illustrates the quantum efficiency of several commercial photocathodes. From Figure 6 (Hallensleben, *et al*, 1999) it is clear that the Na₂KSb:Cs photocathode (IV) has a high quantum efficiency over the visible spectrum, peaking in the UV near 30 %. The photocathode has an efficiency around 10 % in the red, dropping down below 1 % in the infrared.

Ultraviolet: K₂CsSb

Sommer (1983) reports on his accidental development of the K₂CsSb photocathode in 1963. During the formulation of Na₂KSb:Cs, Sommer accidentally added the caesium before the sodium and observed an unusually high blue response before adding sodium. This accident resulted in the development of the KCsSb photocathode, has a high quantum efficiency in the

UV region. While most often used commercially for detection of blue light, K_2CsSb (VI) has quantum efficiencies approaching 30 % in the UV. As a result, K_2CsSb is almost universally used commercially as a blue through UV detection photocathode (Morton, 1968).

Spectral Response of the PMTs

Energy of the incident light is converted into photoelectrons by the external photoelectric effect of the photocathode of the PMT. The efficiency of transformation which means photocathode sensitivity depends on the wavelength of the incident light. This dependence is called the spectral response characteristics (Figure 5).

Quantum Efficiency and Radiant Sensitivity for the PMTS

Quantum efficiency (QE) means the ratio of the number of photoelectrons emitted from the photocathode to the number of incident photons expressed as a percentage. The (QE) equation is given below (Hamamatsu Photonics and Assemblies, 2005);

$$QE = \frac{\text{Number of Photoelectrons}}{\text{Number of Photons}} \times 100(\%) \quad 2.8$$

Radiant sensitivity (S) means the ratio of the photoelectric current from the photocathode to the incident radiant power at a given wavelength, determined in A/W (ampere per watt). The S equation is given by:

$$QE = \frac{\text{Photoelectric Current}}{\text{Radiant Power of Light}} \times 100(\%) \quad 2.8$$

Radiant sensitivity and quantum efficiency are related to each other at a given wavelength by (Hamamatsu Photonics and Assemblies, 2005);

$$QE = \frac{S \times 1240}{\lambda} \times 100\% \quad 2.9$$

where λ is the wavelength measured in nanometres

The Window Materials of PMTs

Some of the well-known window materials used in PMTs are:

Borosilicate glass

The most commonly used material is the borosilicate glass. It sends light from the infrared to around down to a wavelength of 300 nm (Figure 5). It includes very little potassium (K_2O and ^{40}K) which is able to create unwanted background noise because of its radioisotopes. For this reason, the low noise borosilicate glass (this is called K-free glass) may be used for scintillation counting applications (Figure 5).

UV-transmitting glass

This glass transmits ultraviolet light well and is widely used. The UV break off wavelength is about 185 nm (Figure 5).

Synthetic silica

Synthetic silica transmits ultraviolet light down to 160 nm (Figure 5). Silica is unsuitable for the stem material of tubes because of having a different thermal expansion coefficient from kovar metal which is used for the tube leads.

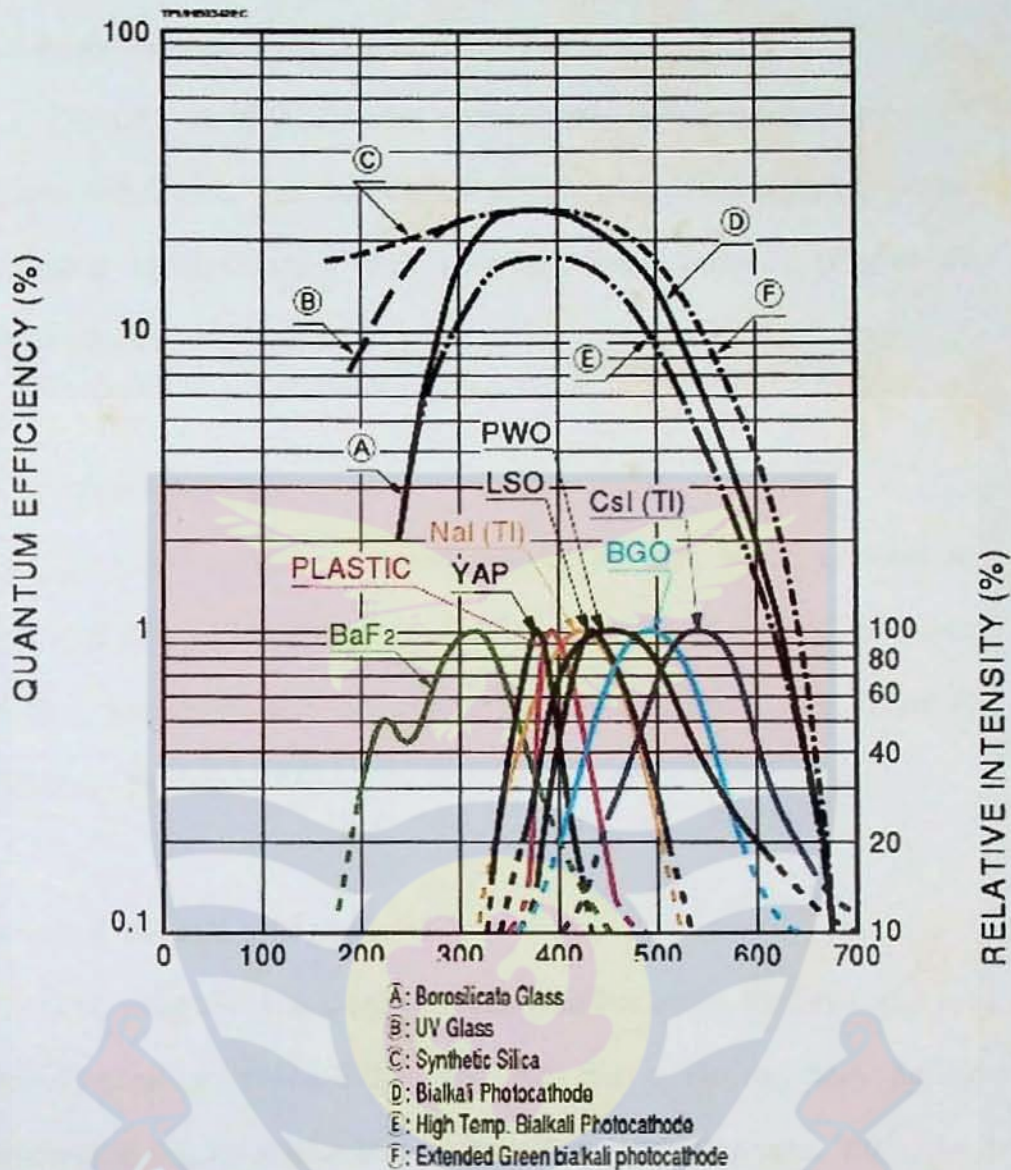


Figure 5: Typical Spectral Response and Emission of PMTs The photocathode material on the long wavelength edge and the window material on the short wavelength edge determine the spectral response range (Hamamatsu Photonics, 2006).

The Dynodes (Electron Multiplier) of PMTs

A low noise electron multiplier which increases electrons in vacuum with a secondary emission process causes the higher sensitivity (high gain and high signal to noise (S/N) ratio) of PMT.

The Linear-Focused Type (LFT)

The LFT of PMT dynodes continuously increases the number of electrons and focuses the electron paths. This type of multiplier provides fast timing characteristics, high gain and high linearity (Figure 6) (Hamamatsu Photonics, 2006).

The venetian-blind type

The venetian-blind is another type of dynodes which contains an assembly of parallel strips. This type of dynodes provides great collection efficiency, and respectable immunity to external magnetic fields (Figure 6) (Hamamatsu Photonics, 2006).

The box or box and grid type

This multiplier has a big collection surface at the first dynode, and therefore great collection efficiency, but has a bit degraded timing characteristics (Figure 6) (Hamamatsu Photonics, 2006; Photonics, 2007).

The circular cage type

The circular cage type multiplier leads to highly compact arrangements (Figure 6) (Hamamatsu Photonics, 2006; Photonics, 2007)

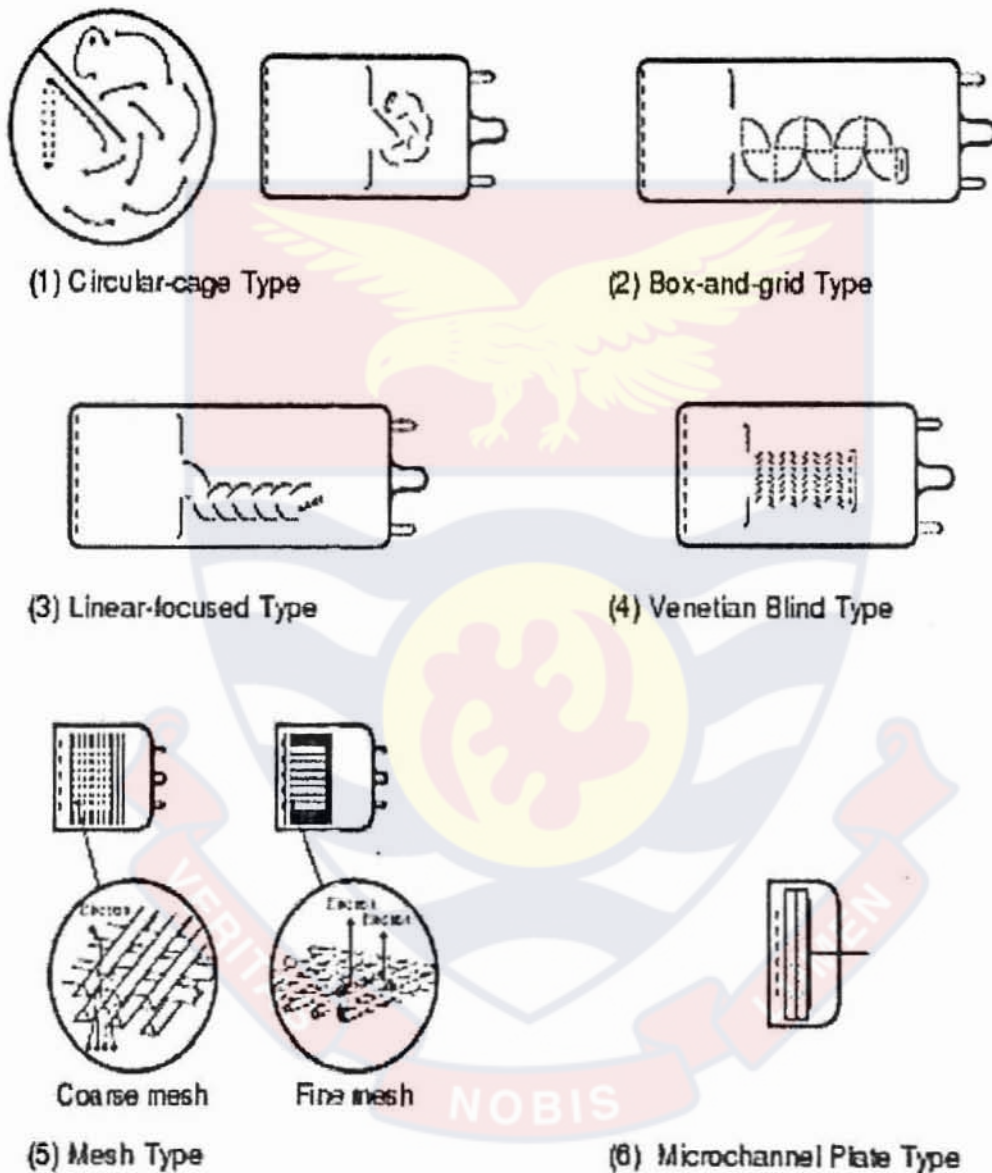


Figure 6: The schematic view of the dynode (electron multipliers): (1) circular cage, (2) box-and-grid (3) linear focusing, (4) venetian blind, (5) foil and (6) MCP (Hamamatsu Photonics, 2006).

The Microchannel plate (MCP) type of dynode

The Photomultiplier contains a microchannel-plate electron increase with a proximity focused cathode at one side and an anode at the other. The Microchannel plate where one electron at the input is multiplied is a compact aggregation of parallel glass tubes of microscopic diameter (6 - 25 μ) (Hamamatsu Photonics, 2007).

The foil type

The foil multiplier with dynodes is pierced by metal foil, which is a precision-designed alternative to standard mesh dynodes. Foil dynodes which supply quite low crosstalk are utilized in the segmented tubes of multi-channel PMTs (Figure 6) (Hamamatsu Photonics, 2007)

The Anode of PMTs

The anode of the PMTs is an electrode which collects secondary electrons multiplied in the cascade process through multi-stage dynodes and outputs the electron current to an external circuit (Hamamatsu Photonics Assemblies, 2005).

The PMT anode current has a relationship with the photoelectric output from the photocathode and gain. Photoelectric current is proportional to the density of the incident light (Hamamatsu Photonics, 2007).

The Gain (Current Amplification)

An electric field accelerates photoelectrons which are emitted from a photocathode to strike the first dynode and produce secondary electron emissions. These secondary electrons then beat upon the next dynode to generate additional secondary electron emissions. Repeating this cascade process through successive dynode stages, a high gain is achieved. Thus a little photoelectric current from the photocathode can be detected as a large output current from the anode of the PMT. Gain is the ratio of the anode output current to the photoelectric current from the photocathode. Ideally the gain of the PMT is shown as δ^n , where n is the number of dynode stages and δ is an average secondary emission factor. The secondary electron emission ratio, δ is given by (Hamamatsu Photonics Assemblies, 2005):

$$\delta = AE^\alpha \quad 2.10$$

where A is a constant, E is the voltage between the dynode stages, and α is a coefficient defined by the dynode material and the geometric structure. Its value is frequently between 0.7 and 0.8. If a voltage (V) is applied between the cathode and the anode of the PMT having n dynode stages, the gain G is defined as (Hamamatsu Photonics Assemblies, 2005);

$$G = \delta^n = (AE^\alpha)^n = \left\{ A \left(\frac{V}{n+1} \right)^\alpha \right\}^n = \frac{A}{(n+1)^{\alpha n}} V^{\alpha n} = KV^{\alpha n} \quad 2.11$$

where (K is a constant).

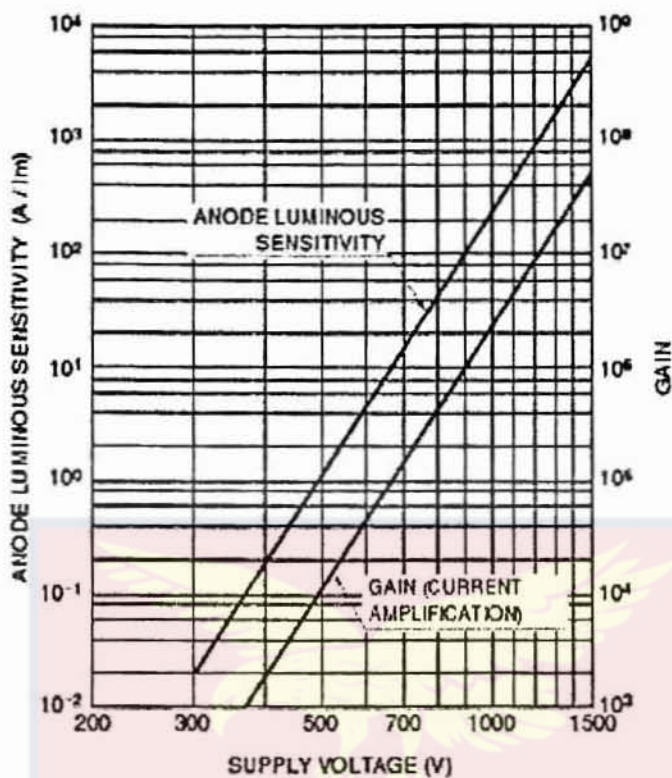


Figure 7: Sample plot of gain vs. supply voltage for PMTs (Hamamatsu Photonics, 2006)

Figure 7 shows the gain characteristics of a PMT. Due to the fact that PMTs usually have 8 to 12 dynode stages, the changes in applied voltage between stages increase the anode output directly by the 6th to the 10th power. The output signal of the PMT is very sensitive to fluctuations in the power supply voltage; hence the power supply should be extremely stable and demonstrate minimum ripple, drift and temperature coefficient (Hamamatsu Photonics and Assemblies, 2005).

The Anode dark current of PMTs

A small quantity of output current which occurs in a PMT even if it is in complete darkness is called the anode dark current. The dark current and the noise are crucial factors to define the lower limit of light detection. Main

reasons of the dark current are explained as follows (Hamamatsu Photonics and Assemblies, 2005):

Thermionic emission of electrons

Because the materials of the photocathodes and dynodes have very low work functions, they emit thermionic electrons even at room temperature. The dark current originates mostly from the thermionic emission of the photocathode, and it is increased by the dynodes (Hamamatsu Photonics, 2007).

Ionization of residual gases

The flow of photoelectrons can ionize the remaining gases inside the PMT. If these ions hit the photocathode or earlier stages of dynodes, secondary electrons can be emitted. Therefore, this effect causes relatively large output noise pulses which are generally observed as after pulses following the primary signal pulses which may be a problem in detecting short light pulses (Hamamatsu Photonics and Assemblies, 2005).

Glass scintillation

In case of deviation of electrons from their normal trajectories and hitting the glass envelope, scintillations may happen and dark pulses may occur. PMTs may be used with the anode at a high voltage and the cathode at the ground potential so that these pulses can be eliminated (Hamamatsu Photonics and Assemblies, 2005).

Ohmic leakage

Insufficient insulation of the glass stems base and socket results in ohmic leakage, which may be another source of dark current. This primarily occurs in operation of a PMT at a low voltage or low temperature. In addition, dirt and humidity on the surface of the tube may create ohmic leakage (Hamamatsu Photonics and Assemblies, 2005).

Field emission

In operation of the PMT at a voltage close to the maximum value, strong electric fields causing dark pulses may emit electrons from electrodes (Hamamatsu Photonics and Assemblies, 2005).

The Collection Efficiency of PMTs

In order to multiply efficient electrons at each stage of dynode, the electron multiplier mechanism of a PMT is designed with consideration to the electron trajectories. Although some of the electrons can deviate from their proper trajectories, they do not contribute to multiplication very much (Hamamatsu Photonics, 2005)

Generally, the probability of photoelectrons landing on the effective area of the first dynode is called the collection efficiency. The effective area is the area of the first dynode in which photoelectrons may be multiplied effectively at the successive dynode stages without deviating from their proper trajectories. In spite of existing secondary electrons which do not contribute to multiplication at the second dynode or latter dynodes, they will

have less effect on the total collection efficiency as the number of secondary electrons emitted increases greatly. So the photoelectron collection efficiency at the first dynode is important.

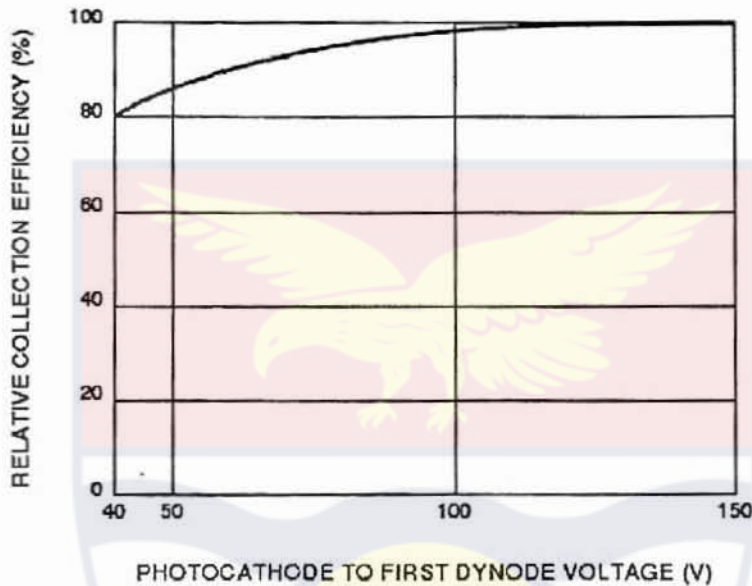


Figure 8: Typical collection efficiency on PMT (Hamamatsu R6095) as a function of cathode-to-first dynode voltage.

Figure 8 shows that approximately 100 volts must be applied between the cathode and the first dynode. Energy resolution, detection efficiency and signal-to-noise ratio in scintillation counting are influenced by the collection efficiency. The detection efficiency is the proportion of the detected signal to the input signal of a photomultiplier tube (Hamamatsu Photonics, 2005).

The collection efficiency of PMTs, a subjective parameter, is difficult to measure and for which no standardized methods have been defined. It differs considerably between PMT types, reflecting differently designed electro-optical input systems.

High Voltage Power Supplies

High voltage D.C. power supply is widely used in research work (especially in the field of applied physics) and in industry level the main application of high voltage D.C., power supply is in proof design of high voltage cables with relatively large capacitive load, which draws high current if it is tested with A.C. high voltage power supply of sinusoidal waveform instead of d.c. voltage (Kuffel *et al.* 2000).

There are several application of D.C. high voltage, in the field of electrical engineering and applied physics, such as electron microscope, X-rays, electrostatic precipitators, particles accelerator in nuclear physics, dielectric testing and so on (Naidu and Kamaraju, 2004).

High voltage equipment are used to study the dielectric behaviours under all conditions where the equipment apparatus are likely to encounter. The tests are conducted with voltage higher than the normal working voltage to find out the safety factors over the working conditions and to ensure that the working margin is neither too high nor too low (Dwivedi, and Daigavane, 2011)

The high voltages, in use, can be divided in to the following categories,

- i) A.C. high voltage
- ii) D.C. high voltage and
- iii) Transient voltage (Mazen and Radwan, 2000)

Joseph (2001), presented his paper on the basic operation of multiplier circuit such as half wave voltage doubler and tripler circuits, and discussed guide lines for electronic components selection for diodes and capacitors.

Spencer *et al.* (2001) designed prototype surface mounted Cockcroft-Walton board and tested for use in battery operated, palm sized radiation

detection device and it took around output voltage of 1 kV and current less than 15 mA (approx.). In addition to circuit components, the board contains sockets which hold two Hamamatsu R7400P PMTS.

Voltage-Multiplier Circuits

Voltage-multiplier circuits are employed to maintain a relatively low transformer peak voltage while stepping up the peak output voltage to two, three, four, or more times the peak-rectified voltage.

Aintablian and Hill (1994) discussed about the single phase harmonic reduction circuit based on voltage multiplier circuit using switch operated on line frequency instead of using switch mode technology. The advantage of this circuit was that of low cost, high reliability and simple control. The disadvantage of this circuit was that it could not completely control the harmonic current. John (1993), explained single phase voltage doublers, pulse width modulation (PWM) boost rectifiers and has obtained three types of switching pattern namely unipolar PWM, bipolar PWM and phase adjusted unipolar PWM. When high voltage output is required, the voltage doublers rectifier is able to generate a. c. line current with lowest current distortion. Yamamoto *et al.* (2000), proposed power factor correction scheme using voltage doublers rectifier circuit without switching device.

Voltage Doubler Circuit

The network of Figure 9 is a half-wave voltage doubler. During the positive voltage half-cycle across the transformer, secondary diode D_1 conducts (and diode D_2 is cut off), charging capacitor C_1 up to the peak rectified voltage (V_m).

Diode D_1 is ideally a short during this half-cycle, and the input voltage charges capacitor C_1 to V_m with the polarity shown in Figure 10(a). During the negative half-cycle of the secondary voltage, diode D_1 is cut off and diode D_2 conducts charging capacitor C_2 . Since diode D_2 acts as a short during the negative half-cycle (and diode D_1 is open), we can sum the voltages around the outside loop

Figure 10(b)

$$-V_m - V_{c1} + V_{c2} = 0 \quad 2.12$$

$$-V_m - V_m + V_{c2} = 0 \quad 2.13$$

From which

$$V_{c2} = 2V_m \quad 2.14$$

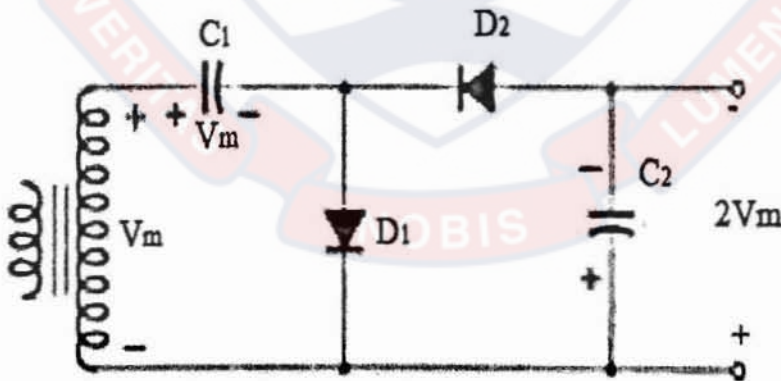


Figure 9: Half – wave voltage doubler (Boylestad, and Nashelsky 1999).

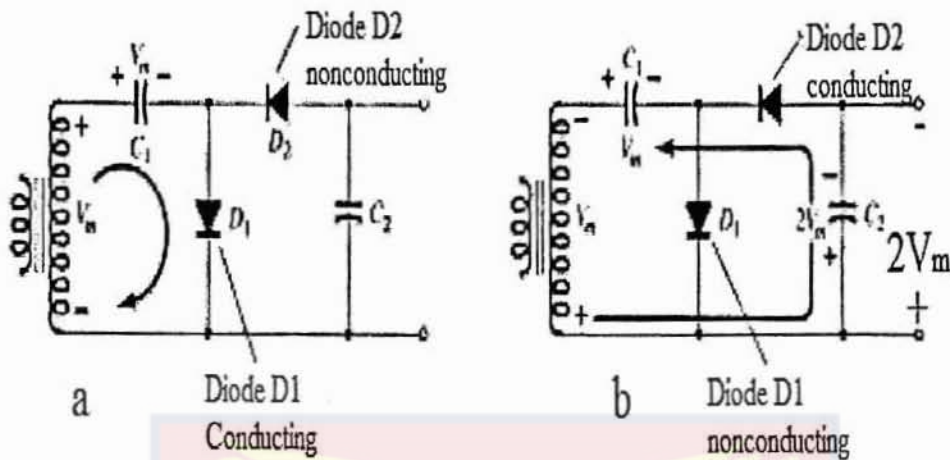


Figure 10: Half – wave voltage doubler operation showing each half-cycle of operation. a).positive half-cycle, b) negative half cycle (Boylestad, and Nashelsky 1999)

On the next positive half-cycle, diode D_2 is non-conducting and capacitor C_2 will discharge through the load. If no load is connected across capacitor C_2 both capacitors stay charged— C_1 to V_m and C_2 to $2V_m$. If, as would be expected, there is a load connected to the output of the voltage doubler, the voltage across capacitor C_2 drops during the positive half-cycle (at the input) and the capacitor is recharged up to $2V_m$ during the negative half-cycle. The output waveform across capacitor C_2 is that of a half-wave signal filtered by a capacitor filter. The peak inverse voltage across each diode is $2V_m$. (Boylestad, and Nashelsky 1999).

Voltage Tripler and Quadrupler

Figure 11 shows an extension of the half-wave voltage quadrupler, which develops three, four and n times the peak input voltage. It should be obvious from the pattern of the circuit connection how additional diodes and capacitors may be connected so that the output voltage may also be five, six, seven, and so on, times the basic peak voltage (V_m).

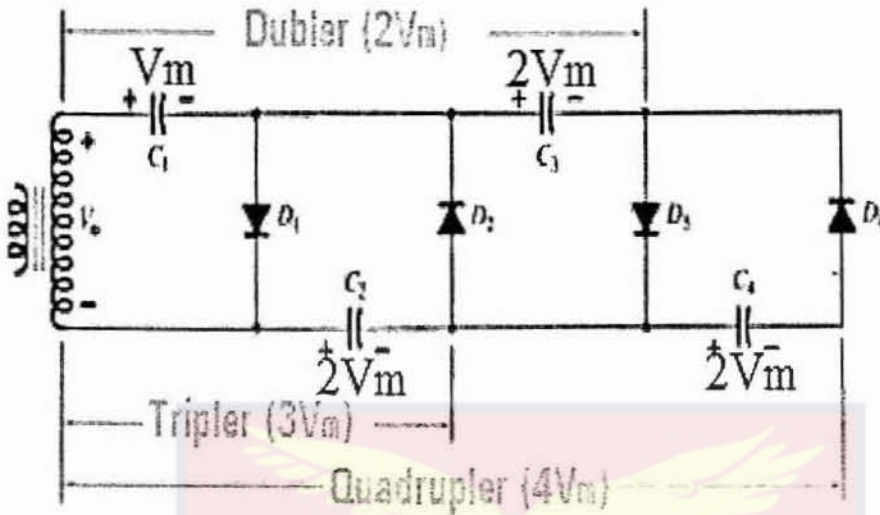


Figure 11: A voltage quadrupler circuit. (Boylestad, and Nashelsky, 1999)

In operation capacitor, C_1 charges through diode D_1 to a peak voltage, V_m , during the positive half-cycle of the transformer secondary voltage. Capacitor C_2 charges to twice the peak voltage $2V_m$ developed by the sum of the voltages across capacitor C_1 and the transformer, during the negative half-cycle of the transformer secondary voltage (Boylestad, and Nashelsky, 1999).

During the positive half-cycle, diode D_3 conducts and the voltage across capacitor C_2 charges capacitor C_3 to the same $2V_m$ peak voltage. On the negative half-cycle, diodes D_2 and D_4 conduct with capacitor C_3 , charging C_4 to $2V$ the voltage across capacitor C_2 is $2V_m$, across C_1 and C_3 it is $3V_m$, and across C_2 and C_4 it is $4V_m$. If additional sections of diode and capacitor are used, each capacitor will be charged to $2V_m$. Measuring from the top of the transformer winding (Figure 11) will provide odd multiples of V_m at the output, whereas measuring the output voltage from the bottom of the transformer will provide even multiples of the peak-voltage, V_m .

The transformer rating is only V_m , maximum, and each diode in the circuit must be rated at $2V_m$ PIV. If the load is small and the capacitors have little leakage, extremely high dc voltages may be developed by this type of circuit, using many sections to step up the dc voltage (Boylestad, and Nashelsky, 1999).

The Cockcroft Walton High Voltage Supply

N-stage single-phase cascade Cockcroft–Walton High voltage circuit is shown in Figure 12.

Cascade Voltage Multiplier with no Load

Figure 12 shows the n-stage single phase cascade voltage multiplier with no load ($I = 0$), the portion (0 - n' - V_t) is a half-wave rectifier circuit in which C_n charges up to a voltage of $+V_{max}$ if V_t has reached the lowest potential, $-V_{max}$. If C_n is still uncharged, the rectifier D_n conducts as soon as V_t increases. As the potential of point n' swings up to $+2V_{max}$ during the period $T = 1/f$, point n attains further on a steady potential of $+2V_{max}$ if V_t has reached the highest potential of $+V_{max}$. The part (n' - n - 0) is therefore a half-wave rectifier, in which the voltage across D'_n can be assumed to be the a.c. voltage source. The current through D_n that charged the capacitor C_n was not provided by D'_n , but from V_t and C_n . It is assumed that the voltage across C_n is not reduced if the potential n' oscillates between zero and $+2V_{max}$. If the potential of n', however, is zero, the capacitor C'_{n-1} is also charged to the potential of n, i.e. to a voltage of $+2V_{max}$. The next voltage oscillation of V_t

from $-V_{\max}$ to $+V_{\max}$ will force the diode D_{n-1} to conduct so that C_{n-1} will also be charged to a voltage of $+2V_{\max}$.

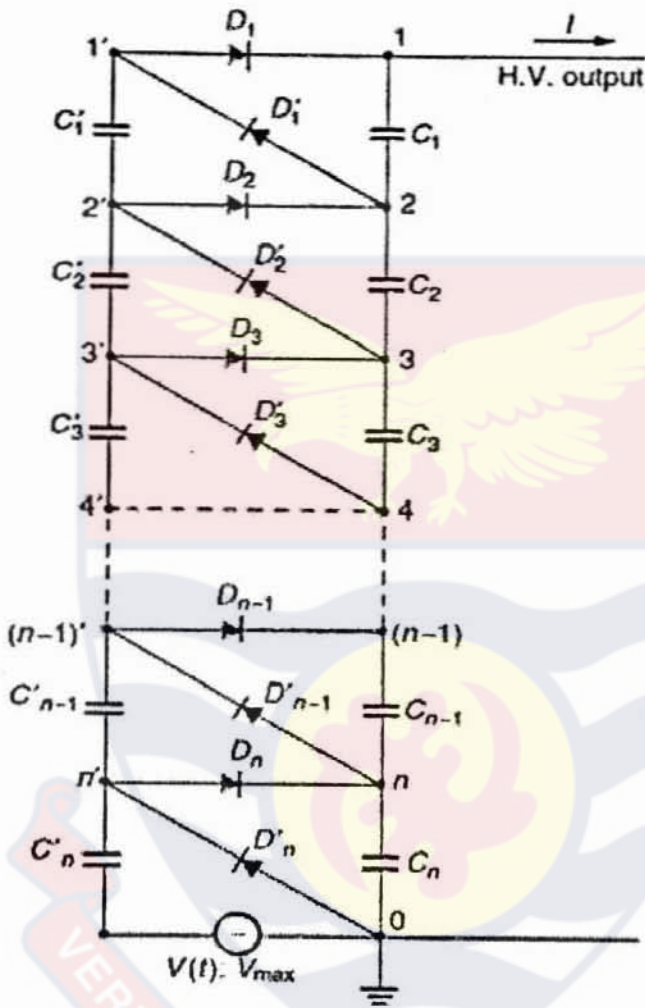


Figure 12: Cascade of the Cockcroft-Walton 4 V multiplier Circuit (Dwivedi and Daigavane, 2001)

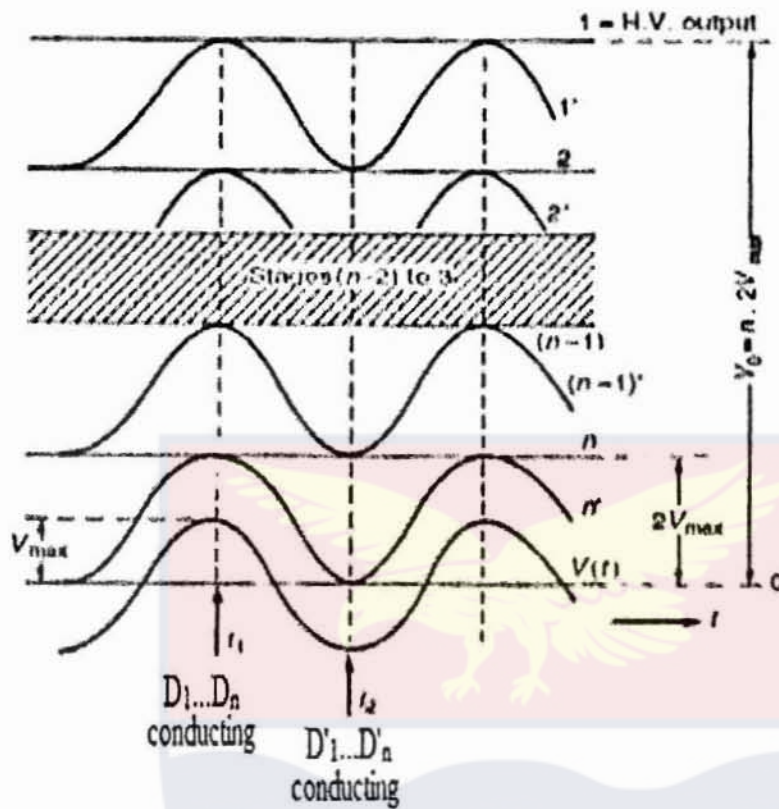


Figure 13: Steady state potentials at the nodes of the circuit are sketched for the circuit for zero load conditions ((Dwivedi and Daigavane, 2001)

From the circuit in Figure 13, it can be seen that:

1. The potential at the nodes $1', 2', \dots, n'$, are oscillating due to the voltage oscillation at V_t .
2. The potentials at the nodes $1, 2, \dots, n$, remain constant with reference to ground potential
3. The voltages across all capacitors are of dc type, the magnitude of which is $2V_{max}$ across each capacitor C_n which is stressed with V_{max} only.
4. Every reciter diode $D_1, D'_1, \dots, D_n, D'_n$, is stressed with $2V_{max}$ or twice A.C. peak voltage.
5. The HV output will reach a maximum voltage of $2nV_{max}$.

Cascade Voltage Multiplier with Load

If the generator supplies any load current I , the output voltage will never reach the value $2nV_{max}$. There will also be a ripple on the voltage, and therefore we have to deal with two quantities: the voltage drop ΔV_0 and the peak-to-peak ripple $2\delta V$. The sketch in Figure 14 shows the shape of the output voltage, ΔV_0 , and $2\delta V$.

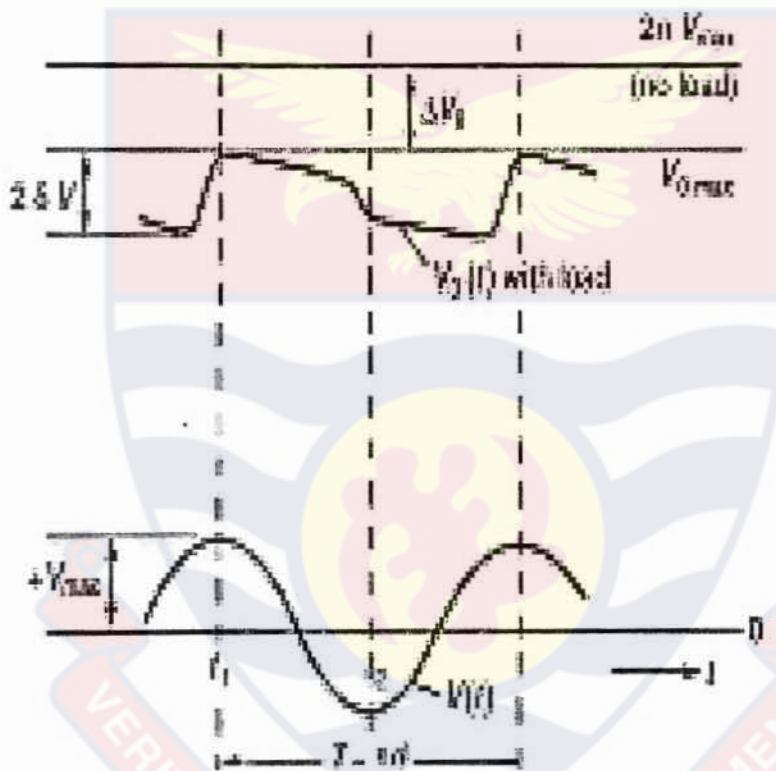


Figure 14: Loaded cascade circuit, showing voltage drop ΔV_0 and δV (Dwivedi and Daigavane 2001)

Let a charge q be transferred to the load per cycle, which is equal to the multiplication of the current and the time $q = I \times T$. This charge comes from the series connection of $C_1 \dots C_n$. If no charge would be transferred during T from this stack via $D'_1 \dots D'_n$ to the oscillating column however, just before the time instant t_2 every diode $D'_1 \dots D'_n$ transfers the same charge q , and each of these

charges discharges all capacitors on the smoothing column between the relevant node and ground potential. The total ripple voltage (Zaengl and Kuffel, 2000):

$$\delta V = \frac{1}{2f} \left(\frac{1}{C_1} + \frac{2}{C_2} + \frac{3}{C_3} + \dots + \frac{n}{C_n} \right) \quad 2.15$$

Thus in a cascade multiplier the lowest capacitors are responsible for most ripples and it would be desirable to increase the capacitance in the lower stages. This is, however, very inconvenient for HV cascades, as a voltage breakdown at the load would completely overstress the smaller capacitors within the column. Therefore, equal capacitance values are usually provided, and with $C=C_1=C_2=C_3\dots C_n$

$$\delta V = \frac{I}{Cf} \left(\frac{n(n+1)}{4} \right) \quad 2.16$$

To calculate the total voltage drop ΔV_0

$$\Delta V_0 = \frac{I}{Cf} \left(\frac{2n^3}{3} + \frac{n^2}{2} - \frac{n}{6} \right) \quad 2.17$$

For a given number of stages, this maximum voltage or also the mean value $V_0 = V_{0\max} - \delta V$ will decrease linearly with the load current, I (Kuffel, Zaengl, Kuffel, 2000)

Where $V_{0\max} = 2nV_{\max} - \Delta V_0$

PMT Supply and Circuits

Correct use of a photomultiplier calls for observance of certain rules and circuit techniques. For photomultiplier tube operation, a high voltage from 500 to 3000 volts is usually applied across the cathode and anode, with a proper voltage gradient set up between the photoelectron focusing electrode, dynodes and,

depending on tube type, an accelerating electrode (accelerator). Those described here are indicative of present-day practice and sufficient to serve as a working guide (Flyckt, and Marmonier, 2002).

Voltage Polarity

There are two ways of applying the high voltage to a photomultiplier:

Positive polarity, with the cathode earthed and the anode at high positive potential (Figure 2.15 a).

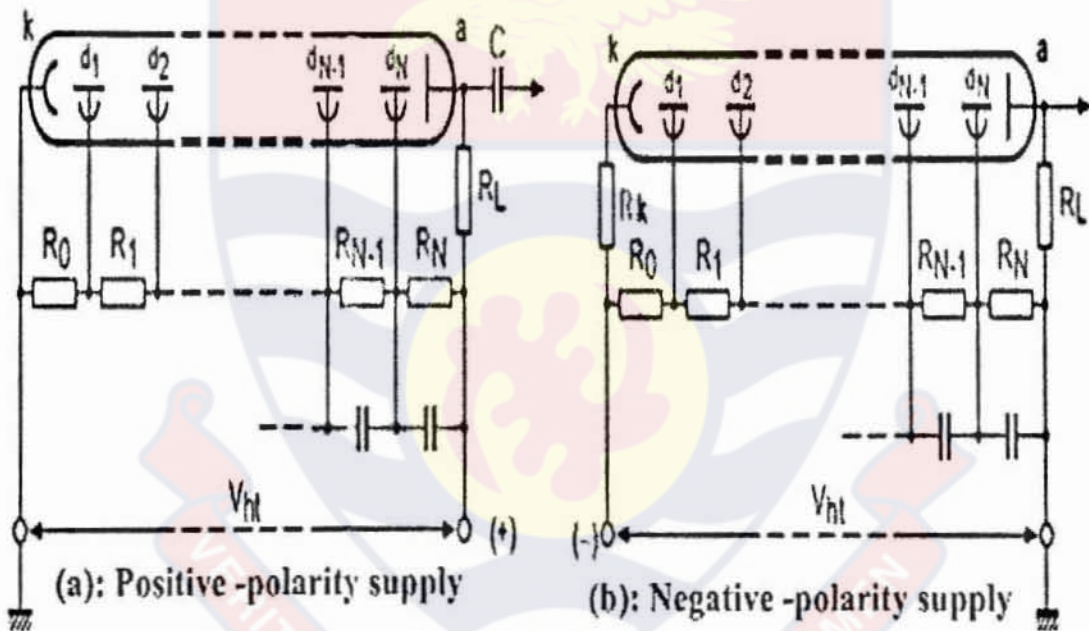


Figure 15: PMT high voltage (HV) polarity (a): Positive – polarity supply (Flyckt, and Marmonier, 2002)

Negative polarity, with the anode earthed and the cathode at high negative potential (Figure 15 b). The choice depends on the application.

For pulse counting, positive polarity is usually preferred; the capacitor C isolates the measuring circuits from the high voltage. Positive polarity is convenient because it does not necessitate insulating the tube from its

surroundings. Magnetic screens and the coatings of scintillators should, however, be kept at photocathode (earth) potential.

For applications involving detection of continuous flux or very brief pulses, where use of a coupling capacitor would be unpractical, negative polarity has to be used. This necessitates special precautions to minimize its effect on dark current and to guard the PMT against the potentially destructive effect of voltage gradients across the glass.

With tubes whose dark current is low (those with alkali cathodes, for example), the time required for the dark current to settle after switch-on may delay measurements for half an hour or more. With all tubes, insulation defects or capacitive currents between the cathode and nearby earthed parts may make the dark current high and unstable. One way to guard against this is to coat the envelope with a conductive layer (e.g. metallic paint) to neutralize any potential gradients on the glass that might give rise to leakage currents, and connect the conductive coating to cathode potential via a safety resistor of, say, 10 M Ω . Enclose the conductive coating in an insulating coating with a high insulation resistance. If good heat transfer through the coating is required a material with high thermal conductivity should be used.

Rate of Voltage Application

Positive polarity

If the high voltage is applied abruptly to a photomultiplier connected in positive polarity (Figure 15a), an initial pulse of amplitude $V_m R_E / (R_L + R_E)$ is coupled through the capacitor to the preamplifier input

and causes damage. To avoid this it is advisable to use a circuit decoupling network (shown dotted in Figure 16) with a time constant $R_t C_t$ of at least one second. An alternative is to shunt a protection diode across the resistor R_E to eliminate all positive-going pulses at the amplifier input.

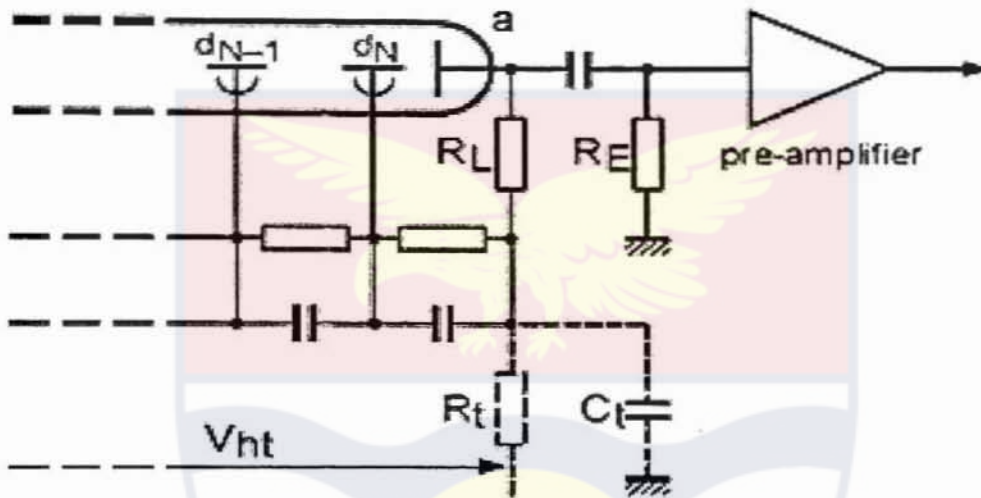


Figure 16: Network for decoupling the high-voltage switch-on transient from the amplifier input. (Flyckt, and Marmonier, 2002)

Negative polarity

If voltage is applied abruptly to a tube connected in negative polarity, the amplitude of the initial dark-current transient may be high enough to damage sensitive measuring apparatus. Applying the voltage gradually reduces the transient or may even eliminate it. The RC time constant should be a few seconds.

Voltage dividers

The choice of voltage divider, including the type of voltage distribution, depends on the application of the tube; e.g. continuous, pulse, or high-current operation, etc., and the performance required; e.g. gain, linearity, timing, stability, etc. (Flyckt, and Marmonier, 2002).

Types of voltage distribution

Recommended voltage distributions are given in the data sheets for each tube. There are three main types, designated A, B and C (Flyckt, and Marmonier, 2002).

Type A (*equal steps*, Figure 17(a))

Voltages between all the iterative dynodes are equal. This distribution gives maximum gain for a given supply voltage and is particularly suitable for photometry and nuclear spectrometry applications.

Type B (*progressive*, Figure 17(b))

Inter-dynode voltages increase progressively in the anode direction, becoming 8 to 10 times as high in the last stages as in the first. This distribution makes it possible to obtain anode pulses of several hundred milliamperes peak with good linearity. Gain, however, is much lower than with type A distribution for the same total high voltage.

Type C (intermediate, Figure 17(c))

Inter-dynode voltages increase only in the last stages. Time characteristics are optimized; gain and pulse linearity are also satisfactory. So, type C distribution is particularly suitable for fast response photomultipliers.

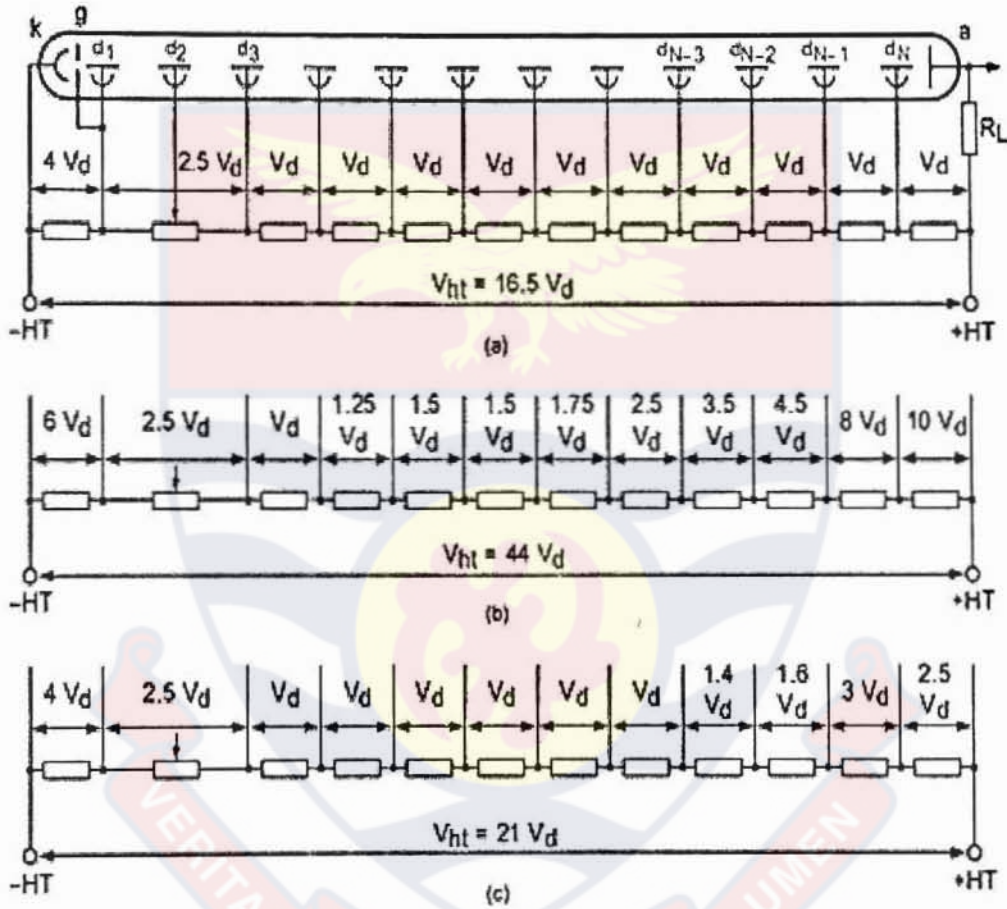


Figure 17: Voltage dividers: (a) type A equal step, (b) type progressive, (c) type C intermediate (Fyckt and Marmonier, 2002)

Resistive dividers

Design of a resistive voltage divider depends on the supply voltage, the voltage distribution, and the anticipated mean anode current I_a . To ensure that voltage variations due to anode current variations are negligible,

the nominal divider current I_p must be much larger than I_a ; a good rule (Fyckt and Marmonier, 2002) is:

$$\frac{I_p}{I_a} \geq 100 \quad 2.18$$

Consider a type C voltage distribution with $V_{ht} = 2500$ V, (Figure 17(c)) an inter-dynode voltage increment V_d , and a division ratio such that there are precisely 21 such increments. Let the maximum anticipated mean anode current I_a be $10 \mu\text{A}$. The divider current I_p must then be at least 1 mA, which means a total divider resistance of $2.5 \text{ M}\Omega$ and an incremental resistor value of $2.5 \times 10^6/21 \approx 120 \text{ k}\Omega$.

The resistors must be properly rated for power and voltage. The latter is important because some of them must withstand several hundred volts continuously. Tolerances should be not greater than 5%. The ratio specified by Eq. 2.18 represents a minimum for maintaining good linearity. Two other considerations limit the maximum value of the ratio.

Heat due to dissipation in the divider ($I_p^2 R$) can cause an increase in the dark current, especially if the divider and tube are housed close together or with the tube vertical, cathode uppermost.

Low divider current gives some protection against accidental overexposure of the cathode; as soon as anode current rises proportionately, gain drops abruptly and prevents the anode current from becoming excessive.

Zener-diode dividers

Zener diodes can be substituted for some of the resistors in the divider to keep certain inter-electrode voltages constant. They can be used between cathode and first dynode to keep input collection efficiency constant regardless of supply voltage and gain setting; and between the dynodes of the first two multiplier stages to keep the gains of those stages constant (Figure 18(a)). This is useful where certain minimum voltages are necessary in the first stages because S/N or PHR is critical but the overall gain need not be high. It cannot be done, however, in those fast-response tubes that incorporate an accelerating electrode internally connected to one of the higher ranking dynodes; the potential of such an electrode must be in constant proportion to the voltage between cathode and first dynode.

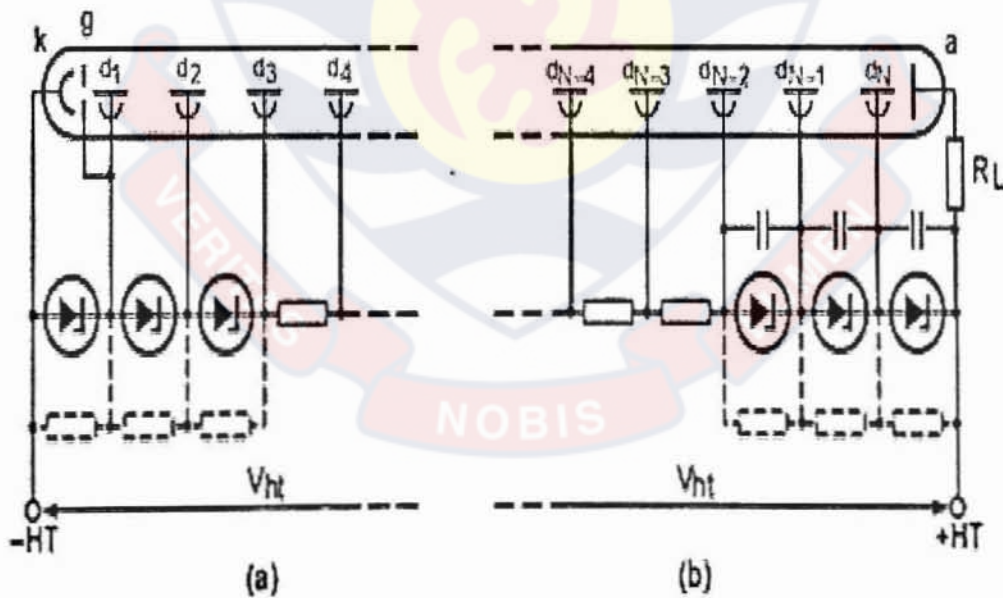


Figure 18: Inter-electrode voltage stabilization with zener diode: a) in first stage, b) in last stages, (dashed lines, protection resistors)

Another place to use zener diodes is in the last stages of the divider (Figure 18 (b)), to stabilize the voltages there throughout a wider range of anode current variations. This also makes it possible to accommodate smaller ratios of I_p/I_a than with a purely resistive divider.

In certain applications a drawback of using zener diodes is that they limit the freedom of gain adjustment. Altering the supply voltage to adjust the gain would also alter the overall voltage distribution, for it would affect the voltages across the resistor stages but not the zener-stabilized ones. As linearity is very dependent on the overall voltage distribution, a divider with zener diodes should be designed for a specific supply voltage and that voltage should be adhered to as closely as possible. Departure from it invites the risk of either over-linearity or premature saturation. The risk is considerably less if only the very last stage is zener stabilized.

Whether zener diodes are used in the higher or lower stages of the divider, they should be shunted by resistors to protect those stages from receiving the full supply voltage in the event of a diode going open-circuit. The values of the resistors should be 2 to 3 times what they would be in a purely resistive divider (Flyckt and Marmonier, 2002).

The temperature coefficients of the zener diodes are an important consideration. Variation of zener voltage with temperature can cause variation in gain. Note, though zener-diode dividers offer some advantages in special situations, these advantages are sometimes over-stressed and often the best solution is a specially tailored resistive divider.

Decoupling

Provided the dynodes are adequately decoupled, instantaneous values of current in pulse operation may greatly exceed the mean value of the divider current. In observing, the rule of Eq.2.18 the value taken for I_a should be the mean anode current based on the anticipated pulse amplitude and duty factor. Decoupling may be either parallel (Figure 19(a)) or series (Figure 19(b)); the former requires high-voltage capacitors which are larger and more expensive (Flyckt and Marmonier, 2002).

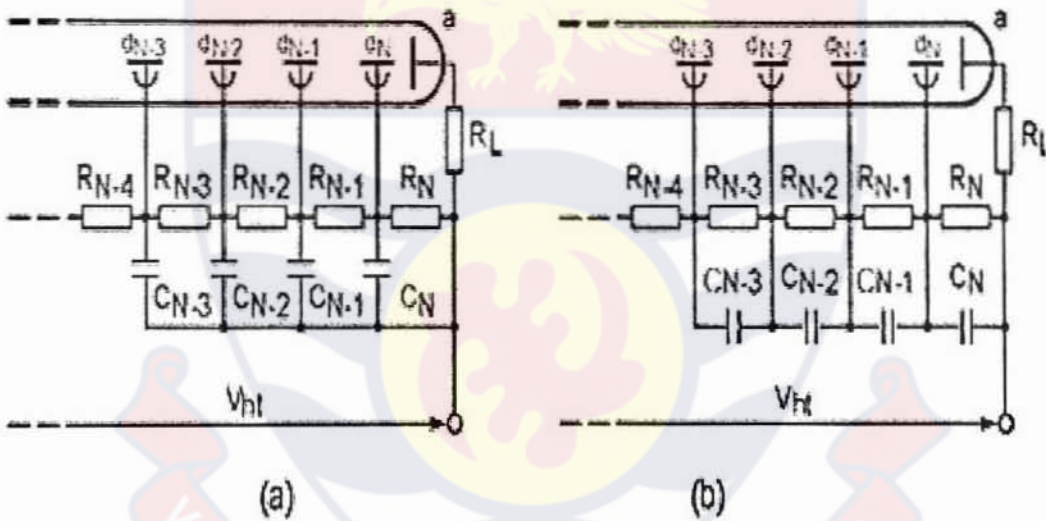


Figure 19: Dynode decoupling: (a) parallel (b) series (Marmonier, 2002)

The decoupling capacitors act as reservoirs to restore the charge transferred by pulses passing through the tube. Let Δq_N be the pulse charge supplied by the last dynode, and ΔV_N the maximum voltage change that can be tolerated on that dynode. The required value of capacitor C_N is then given by

$$C_N \geq \frac{\Delta q_N}{\Delta V_N} \quad 2.19$$

The charge added per stage increases in direct proportion to the gain;

therefore, the required value of C_{N-1} is

$$C_{N-1} = \frac{C_N}{g_N} \quad 2.20$$

Where g_N is the gain due to dynode d_N . If all stages have equal gain, the general expression for the required capacitance in the i -th stage is simply

$$C_i = \frac{C_N}{g^{N-i}} \quad 2.21$$

Working backwards from the last stage to the first, this rule should be applied until the value it gives for C_i is comparable to the stray capacitance of the stage (usually about 20 pF).

The foregoing is based on the assumption that the voltage changes ΔV_i on the dynodes occur independently of each other, but that is not always so. Consider the case where the pulse duration is large compared with the overall transit time, and the dynodes are series decoupled. The voltage changes can then be fed back down the decoupling network in such a way that

$$\Delta V_i = \sum_{j=i}^N \Delta V_j \quad 2.22$$

For adequate decoupling the capacitance in each stage except the last must then be increased by a safety factor about equal to the stage gain.

Equation 2.21 then becomes

$$C_i' = g \frac{C_N}{g^{N-i}} = \frac{C_N}{g^{N-i-1}} \quad 2.23$$

A photomultiplier adjusted for an overall gain of 3×10^5 detects NaI(Tl) scintillation pulses due to γ -radiation from a ^{60}Co source. The full width at half maximum of the resulting anode pulses is about $0.3 \mu\text{s}$, and their amplitude about 1 mA; the pulse charge is therefore

$$\Delta q_N \approx I_a t_w = 0.3 \times 10^{-9} \text{ C} \quad 2.24$$

If the maximum tolerable change in last-dynode voltage is $\Delta V_N = 1 \text{ V}$ (i.e. about 1% of the interdynode voltage), the minimum decoupling capacitance required at that dynode (Marmonier, 2002) is:

$$C_N \geq \frac{\Delta q_N}{\Delta V_N} = 0.3 \text{ nF} \quad 2.25$$

The decoupling capacitors recharge with a time constant determined by the divider resistances. It is not necessary for each capacitor to recharge fully before every pulse but only for it to recover the charge lost during the preceding pulse. What is important is that the amplitude of the capacitor voltage variation in each stage should not exceed the tolerable value of ΔV_i in that stage. This condition is satisfied when the rule given in Equation 2.18 is observed; that is, when (Flyckt and Marmonier, 2002)

$$I_a \leq \frac{I_p}{100} = \frac{V_{ht}}{100 \sum_{i=1}^N R_i} \quad 2.26$$

where V_{ht} is supply voltage and R_i the voltage divider resistance at each stage. Together, Equation 2.19 and (2.20) define the minimum capacitance needed to decouple each stage, and Equation 2.26 the minimum divider current

to restore the capacitor charges. Apart from considerations of bulk and cost, there is no strict upper limit to the decoupling capacitances.



CHAPTER THREE

THEORY OF PHOTOEMISSION AND GAMMA CAMERA

Overview

Photoemission experiments are almost the only check we have on bands deep below the Fermi level, yet until recently much of the information contained in these experiments has not been exploited because relatively crude interpretation has been made of these experiments. For example, angle integrated photoemission experiments are usually compared with a density of states calculation and only rarely are refinements such as matrix elements included, still less corrections for surface effects, etc. This is perhaps surprising, because the relevant pieces of theory have been available separately for some time. Only the drawing together of these pieces into one coherent calculation is required. So a detailed theory of photoemission which enables us to interpret experimental data with the best possible resolution that current theories allow is presented in this section.

The photon field gives rise to photoemission *via* a perturbing term in the Hamiltonian (Pendry and Hopkinson, 1978)

$$\Delta = \frac{1}{2c}(P \cdot A + A \cdot P) \quad 3.1$$

where

$$A = a \cos(q \cdot r - \omega t)$$

and

P is - the momentum of the photoelectron.

The photon energy is typically in the 10eV-200eV range. The A -vector should have dielectric correction made to it which in principle may be quite

complicated, but it is found by experience that it is often satisfactory only to calculate the classical refraction at the surface changing the direction of the incident light beam, though as it will be mentioned later in the paper that, there are some reservations about this simple approximation. With the assumption that the dielectric constant produces only a straightforward refraction at the surface, we can transform (Equation 3.1) to give the form which we use for calculation. The positive frequency component has amplitude (Pendry and Hopkinson, 1978),

$$\Delta = \frac{a\Delta V}{2\omega c} \exp(iq.r) \quad 3.2$$

In this section formulae are expressed in a.u. in which $\hbar = m = e = 1$ and the velocity of light $c = 137$.

Because photoemission involves several different theories being mixed together, the details of calculations are quite involved, but in spite of this the underlying theory is not very complex, and to show this a simple *golden rule* expression for the photocurrent (Pendry and Hopkinson, 1978)

$$I(k_{\parallel}, E+\omega) = \sum \frac{L}{k_z^+} \left| \langle k_{\parallel}, E+\omega | \Delta | j, E \rangle \right|^2 \quad 3.3$$

The final state which carries the photoelectrons out of the crystal is simply the time reversal of a LEED state, and can be calculated using LEED theory. Its direction is specified by k_{\parallel} , momentum parallel to the surface. The initial state is a linear combination of Bloch waves of the crystal adjusted so as to meet the boundary conditions at the crystal surface. It can be calculated by conventional band theory techniques such as have been applied to investigation of surface states. Although techniques are available for evaluating Equation 3.3,

are not very convenient computationally, and in any case shall: need to make an important extension of the *golden rule* theory which will not be possible within the framework of Equation 3.3.

The philosophy of the *golden rule* is that the occupied states have been sitting in the crystal for an infinite length of time. They are stationary states of the crystal, and when the photon field arrives it couples them to other stationary states at higher energies which can couple to the detector. This is a static picture of the photoemission process, and in contrast we shall develop a dynamic method of calculating in which we do not calculate the stationary states, but instead we evaluate the matrix element by making use of scattering theory. To this end Equation 3.3 is re-written as (Pendry and Hopkinson, 1978);

$$I(k_0, E + \omega) = \sum_j \frac{L}{k_z^+} \langle k_0, E + \omega | \Delta | j, E \rangle \langle j, E | \Delta^\dagger | k_0, E + \omega \rangle \quad 3.4$$

Next we make two substitutions. Firstly, the final state is re-written in terms of a source term on which the Green's function at high energies $G_2^+(E + \omega)$ acts. The second substitution recognises that the sum over occupied states can also be written in terms of a Green's function $G_1^+(E)$:

$$\langle r | k_0, E + \omega \rangle = (\langle r | G_2^+ | \varphi^* \rangle)^* = \langle r | G_2^- | \varphi \rangle \quad 3.5$$

where

$$\langle r | \varphi \rangle = \frac{1}{\pi} \exp(ik_0 \cdot r_0) \delta(z - Z) \quad 3.6$$

$$\sum_j |j, E\rangle \langle j, E| = -\frac{1}{\pi} \text{Im} G_1^+(E) \quad 3.7$$

L is the length of a large box confining the experiment; Z is the plane of observation. Substituting both these expressions back into (Equation 3.4) we regain a new expression for the photocurrent (Pendry and Hopkinson, 1978).

$$I(\mathbf{k}_\parallel, E + \omega) = -\pi^{-1} \text{Im} \langle \varphi | G_2^+ \Delta G_1^+ \Delta^\dagger G_2^- | \varphi \rangle \quad 3.8$$

This expression is the same as the one derived by (Caroli, *et al*, 1973). We can go on to re-interpret the Green's function, not as an expansion over stationary states, but in its alternative guise as a propagator which sums over all scattering paths within the crystal (Pendry, 1964).

Let us give a step-by-step account of the calculation. We begin with a plane wave headed towards the crystal (we shall time-reverse this part of the calculation by complex conjugation eventually) and using LEED theory we can calculate the function $\langle r | G_2^+ | \varphi \rangle$ by summing all scattering paths between layers of atoms and within layers of atoms. In particular, the amplitudes of this state, the time reversal of the outgoing wave, near the centres of the atoms (Pendry and Hopkinson, 1978) is:

$$\frac{1}{L} \sum_{lm} A_{2lm}(s) \psi_{2l}(|r - R_j|) Y_{lm}(r - R_j) \exp(i\delta_{2l}) \quad 3.9$$

where ψ_{2l} is the solution of the radial Schrodinger equation and δ_{2l} is the phase shift for angular momentum. Subscript $\ll s \gg$ refers to the layer in which the atom finds itself and R_j is the position of the atom relative to the origin in that layer. k_\parallel is the crystal momentum parallel to the surface which is conserved in the calculation, since we assume a perfectly periodic surface. Next we take the photon field which can be expressed as (Pendry and Hopkinson, 1978):

$$\Delta^\dagger = \frac{|a|}{2\omega c} \frac{dV}{dr} \frac{4\pi}{3} \sum_{m=-1}^{+1} Y_{lm}^*(a) Y_{lm}(r-R_j) \exp(-iq.R_j) \quad 3.10$$

and we assume that any necessary corrections to the \mathbf{A} -vector have been made. Tracing through the next step in equation (3.8), the photon field acting on the incident wave, acts as a source of holes in the crystal. The waves radiating from the j th atom, as yet uncorrected for multiple scattering, are (Pendry and Hopkinson, 1978):

$$\frac{1}{L} \sum_{lm} B_{ilm}^{(0)} \psi_{il}^+(|r' - R_j|) Y_{lm}(r' - R_j) \exp(-i\delta_{il}) \quad 3.11$$

where

$$B_{ilm}^0 = \frac{-ik_1 4\pi |a| \exp(-iq.R_j)}{6\omega c} \sum_{l'm'} A_{2l'm'}^* Y_{l'm'+m}^*(a) \exp(i\delta_{il} - i\delta_{2l'}) X \int_0^\infty r^2 \psi_{il}(r) \frac{dV}{dr} \psi_{2l'}(r) dr \int Y_{lm} Y_{l'm'+m} Y_{l'm'}^* d\Omega \quad 3.12$$

K_l is the wave-vector of the hole wave function, and δ_{il} the phase shift, ψ_{il} the regular solution and the outgoing wave solution for the hole in the l^{th} angular momentum channel. Each atom radiates an outgoing hole-wave. The calculation must let these waves interfere with one another, scatter off all layers of atoms, scatter off the surface barrier and finally evaluate the total wave field accumulating at every atom centre. Let us suppose this has been done and that the total hole-wave field is given by (Pendry and Hopkinson, 1978)

$$\frac{1}{L} \sum_{lm} C_{ilm} \psi_{il} Y_{lm} \exp(i\delta_{il}) + B_{ilm}^{(0)} \psi_{il}^* Y_{lm} \exp(-i\delta_{il}) \quad 3.13$$

All that remains to be done is to complete the matrix element by taking a scalar product with the original incident wave field. The summation is over the contribution of each atom within the crystal to the photocurrent. This may be positive or negative, because of interference of contributions from different atoms, but of course the total current must remain positive. Though we have not mentioned it specifically in our account, the gradient of the potential of the surface barrier also acts as a source of holes, and takes part in the photoemission process. We shall see in a subsequent section that this can be a large contribution to the photocurrent in some materials.

Hole-lifetimes

So far we have merely reformulated the *golden rule*, but we wish to introduce an element to our calculation that is not present within the *golden rule* formulation: the life time of the hole left behind in the crystal. It is evident that this life time must affect spectra because the uncertainty principle dictates that the shorter the lifetime the less detail will be the apparent in the photocurrent. The golden rule has no knowledge of the lifetime of the hole state and implicitly assumes that this state is infinitely long-lived, because it works in terms of static states. However, our formula though derived from the *golden rule* in the first instance, is capable of generalisation to include the hole life time. This is because the philosophy of interpretation of Equation 3.8 is quite different. The photon operates on the ground state of the crystal to produce an electron and a hole. G_1^+ is the Green's function for the hole state, not for the occupied

electronic states. Since the hole only appears on the scene at the moment of its creation, it is now sensible to talk of giving this state a finite lifetime.

Photoemission Studies of Copper and Silver: Theory

Steps of Photoemission from Solids

Photoemission from solids is a two- step process. Electrons are first optically excited into states of higher energy; then they move to the surface of the solid, with or without scattering, and escape into vacuum. As a result, measurements of the spectral distribution of the photoelectric yield, and of the energy distribution of photoemitted electrons at individual photon energies, can be used to study both the optical excitation process and the electron-scattering process in solids. The main purposes of this paper are to explain how the effects of electrons which escape after one or more inelastic-scattering events can be separated from the effects of those which escape without significant inelastic scattering in photoemission, and to outline methods by which the data can be interpreted in terms of band structure, optical excitation probabilities, and scattering probabilities (Berglund, and Spicer, 1964).

In the past photoemission has been considered by many authors (Flower, 1931, Apker *et al*, 1948; Kane, 1962; Gobel and Allen, 1962). However, the emphasis has been on the details of this phenomenon at photon energies near the threshold. In this paper, photoemission at photon energies well above the threshold is emphasized.

It will be shown that photoemission data can be used to determine whether an optical transition is direct or not; that is, whether direct conservation of k vector in an optical transition is required. If it is found that direct conservation of k vector is not necessary in an optical transition, there are two possible explanations. Either the transition is indirect, k vector being conserved by some mechanism such as phonons (Hall, Bardeen, and Blatt, 1954), or conservation of k vector as a selection rule is not important (Spicer, 1963). All optical transition in which direct conservation of k vector is not important will be referred to as non-direct transitions.

Probability of Electron Escape without Inelastic Scattering

Consider an electron excited to some energy E and momentum p at a distance x from the surface of a semi-infinite solid. This electron has just been excited to this state by absorption of a photon. In order for the electron to escape from the solid without any loss of total energy, it must (1) reach the surface of the solid without suffering an inelastic collision, and (2) have a crystal momentum component perpendicular to the photoemitting surface greater than some critical value (Berglund and Spicer, 1964).

An exact treatment of the scattering and escape problem presents extreme difficulties and will not be attempted here. Rather the following simplifying assumptions will be made:

- 1 The distribution in direction of the excited electrons is isotropic.
- 2 Only inelastic scattering events need be considered.
- 3 The probability of inelastic scattering can be described in terms of a

mean free path l , which is a function only of the electron energy.

- 4 The inelastic scattering is isotropic.
- 5 In order to escape over the surface barrier, the electron must have a component of its total crystal momentum p , perpendicular to the surface which is greater than some critical value p_c . The escape probability is assumed to be unity if this condition is satisfied. Since the samples studied consisted of un-oriented poly-crystals, the first assumption was probably satisfied in a macroscopic sense.

The third and fourth assumptions cannot be expected to be exact; however, deviations from them would probably not cause first-order errors in the present work. Greater care would have to be taken if measurements were made on single crystals (Kane, 1962).

The fifth assumption involves the probability of escape of an electron which reaches the surface. As will be seen in the equations derived, p and p_c appear only in terms of the form $(1-p_c/p)$. In principle these could be calculated from the known band structure. One effect of elastic scattering will be to scatter electrons into the proper direction for escape. Since these assumptions are not exact, the treatment given here must be considered as only a first approximation.

If θ is the angle between the direction of electron momentum upon excitation and the normal to the photoemitting surface as the electron move a distance $x/\cos\theta$ to reach the surface. The probability of the electron escaping without loss of energy following excitation to energy E , (Berglund and Spicer, 1964) is:

$$p_{esc}(E, x) = \frac{1}{2} \int_0^{\cos^{-1}(p_c/p)} e^{-x/l \cos \theta} \sin \theta d\theta \quad \text{if } p \geq p_c \quad 3.14$$

$$= 0 \quad \text{if } p \leq p_c$$

where l is the mean free path for inelastic-scattering characteristic of electrons with energy E . Changing variables so that $z = \cos \theta$

$$p_{esc}(E, x) = \frac{1}{2} \int_{p_c/p}^1 e^{-x/lz} dz \quad \text{if } p \geq p_c$$

$$= 0 \quad \text{if } p < p_c \quad 3.15$$

This integral does not have a simple closed-form solution. However, $p_{esc}(E, x)$ can be used in the integral form, the integration being performed later.

In optical absorption, the rate per unit area at which electrons are excited to energies between E and $E+dE$, in a slab of width dx located a distance x from the surface on which the light is incident, has the form

$$G(E, x) dE dx = G_0(E) dE e^{-\alpha x} dx \quad 3.16$$

where α is the absorption coefficient. $G_0(E)$ will be defined later. From Equations (3.15) and (3.16), the rate of escape of electrons with energy between E and $E+dE$ (Berglund and Spicer, 1964) is:

$$R'(E, x) dE = \int_0^{\infty} p_{esc}(E, x) G(E, x) dE dx \quad 3.17$$

$$R'(E) dE = G_0(E) dE \int_0^{\infty} p_{esc}(E, x) e^{-\alpha x} dx$$

In Equation 3.17 the photoemitting solid has been assumed to be semi-infinite to allow the upper limit in the integration to be infinite.

Carrying out the integration in Equation 3.17 first with respect to x , integration with respect to z gives the result:

$$R(E)dE = \frac{G_0(E)dE}{2\alpha} \left\{ 1 - \frac{p_c}{p} - \frac{1}{\alpha l} \ln \left[\frac{1 + \alpha l}{1 + (p_c/p)\alpha l} \right] \right\} \quad p \geq p_c \quad 3.18$$

$$= 0 \quad p \leq p_c$$

This expression is rather difficult to interpret in its present form. It can be written in a form that is more meaningful if the logarithm in Equation 3.18 is expanded in an infinite series (Berglund and Spicer, 1964) and

$$\begin{aligned} & -\frac{1}{\alpha l} \ln \left[\frac{1 + \alpha l}{1 + (p_c/p)\alpha l} \right] \\ &= +\frac{1}{\alpha l} \ln \left[1 - \frac{[1 - (p_c/p)]\alpha l}{1 + \alpha l} \right] \\ &= -\frac{1}{\alpha l} \left\{ \frac{[1 - (p_c/p)]\alpha l}{1 + \alpha l} + \frac{[1 - (p_c/p)]^2 \alpha^2 l^2}{2(1 + \alpha l)^2} + \frac{[1 - (p_c/p)]^3 \alpha^3 l^3}{3(1 + \alpha l)^3} + \dots \right\} \quad 3.19 \end{aligned}$$

Substitute Equation 3.19 into Equation 3.18 and collecting terms gives:

$$R'(E)d(E) = \frac{\frac{1}{2}[1 - (p_c/p)]G_0(E)d(E)}{\alpha + (1/l)} \left[1 - \frac{[1 - p_c/p]}{2(1 + \alpha l)} - \frac{[1 - (p_c/p)]^2 \alpha l}{3(1 + \alpha l)^2} + \dots \right]$$

$$= 0 \quad \begin{array}{l} p \geq p_c \\ p \leq p_c \end{array} \quad 3.20$$

Equation 3.20 can be further simplified if a threshold function $C(E)$ is defined where

$$C(E) = \begin{cases} \frac{1}{2}[1 - (p_c/p)] & p \geq p_c \\ 0 & p \leq p_c \end{cases} \quad 3.21$$

and if the finite series in Equation 3.20 is represented by a correction factor K . This correction factor has been evaluated, and plotted as a function of $C(E)$ and αl . Using Equation 3.21 and the correction factor K , Equation 3.20 becomes

$$R'(E)dE = \frac{KC(E)G_0(E)dE}{\alpha + (1/l)} \quad 3.22$$

The threshold function $C(E)$ depends on the crystal momentum p and the critical crystal momentum for escape p_c . As a result, it is a complicated function. However, using Equation 3.8, it can be seen that $C(E)$ is zero for electron energies less than the threshold energy for photoemission, and is 0.5 for electron energies well above threshold (Berglund and Spicer, 1964).

Probability of Electron Escape after One Inelastic Scattering

In both copper and silver, the effect of electron scattering is small enough over the electron energy range studied (0 to 11.5eV above the Fermi level) that only those electrons which escape without scattering and those which scatter once before escaping need be considered.

Consider an electron excited to energy E' a distance x from the surface. The probability of this electron escaping between E and $E+dE$ after scattering once is the product of three probabilities:

1. The probability that the primary electron will scatter after moving a distance r in the solid at an angle θ with respect to the normal to the photoemitting surface;
2. The probability that this electron will be scattered in this scattering process to an energy between E , and $E+dE$: and
3. The probability that it will escape after the scattering event without further scattering (Berglund and Spicer, 1964).

The first probability if the electron velocity direction is random is

$$p_1 = \left[\frac{1}{2} e^{-r/l'} \sin \theta d\theta \right] (dr/l'), \quad 3.23$$

where l' is the mean free path for inelastic scattering for electrons with energy E' . The probability of the electron being scattered to an energy between E and $E+dE$, p_2 , will depend on the scattering mechanism and will be derived for particular cases later. It will be assumed, however, that the electron velocity direction after scattering is random and independent of its initial velocity.

The third probability is given by Equation 3.15 where the distance of the electron from the photoemitting surface at the time of scattering event is

$(x - r \cos \theta)$ (Berglund and Spicer, 1964)

$$p_3 = \frac{1}{2} \int_{p_c/l'}^1 e^{(-x+r \cos \theta)/l_z} dz \quad \begin{matrix} p \geq p_c \\ p \leq p_c \end{matrix} \quad 3.24$$

The probability of an electron escaping after scattering with energy between E and $E+dE$ is given by the product of p_1 , p_2 , and p_3 integrated over all r , z and θ for $\theta > \pi/2$, the limits on r are 0 and ∞ . For $r < \pi/2$, the upper

limits on r is given by $r \cos \theta = x$. If it is assumed that an electron with energy E' which reaches the surface of the photoemitter without scattering escapes with unity probability, and is no longer available to produce electrons with energy E' under this conditions, the probability of electron escape after one scattering event (Berglund and Spicer, 1964) is:

$$p_{esc}''(E', E, x) = \frac{p_2}{4l'} \left[\int_{\pi/2}^{\pi} d\theta \int_0^{\infty} dr \int_{r_c/p}^1 dz e^{-r/l'} e^{(-x+r \cos \theta)/l_z} \sin \theta + \int_0^{\pi/2} d\theta \int_0^{r_c \cos \theta} dr X \int_{r_c/p}^1 dz e^{-r/l'} e^{(-x+r \cos \theta)/l_z} \sin \theta \right] \quad 3.25$$

Changing variables so that $y = \cos \theta$, and integrating Equation 3.25 over r , gives (Berglund and Spicer, 1964):

$$p_{esc}''(E', E, x) = \frac{p_2}{4l'} \left[\int_{-1}^0 dy \int_{r_c/p}^1 dz \frac{e^{-x/l_z}}{(1/l') - (y/l_z)} + \int_0^1 dy \int_{r_c/p}^1 dz \frac{(1 - e^{-x/l'} y + x/l_z) e^{x/l_z}}{(1/l') - (y/l_z)} \right] \quad 3.26$$

Electrons are excited to energy E' according to Equation 3.16, so the rate of escape of electrons after scattering once with energy between E and $E+dE$ (Berglund and Spicer, 1964) is:

$$R^*(E', E) dE dE' = \int_0^{\infty} \left[G_0(E') dE' e^{-\alpha x} p_{esc}''(E', E, x) \right] dx \quad 3.27$$

Substituting Eq 3.26 in Eq 3.27 and carrying out integration over x and y gives

$$R^*(E', E) dE dE' = \frac{p_2 dE G_0(E') dE'}{4} \int_{r_c/p}^1 \left[\frac{1}{\alpha l'} \ln(1 + \alpha l') + \frac{l_z}{l'} \ln(1 + \frac{l'}{l_z}) \right] X \frac{dz}{\alpha + (1/l_z)} \quad 3.28$$

This integration may be carried out exactly, but the result is rather difficult to interpret. A considerable simplification can be made with very little in accuracy as follows: The major contribution to the integral occurs for z near unity. Since in metals l' (the mean free path for scattering at energy E') is generally shorter l (the mean free path of scattering at energy E) and $x \ln[1 + \frac{1}{x}]$ is very slowly varying function of x for large x , very little error is introduced by inserting $z=1$ in the $(l_z/l') \ln[1 + (l'/l_z)]$ term in Equation 3.28.

Under this approximation, Eq. 3.28 becomes (Berglund and Spicer, 1964)

$$R^*(E', E) dE dE' = \frac{KC(E) p_2 dE G_0(E) dE'}{\alpha + 1/l} \frac{1}{2} \left[\frac{1}{\alpha l'} \ln(1 + \alpha l') + \frac{l}{l'} \ln(1 + \frac{l'}{l}) \right] \quad 3.29$$

The total energy rate of escape of electron with energy between E and $E+dE$ after scattering once is Equation 3.29 integrated over all E' .

$$R^*(E) dE = \frac{KC(E) dE}{\alpha + (1/l)} \int_E^\infty \frac{1}{2} \left[\frac{1}{\alpha l'} \ln(1 + \alpha l') + \frac{l}{l'} \ln(1 + \frac{l'}{l}) \right] p_2 G_0(E') dE' \quad 3.30$$

Note that if $\alpha l'$ and l'/l are much smaller than unity, Eq. 3.30 simplifies to

$$R^*(E) dE = \frac{KC(E) dE}{\alpha + (1/l)} \int_E^\infty p_2 G_0(E') dE' \quad 3.31$$

Combining Equation s. 3.20 and 3.30, the rate of escape of electrons with energy between E and $E+dE$, considering only electrons which do not scatter and those which scatter once, (Berglund and Spicer, 1964) is:

$$R(E)dE = \frac{KC(E)dE}{\alpha + (1/l)} \left[G_0(E) + \int_E^{\infty} \frac{1}{2} \left[\frac{1}{\alpha l'} \ln(1 + \alpha l') + \frac{1}{l'} \ln \left(1 + \frac{l'}{l} \right) \right] p_2 G_0(E') dE' \right]$$

3.32

The expression given in Equation 3.30 for the rate of escape of electrons after scattering once is easily interpreted. The $(l/l') \ln[1 + (l'/l)]$ term represents those electrons initially excited to energy E' which are moving away from the photoemitting surface. These electrons eventually will be scattered regardless of the value of the mean free path for scattering, and their probability of escaping after scattering once will depend on the ratio of the mean free paths l'/l . This shows that inelastic scattering will affect photoemission data even when l is much longer than the optical absorption depth. The $(1/\alpha l') \ln(1 + \alpha l')$ term represents those electrons initially excited to energy E' which are moving toward the photoemitting surface. The probability of these electrons escaping after scattering once will depend on the probability of their scattering once before reaching the surface. If $l' > 1/\alpha$ most of these electrons will escape without scattering. If $l' \ll 1/\alpha$ few will escape without scattering (Berglund and Spicer, 1964).

Effect of Elastic Scattering

It has been assumed in the previous sections that the mean free path for inelastic scattering is much shorter than the mean free path for elastic scattering. However in copper and silver electron-phonon interaction is a moderately strong scattering mechanism. This scattering process involves an energy loss small enough compared to the resolution of photoemission measurements that the process may be considered as elastic. An estimate of the energy loss per collision can be obtained in the following way. In a phonon collision, a phonon is either absorbed or emitted with probability proportional to n and $n+1$, respectively, where n is the equilibrium density of phonons in the metal. Assuming the phonon energy corresponds to the Debye temperature ($\approx 0.03 eV$ in *Cu*, and $\approx 0.02 eV$ in *Ag*) (Kittel, 1960), the energy loss per collision can be averaged over emission and absorption according to the probabilities involved, phonon emission corresponding to electron energy decrease equal to the phonon energy, and phonon absorption corresponding to an electron energy increase of the magnitude.

The probability of escape of an electron with energy E a distance x from the surface of a photoemitter can be approximated in this case by Spicer, (1960),

$$P_{esc}(E, x) = B(E)e^{-x/L} \quad 3.33$$

where $B(E)$ is a function which takes into account the threshold, and L is the attenuation length which depends on the mean free paths for inelastic and elastic collisions. Using Equation 3.33, calculations similar to those resulting in Equation 3.20 (Berglund and Spicer, 1964) give,

$$R(E)dE = \frac{B(E)G_0(E)dE}{\alpha + (1/L)} \quad 3.34$$

Stuart, Wooten and Spicer, (1963); and (1964), have used the Monte Carlo method to determine L for various values of the mean free paths. In Copper and silver, the absorption coefficient is of the order of l in the visible and ultraviolet (Ehrenreich and Philipp, 1962) (and the mean free paths for phonon scattering are approximately 500 \AA at the Fermi energy (Kittel, 1962). Even allowing for the fact that the mean free path for elastic scattering at high-electron energies may be somewhat lower than the mean free paths for phonon scattering at the Fermi energy, when the mean free path for inelastic collisions is less than 500 \AA , L approaches the value of the inelastic collision mean free path. For these reasons, in copper and silver Equation 3.20 may be used as a good approximation over the entire range of electron energies to be studied, if the small effect of elastic collisions is included in the threshold function $C(E)$.

Relation of Electron Energy Distribution to Optical Transition

Probabilities

The absorption coefficient of a solid α at frequency, ν may be defined as (Berglund and Spicer, 1964):

$$\alpha(\nu) = \int_0^{\infty} \alpha_{\nu}'(E)dE, \quad 3.35$$

if all photons corresponding to frequency, ν are absorbed in exciting electrons in the solid to higher energy states. In Equation 3.35, $\alpha'_\nu(E)dE$ is the part of $\alpha(\nu)$ due to electronic transitions to energy states between E and $E+dE$. If n_p is the flux of photons at frequency ν per unit area absorbed by the photoemitting material, then $G(E, x)dEdx$ in Equation 3.16 due to optically excited electronic transitions is

$$G(E, x)dEdx = n_p \alpha'_\nu(E) dE e^{-\alpha(\nu)x} dx \quad 3.36$$

This defines $G_0(E)$ in Equation 3.16 as $n_p \alpha'_\nu(E)$. Substituting this $G_0(E)$ in Equation 3.32, the number of electrons per absorbed photon at frequency ν emitted with energy between E and $E+dE$ (Berglund and Spicer, 1964) is

$$\begin{aligned} N(E)dE &= \frac{R(E)dE}{n_p} = \\ &= \frac{KC(E)dE}{\alpha + (1/l)} \left(\alpha'_\nu(E) + \int_E^\infty \frac{1}{2} \left[\frac{1}{\alpha l'} \ln(1 + \alpha l') + \frac{l}{l'} \ln \left(1 + \frac{l'}{l} \right) \right] p_2 \alpha'_\nu(E') dE' \right) \end{aligned} \quad 3.37$$

The transition probability per second per unit volume for electrons with energy E_0 in solid in the presence of an electromagnetic field at frequency ν can be determined using first and/or second-order time dependent perturbation theory if the wave functions in the solid are known. Assume that this probability is $N_T(E, E_0, \nu)$, where E is the energy of the electron after excitation, E_0 is the initial energy, and ν is the frequency of the electromagnetic field. Since conservation of energy requires that $E = E_0 + h\nu$, N_T is not an independent

function of both E_0 and E . The power absorbed per unit volume by the solid is then (Berglund and Spicer, 1964);

$$P = h\nu \int_0^{\infty} N_T(E, E_0, \nu) dE. \quad 3.38$$

Remembering that the conductivity $\sigma(\nu)$ is defined at optical frequencies in terms of the absorption of power per unit volume, $\sigma \mathcal{E}_0^2 / 2$, where \mathcal{E}_0 is the amplitude of the electric vector of the field (Berglund and Spicer, 1964).

$$\sigma(\nu) = \frac{2h\nu}{\mathcal{E}_0^2} \int_0^{\infty} N_T(E, E_0, \nu) dE. \quad 3.39$$

The absorption coefficient of a solid α is defined in terms of the conductivity

$$\alpha(\nu) = \sigma(\nu) / n(\nu) c \epsilon_0, \quad 3.40$$

Where n is the index of refraction, c is the velocity of light in free space, and ϵ_0 is the permittivity of free space. Using Equation 3.39 and Equation 3.40 (Berglund and Spicer, 1964);

$$\alpha(\nu) = \frac{2h\nu}{n(\nu) c \epsilon_0} \int_0^{\infty} N_T(E, E_0, \nu) dE. \quad 3.41$$

Comparing Equation 3.39 to Equation 3.33,

$$\alpha_{\nu}(E) = \frac{2h\nu}{n(\nu) c \epsilon_0} N_T(E, E_0, \nu). \quad 3.42$$

It is evident from Equation s. 3.42 and 3.37 that if the electrons that escape without scattering with significant energy loss can be separated from those which escape after scattering with significant energy loss, the energy

distribution of the photoemitted electrons at various photon energies can be used to gain a great deal of information on transition probabilities, including selection rules and densities of states.

Electron-Electron Scattering

An important inelastic-scattering mechanism in metals is electron-electron scattering. Motizuki and Sparks (1963), have calculated the probability per second of electron in state (E', k') being scattered to state (E, k) by electron-electron scattering in state (E_0, k_0) to state (E_1, k_1)

$$P = \left(\frac{2\pi}{\hbar}\right) |\langle k', k_0 | H_{sr} | k, k_1 \rangle|^2 \delta[(E' - E) - (E_1 - E_0)] \quad 3.43$$

H_{sr} is the perturbation Hamiltonian applicable to the electron-electron scattering process. To find the total probability per second of an electron energy E' being scattered to any other energy E , (3.43) must be summed over all possible states corresponding to k', k_0, k, k_1, E, E_1 and E_0 . This summation may be carried out if the wave function and selection rules are known. It will be assumed that the matrix element in Equation 3.43 is independent of the k vectors of the electrons involved, and has a value represented by M_s (Berglund and Spicer, 1964).

Under the approximation that the matrix element in Equation 3.43 is independent of the k vector the summation described above can be changed to an integral by including the appropriate densities of states and Fermi functions in the standard way. Using this approach, the probability per second of an electron with energy E' being scattered to an energy between E and $E+dE$ is

$$p_s(E', E)dE = \int_0^{\infty} \left\{ \frac{2\pi}{\hbar} |M_s|^2 \rho(E)\rho(E_0)\rho(E_0 + E' - E) \dots \times F(E_0)[1 - F(E_0 + E' - E)][1 - F(E)]dE \right\} dE_0 \quad 3.44$$

Where $|M_s|^2$ is the squared matrix element in Equation 3.44, $F(E)$ is the Fermi function, $\rho(E)$ is the density of states, and variable E_1 has been removed using the energy delta function in Equation 3.43. Defining (Berglund and Spicer, 1964);

$$g_s(E', E) = \int_0^{\infty} \frac{2\pi}{\hbar} |M_s|^2 \rho(E_0)\rho(E_0 + E' - E)F(E_0)[1 - F(E_0 + E' - E)]dE_0 \quad 3.45$$

Equation 3.44 becomes

$$p_s(E', E)dE = \rho(E)[1 - F(E)]g_s(E', E)dE \quad 3.46$$

And the total probability per second of an electron with energy E' being scattered to any energy (Berglund and Spicer, 1964) is

$$P_s(E') = \int_0^{\infty} p_s(E', E)dE \quad 3.47$$

Note that this probability $P_s(E')$ is the reciprocal of the life time $\tau(E')$ for electron-electron scattering of an electron with energy E' . If a group velocity $v_g(E')$ is defined which applies to electrons of energy E' , the mean free path for electron-electron scattering $l(E')$ is given by (Berglund and Spicer, 1964):

$$l(E') = v_g(E')\tau(E') = v_g(E')/P_s(E') \quad 3.48$$

Given that an electron with energy E' suffers an electron-electron scattering event, the probability p_2 of its scattering to lower energy between E and $E+dE$ must be (Berglund and Spicer, 1964):

$$p_2 = p_s(E', E)dE / P_s(E') \quad 3.49$$

In addition to the scattering of an energetic electron down to an energy between E and $E+dE$ included in Equation 3.49, there is also the scattering of an electron from a state below the Fermi level must be included in p_2 . Fortunately, this scattering effect can be included in p_2 in a simple way. The excitation of electrons from states below the Fermi level by the scattering can be included by using l

$$p_2 = 2p_s(E', E)dE / P_s(E') \quad 3.50$$

Substituting Equation 3.50 in Equation 3.37,

$$N(E)d(E) = \frac{KC(E)dE}{\alpha + (1/L)} \left[\alpha_v'(E) + 2 \int_E^{\infty} \frac{1}{2} \left[\frac{1}{\alpha l'} \ln(1 + \alpha l') + \frac{l}{l'} \ln\left(1 + \frac{l'}{l}\right) \right] \times \frac{p_s(E', E)}{P_s(E')} \alpha_v'(E') dE' \right] \quad 3.51$$

In many cases, $\alpha l' \ll 1$, $l'/l \ll 1$ and the Fermi function at absolute zero may be used in the equations. Under these assumptions equation 3.51 simplifies to (Berglund and Spicer, 1964):

$$N(E)dE = \frac{KC(E)dE}{\alpha + (1/L)} \left[\alpha_v'(E) + 2 \int_E^{E_F + h\nu} \frac{p_s(E', E)}{P_s(E')} \alpha_v'(E') dE' \right] \quad 3.52$$

where E_F is the Fermi energy. Another effect of electron-electron scattering is shown in Equation 3.52. Due to the factor of 2 before the scattering term, an

increase in quantum yield may occur. That is, optically excited energetic electrons may scatter once before escaping, exciting a second electron from a state below the Fermi level which may also escape. This may result in a quantum yield greater than unity (Berglund and Spicer, 1964).

Derivation of an expression for Quantum Yield

Spicer (1958) developed a model or theory for photoemission, often called The Tree Step Model, that for the first time treated photoemission as a bulk process and treated it in terms of bulk optical constants and electron scattering lengths, as well as surface properties such as the position of the vacuum level (work function) at the surface of the solid Spicer (1993).

The three step model was derived to give the quantum efficiency of photo emitters as a function of photon energy.

Essential to the Three—Step model is the recognition that bulk absorption coefficient governs the excitation of photoelectrons. The light intensity, $I(x, h\nu)$, after it transverses a thickness x of a solid is given by (Spicer and Herrera-Gomez, 1993):

$$I(x, h\nu) = I_0(h\nu)[1 - R(h\nu)]e^{-\alpha(h\nu)x} \quad 3.53$$

where $I_0(h\nu)$ is the incident intensity of light of photon energy $h\nu$, $R(h\nu)$ is the light reflectivity from the surface of the solid, and $\alpha(h\nu)$ is the absorption coefficient of the solid. Thus, the amount of light absorbed at a distance x from the surface is (Spicer and Herrera-Gomez, 1993):

$$dI(x) = (1-R)I_0 e^{-\alpha(h\nu)x} \quad 3.54$$

Some of the photoexcited electrons will travel to the surface and escape. The contribution $di(x)$ to the photoemission yield from excitation in the slab of thickness dx at x is given by (Spicer and Herrera-Gomez, 1993):

$$di(x) = P_{\alpha\alpha}(h\nu, x, dx)P_T(h\nu, x)P_E(h\nu) \quad 3.55$$

where $P_T(h\nu, x)$ is the probability that electrons (excited by photons of energy $h\nu$ at a distance x from the surface) will reach the surface with sufficient energy to escape. Because the scattering probability is proportional to the distance travelled, it can be shown that (Spicer, 1958).

$$P_T(x, h\nu) = \exp\left\{-\frac{x}{L(h\nu)}\right\} \quad 3.56$$

$P_E(h\nu)$ is the probability of escape of electrons reaching surface with sufficient energy to escape. $P_{\alpha\alpha}(h\nu, x, dx)$ is the probability of exciting electrons above Vacuum Level (VL) in the slab between x and $x+dx$, and is given by

$$P_{\alpha\alpha}(h\nu, x, dx) = \alpha_{PE}(h\nu)I(x)dx = \alpha_{PE}(h\nu)I_0(1-R)e^{-\alpha x} dx \quad 3.57$$

We then have

$$di(x) = I_0(1-R)\alpha_{PE}e^{-\alpha x}e^{-\frac{x}{L}P_E(h\nu)}dx \quad 3.58$$

For a semi-infinite slab, the total electron yield is $i(h\nu) = \int_0^{\infty} di(x)$ then

$$i(h\nu) = I_0(1-R) \frac{\alpha_{PE} P_E}{\alpha + \frac{1}{L}}(h\nu) \quad 3.59$$

The quantum yield (QY) is defined as the number of electrons emitted per absorbed photon:

$$QY(h\nu) = \frac{i(h\nu)}{I_0(1-R)} = \frac{\alpha_{PE} P_E}{\alpha + \frac{1}{\alpha L}} \quad 3.60$$

where I_0 , R , α_{PE} , α , L , and P_E are all functions of $h\nu$.

This is the basic equation for photoemission quantum yield.

We rewrite Equation 3.60 as follows (Spicer and Herrera-Gomez, 1993);

$$QY = \frac{\alpha_{PE} P_E}{\alpha + \frac{l_a}{L}} \quad 3.61$$

where $l_a(h\nu) = 1/\alpha(h\nu)$ is the absorption length, l_a/L is the ratio of absorption length to scattering length, and α_{PE} is the fraction of electrons excited above vacuum level.

For example, in the hard ultraviolet region ($h\nu \approx 5 \text{ eV}$), l_a/L might be high as 10^4 for Cs metal it can be 10^3 in the near ultraviolet ($h\nu \approx 5 \text{ eV}$). Thus the yields will be very low. However, in some semiconductors it can be close to unity in the visible or infrared. This is what makes possible the high quantum

efficiency of semiconductors Cs_3Sb , $[Cs]Na_2KSb$, (Spicer, 1958; Bell, 1973) and the negative affinity GaAs (Spicer, 1977; Escher, 1980 and Spicer, 1961)

The Gamma Camera

The major components of gamma camera are the sodium iodide NaI(Tl) scintillation crystal, a multi-hole collimator, a light guide or optical coupling silicon grease, a hexagonal array of photomultiplier tubes (PMTs) and analog electronics for position encoding and pulse height analysis. The system is contained in a lead shield of sufficient thickness to minimize background from radiation sources outside the Field of View (FOV) of the camera.



Plate 1: The LFOV Gamma Camera at the Korle Bu Teaching Hospital (September, 2009.)

The basic description and operation of the camera and the importance of each of the components parts are discussed in here.

Basic Components and Operation of Gamma cameras

The diameter of gamma camera scintillator is dependent on the application of the device. For example, a 25 cm diameter crystal might be used for a camera designed for cardiac applications while a larger 40 cm crystal would be used for producing images of the lungs.

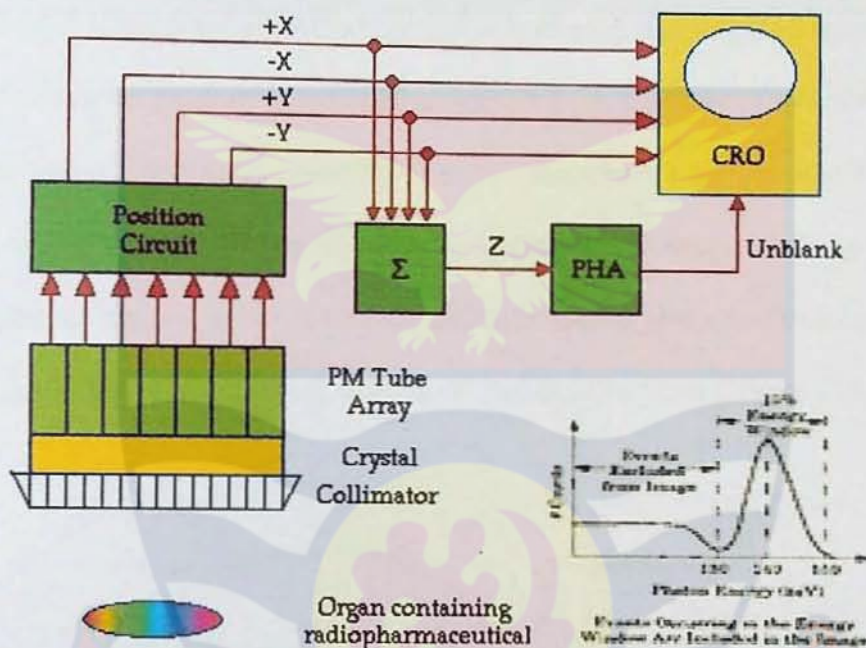


Figure 20: Scintillation camera incorporates collimator, scintillation crystal, photomultiplier tubes, and electronic circuitry to generate position (x, y) and energy (Z) of photons emitted by radiopharmaceutical distribution in patient (<http://www.mediawiki.org/wiki/MediaWiki>)

Photons emitted by radionuclides in the patient or test source reach the NaI(Tl) crystal after first passing through a lead collimator. The collimator defines the direction of acceptance of the photons.

Most collimators are of the parallel hole, diverging, converging, or pinhole type. More complex collimator designs, such as fan beam, are also used.

The crystal is viewed by photomultipliers from its back surface, either directly or through a light guide. The photomultipliers are fed from a common high voltage supply and the voltage or gain is slightly adjustable at each tube.

When a photon interacts with the crystal, it produces a light scintillation that spreads through the crystal and is detected by the PMTs (Figure 20). The fraction of the light that strikes the photocathode of each photomultiplier varies inversely with the distance of the photomultiplier from the point of interaction. The position of the photon interaction can be determined from the amplitude distribution of the pulses from the photomultipliers in the array caused by this single gamma ray interaction. This information is used to give a spatial location to the photon interaction defined in an X–Y coordinate system (Figure 21).

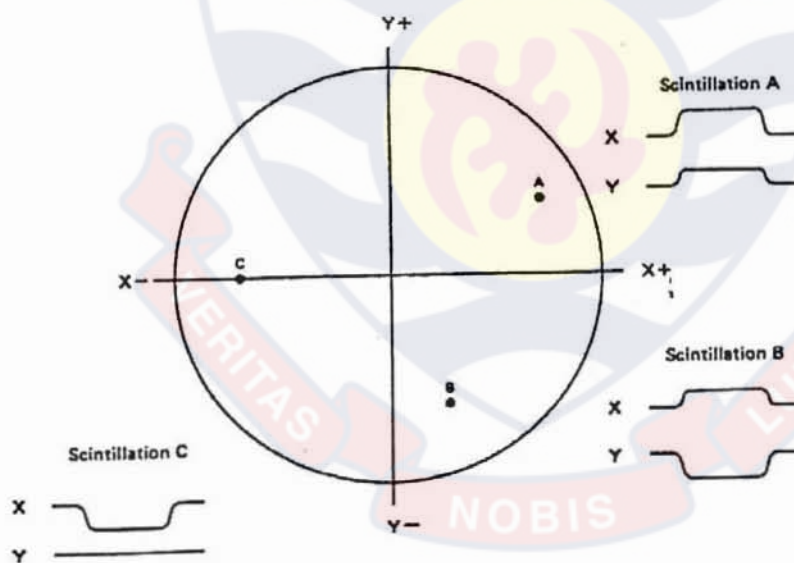


Figure 21: The X–Y coordinate system of a scintillation camera, shown superimposed on the crystal face. Outside the coordinate system are shown examples of the X and Y signals (short duration voltage pulses) resulting from scintillation events occurring in different parts of the crystal (IAEA human health series, 2009)

At the same time, the X-Z and Y-Z signals are used to deflect the beam, causing a brief flash to appear on the oscilloscope face at a position corresponding to that of the original scintillation. If a persistence oscilloscope is used, the flashes remain visible sufficiently long to form an image on the persistent phosphor screen. If a conventional oscilloscope is used, or an image formatting device incorporating such an oscilloscope, a permanent record is obtained by recording the flashes on film for a preset count or a preset time. The X-Z and Y-Z signals may also be digitized by analogue to digital converters (ADCs) for storage and later processing on a computer that is directly interfaced to one or more scintillation cameras. The Z pulse is used to start the digitization of the position pulses.

Position Determination “the Anger Logic”

To provide positional information from the analogue outputs of the photomultiplier tubes, a resistive-coupled network is used. The output signals are attenuated by a resistor matrix, where the values of the resistors correspond to the positions of the photomultiplier tubes. An example of a simple resistor network containing outputs from seven photomultiplier tubes is shown in (Figure 22). The relative intensity of these signals determines the x, y position of the scintillating event and provides signals for (x^+, x^-, y^+, y^-) to produce an image on a cathode ray oscilloscope (CRO) or storage oscilloscope (Webb, 2000). The total intensity of the signal, z, is given by

$$z = x^+ + x^- + y^+ + y^- \quad 3.62$$

and the x and y positions by

$$\begin{aligned}x &= k(x^+ - x^-) / z & 3.63 \\y &= k(y^+ - y^-) / z & 3.64\end{aligned}$$

where k is a constant. The above formulas in the literature are called as “the Anger logic” (Webb, 2000; Hine, 1967).

The total energy, z -signal is analysed by a discriminator, (a Single Channel Analyser) with discrimination levels set to determine whether the z -signal corresponds to the full energy of the gamma photon, i.e. the photopeak (Webb, 2000; Hine, 1967; Tait, 1980; Kowalski, 1970). The discriminator is used to choose the photopeak of the radionuclides that are used for clinical studies.

The pulses from all the photomultipliers are electronically processed after passing through a pre-amplification stage so that the positional information is not dependent upon the photon energy. This is performed in the energy correction circuit where the X and Y signals are divided by the Z signal (Equations 3.3 and 3.4). Furthermore, the Z signal is sent to the pulse height analyser (PHA). If the Z signal falls within the PHA window set for the radionuclide in use, the PHA enables the $X-Z$ and $Y-Z$ signals to be recorded. In an analogue camera, this is usually achieved in a cathode ray oscilloscope.

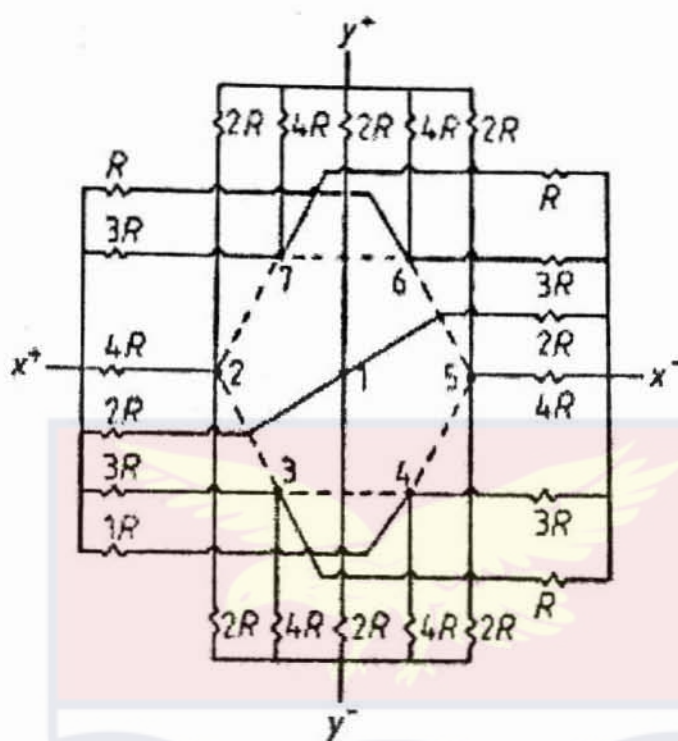


Figure 22: An example of a resistor network used to provide positional information from seven analogue photomultiplier outputs (Webb, 2000)

The face of the oscilloscope is normally kept dark. This is achieved by blocking the electron beam from the oscilloscope face with a negatively biased grid. When the amplitude of the Z signal falls within the preset PHA window, an unblanking signal is generated; this causes the grid to become positive and allows the beam to pass.

The Scintillation Crystal

Most common scintillation crystal used in nuclear medicine is a thin and large circular crystal made of sodium iodide (NaI), activated with a trace of thallium (TI) as scintillator. It has a diameter of 30-50 cm and its thickness is a trade-off between intrinsic resolution and detection efficiency of the incident

photons, a crystal thickness of 9-12 mm provides the best compromise between resolution and efficiency (Webb, 2000; Knoll, 2000; Farrand, 1999). The intrinsic efficiency for this thickness is high, as can be seen in Figure 23.

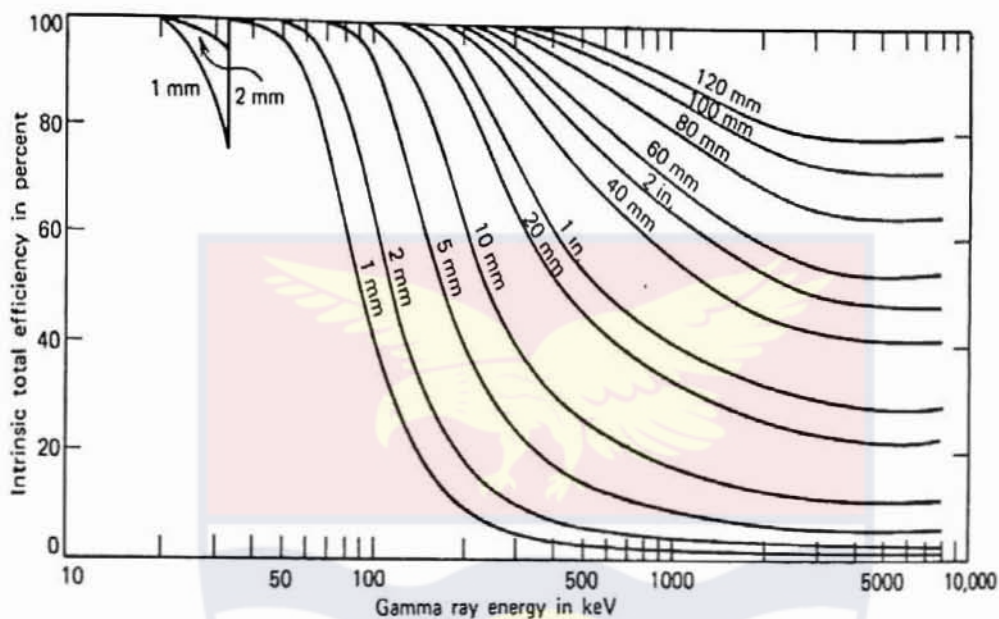


Figure 23: Intrinsic total detection efficiency of gamma rays with perpendicular incidence for various thickness of a NaI(Tl) scintillator (Knoll, 2000)

Detector efficiencies are usually measured and quoted as absolute photopeak efficiencies for detection of gamma rays from unattenuating point sources. Therefore their energy dependence is dominated by intrinsic efficiency (ϵ_{int}) at higher energies and by absorption efficiency (ϵ_{abs}) at lower energies.

The absorption efficiency takes into account the effects of intervening materials (such as the detector housing, special absorbers, etc.) that absorb some of the incoming radiation before it interacts with detector volume. It is especially important that this term should be less than one for low energy photons for which absorption effects are pronounced. The mathematical equation for ϵ_{abs} :

$$\epsilon_{absp} = \exp\left[-\sum \mu_i(E_\gamma)\rho_i\chi_i\right] \quad 3.65$$

where μ_i , ρ_i , and χ_i are mass absorption coefficient, density, and thickness of the i^{th} intervening material, and the summation is over all types of intervening materials.

The crystal has high atomic number ($Z=53$) and density ($\rho=3.69 \text{ g/cm}^3$), and linear coefficient at 150 keV is 2.22 cm^{-1} . Hence 90 % of the 150 keV photons are absorbed in about 10 mm. Sodium Iodide (Figure 24) but a crystal of this thickness becomes rapidly less sensitive above 300 keV. Sodium Iodide NaI(Tl) detector has a light transmission decay constant of 230 ns which means that event rates of many tens of thousands of counts per seconds (kcps) can be attained without serious degradation of performance (Jonasson, 2003).

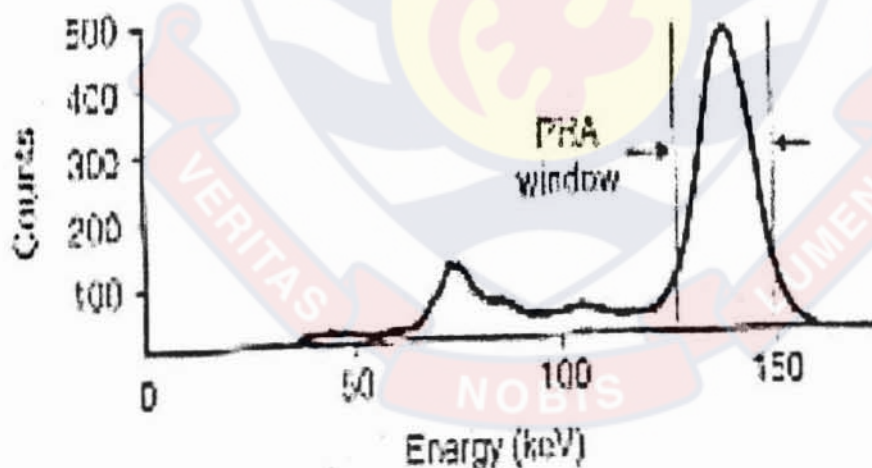


Figure 24: Energy spectrum from a thin NaI (Tl) crystal (Webb, 2000).

The NaI(Tl) scintillator emits blue light-green with peak wavelength $\lambda \approx 475 \text{ nm}$. The crystal is fragile, very sensitive against temperature changes and easy to damage. In addition it is hygroscopic and therefore, it is encapsulated in an

aluminium cylinder with one flat window made of Pyrex glass facing the photomultiplier tubes.

The Na(Tl) scintillator crystal emits blue-green light (means a wavelength $\lambda \approx 415$ nm) and this spectral output matches well the light-photon response characteristics of standard bialkali (SbK₂Cs) photomultiplier tubes, Figure 25 (Webb, 2000).

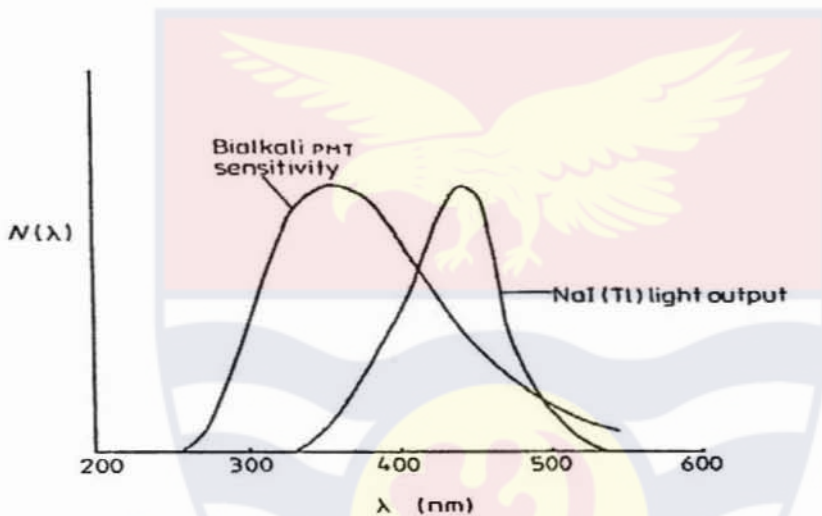


Figure 25: The spectral response of a bialkali photomultiplier tube compared with light output from a NaI (TI) scintillator (Webb, 2000).

Light guides

Owing to high refractive index of sodium iodide NaI(Tl) scintillator (1.85), it is necessary to provide a *light guide* to interface the scintillator to the photomultiplier. This minimizes the light losses in the transport of light to the photomultipliers. The guides are made of a transparent plastic with refractive index close to 1.85 and are carefully shaped to match the shape of the PMT cathode. Other type of guide is the optical coupling grease which are spread across the PMT to increase coupling of light from the scintillator to the PMT.

The light guide also helps to minimize the variation of light collection efficiency across the face of the scintillator.

The Detector assembly

The photomultiplier tubes are optimally arranged and closely packed onto the surface of a circular scintillation crystal in a hexagonal array (Figure 26) containing 7, 19, 27 and 61 PMTs (Webb, 2000).

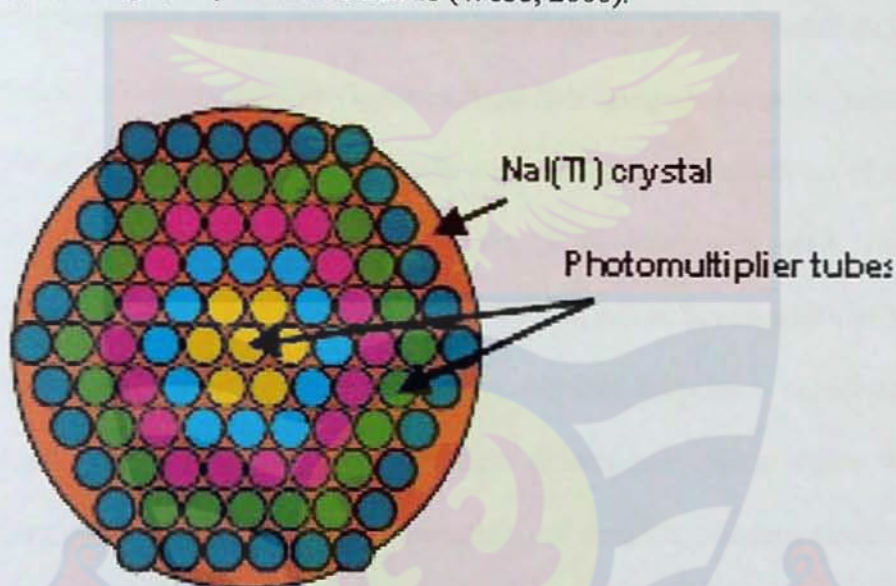


Figure 26: The optimal arrangement of PMTs array on the surface of the circular Sodium Iodide, NaI (TI) scintillation crystal (Jonasson, 2003).

The number of photomultiplier tubes affects the intrinsic resolution of the camera. The PMTs must have matched amplification (gain) characteristics in order to provide a uniform count density (flood field uniformity) when the crystal is 'flooded' with a spatially uniform flux of photons. If one photomultiplier has a markedly lower gain than those surrounding it, the area of the image corresponding to the location of that tube will appear as one of lower sensitivity (IAEA Human Health Series, 2009).

The width of the photopeak is highly dependent upon the precise adjustment of the gains of the photomultipliers. Each photomultiplier produces a unique photopeak and when these are summed to form the Z signal, all of the photopeaks should coincide. However, because of small gain differences between individual photomultipliers, this is rarely the case. Photomultipliers with gains lower than the average contribute information to the low side of the composite photopeak and those with gains higher than the average contribute to the high side. In order to achieve a uniform flood field image, the window width of the Pulse Height Analyser (PHA) must encompass the contributions of all photomultipliers. For this reason, typically a 20 % window is used. This window, centred on the 140 keV photopeak of ^{99m}Tc , would have a width of 28 keV, ranging from 126 to 154 keV. Such a window includes a significant amount of scattered radiation originating from photon interactions within the patient and leads to a loss of image resolution and contrast. Modern cameras allow the use of a 15 % energy window because of linearity and energy correction circuits. If the window is offset to the high side (asymmetric high energy window) of the photopeak, the information contributed by the lower gain photomultipliers will be progressively eliminated and the image areas corresponding to these tubes will have a lower count density. Correspondingly, if the window is offset to the low side of the peak (asymmetric low energy window), the information contributed by the higher gain photomultipliers will be progressively eliminated and the areas corresponding to these tubes will have a higher count density.

If the window width is narrowed but remains centred on the photopeak, areas corresponding to photomultipliers both of lower gain and of higher gain will be progressively eliminated. Thus, uniformity across the field of view is a function of proper placement of the PHA window, which can only be achieved by daily calibration. Uniformity is also a function of the window width, photon energy and the proper tuning of all photomultipliers (IAEA Quality Control Atlas for scintillation camera systems, 2003).

Collimators

A collimator is used to select the direction photons incident on the camera and determines the geometrical field of view (FOV), the spatial resolution and the sensitivity of the system (Webb, 2000). A range of collimators is required to image different photon energies and to achieve sufficient compromise between spatial resolution and sensitivity. The most commonly used are the parallel-hole, converging, diverging and pinhole collimators. These types exist as low- or middle-energy collimators depending on the required thickness of absorber.

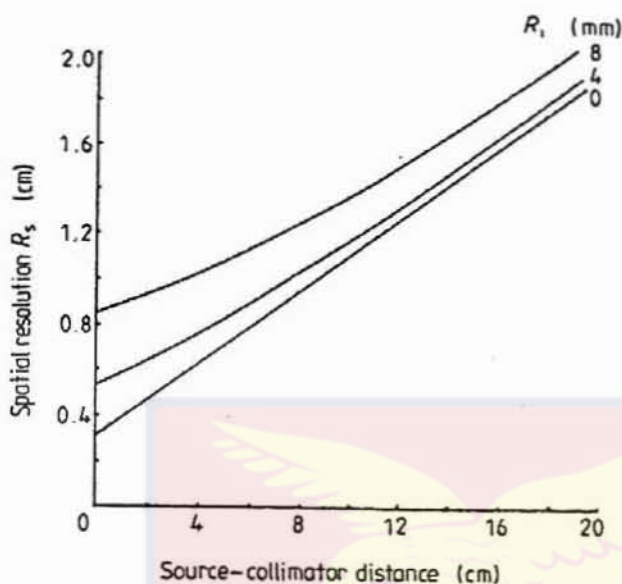


Figure 27: The variation of spatial resolution R_s as function of source-to-collimator distance for a range of intrinsic resolution values (R_i) for a parallel-hole collimator (Webb, 2000).

The spatial resolution is strongly dependent on the distance between the source and the collimator (Webb, 2000). In Figure 27, one can see that the spatial resolution (R_s) vary with the source-to-collimator distance for given values of intrinsic resolutions (R_i).

General Purpose low energy parallel collimator

The general-purpose low-energy multihole collimator consists of a lead disk, typically 25 mm thick, and is equipped with $\sim 25 \text{ holes/cm}^2$ closely packed circular or hexagonal holes. The holes have a diameter of 2.5 mm and the lead between them, called septa is 0.3 mm thick. This type of collimator can be used for energies up to 150 keV, e.g. ^{99m}Tc .

High resolution collimator

A high-resolution collimator would have more and smaller holes per cm^2 and therefore lower sensitivity. This kind of collimator often used when high resolution is required and the total number of detected photons is acceptable depends of course on the amount of radioactivity and the imaging time.

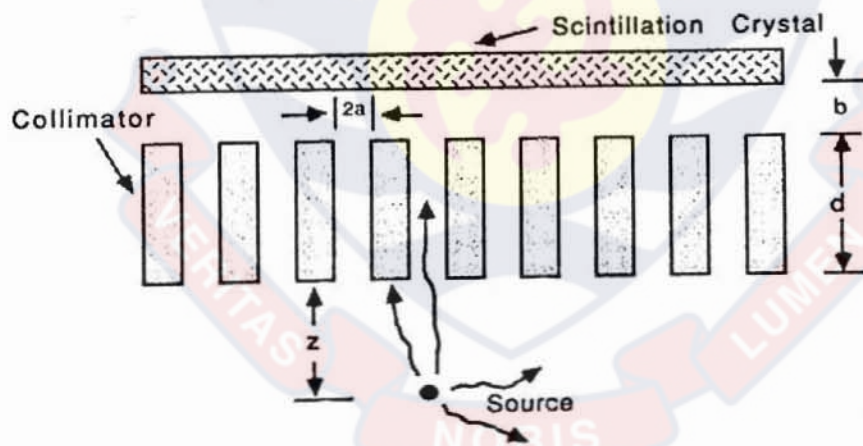
High sensitivity collimator

A "high-sensitivity" collimator has fewer and larger holes and consequently poorer resolution. This type is used for dynamic imaging where short exposure times are necessary and poorer resolution must be accepted. For energies up to 400 keV, e.g. ^{111}In , ^{67}Ga , and ^{131}I , one will use a medium-energy collimator. It has thicker septa (1.4 mm), consequently fewer holes, and much lower sensitivity.

The purpose of the collimator is to only accept incident photons perpendicular to the holes to reach the scintillation crystal. The septa absorbs all but few percent of the Gamma rays with a direction that transverse the septa. It is also possible that the photons can be Compton-scattered in the patients body and pass through the collimator. However, these gamma rays will have less energy and thus can be rejected by energy discrimination, as it will be discussed later.

The Parallel Multihole Collimator

The parallel-hole type of collimator is the most commonly used in radionuclide imaging (Webb, 2000; Bushberg, *et al.*, 1994; Shung, *et al.*, 1992, Farr and Allisy-Roberts, 1999) It consists, as for all multihole collimators of an array of holes separated by lead septa. The holes are orientated perpendicular to the surface of the crystal, and therefore the size of the image of the radionuclide distribution has a one-to-one ratio. As mentioned above the collimator has a major effect on the spatial resolution and determines the detection efficiency of the gamma camera. The spatial resolution FWHM (Full Width Half Maximum) is related to the width of the average intensity distribution from a point source placed at a distance z from the collimator face (Figure 28).



The principle of a parallel multi-hole collimator

Figure 28: The principle of a parallel multihole collimator (Shung *et al.*, 1992),

The spatial resolution can be expressed as (Shung *et al*,1992):

$$R_s = \frac{2a(d+z+b)}{d} \quad 3.66$$

where R_s is the spatial resolution, $2a$ is the diameter of the collimator hole, d is the length of the collimator and b is the gap between the back of the collimator and the image plane inside the crystal, Figure 28 (Shung, *et al*; 1992).

The Diverging Multihole Collimator

The diverging multihole collimator, were used earlier for imaging large objects, e.g. lungs, with a small camera, due to its reduction effects, nowadays the small cameras have almost disappeared and have been taken over by the large field of view cameras (Figure 29).

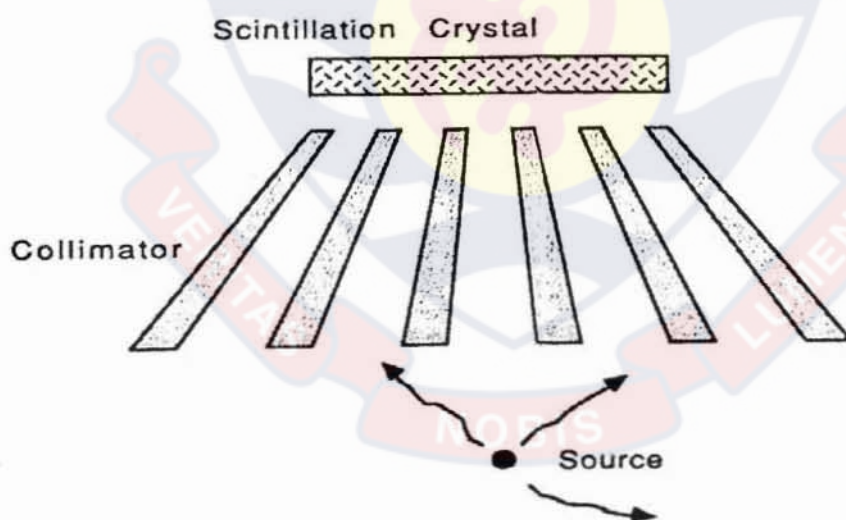


Figure 29: The principle of a diverging multihole collimator (Shung *et al*, 1992).

Preventive maintenance

In contrast to the care, handling and protection programme, the preventive maintenance programme is designed and implemented against possible faults to the instruments. It should be periodically carried out and checked using the necessary quality control tests. A good preventive maintenance programme should include the following main procedures:

- 1 Quality checks of parts, electronic circuits, components, connectors and cabling, etc.
- 2 Inspection of detector/sensor condition.
- 3 Checks of low and high voltage power supplies.
- 4 Bias adjustment, preliminary adjustment of energy and position signals and preamplifier fine tuning, etc.
- 5 Calibration of all correction circuits (e.g. energy, linearity, uniformity and attenuation corrections).
- 6 Inspection of the integrity and stability of moving parts, with due consideration given to the lifetime and wear of components in frequent use, such as cables, relay switches, etc
- 7 As in the case of corrective maintenance (repairs), preventive maintenance is machine dependent. As such, the protocols will differ from machine to machine. Usually, preventive maintenance is periodically carried out by qualified service engineers through contracted service. In addition, all documentation, including service manuals and circuit diagrams, necessary test tools and radiation sources,

must be obtained at the procurement stage (IAEA Human Health Series, 2009).

Quality control records

Record keeping is of great importance in a quality management programme. The operational, quality control and maintenance records for each instrument should be assembled in appropriate log books and retained with the instrument. The records should include the results of the acceptance, reference and routine tests carried out for quality control, a record of preventive maintenance carried out and a record of failures, with details of their repair.

The responsible person(s) should sign all entries. In addition, it is helpful to assemble and maintain a complete procedure manual detailing all clinical and test protocols. Indeed, such procedure manuals are required by accreditation organizations. It is essential that all concerned appreciate the meaning of the records kept. Record sheets should be so designed that they are appropriate, easy to complete and easy to understand; explanatory notes should be provided, if necessary. Only essential data and results should be recorded; raw data can be kept in a separate book or file. Control charts and graphs displayed on the wall near the instrument are helpful in quickly ascertaining its long term stability and in stimulating regular testing.

Images obtained in quality control testing should be kept in chronological order, either in a logbook or in electronic form, together with the relevant imaging parameters and the results of other quality control tests on the instrument. They should be frequently reviewed for evidence of deterioration in

performance, which may not be initially apparent. Records showing repeated failure and/or progressive degradation of performance provide unquestionable evidence for complete instrument overhaul or replacement. If the records or logbooks are set up as digital records, there must be a suitable backup of the records (IAEA Human Health Series, 2009).

Gamma camera performance characteristics

The performance of gamma camera system is defined by the sharpness and detail of the images it produces, the efficiency with which it detects incident radiation, its ability to measure the energy of the incident γ rays (to minimize scatter), and counting rate it can handle without significant dead time losses.

A gamma camera is not capable of producing “perfect” images of the radionuclide distribution. Certain inherent imperfections arise from the performance characteristics of the detector, its associated electronic circuitry, and the collimator. Image artefacts also can be caused by malfunctions of various camera components. This section describes the major factors that determine gamma camera performance and examine the limitations that can lead to artefacts in gamma camera images and their corrections (Cherry *et al* 2003).

Intrinsic Spatial Resolution

Spatial resolution is a measure of the sharpness and detail of a gamma camera image. Spatial resolution is also defined as the performance characteristic of a scintillation camera that describes its capability to resolve

two separate point or line sources of radiation as separate entities. Spatial resolution is conventionally quantified either as the full width at half maximum (FWHM) of the response to a thin line source perpendicular to the long axis of the source, or as the minimum separation of two sources that can just be distinguished from each other (IAEA human health series, 2009). Spatial resolution can also be defined as a measure of the sharpness and detail of gamma camera image. Sharp edges or small pointed objects produce blurred rather sharply defined images. Part of the blurring arises from collimator characteristics and part arises from NaI(Tl) detector and positioning electronics. The limit of spatial resolution achievable by the detector and electronics, ignoring the blurring due to collimator is called the intrinsic spatial resolution of the camera. Intrinsic spatial resolution is limited primarily by two factors. The first is multiple scattering of photons within the detector. The second and primary cause of limited intrinsic resolution is the statistical fluctuation in the distribution of light photons among photomultiplier tubes (PMTs) from one scintillating event to another. The actual number recorded from one event to the next varies with a standard deviation given by \sqrt{N} . The change of intrinsic spatial resolution as a function of γ -ray energy is shown in Figure 31. The resolution is calculated as the full width at half maximum (FWHM) of a profile drawn perpendicular to the image of the lines at various locations in the field of view. Intrinsic resolution becomes worse with decreasing γ -ray energy because lower energy γ -rays produce fewer light photons per scintillation

event. As a rule of thumb, intrinsic resolution is proportional to $\frac{1}{\sqrt{E}}$, where E is the γ -ray energy (Cherry *et al* 2003).

Intrinsic resolution also depends on detector crystal thickness. Thicker detectors results in greater spreading of scintillation light before it reaches the PMTs. Furthermore, there is a greater likelihood of detecting multiply Compton- scattered events in thicker detectors, particularly with higher energy nuclides. These are the primary reason why gamma cameras use relatively thin detectors in comparison with NaI(Tl) systems that are used for counting applications. Figure 31 shows a plot of the intrinsic spatial resolution as a function of crystal thickness for 140-keV γ -rays intrinsic resolution improves with increased efficiency of collection of scintillation photons (Cherry *et al* 2003).

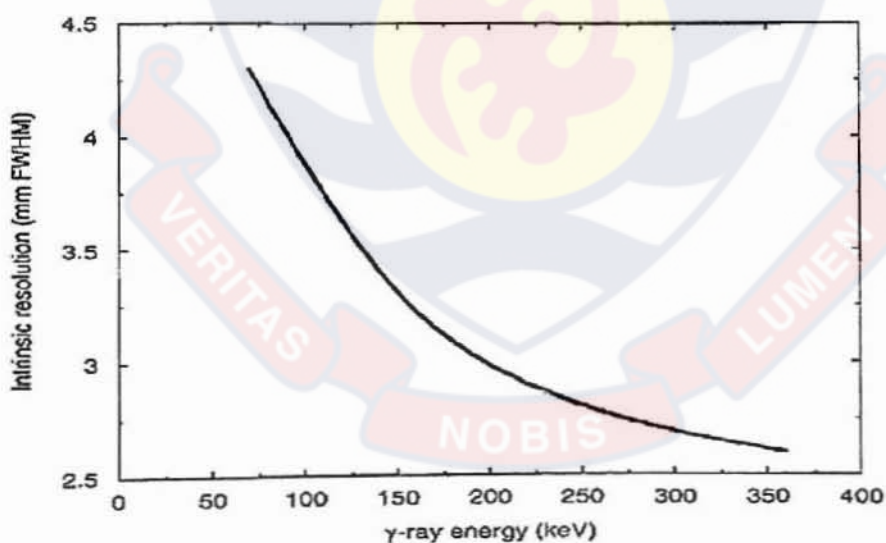


Figure 30: Intrinsic spatial resolution of gamma camera as a function of γ -ray energy for a 6.3-mm thick NaI(Tl) crystal (Cherry *et al* 2003).

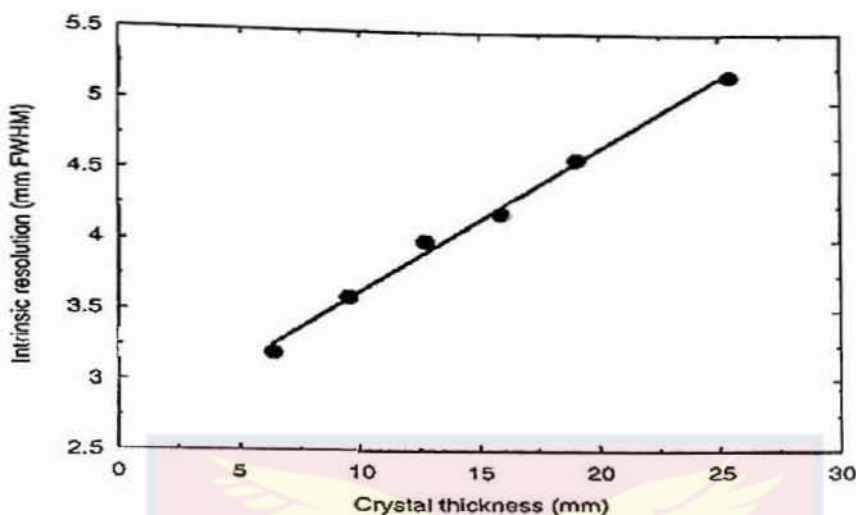


Figure 31: Intrinsic spatial resolution of a gamma camera at 140 keV as a function of crystal thickness (Cherry *et al* 2003).

Energy resolution

The energy resolution is the ability of an imaging system to distinguish between the photopeaks of different radionuclides. If the energy resolution is good the photopeaks will be very tall and narrow. Energy resolution describes the capability of the scintillation camera to distinguish between photons of different energies, in particular between primary and scattered radiation (IAEA Human Health Series, 2009).

Energy resolution like the intrinsic spatial resolution, depends largely on statistical fluctuations in the number of light photons collected from scintillating event. Thus good light collection efficiency is a prerequisite for good energy resolution. Energy resolution of gamma cameras improves approximately in proportion to $1/\sqrt{E}$. For gamma cameras, the energy resolution is typically in the range 9 % to 11 % range for ^{99m}Tc . Figure 32 shows a typical gamma camera spectrum for ^{99m}Tc with the pulse height analyzer

window set at 150 keV. The energy window, is a commonly setting at 15% for clinical studies.

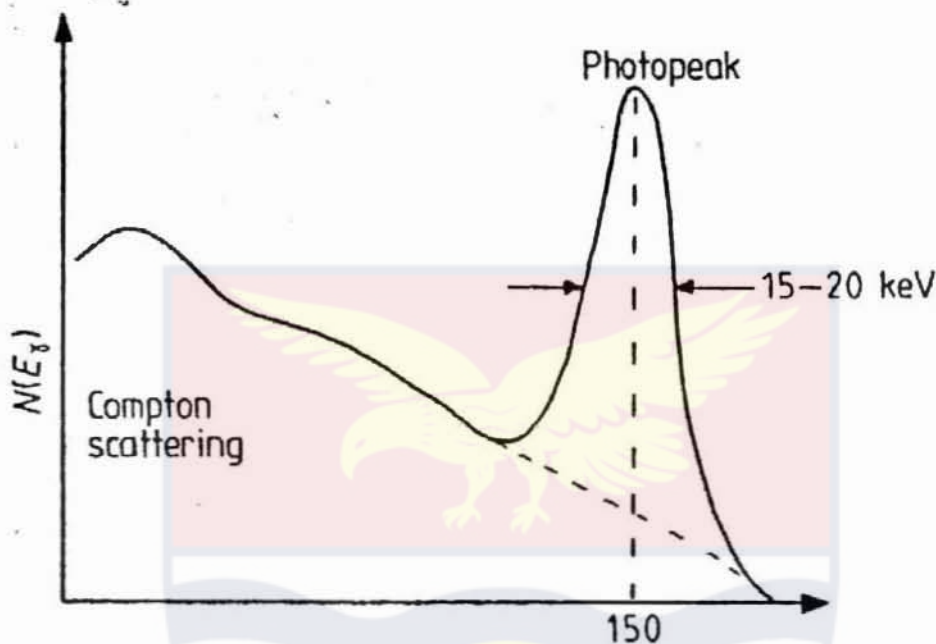


Figure 32: The energy resolution of a thin NaI(Tl) crystal at 150 keV using a point source of ^{99m}Tc (Webb, 2000).

Performance at High Counting Rates

Anger Cameras, like other radiation detectors, suffer the effects of pulse pileup, as mentioned by Lewellen, *et al* (1989). During high count-rate studies, pulse pileup is responsible for increased camera dead-time losses and image distortion with loss of image contrast and detail. A continuing goal of camera designers has been to provide high-counting-rate capabilities with minimal dead-time losses and acceptable image quality (i.e., minimum displaced counts, loss of spatial and energy resolution, and loss of uniformity).

The basic problem during high counting-rate studies is the response of the amplifier that shapes each of the preamplifier pulses (Sorenson, 1987; Leo,

1987; Nicholson, 1974, Rollo, 1977). In most gamma cameras, there is a set of amplifiers that integrate the detector pulses to produce a shaped output pulse whose height is proportional to the amount of energy deposited by scintillation crystal. The input signals to these integrators may be relatively long tailed pulses. Ideally, the entire preamplifier pulse should be integrated in order to obtain the best of measurement of the event's energy.

However, a long integration time increases the probability that two or more events will be integrated together (pulse pileup) to produce a single distorted output pulse (Figure 33). These distorted output pulses are used in the subsequent signal processing of the camera.

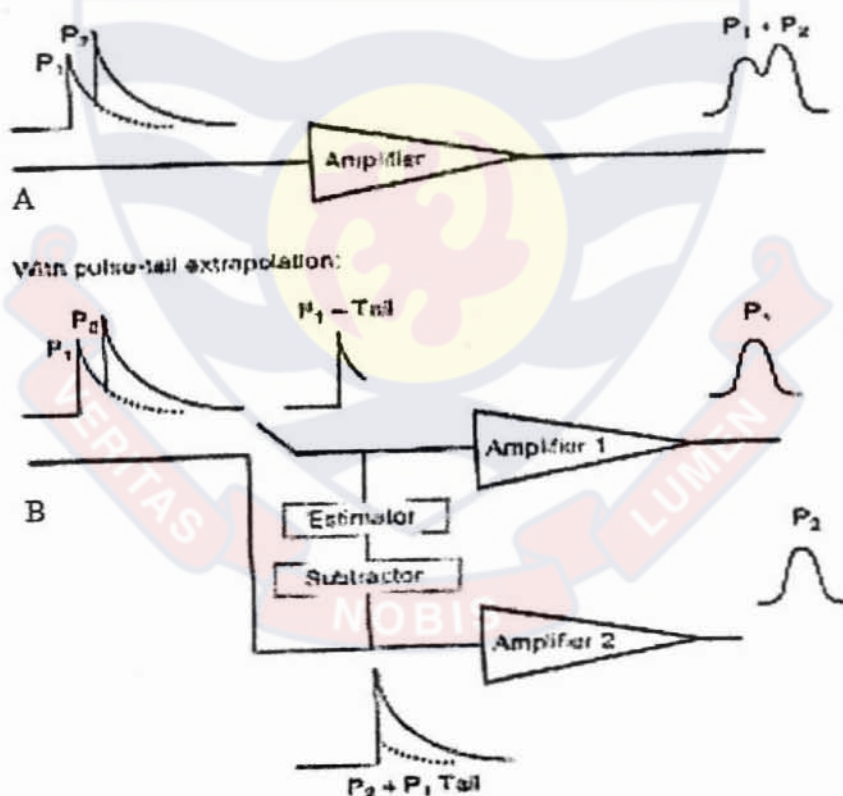


Figure 33: A) Show the Single distorted output pulse from the amplifier that results when two analog pulses arrive too close together in time. B) Shows the pulse pileup correction using the pulse-tail extrapolation techniques (Cherry *et al* 2003).

One commonly implemented method for pulse pileup reduction is to have the integrator process only the first part of the pulse. This strategy diminishes the effects of the succeeding pulses but degrades energy and spatial resolution. Pulse pileup is not eliminated, but higher counting rates are required before it is prominent. A second commonly implemented method for pile-up rejection is to start a timer when the integrator output pulse rises above a very low voltage level (Nicholson, 1974). If the output pulse does not return close to its baseline value by a preset time, then the pulse is considered distorted and it is rejected. With this method, increasing numbers of events are discarded at increasing event rates.

Another problem of the amplifier system at high counting rates is baseline shift. Baseline shift is usually corrected in scintillation cameras using pole zero cancellation or baseline restoration (Sorenson, 1987; Leo, 1987; Nicholson, 1974). In all of these approaches, little is really done to adjust for the voltage pedestal under a pulse caused by a preceding pulse's tail (Cherry *et al*, 2003).

Many gamma cameras now incorporate circuits that continuously monitor the decay of a pulse and use a method based on *pulse-tail extrapolation* for pileup correction.

Consider two γ -ray interactions that occur closely together in time and create over-lapping pulses. When the second γ -ray arrives, the decay of the first pulse created by the first γ -ray immediately deviates from the expected exponential decay and the gamma camera signal is switched to a second amplifier circuit.

Estimator circuitry in the first amplifier circuit completes the signal from the first γ -ray by extrapolating the remainder of the tail of the pulse with an exponential function based on the decay time of Na(Tl). At the same time, this extrapolated tail is also sent to the second amplifier circuit and subtracted from the second pulse. This removes the contribution of the pulse generated by first γ -ray from the second γ -ray (Cherry *et al*, 2003). This process is summarized in Figure 33.

Quality Control and Non-uniformity

The non-uniformity of response of the gamma camera can be determined by both global (integral) uniformity and local (differential) uniformity measurements (Figure 34). Integral uniformity is an indication of the extreme range of variation in regional sensitivity over a defined field of view and is given by NEMA as

$$U_I(\%) = \frac{(\max - \min)}{(\max + \min)} \times 100 \quad 3.67$$

where 'max' is the maximum pixel count and 'min' is the minimum pixel count. Differential uniformity indicates a maximum rate of change of sensitivity over a predetermined short distance within the FOV and is given by NEMA as

$$U_D(\%) = \frac{(hi - low)}{(hi + low)} \times 100 \quad 3.68$$

where 'hi' and 'low' are the maximum and minimum pixel counts for all rows and columns within a localized line of five pixels for which hi-low is the largest deviation.

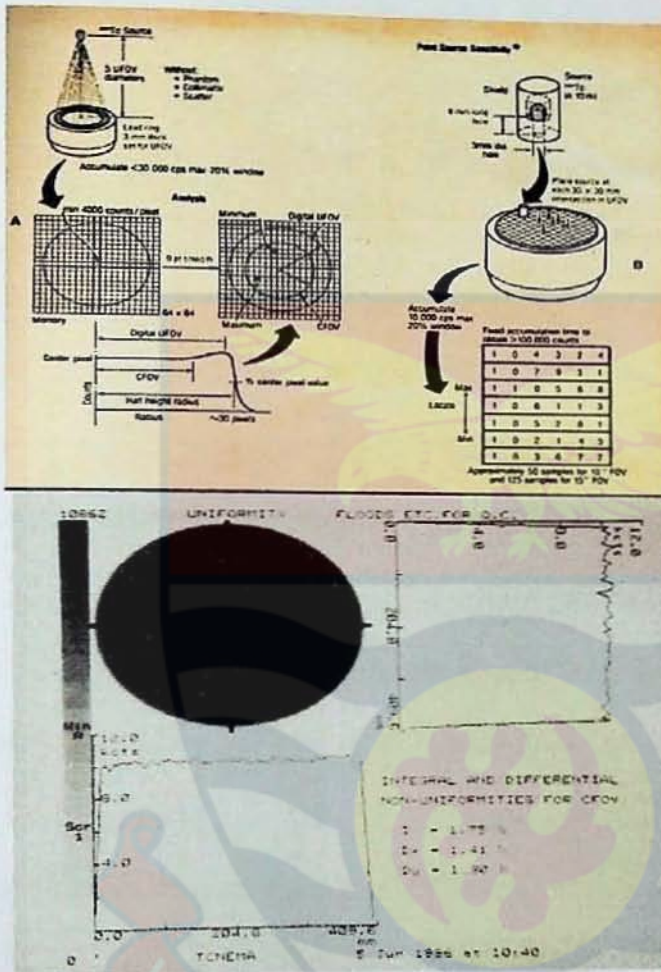


Figure 34: Illustrations of integral and differential non-uniformity obtained from a modern digital gamma-camera systems (IGE, STAR-CAM), (Early and Sodee, 1985)

Basis of schemes for testing scintillation camera performance

Various levels of performance testing are required in the life of any scintillation camera. Initially, manufacturers perform a set of tests on each camera in the factory to determine if published specifications are met. In the USA, factory testing is done according to protocols developed by NEMA.

Results for each camera are compared with the published specifications before the shipment is authorized. The NEMA performance standards (NEMA, 2001) are recognized throughout the world. Hence, for new cameras, one manufacturer's specification is directly comparable to another's. The tests involved are mostly intrinsic tests, that is, they are tests on the camera without a collimator or other accessories. These tests reflect only the camera's characteristics, not necessarily its operating performance under clinical conditions. Alternative test protocols are those of the International Electrotechnical Commission (IEC 60789-2, 1998; IEC 61675-3, 1998; IEC 60789-1-am1, 1998; IEC 60789, 3rd ed, 2005).

The user should be aware of which test protocols have been followed by the manufacturer to provide the specifications for a particular system. The camera should be acceptance tested by the user after installation to determine if, once installed, it performs according to the specifications of the manufacturer. This testing must be rigorous and similar enough to the NEMA or IEC protocols so that comparable results are obtained. When comparing test results with specifications provided by the manufacturer as measured according to NEMA or IEC protocols, the user must be aware of the energy window width applied. While performing acceptance tests, reference tests should be initiated. Reference tests reflect operating performance under clinical conditions, can be repeated in routine testing, and are often system tests performed with collimator mounted, added accessories and a variety of clinically used radionuclides. Reference tests are more suited to being carried out by the user and can be adapted to local conditions and requirements. A number of organizations have

developed test protocols for reference tests, among them the American Association of Physicists in Medicine (AAPM, 1980; AAPM, 1981; AAPM, 1987) and the Institute of Physics and Engineering in Medicine (IPEM, 2003). These tests, along with some acceptance tests, provide the basis of routine testing. Last, but most important, operational checks must be initiated which are to be performed each day that the instrument is used (IAEA Human Health Series, 2009).



CHAPTER FOUR

DESIGNED AND FABRICATION OF PMT CASING, EXPERIMENTAL SET – UP AND PMT MEASUREMENTS

Overview

The main work of the thesis is found in this chapter. The work involved the design and fabrication of a PMT casing, followed by the design and construction of high voltage and low voltage supplies and lastly the operation and testing of the voltage supplies were discussed.

1. Design and construction of the casing (housing) of the PMT testing instrument.
2. Design and construction of high voltage and low voltage supplies
3. Design and construction of oscillator circuit that was used to switch on the LED to emit the reference blue light for the PMT under test.

Design and Fabrication of a PMT Casing

The casing of the PMT testing instrument measured $L = 30.48$ cm, $B = 39.37$ cm, and $H = 51.28$ cm. Target 3001! PCB (Printed Circuit Board) layout Computer Aided Design (CAD) software was used to design the casing of the PMT testing instrument. The designed casing is shown in Figure 4.1. The block diagram of the casing with the dimensions was manufactured by the Mechanical workshop of the Ghana Atomic Energy Commission. The completed casing is shown in Plate 4.5. The chamber of the completed instrument showing the PMT under test and the reference (blue) light is indicated Plate 4.2.

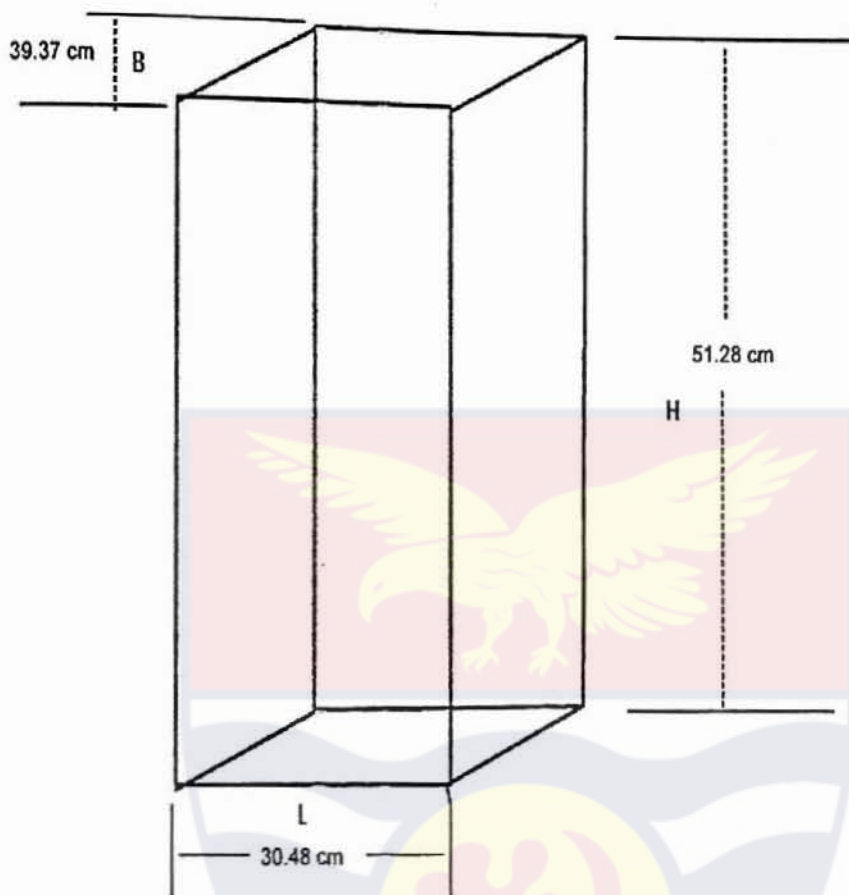


Figure 35: A Block diagram of the casing for the PMT testing instrument

Material selection for the casing of the PMT instrument

Material selection for the PMT casing was very important because of the following reasons: 1). High voltage of about -2000V DC was used for the measurement. 2) PMTs are very sensitive to light and therefore light must be prevented from entering the housing when HV was applied to the PMT under test, in order not to damage it. 3) Currents and voltages that measured were very small (pA and pV) and so the material should avoid current loop and also

ensure that the chamber of the housing provide the necessary shielding against electromagnetic interference.

Two materials were available for selection, namely; Wooden and Metallic materials. The metallic material was chosen for the casing.

High Voltage Power Design Constraints

Stray capacitance

Stray capacitance becomes an important consideration as input frequency increases. As the following expression indicates, an increase in frequency decreases the capacitive reactance, resulting in increased current flow through the insulating materials.

$$X_c = \frac{1}{(2\pi fC)} \quad 4.1$$

Power losses through insulation, which are negligible at 60Hz, become significant at high frequency.

Leakage Losses

Losses due to leakage in diodes, capacitors and insulation are significant considerations in applications using very low capacitor values (i.e. night vision power supplies) and in applications, which operate at high temperatures (>125°C). Figure 36 shows some of the factors affecting high voltage multiplier efficiency and includes stray capacitance, and leakage currents in diodes.

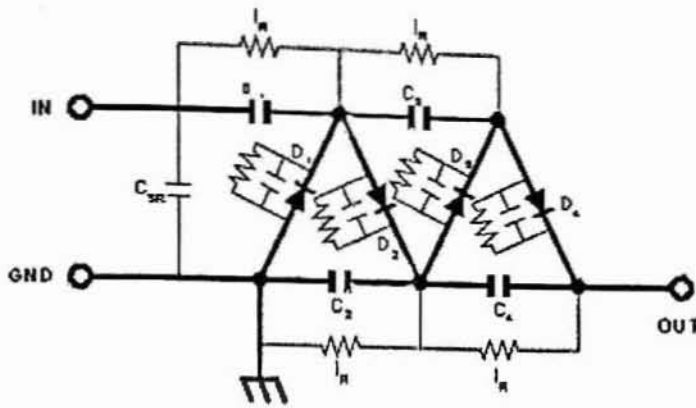


Figure 36: Factors that affect efficiency of high voltage power supply

Voltage Regulation of the designed High Voltage supply

DC output voltage drops as DC output current is increased. Regulation is the drop, from the ideal, in DC output voltage at a specified DC output current (assuming AC input voltage and AC input frequency are constant). A close approximation for series half-wave multipliers can be expressed as:

$$V_{reg} = \frac{\left[I \left(N^3 + \left(\frac{9N^2}{4} \right) + \left(\frac{N}{2} \right) \right) \right]}{12fC} \quad 4.2$$

Where: N = # of stages, (1 capacitor and 1 diode = 1 stage)

f = AC input frequency (Hz)

C = capacitance per stage (F)

I = DC output current (A)

Design of High Voltage and Low Voltage Supplies Circuit

The design of the high voltage supply was based on the Cockcroft Walton voltage multiplier circuit. Target 3000! Schematic and Printed circuit boards (PCB) design software was used to design the high and low voltage supply circuits.

The Target 3001! design software has a window that enables a new project to be created. Once the software is opened a new project template appears with the following five options of which the user is required to select one:

1. Single sided PCB with schematic
2. Single sided PCB without schematic
3. Double sided PCB with schematic
4. Double sided PCB without schematic
5. Aluminium front panel

The number (3) was selected for this work since the components for the high voltage supply were many, a printed circuit board that could have electronic components on both sides of the PCB was needed.

Electronic components were called symbols by the by the target software and were called from the symbol library on to the schematic window. The symbols for the CD4011 NAND gate and CD4027 were called first from the library on to the project window and signal wires were used to connect them. The same procedure was used to call the symbols of the transformer, diodes, capacitors, and resistors to have the completed circuit diagram as shown in

Figure 37. The same method was used to design the low voltage supply as shown in Figure 38.

The Operation of High Voltage Power Supply Circuit

The high voltage power supply circuit begins with a voltage oscillator circuit then oscillation is sent to an input of a JK flip flop which divides the frequency by two and provides two outputs with one output inverted to the driver MOSFET transistors which drive the primary of the multiplier transformer in order to increase current in the multiplier diodes, as shown in Figure 36.

Operation of the oscillator section

The oscillator circuit is made up of two CMOS NAND gates (CD4011) connected as inverting NOT gates, U2a and U2b (Figure 38). Suppose that initially the output from the NAND gate U2b is HIGH at logic level "1", then the input must therefore be LOW at logic level "0" (NAND gate principles) as will be the output from the first NAND gate U2a. Capacitor, C_1 is connected between the output of the second NAND gate U2b and its input via the timing resistor, R_4 . The capacitor now charges up at a rate determined by the time constant of R_4 and C_1 .

As the capacitor, C_1 charges up, the junction between the capacitor, C_1 , and the input of the NAND gate U2a via the stabilizing resistor, R_1 decreases until the lower threshold value of U2a is reached at which point U2a changes state and the output of U2a now becomes HIGH. This causes NAND gate U2b

to also change state as its input has now changed from logic "0" to logic "1" resulting in the output of NAND gate U2 becoming LOW, logic level "0".

Capacitor C_1 is now reverse biased and discharges itself through the input of NAND gate U2a. Capacitor, C_1 charges up again in the opposite direction determined by the time constant of both R_4 and C_1 as before until it reaches the upper threshold value of NAND gate U2a. This causes U2a to change state and the cycle repeats itself over again. The frequency oscillations, which is a square wave is given by:

$$f = \frac{1}{2.2(RC)} \quad (\text{Hz}) \quad 4.3$$

Operation of the Multiplier Section

The most commonly used multiplier is the half-wave voltage series multiplier. All voltage multiplier circuits can be derived from the operation of half-wave voltage multiplier principles of operation. The following description assumes no losses and represents sequential reversals of polarity of the transformer (T_s) in Figure 37.

T_s = Negative peak: C_3 charges through D_1 to E_{pk}

T_s = Positive peak: E_{pk} of T_s adds arithmetically to existing potential

C_3 , thus C_2 charges to $2E_{pk}$ through D_2

T_s = Negative peak: C_5 is charged of $2E_{pk}$ through D_3

T_s = Positive peak: C_4 is charged to $2E_{pk}$ through D_4 then $E_{pk}(N)$ where
 N = number of stages.



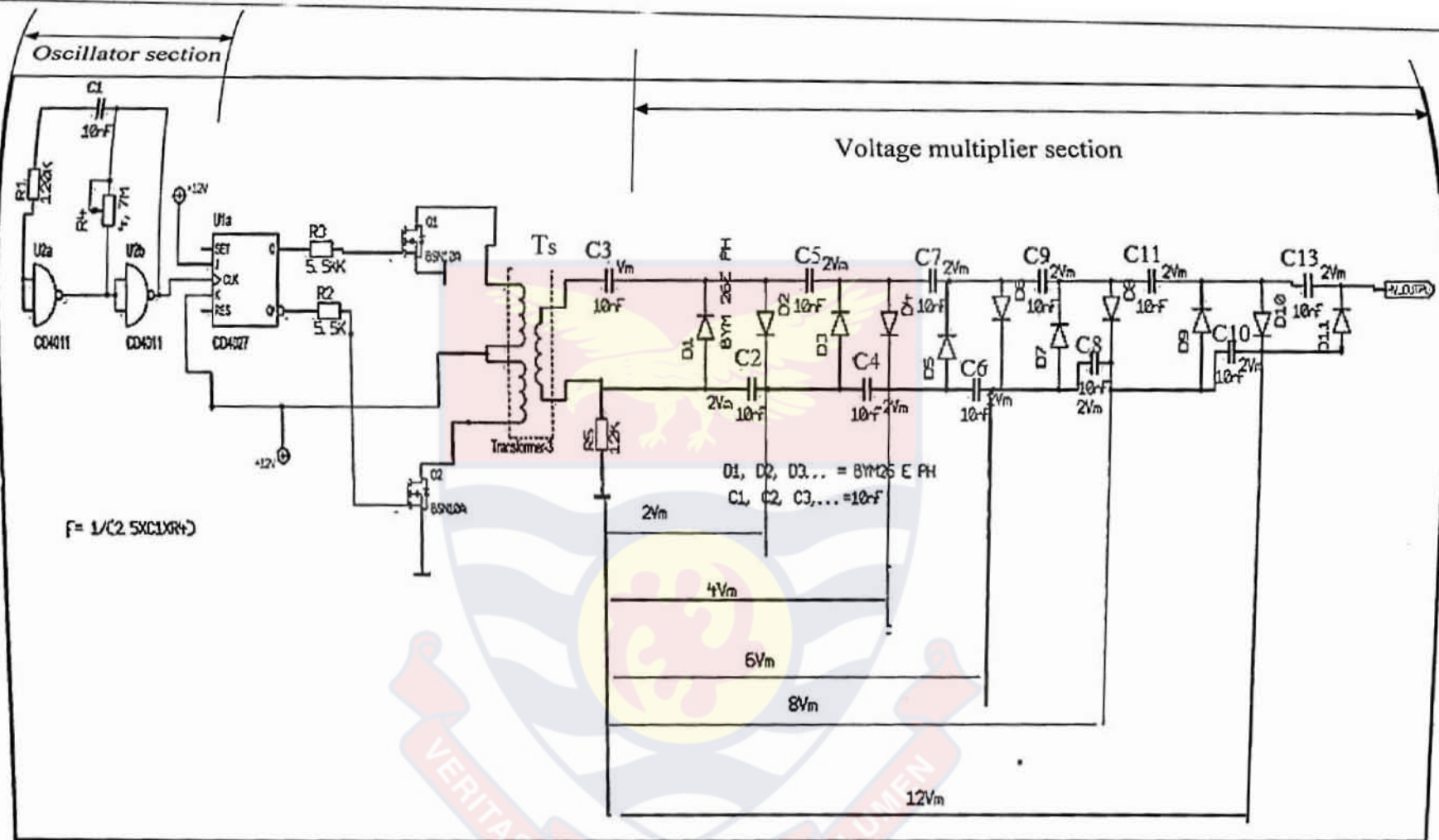


Figure 37: Schematic diagram of the high voltage supply of the PMT testing instrument

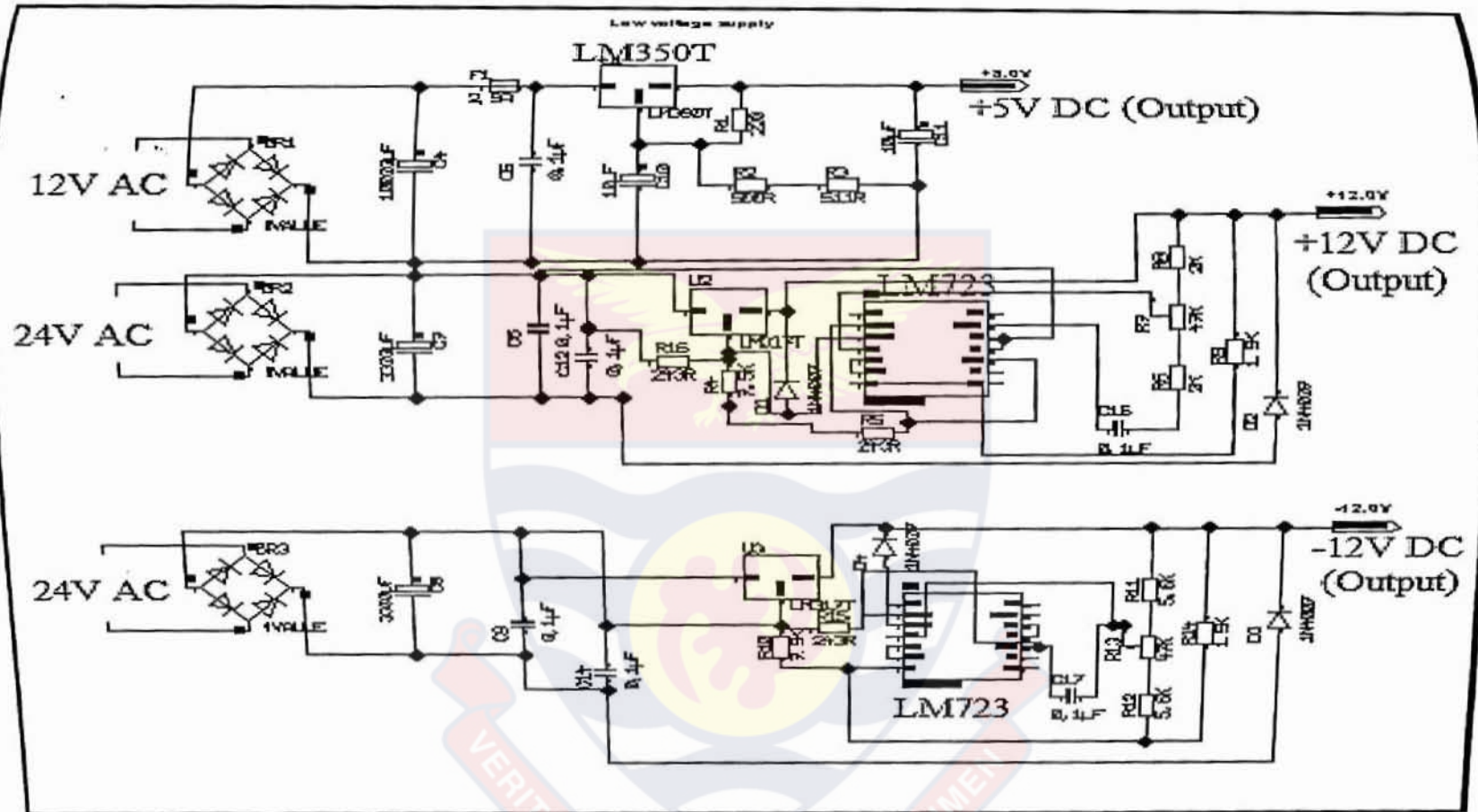


Figure 38: Designed low voltage (dc) power supply circuit using Target 3001! Schematic and PCB design Software V15. A) + 5 V dc supply. B) +12V dc supply. C) -12Vdc supply

The operation of the low voltage supply circuit

The bridge rectifier diodes (Br1) provide rectification (Figure 38) in both directions of the input AC waveforms. Capacitor C_4 works as a reservoir capacitor and charges to the root-mean-square voltage (V_{rms}) of the input AC voltage ($V_{rms} = E_{pk} \times 1.414$). The LM350T, voltage regulator maintains the output voltage at 5V.

The bridge (Br2) rectifier diodes (Figure 38) also provide rectification in both directions of the input AC waveforms. Capacitor C_7 is also a reservoir capacitor for the +12V DC supply. The voltage regulator LM723 maintains the output voltage at +12V.

The -12V supply works as the +12V supply except that the polarity of the components in the supply voltage are reversed.

The construction of the low voltage DC supply

The low supply DC voltages supply (+5V, +12V and -12V) was built on a printed circuit board (PCB). The completed board is shown in Plate 2. The +5V DC power supply was used to supply the Integrated Circuits (IC) in the oscillator section of the HV power supply. The +12V and -12V supplies were used to power the preamplifiers that were attached to PMTs.

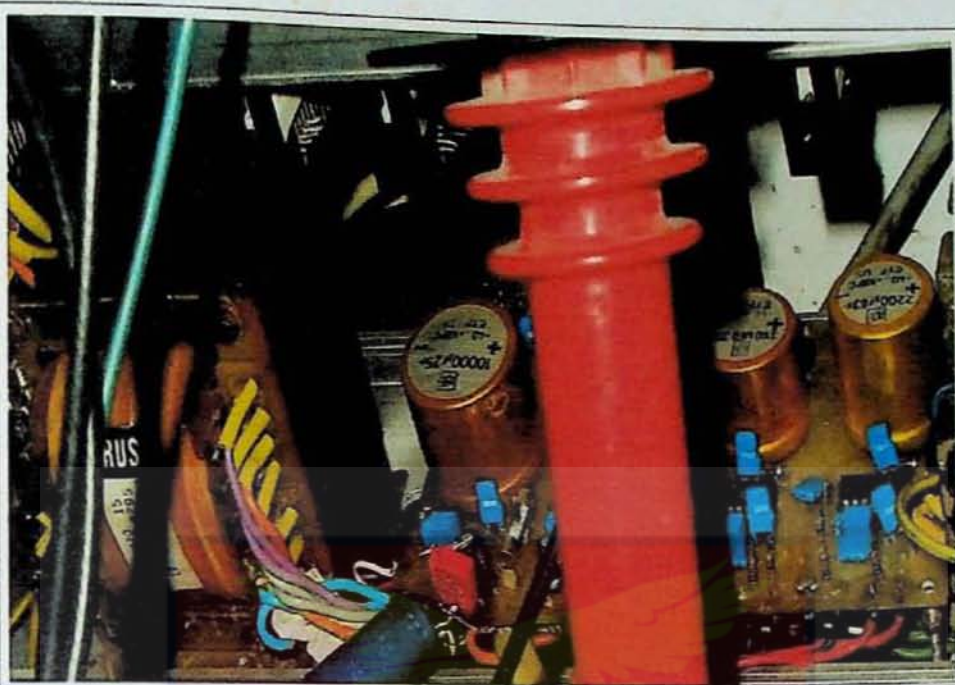


Plate 2: Completed low voltage DC power supply (+5V, +12V and -12V) built on a PCB.

The Construction of the High Voltage power supply circuit

The HV schematic diagram shown in Figure 37 was constructed on a prototyping board. The completed board of the HV supply is shown in Plate 3.

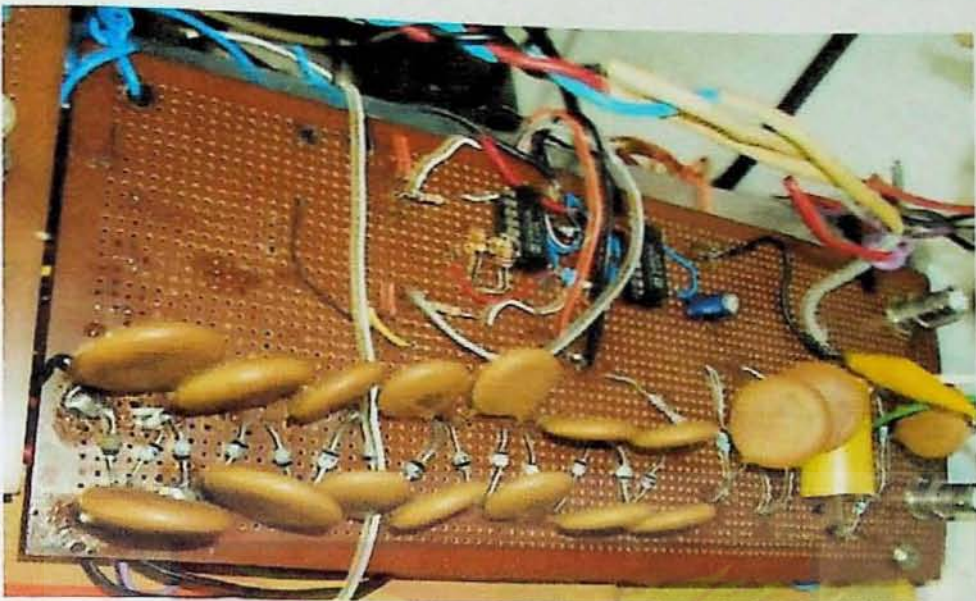


Plate 3: Completed 17 Stage HV power supply built on a Prototyping board



Plate 4: A BNC coaxial cable has tapped a voltage from one of the BNC sockets on the HV supply to the PMT under test in the testing instrument's chamber

Experimental Setup

The Block diagram of the experimental setup

The oscillator circuit produces square wave oscillations at a frequency of 31 kHz, marked *A* in the block diagram (Figure 39). The output of the oscillator was applied to a blue LED to emit a blue light at that frequency of 31 kHz marked *B* on the diagram. The PMT under test was then placed in the PMT instruments chamber marked *C* and a high voltage power supply marked *E* was applied to the PMT. The output of the PMT was then oscilloscope.

Operation of the Circuit

The light incident on the PMT was converted to photoelectrons at the same frequency as the blue light (31 kHz). The output of the PMT was simultaneously coupled to the Analogue oscilloscope and the PC scope, marked *D* on the diagram. The high voltage power supply is marked *E*. The Instruments used for the experimental setup are shown in Figure 39.

In effect the experiment was based on the principle of photoelectric effect, i.e., the emitted photoelectron has the same kinetic energy and momentum as the incident photoelectron.

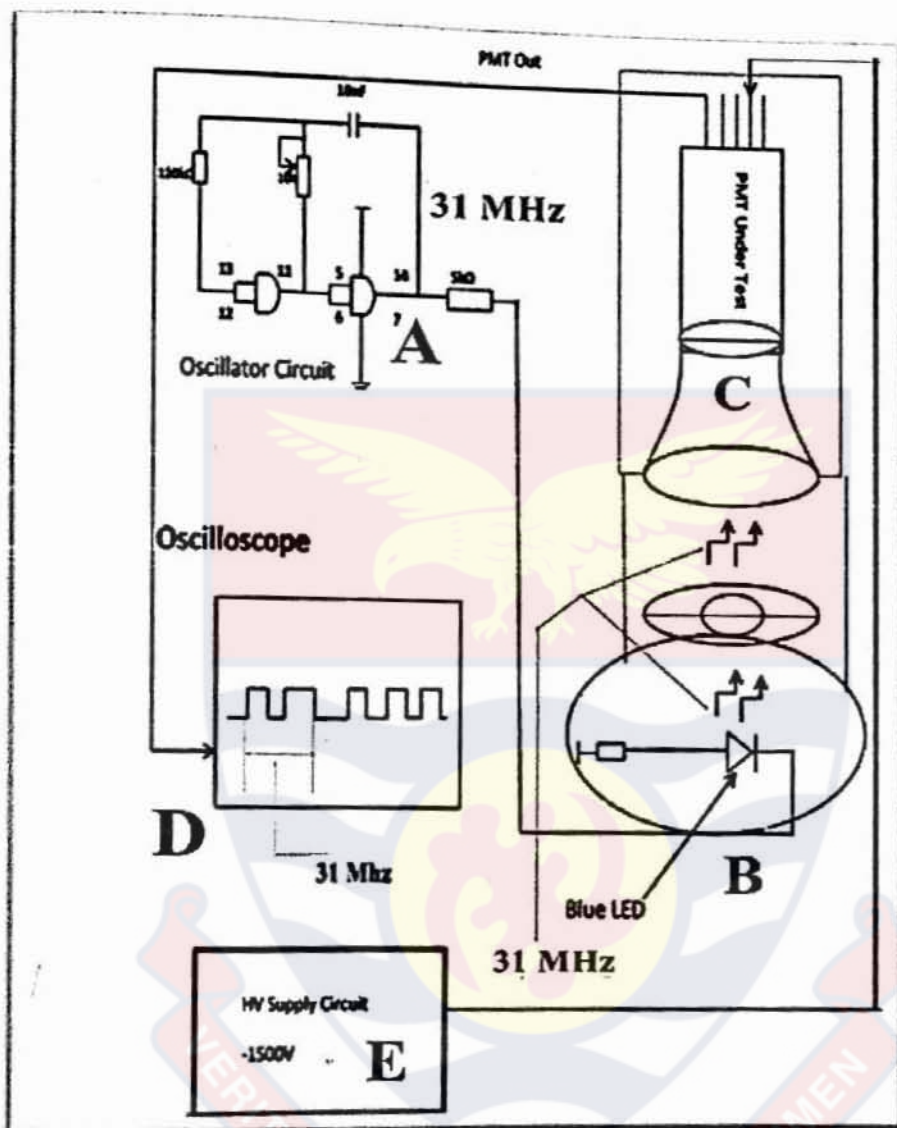


Figure 39: Block diagram of the experimental setup using the designed and fabricated PMT instrument and oscilloscope.

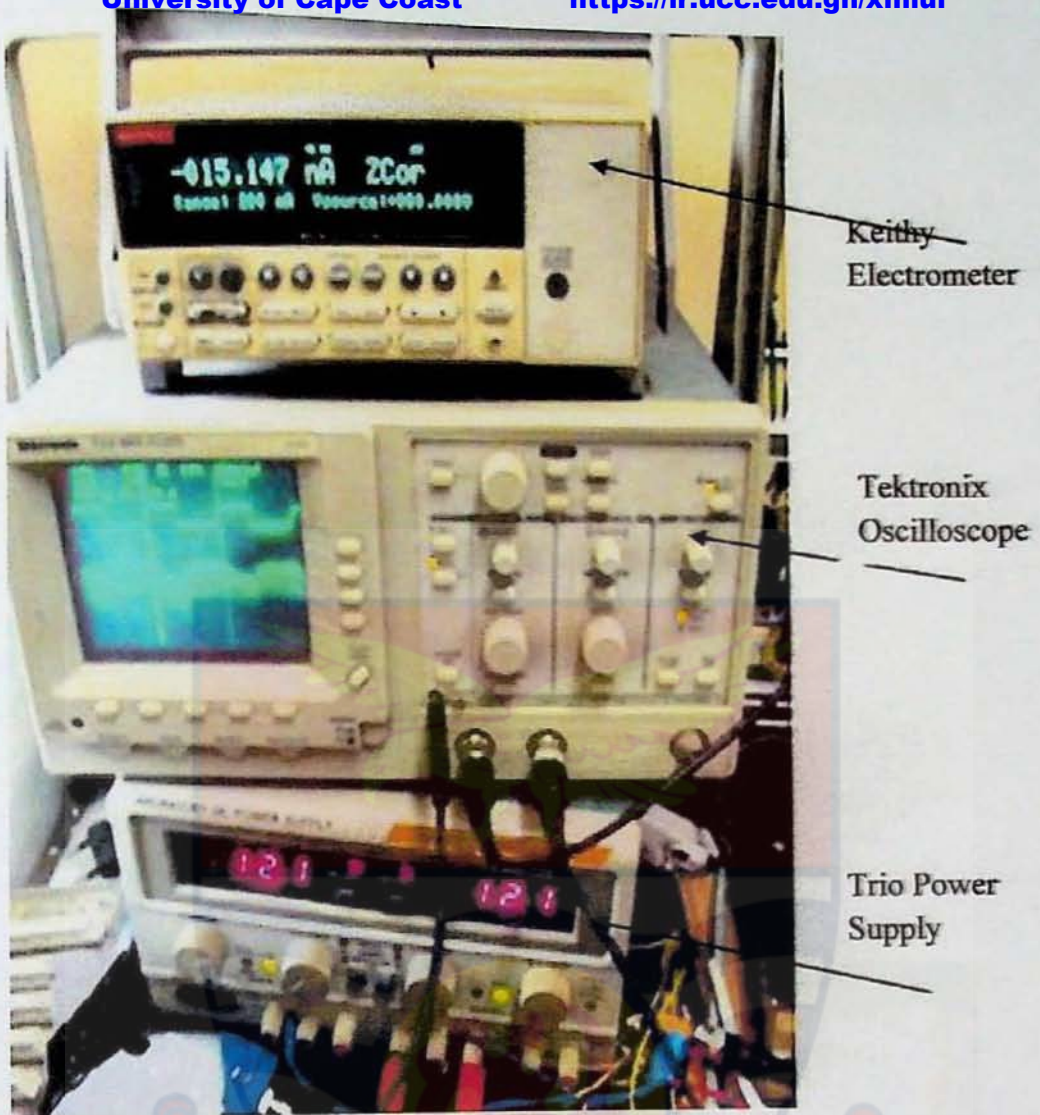


Plate 5: Experimental Setup of Instruments used to measure low currents, low voltages and waveforms of the PMT under test.

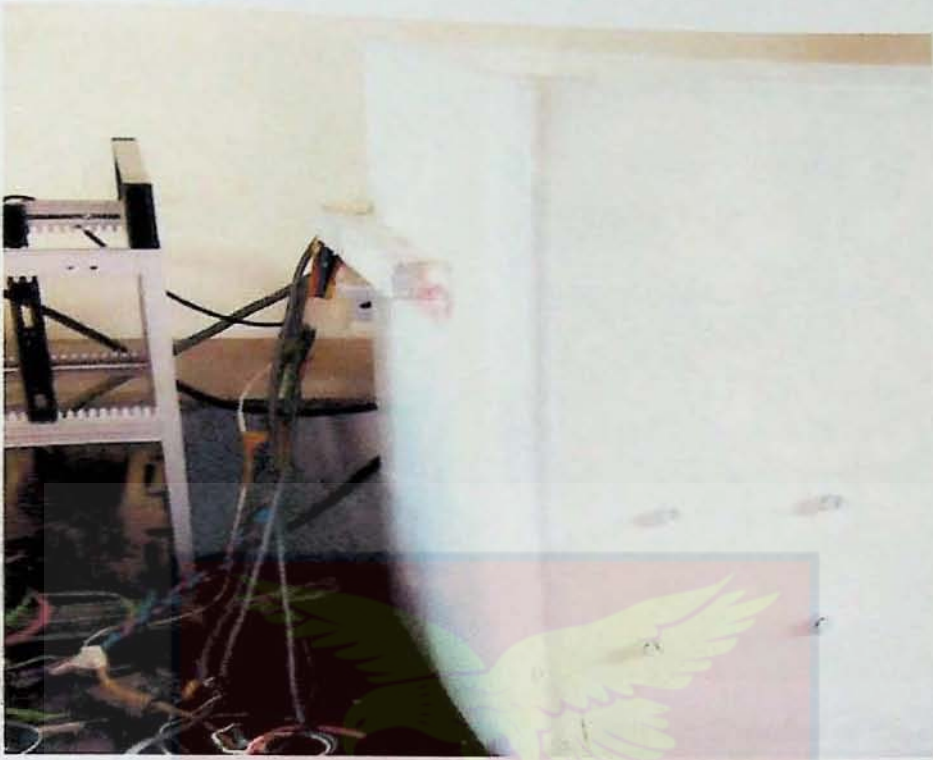


Plate 6: Fabricated instrument for testing and characterization of PMTs, showing power supply and signal cables from the measuring instruments and power supply circuitry



Plate 7: Chamber of fabricated instrument for testing PMTs. The oscillator circuit and PMT under test are shown in the picture



Plate 8: Instrument for testing PMTs being closed for test to begin



Plate 9: Chamber of the PMT instrument showing low intensity blue LED

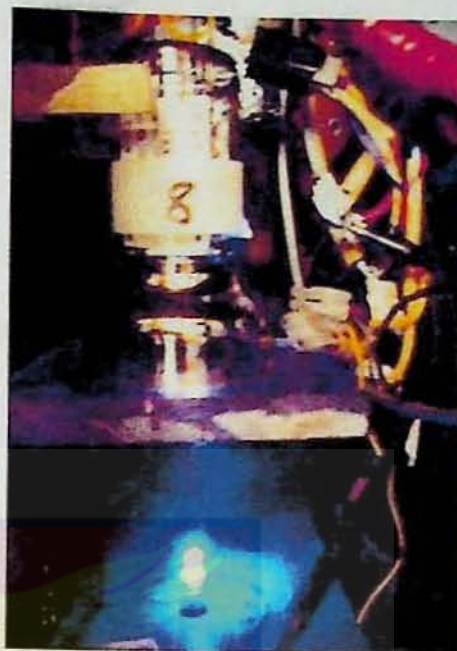


Plate 10: Chamber of the PMT instrument showing high intensity blue LED

PMT Measurements

The measurement of the dark current of a PMT

To measure the dark current of a PMT, the PMT was first placed in the testing device chamber (Plate 6 and Plate 7). While the power supply switch was in off position, the HV connector socket of the PMT was connected to the voltage supply socket, so that the cathode was made negative with respect to the anode, i.e. the negative terminal of the supply was connected to the cathode of the PMT and the positive terminal of the supply was grounded with the anode of the PMT. The door was then closed so that the PMT was not damaged should the power switch was accidentally switched pressed. A dark room was created at the lab by ensuring that there was no light entering the lab.

The PMT was placed in the PMT instrument's chamber for about 15 mins. before the power was switched ON, to ensure that gas in the tube settled down. With the Electrometer connected in series with the anode of the PMT in order to measure current, the instrument was then switched ON and the reading recorded on the electrometer represented the dark current of the PMT. The dark currents of the tubes is shown in Table 3.



Plate 11: The 40 PMTs that were tested in this work

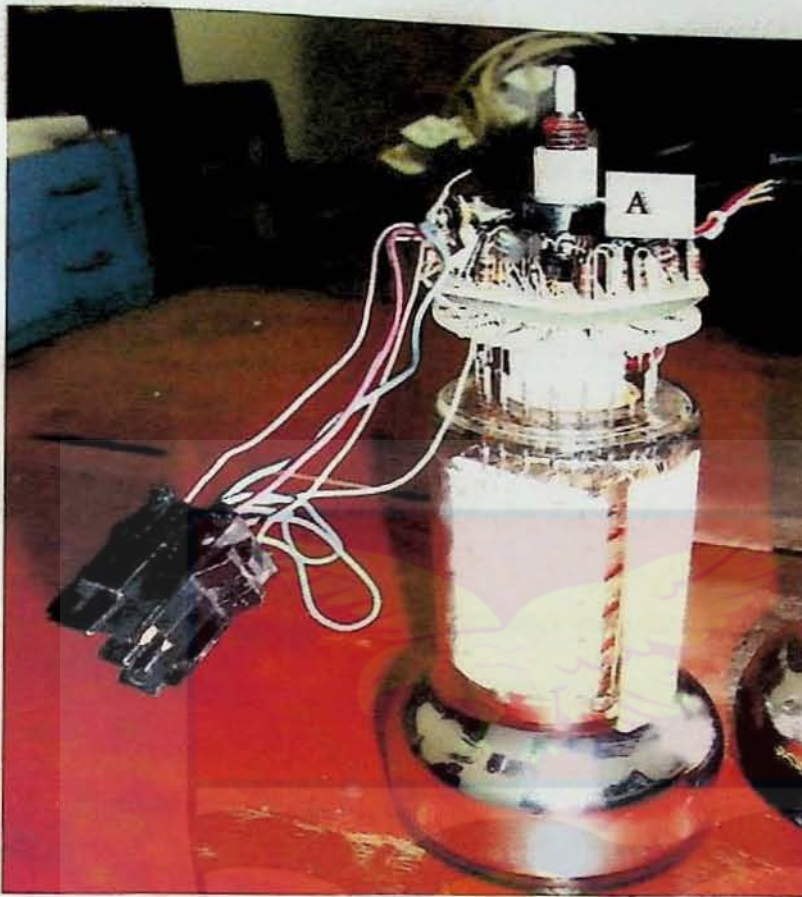


Plate 12: One of the 40 PMTs that was tested in this work. The PMTs were the bialkali type and were manufactured by Philips Corp.

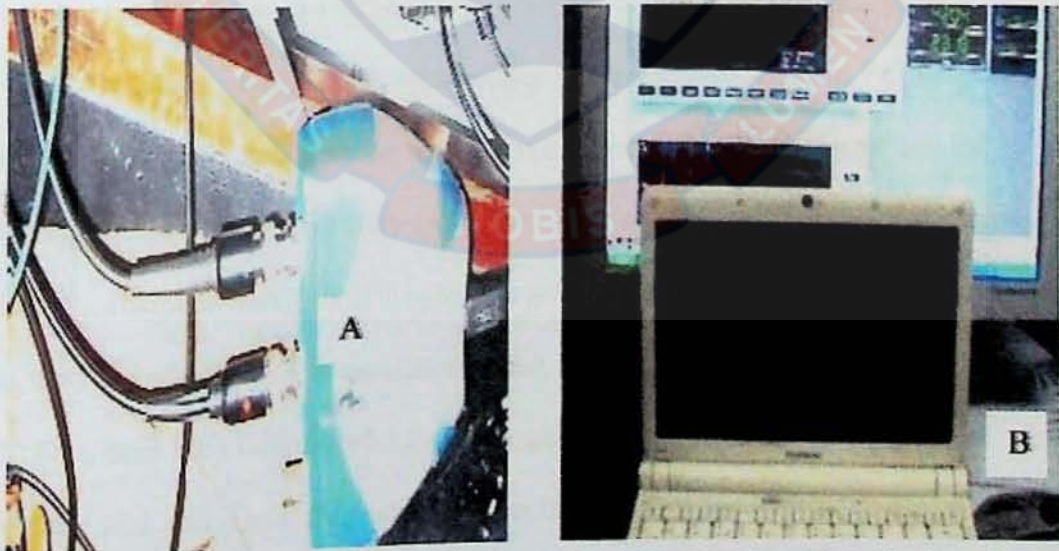


Plate 13: Capture device. A) Two channel capture device . B) A Laptop and an 18 inch Flat screen monitor showing the software.

Measurement of PMT voltage gain with and without the preamplifier connected

Measurement of PMT gain with no preamp connected

Plate 11 shows the forty PMTs that were tested under this work. Plate 12 shows a typical PMT with preamp sitting on top, (A) is the preamplifier.

The preamplifier was designed and manufactured by Siemens the manufacturer of the gamma camera. Plate 4.12 shows the two channel capture device which output is connected to the Personal computer USB slot which and with the installed software constitutes the PC (personal computer Scope (oscilloscope)).

The PMT was placed in the testing chamber as described for the dark current measurement, but unlike the dark current measurement, the PMT need not to wait for 15 mins to settle. The HV supply is then connected to the PMT. The low voltage supply to the preamplifier is left unconnected. The PC scope, and the Tektronix oscilloscope are then connected to the PMT output and the testing equipment door securely closed and locked to prevent any light leakage into the chamber when the HV supply is switched ON. The HV power supply is then switched ON. The oscillator circuit is also switched ON to enable the LED to emit blue (reference) light at a frequency of 31 kHz. The PMT anode voltage and waveform data were simultaneously displayed on the Tektronix oscilloscope (Plate 5) and stored on the PC (Plate 13 (B)).



Plate 14: Two of the PMTs that were tested under this work A) With preamplifier was used for the PMT with preamp measurement. B) PMT with no preamp connected was used PMT without preamp measurement.

Measurement of PMT voltage gain with the preamplifier connected

It became necessary to measure the PMT voltage gain with the preamp connected in this work, because Siemens, the manufacturer of the gamma camera used for this connected all the PMTs outputs to the preamps inputs that sat on top of them (PMTs) and the preamps outputs went to the Summation and differential amplifier boards in the detector assembly of the gamma camera. Therefore after PMTs were tested the combined PMT and its Preamplifier were also tested to know whether there were signal coupling problems or the preamplifiers were faulty.

The measurement of the PMT gain with the preamp connected means that the output of the PMT was connected to the input of the preamp and the

preamp output was fed to the personal computer scope and the Tektronix oscilloscope simultaneously. The measurement was similar to the PMT gain with no preamp connected measurement, except that, the preamplifier power voltage supplies, ± 12 V were now connected. The HV was applied to the PMT and the testing instrument's chamber door was closed. The system was then switched ON and data was captured and stored to the laptop computer. The oscilloscope also displayed the waveforms on its screen. Unlike the laptop, the oscilloscope was analogue one and so digital camera was used to take photograph of the screen and stored on a computer.

Plot of PMT Anode current versus High voltages

Various voltages were obtained at the tapings of the high voltage power supply. A total of eight tapings (Plate 4) were made and voltages obtained were, 300 V, 370 V, 400 V, 500 V, 600 V, 900 V, 1000 V, and 1300 V. Eighteen PMT s out of the 40 PMTs were arbitrary for these measurements. To plot the PMT anode current versus High Voltage, a set of High voltages were selected as indicated. above namely PMT 1, PMT 2... PMT 18. For each PMT, the HV voltage was varied from 300 V to 1300 V and the current for each HV was recorded. The data for this measurement is shown in Table 3 A and B.

Gamma camera boards alignment

Every gamma camera has a procedure for its board's alignment and fine tuning of PMTs. The lay down procedure for alignment and fine tuning of PMTs for the Large Field of View (LFOV) gamma camera by the manufacturers is

found in the service manual and is presented here. The power supplies trim pots namely, ($\pm 15\text{ V}$, $\pm 12\text{ V}$, $\pm 5\text{ V}$, -100 V , -200 V) (Plate 15) were all adjusted for $\pm 0.010\text{V}$ and signal processing boards namely, Summing Amplifier A; Summing Amplifier B; Differential Amplifier, Integrator and pileup control boards (Plate 16) were aligned.

After that the Analyzer I, correction and display, orientation, output driver, and Z display were also aligned. The alignment of the boards was very important since any voltage offset either on X or Y axis would have caused the position sensing (X, Y) amplifiers which determine the location of a scintillating event might have caused a very big offset on the computer screen and no image would have appeared on the screen. After the boards were aligned, the PMTs were well tuned to bring them to the $^{99\text{m}}\text{Tc}$. Energy of 140 keV before quality control could have been performed.

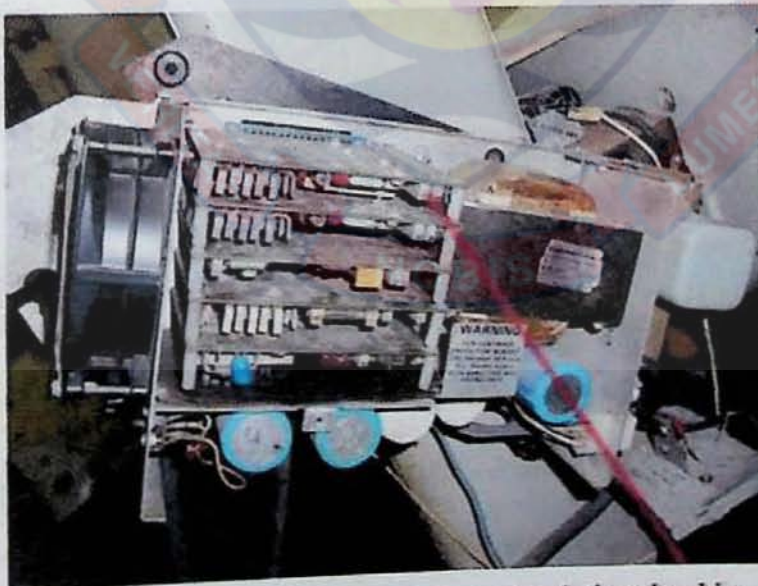


Plate 15: Alignment of detector power supply involved in the adjustment of various pots for the $\pm 5\text{ V}$, $\pm 12\text{ V}$, $\pm 15\text{ V}$ and HV reference voltage.



Plate 16: Analyzer 1, board is placed on a PCB extender board and is being aligned for zero offset voltages

Fine-tuning of PMTs

Fine-tuning is an alignment procedure whereby the detector's high voltage was adjusted to bring all the PMTs to the same voltage which corresponded to the energy of the radioisotope concerned, (eg for ^{99m}Tc , the energy is 140 keV, and each of the PMTs was set to 1.40V; for ^{99m}Tc and ^{57}C the energy was 122 keV, and each of the PMTs was set to 1.22 V). Starting from the centre tube (tube 19) and moving from tube to tube counter clockwise till all the 37 tubes were adjusted and the procedure was repeated at least three times.

The point source was placed directly on each of the photomultiplier tube centres, as drawn on the thin plastic covering the crystal. The point source was moved from tube to tube according to the given order below. The corresponding adjustments on the detector high voltage tuning box were made to centre the meter to 0 ± 1.0 divisions.

Quality Control position of the Detector

After all processor and power supply boards had been aligned and fine tuning PMTs completed, the gamma camera detector was then covered and a $100\mu\text{Ci}$ $^{99}\text{Tc}^m$ point source was placed as indicated in Figure 40. The point source was hanged on the ceiling which was equivalent to 5 times useful field of view (UFOV) of the detector. The analyzer 1 (A1) isotope level was set to 140 keV, and the window level was set to 20 %.

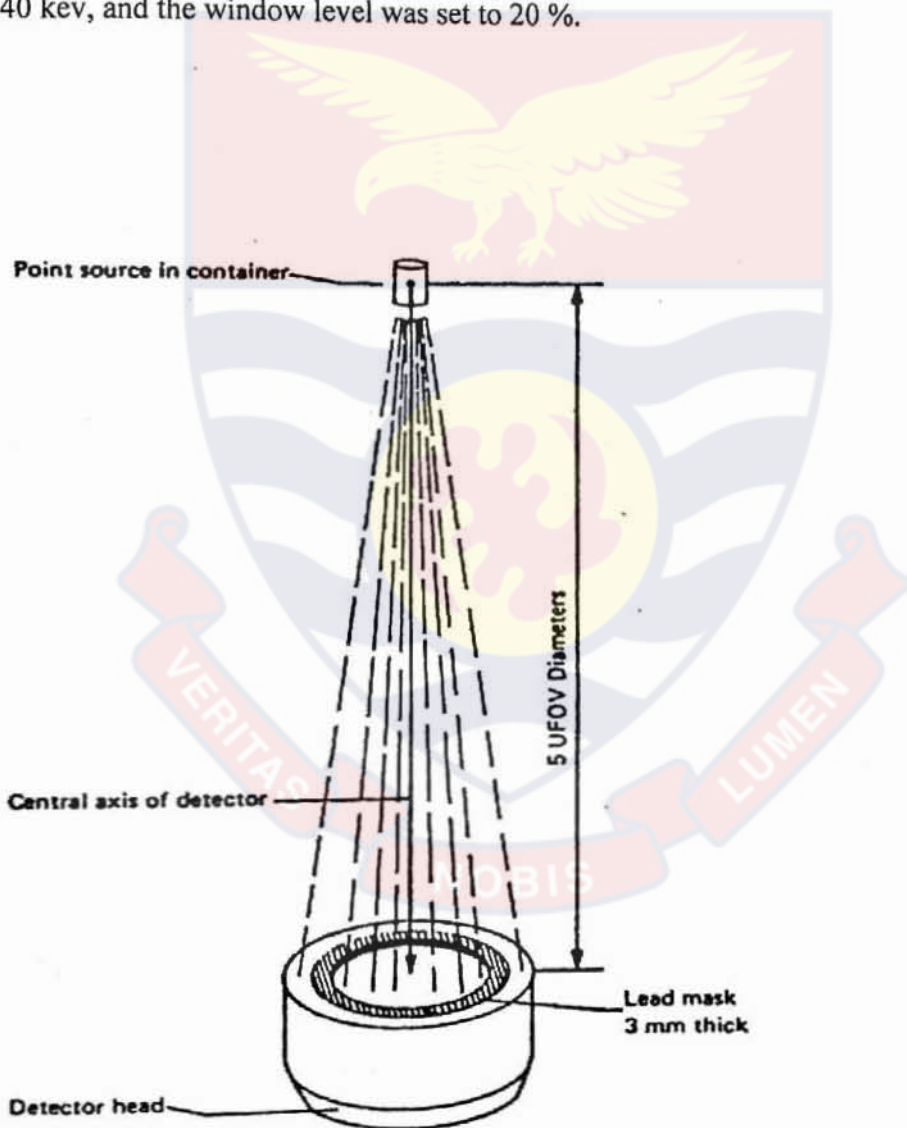


Figure 40: Position of detector and point source for quality control pictures (IEAA, 2003)



Plate 17: Instruments and components that were used in the fine – tuning of the gamma camera PMTs.

A- Four quadrant phantom bar

B- D-Scope

C- Gamma camera detector (head)

D- Isotope level and Window width pots, and Meter

E- PMT HV tuning pots box

CHAPTER FIVE

RESULTS AND DISCUSSION

Overview

Forty PMTs were evaluated with the setup shown in Plate 4 and Plate 5. The PMTs were brought by IAEA to be used as spare parts for the old gamma camera at the NCRNM, Korle Bu. They were taken from an old gamma camera, since the manufacturers had stopped the supply of spare parts, IAEA had to buy used PMTs from MEDX Inc, USA; the company that sold the refurbished camera to IAEA. The company bought used gamma camera from hospitals, refurbish them and sold them to developing countries.

Two measurements were made for each PMT. Due to the bulky nature of the data captured during the measurement, only the data (image) of thirty PMTs were presented in both graphs and table form. The remaining ten were presented in table form {Figure 41 (a and b) to Figure 70 (a and b)}.

RESULTS

PMT voltage gain with and without Preamplifier connected

The results of the measurements are shown in Figure 41 to Figure 70. The first experiment was performed with the preamp disconnected (with no preamp). The theory behind the measurements and sorting of good and bad PMTs was based on photoelectric effect principles which has been extensively covered in the literature review and theory of photoemissions sections of this thesis. The captured data are presented in both table (Table 5.1 (A)) and graphs form (Figure 41 to Figure 70).

The first measurement was to test the PMT with the preamplifier removed. This test was meant to check whether the PMT was good or bad, therefore any scientific or medical equipment that has the PMT as the light detector can be tested with this method. The second measurement was to check for the preamp that the manufacturer of the gamma camera attached to each of the PMTs for the purpose of amplifying and shaping the signals from the PMT for the Summing and differential amplifier boards in the detector of the gamma camera.

A Tektronix oscilloscope was first used to display the output of the measurement but since the oscilloscope was analogue type it could not store the data displayed on its screen, a digital camera had to be used to capture the picture on the oscilloscope screen and later stored on a computer. Taking the picture for each measurement made the experiment very slow and so it was decided to employ a capture device (data acquisition) to make the work faster. A PC oscilloscope (PC scope) called DS1M12, Multifunction Instrument, that was manufactured by USB Instruments was used to capture and display the PMTs outputs on a computer alongside the Tektronix oscilloscope. The USB oscilloscope and waveform generator was a powerful hardware (capture device) with the following features:

1. Two input channel ADC with 12 bit resolution,
2. Simultaneous sampling on both channels, and
3. 32kb waveform buffer.

The scope also has the following features:

1. Timebase-2us/div to 50ms/div in 14 steps,

2. Y-scale 10mV/div to 5V/div,
3. On screen X and Y measurement cursors,
4. FFT spectrum analyser display,
5. Meter display- Min/Max/Mean/ True RMS voltage and
6. Frequency display.

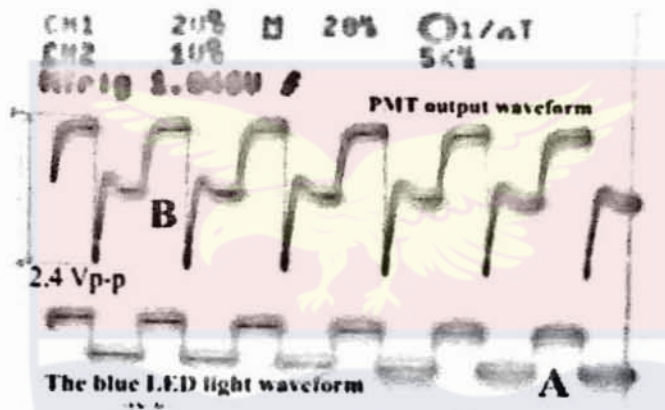


Figure 41a, PMT1: Scope output showing the blue (reference) light output waveform marked 'A' and PMT1 preamp marked 'B'

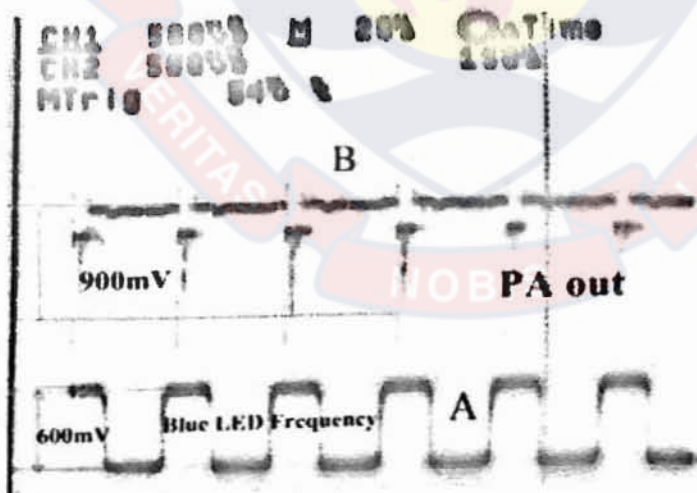


Figure 41b, PMT1: The graph showing the blue (reference) light output waveform marked 'A' and PMT1 preamp marked 'B'

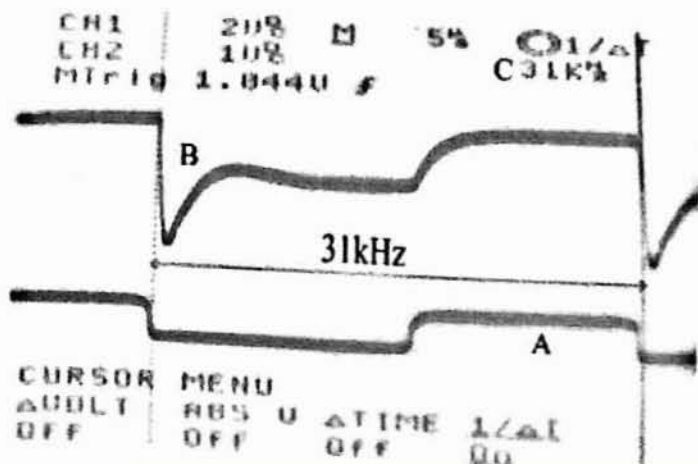


Figure 41c, PMT1: The graph showing measured frequency (c) 31 kHz and calculated frequency (31 kHz) of the reference light (A) and PMT1 output (B)

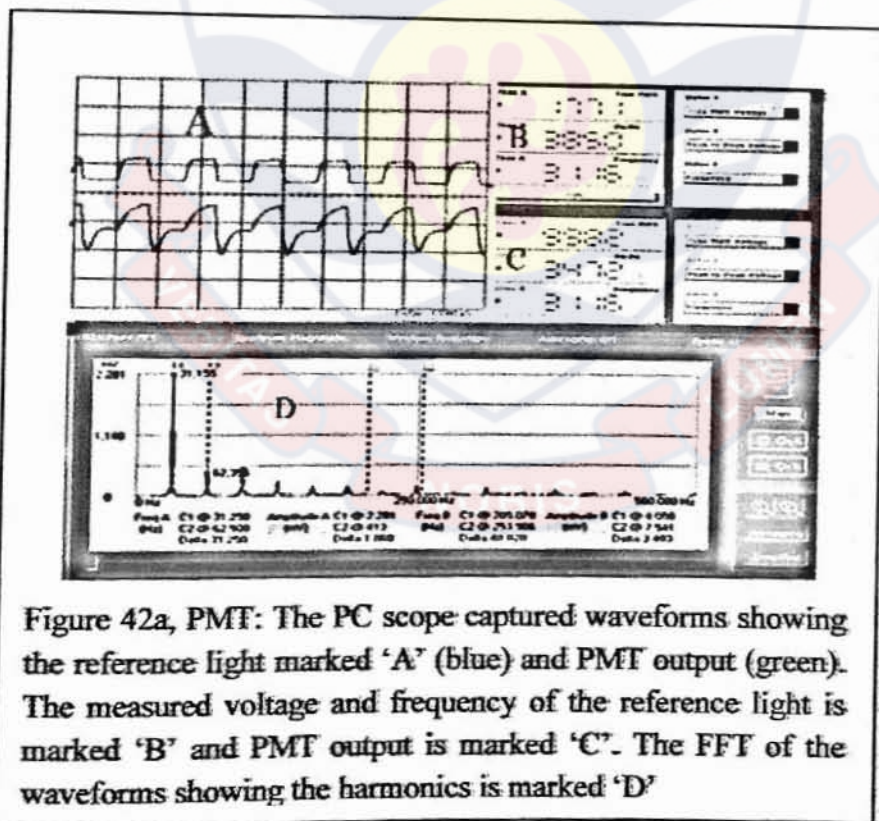


Figure 42a, PMT: The PC scope captured waveforms showing the reference light marked 'A' (blue) and PMT output (green). The measured voltage and frequency of the reference light is marked 'B' and PMT output is marked 'C'. The FFT of the waveforms showing the harmonics is marked 'D'

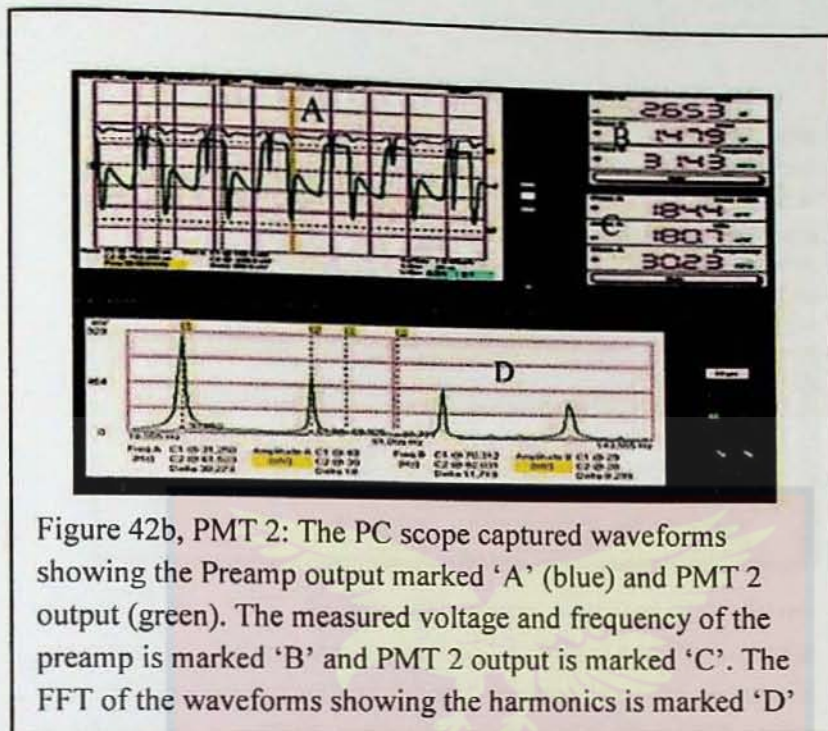


Figure 42b, PMT 2: The PC scope captured waveforms showing the Preamp output marked 'A' (blue) and PMT 2 output (green). The measured voltage and frequency of the preamp is marked 'B' and PMT 2 output is marked 'C'. The FFT of the waveforms showing the harmonics is marked 'D'

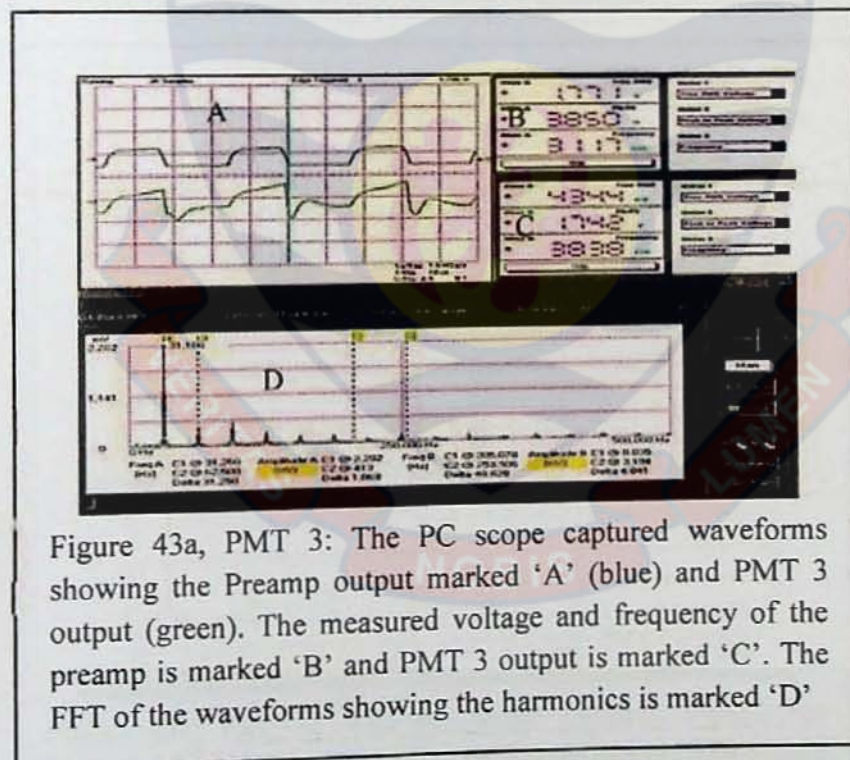
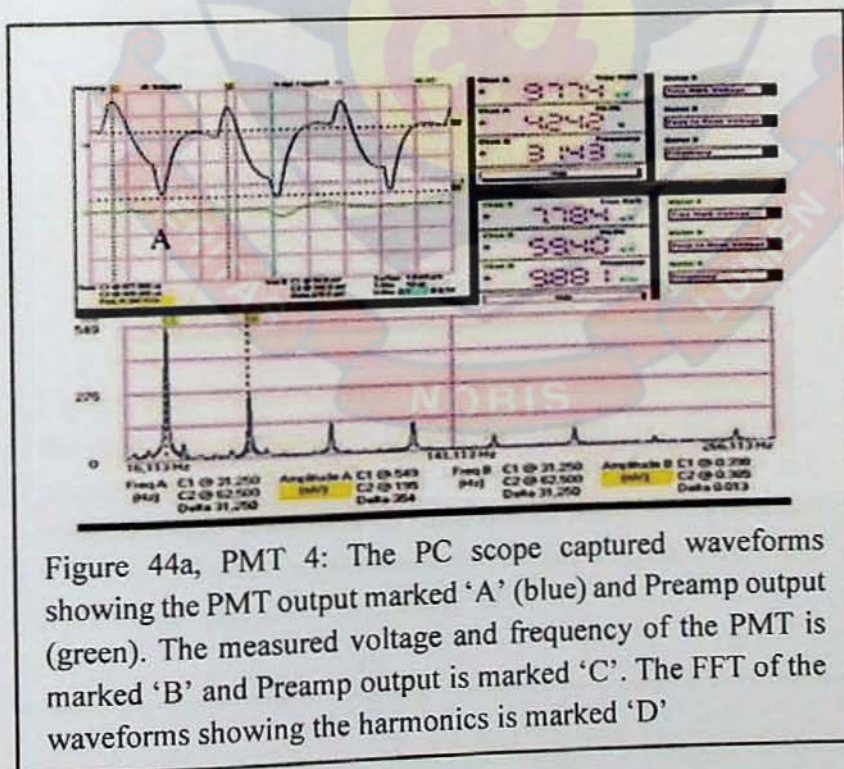
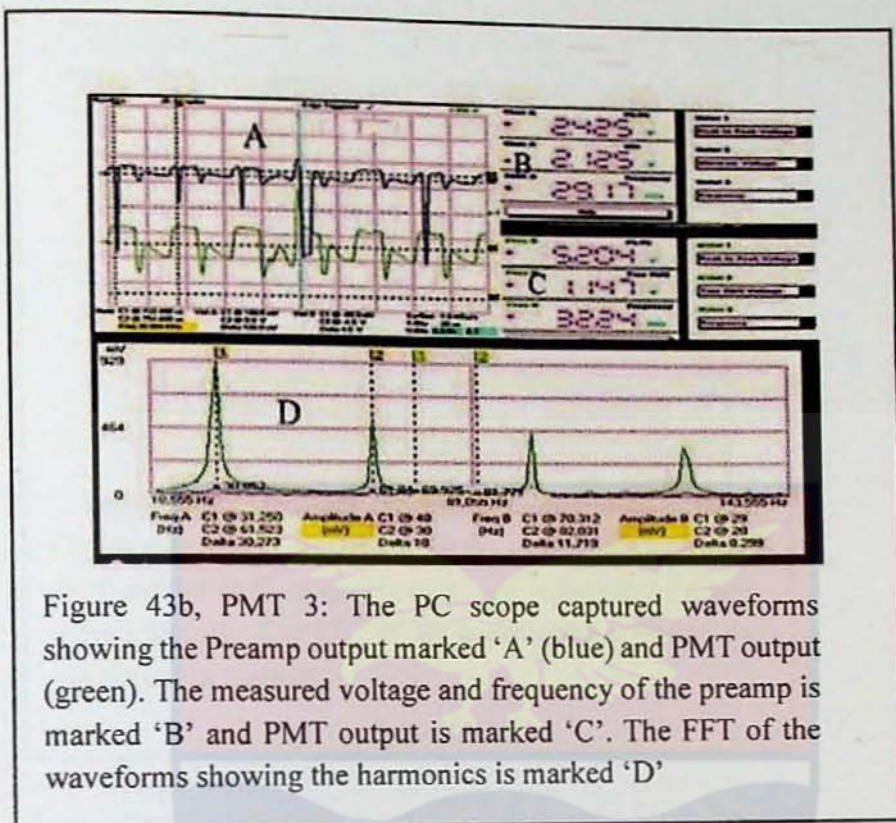


Figure 43a, PMT 3: The PC scope captured waveforms showing the Preamp output marked 'A' (blue) and PMT 3 output (green). The measured voltage and frequency of the preamp is marked 'B' and PMT 3 output is marked 'C'. The FFT of the waveforms showing the harmonics is marked 'D'



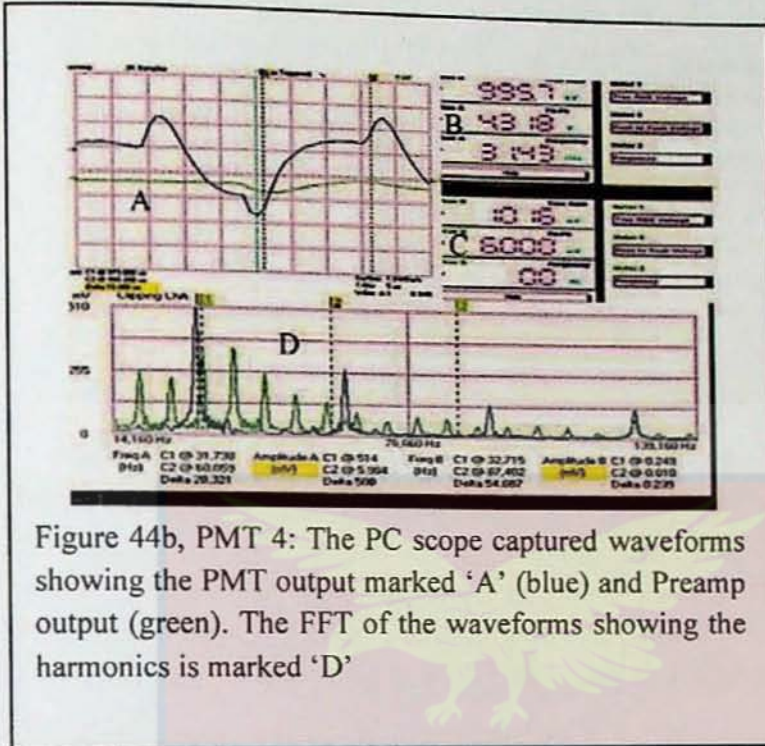


Figure 44b, PMT 4: The PC scope captured waveforms showing the PMT output marked 'A' (blue) and Preamp output (green). The FFT of the waveforms showing the harmonics is marked 'D'

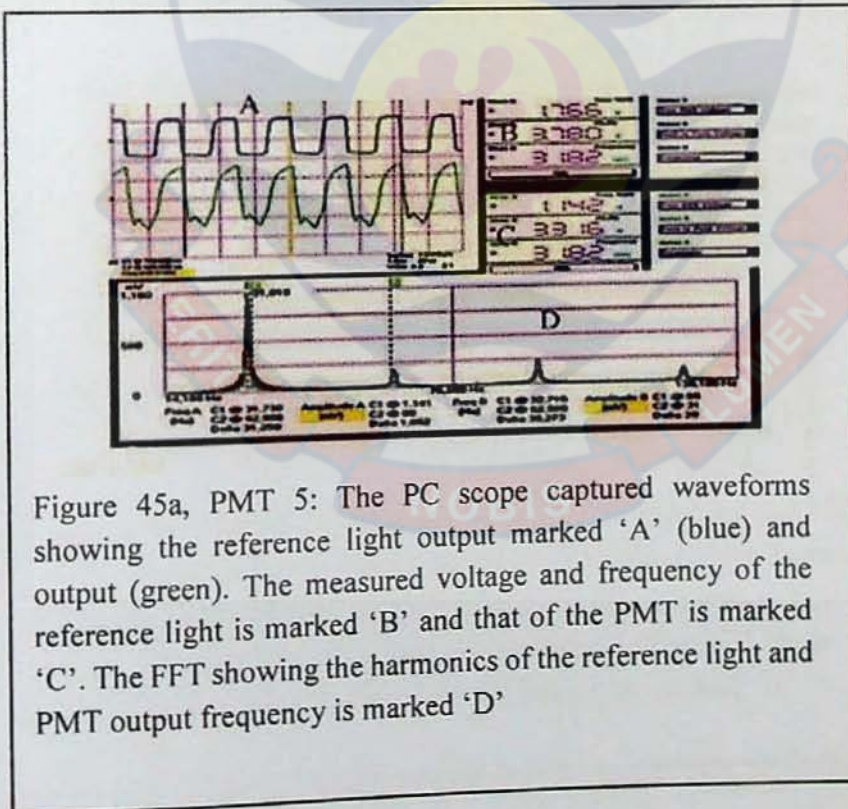


Figure 45a, PMT 5: The PC scope captured waveforms showing the reference light output marked 'A' (blue) and output (green). The measured voltage and frequency of the reference light is marked 'B' and that of the PMT is marked 'C'. The FFT showing the harmonics of the reference light and PMT output frequency is marked 'D'

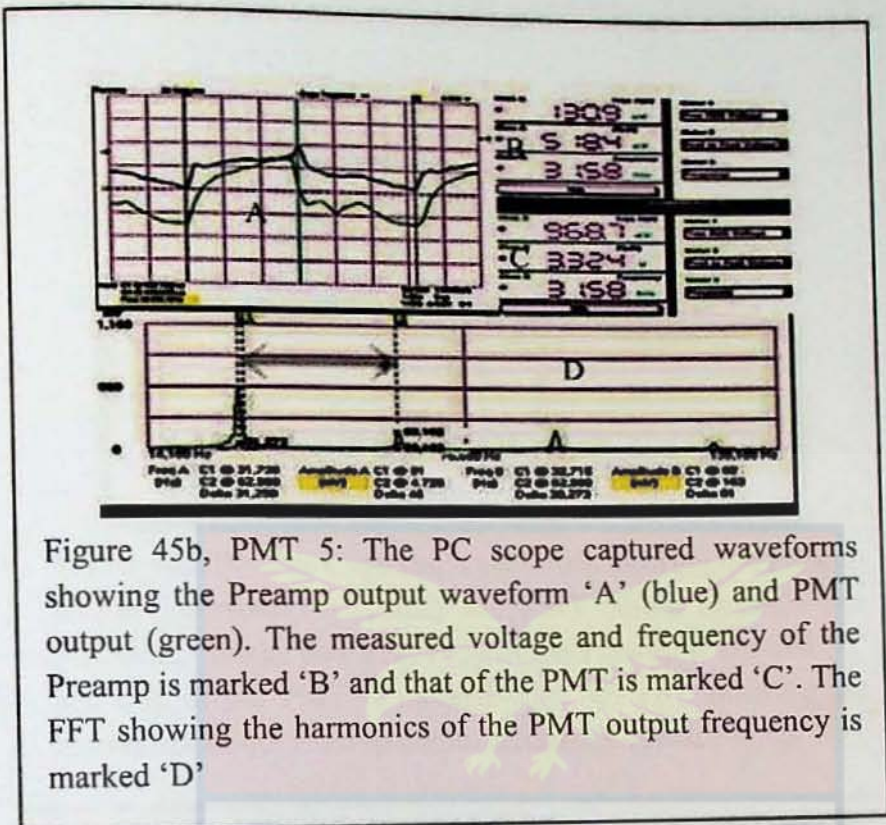


Figure 45b, PMT 5: The PC scope captured waveforms showing the Preamp output waveform 'A' (blue) and PMT output (green). The measured voltage and frequency of the Preamp is marked 'B' and that of the PMT is marked 'C'. The FFT showing the harmonics of the PMT output frequency is marked 'D'

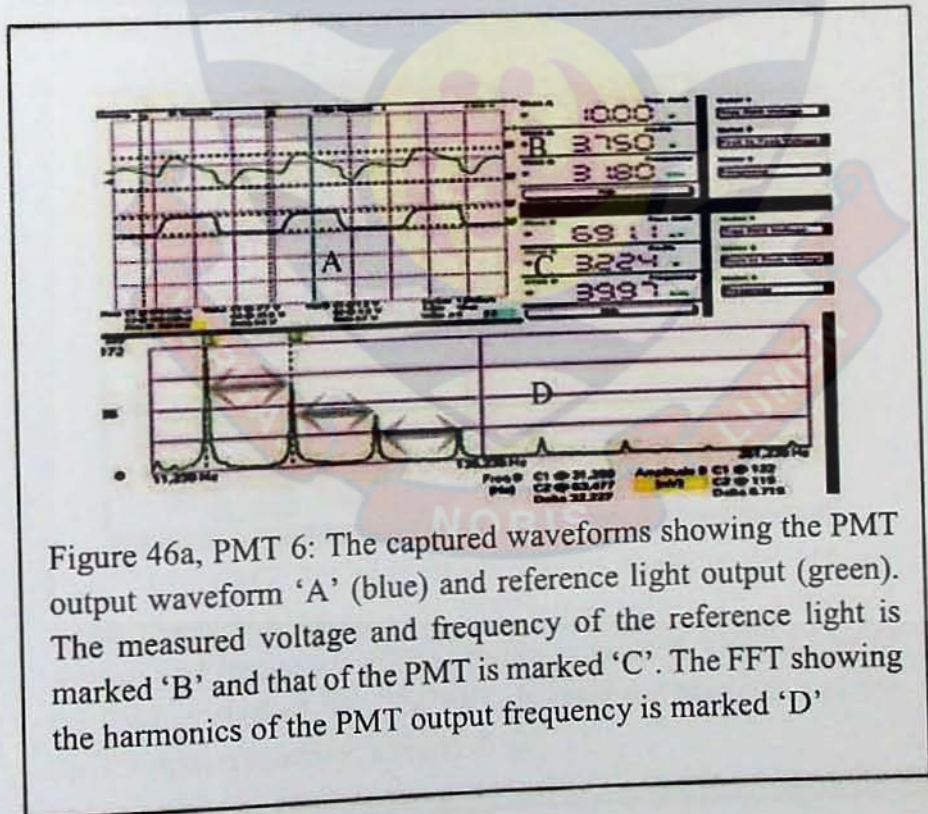


Figure 46a, PMT 6: The captured waveforms showing the PMT output waveform 'A' (blue) and reference light output (green). The measured voltage and frequency of the reference light is marked 'B' and that of the PMT is marked 'C'. The FFT showing the harmonics of the PMT output frequency is marked 'D'

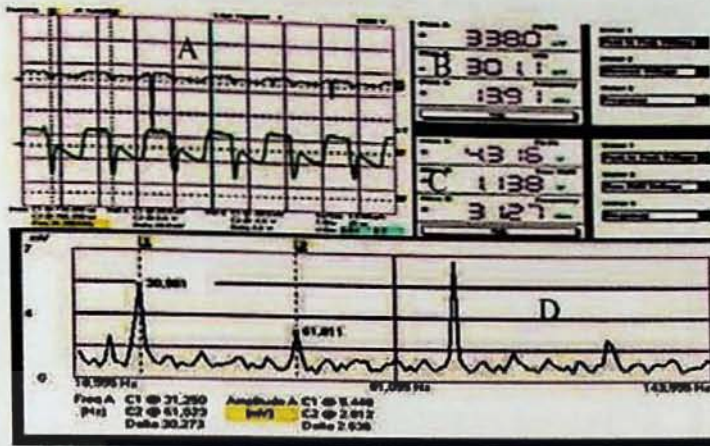


Figure 46b, PMT 6: Captured waveforms showing the Preamp output waveform 'A' (blue) and PMT output (green). The measured voltage and frequency of the Preamp is marked 'B' and that of the PMT is marked 'C'. The FFT showing the harmonics of the Preamp output frequency is marked 'D'

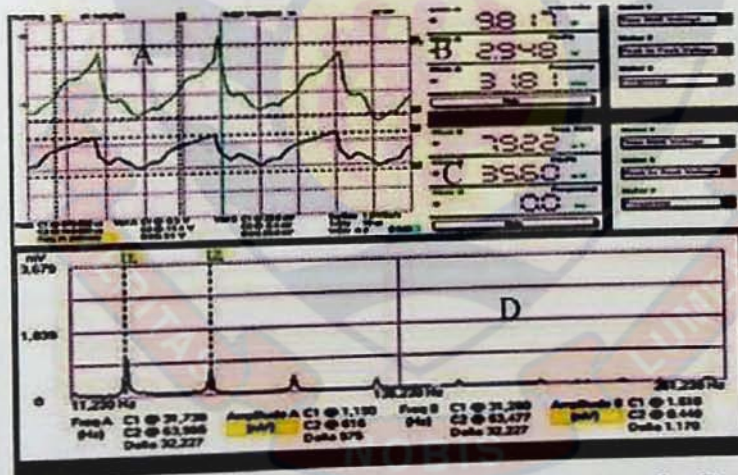


Figure 47a, PMT 7: Captured waveforms showing the Preamp output marked 'A' (green) and PMT output (blue). The measured voltage and frequency of the preamp is marked 'C' and that of the PMT is marked 'B'. The FFT showing the harmonics of the PMT output frequency is marked 'D'

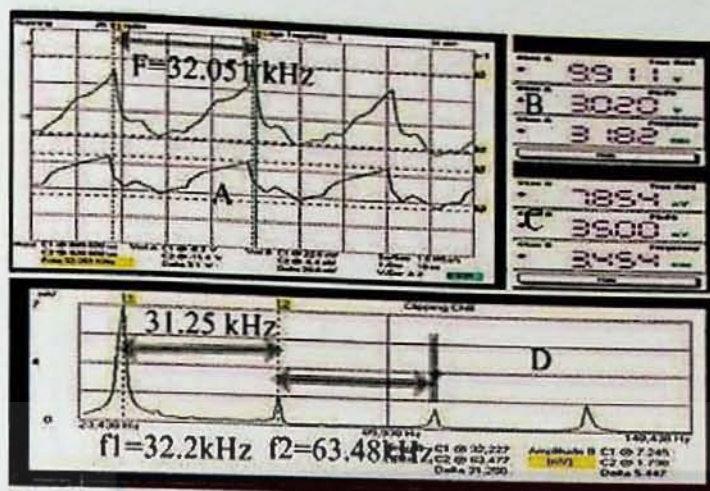


Figure 47b, PMT 7: Comparison between measured frequency of PMT output (31.82 kHz) marked 'B', and preamp output (3.454 kHz) marked 'C' and calculated value ($f=32.051 \text{ kHz}$) marked 'A'

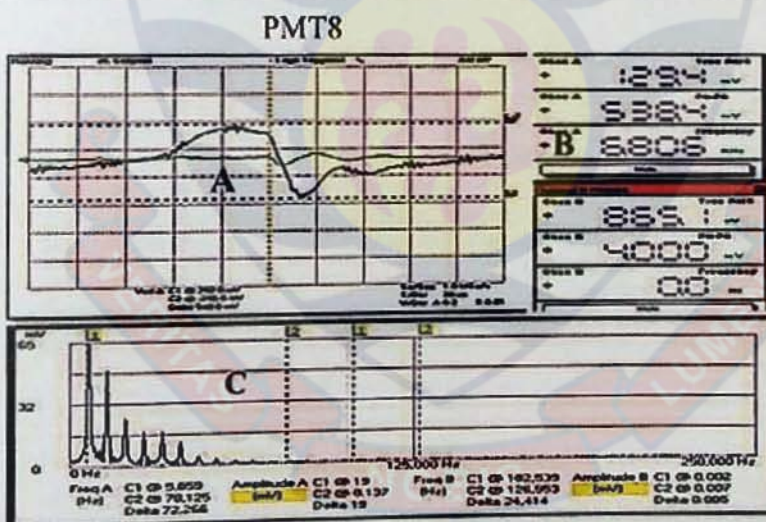


Figure 48a, PMT 8: Picture of observed noise voltage waveform of PMT 8 output when the input reference (blue) light was off (Marked 'A'). The measured voltage was 538 mV_{p-p} having a frequency of 6.806 kHz , (Marked 'B') an indication of bad PMT

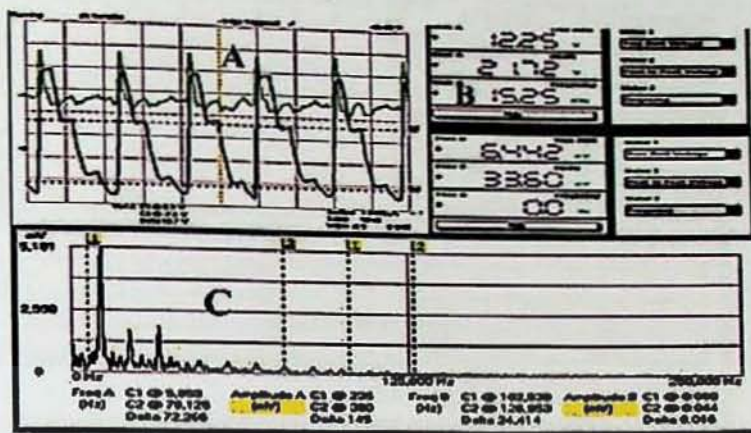


Figure 48b, PMT 8: Picture of observed noise voltage waveform of PMT 8 output when the input reference (blue) light was switched on

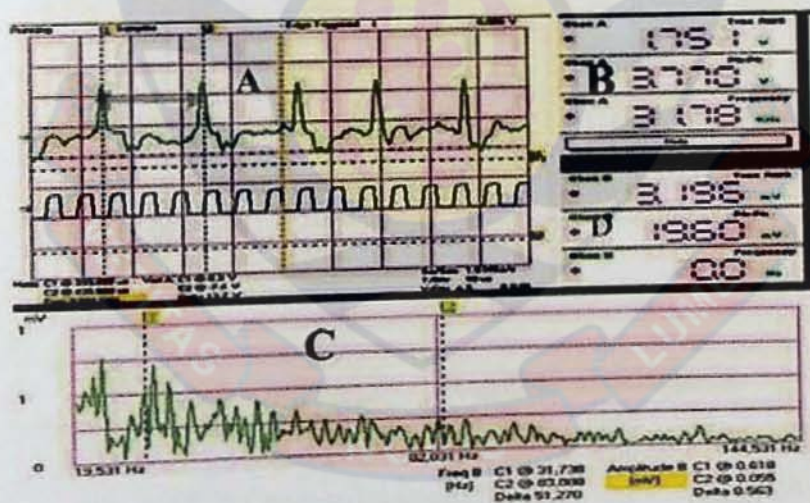


Figure 48c, PMT8: Picture of observed voltage waveform of PMT 8 output when the input reference (blue) light was switched on

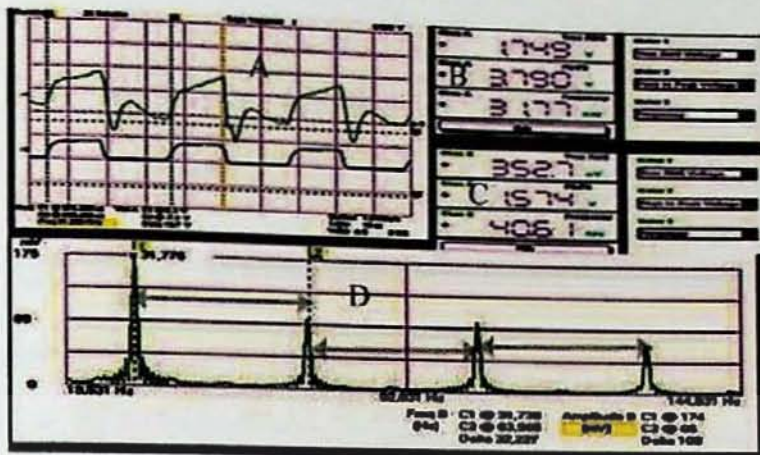


Figure 49a, PMT 9: PC scope captured waveforms showing reference light marked 'A' and PMT 9 output (green). The measured voltage and frequency of the reference light is marked 'B' and that of the preamp output is marked 'C'

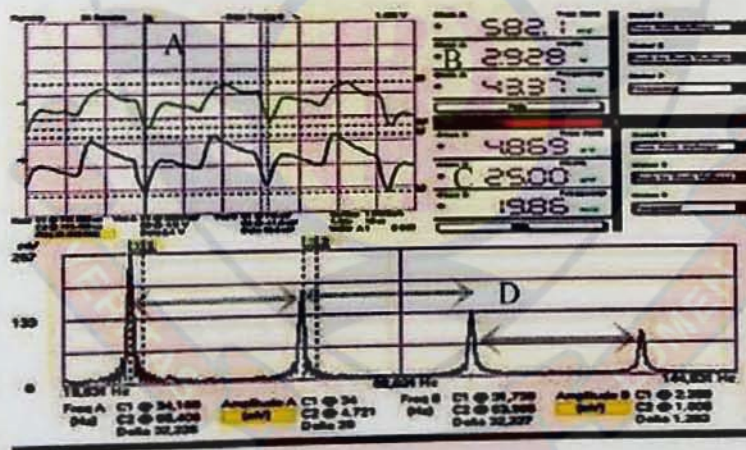


Figure 49b, PMT 9: Captured waveforms showing PMT output voltage, marked 'A' and preamp output (green). The measured voltage and frequency of the PMT output is marked 'B' and that of the preamp output is marked 'C'

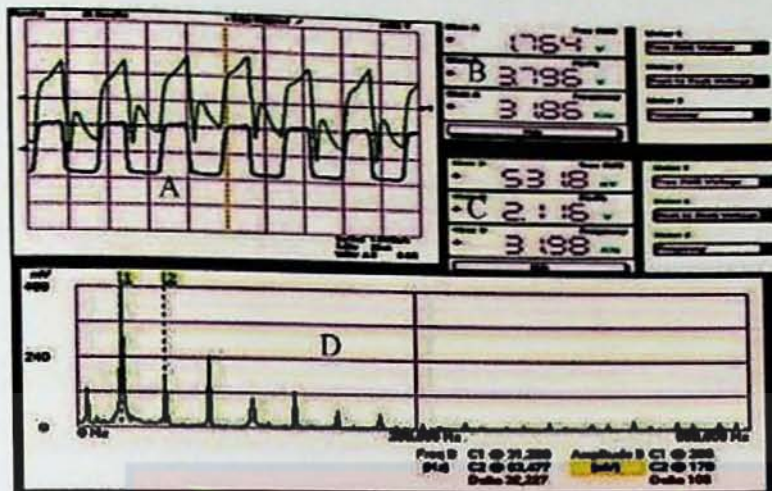


Figure 50a, PMT 10: PC scope captured waveforms showing reference light marked 'A' (blue) and PMT output (green). The measured voltage and frequency of the reference light is marked 'B' and that of the PMT is marked 'C'

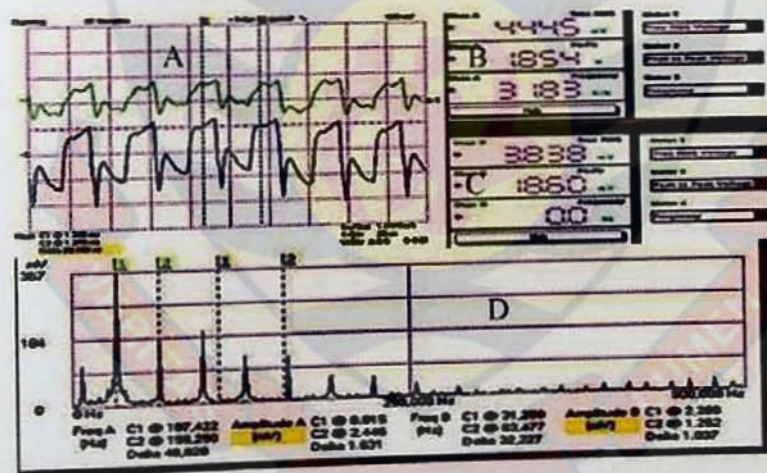


Figure 50b, PMT 10: Captured waveforms showing PMT output voltage marked 'A' (blue) and preamp output (green). The measured voltage and frequency of PMT is marked 'B' and that of the preamp output is marked 'C'

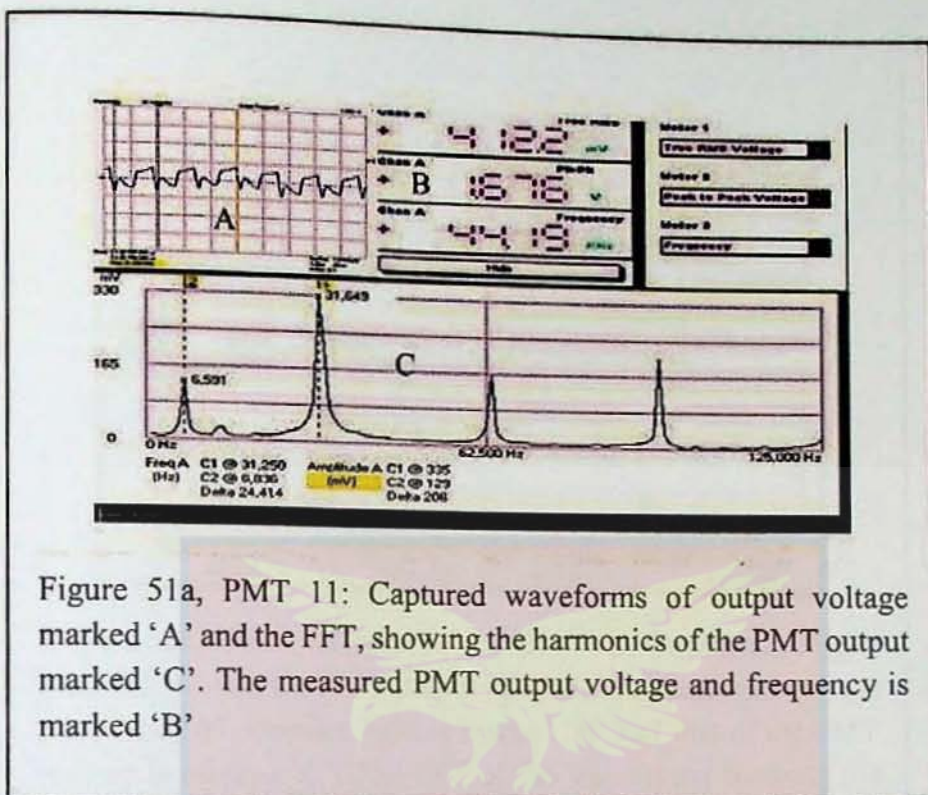


Figure 51a, PMT 11: Captured waveforms of output voltage marked 'A' and the FFT, showing the harmonics of the PMT output marked 'C'. The measured PMT output voltage and frequency is marked 'B'

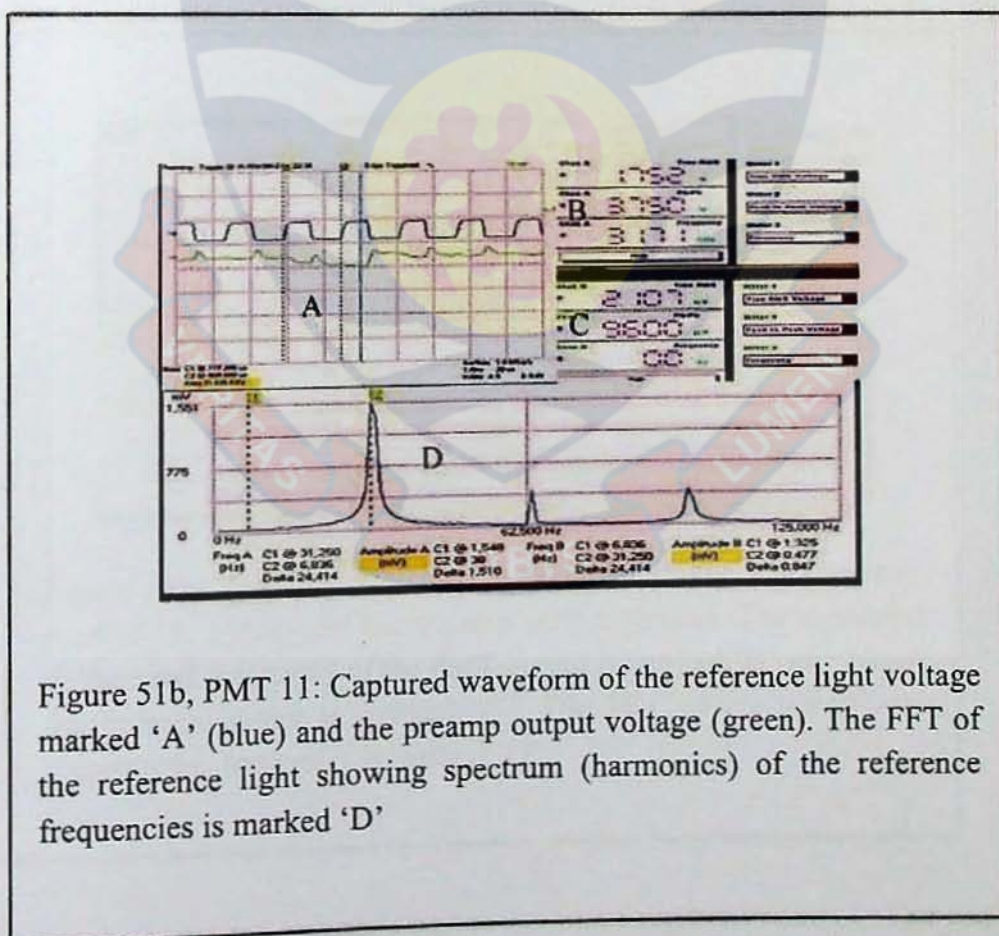


Figure 51b, PMT 11: Captured waveform of the reference light voltage marked 'A' (blue) and the preamp output voltage (green). The FFT of the reference light showing spectrum (harmonics) of the reference frequencies is marked 'D'

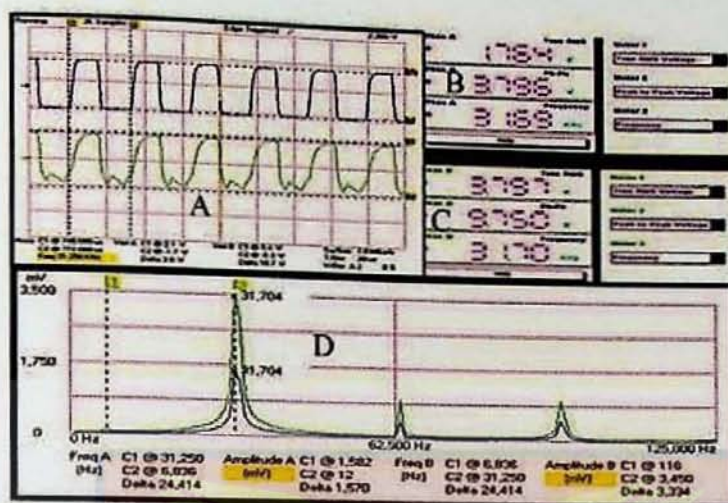


Figure 52a, PMT 12: Captured waveforms of the reference light, marked 'A' and the PMT output (green). The measured voltage frequency of reference light is marked 'B' and that of the PMT output is marked 'C'. The FFT of the waveforms showing the harmonics is marked 'D'

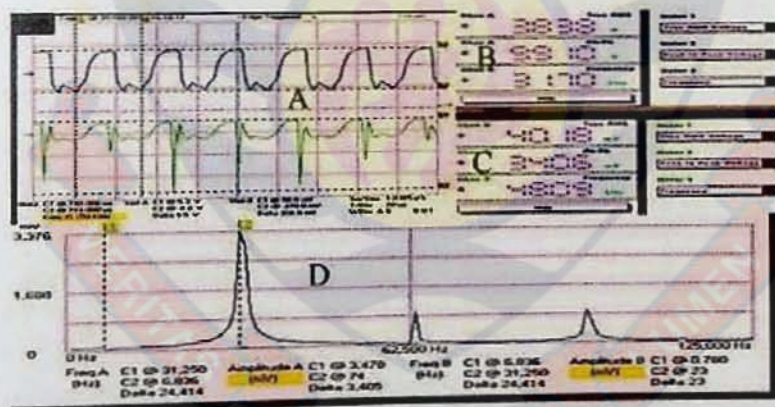


Figure 52b, PMT 12: Captured waveforms of the PMT output, marked 'A' (blue) and the Preamp output (green). The measured voltage and frequency of the PMT output is marked 'B' and that of the Preamp output is marked 'C'. The FFT of the waveforms showing the harmonics is marked 'D'

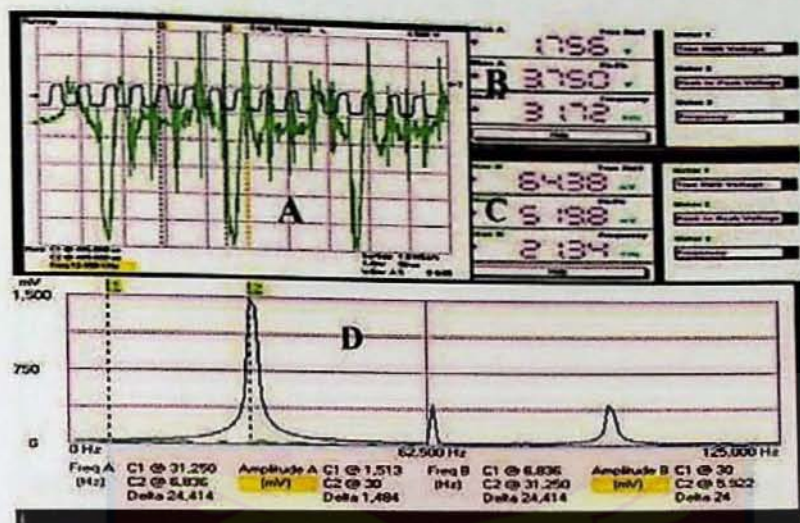


Figure 53a, PMT 13: Captured waveforms showing the reference light voltage marked 'A' (blue) and the PMT output (green). The measured voltage and frequency of reference light is marked 'B' and PMT output is marked 'C'.

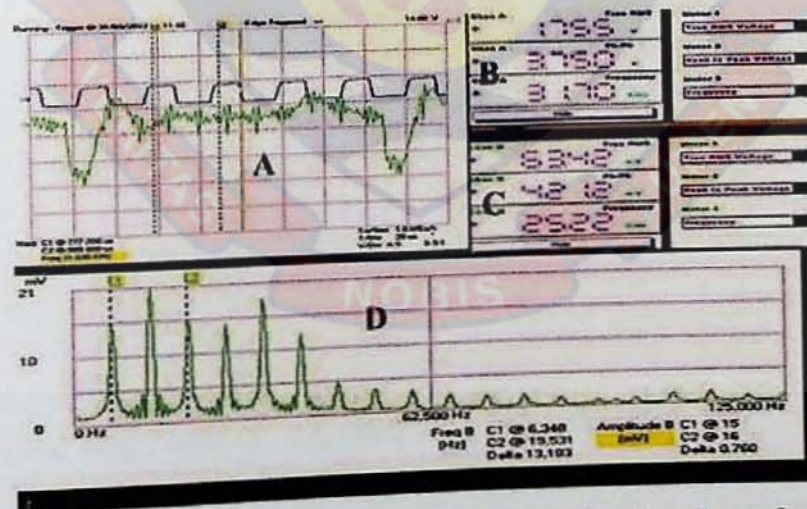


Figure 53b, PMT 13: Captured waveforms showing the reference light voltage marked 'A' (blue) and 1 cycle of PMT13 output (green). The measured voltage and frequency of the PMT output is marked 'B' and PMT output is marked 'C'. The FFT of the waveforms showing the harmonics is marked 'D'

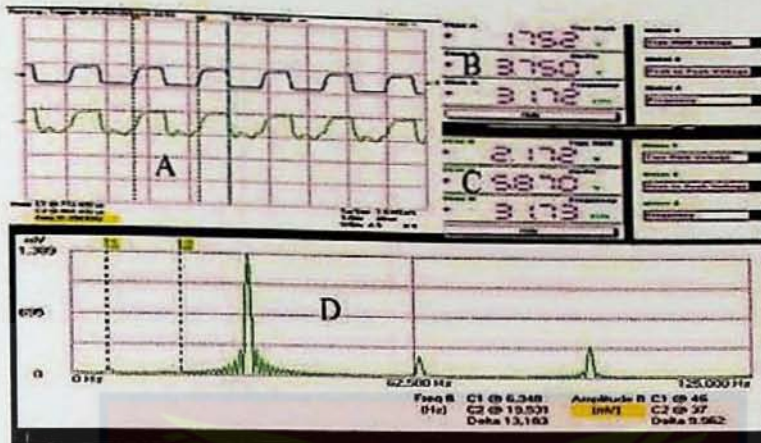


Figure 54a, PMT 14: Captured waveforms showing the reference light voltage marked 'A' (blue) and PMT 14 output (green). The measured voltage and frequency of reference light is marked 'B' and PMT output is marked 'C'. The FFT of the waveforms showing the harmonics is marked 'D'

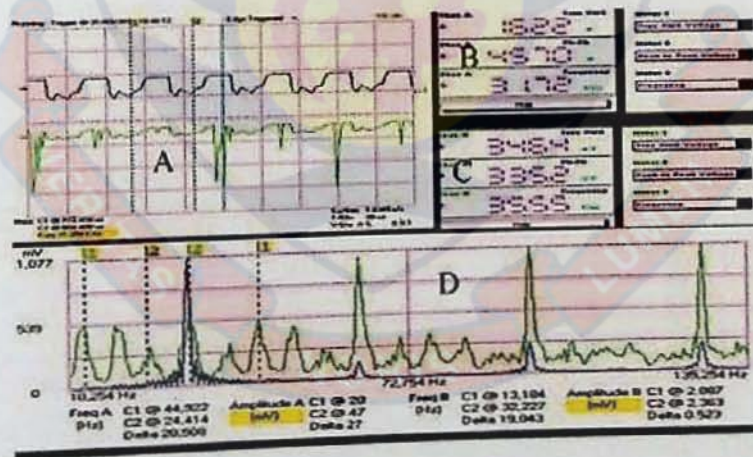
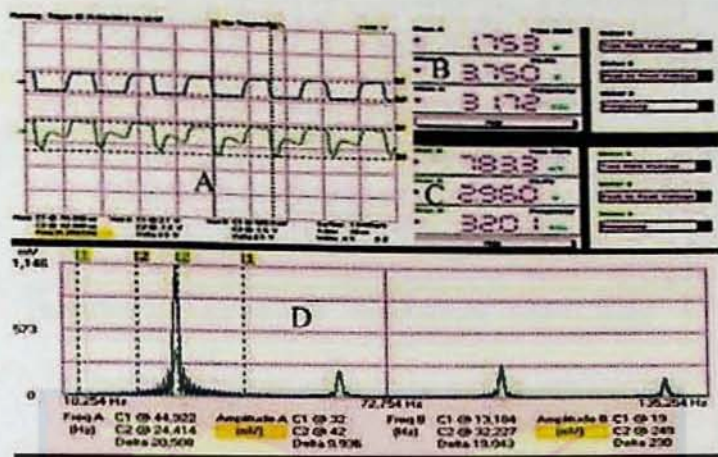
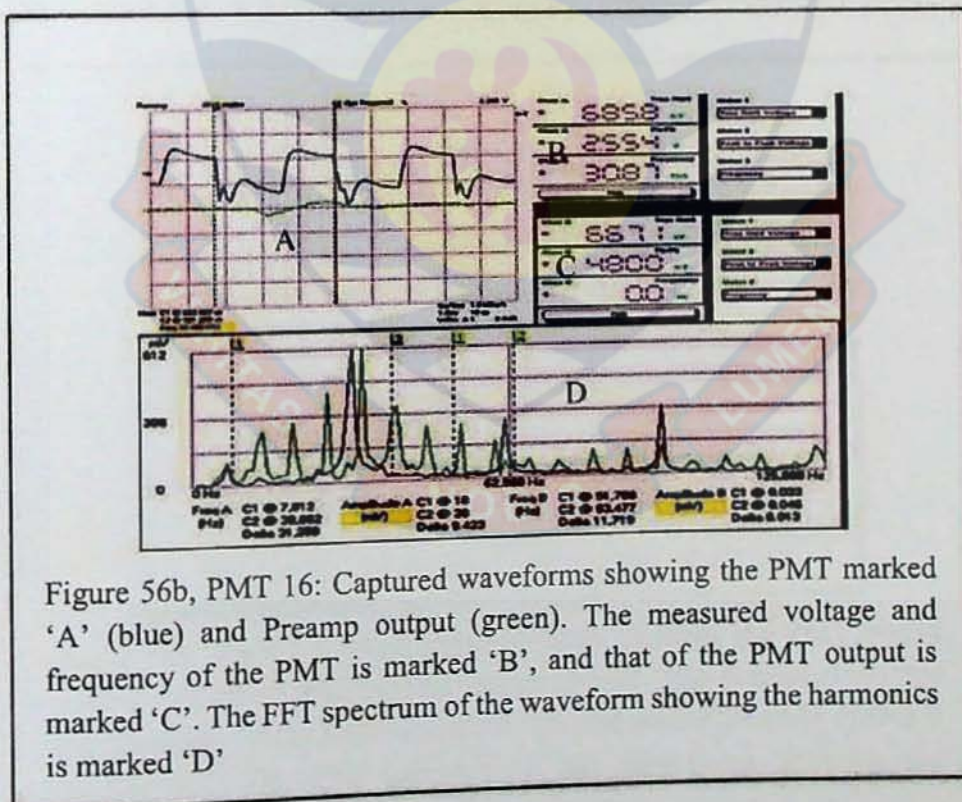
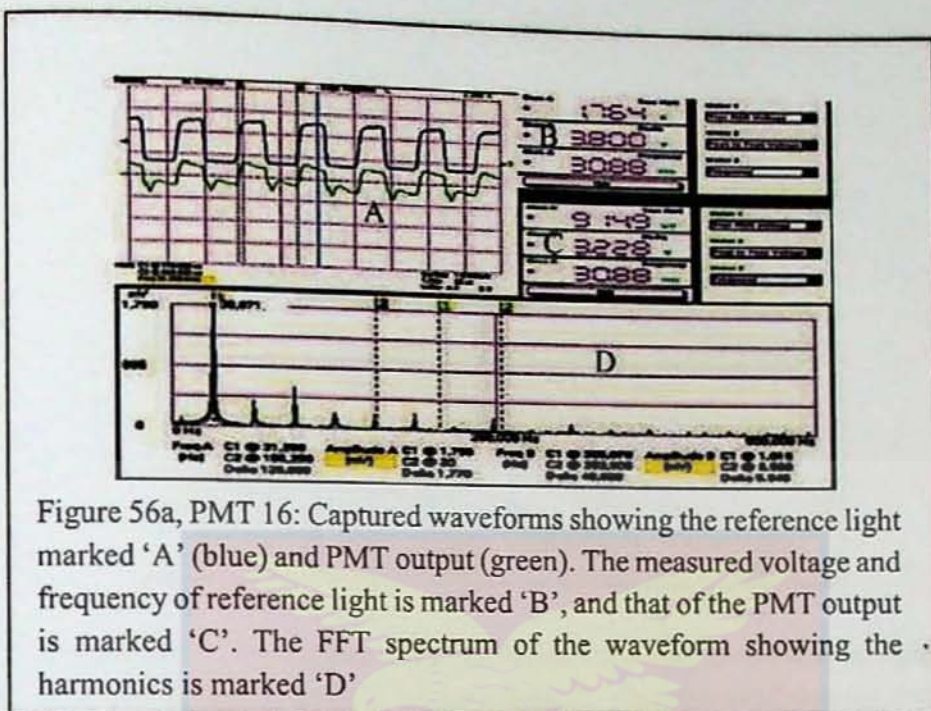


Figure 54b, PMT 14: Captured waveforms showing PMT 14 output voltage marked 'A' (blue) and Preamp output (green). The measured voltage and frequency of PMT output is marked 'B', and Preamp output is marked 'C'. The FFT of the waveforms showing the harmonics PMT 14 and Preamp output is marked 'D'





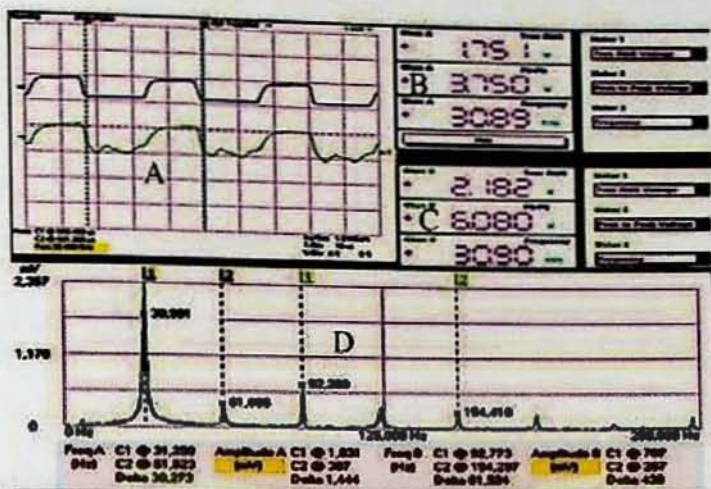


Figure 57a, PMT 17: Captured waveforms showing the reference light marked 'A' (blue) and PMT output (green). The measured voltage and frequency of reference light is marked 'B', and that of the PMT output is marked 'C'. The FFT spectrum the waveform showing the harmonics is marked 'D'

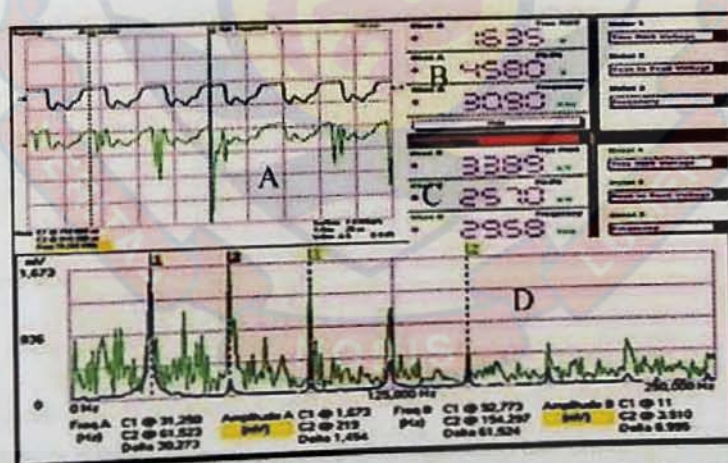


Figure 57b, PMT 17: Captured waveforms showing the PMT output marked 'A' (blue) and Preamp output (green). The measured voltage and frequency of the PMT is marked 'B', and that of the PMT output is marked 'C'. The FFT spectrum of the waveforms showing the harmonics is marked 'D'

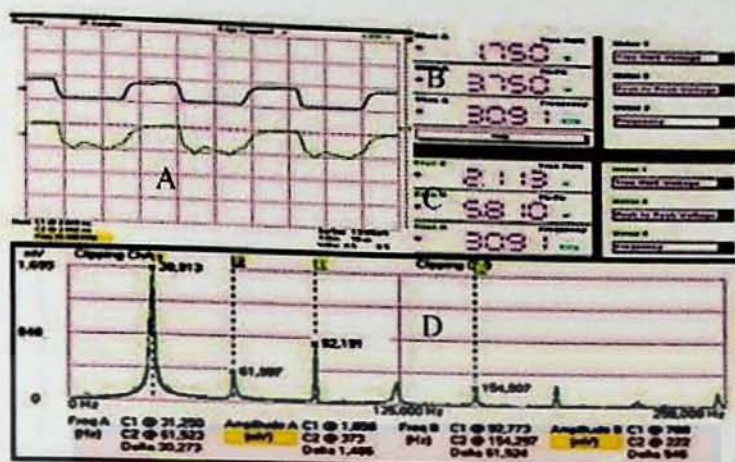


Figure 58a, PMT 18: Captured waveforms showing the reference light marked 'A' (blue) and PMT output (green). The measured voltage and frequency of reference light is marked 'B', and that of the PMT output is marked 'C'. The FFT spectrum the waveforms showing the harmonics is marked 'D'

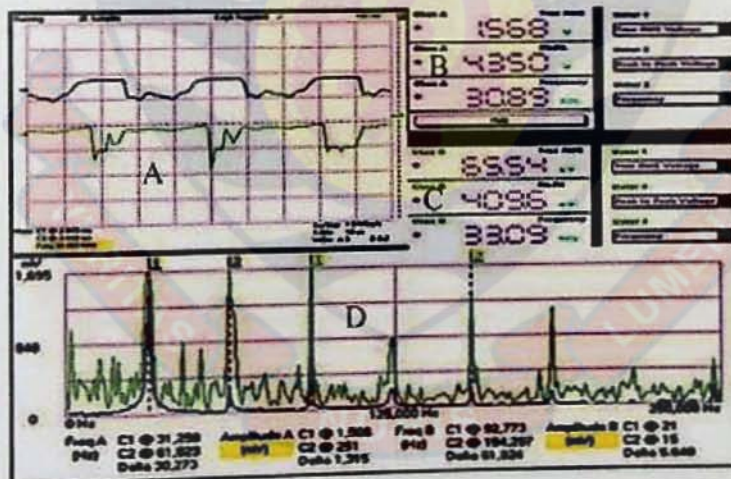


Figure 58b, PMT 18: Captured waveforms showing the PMT output marked 'A' (blue) and Preamp output (green). The measured voltage and frequency of the PMT is marked 'B', and that of the PMT output is marked 'C'. The FFT spectrum of the waveforms showing the harmonics is marked 'D'

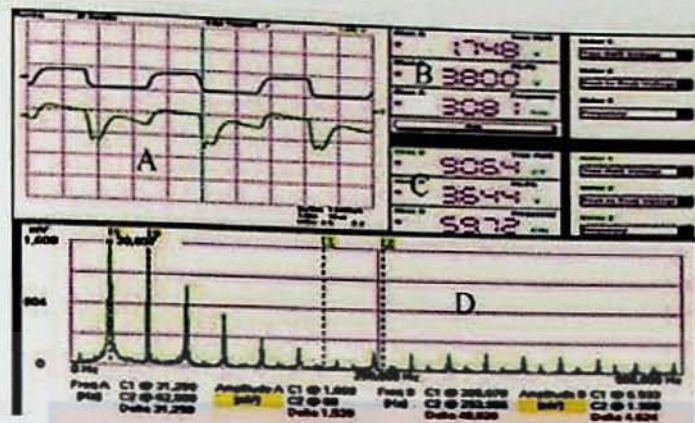


Figure 59a, PMT 19: Captured waveforms showing the reference light marked 'A' (blue) and PMT output (green). The measured voltage and frequency of reference light is marked 'B', and that of the PMT output is marked 'C'. The FFT spectrum the waveforms showing the harmonics is marked 'D'

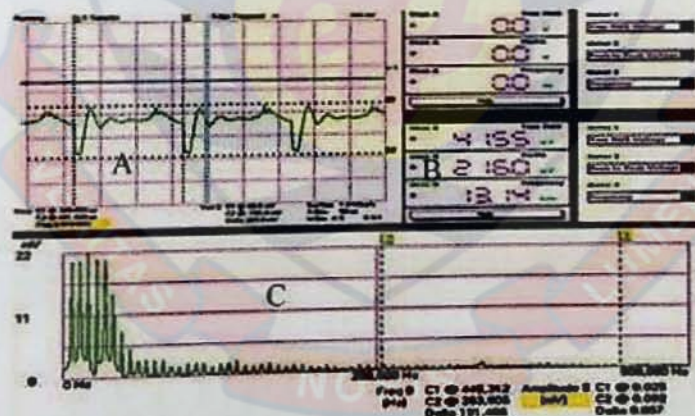


Figure 59b, PMT 19: Captured waveforms showing the PMT output is marked 'A' (blue) and Preamp output (green). The measured voltage and frequency of the PMT output is marked 'B'. The FFT spectrum of PMT 19 waveform showing the harmonics is marked 'C'

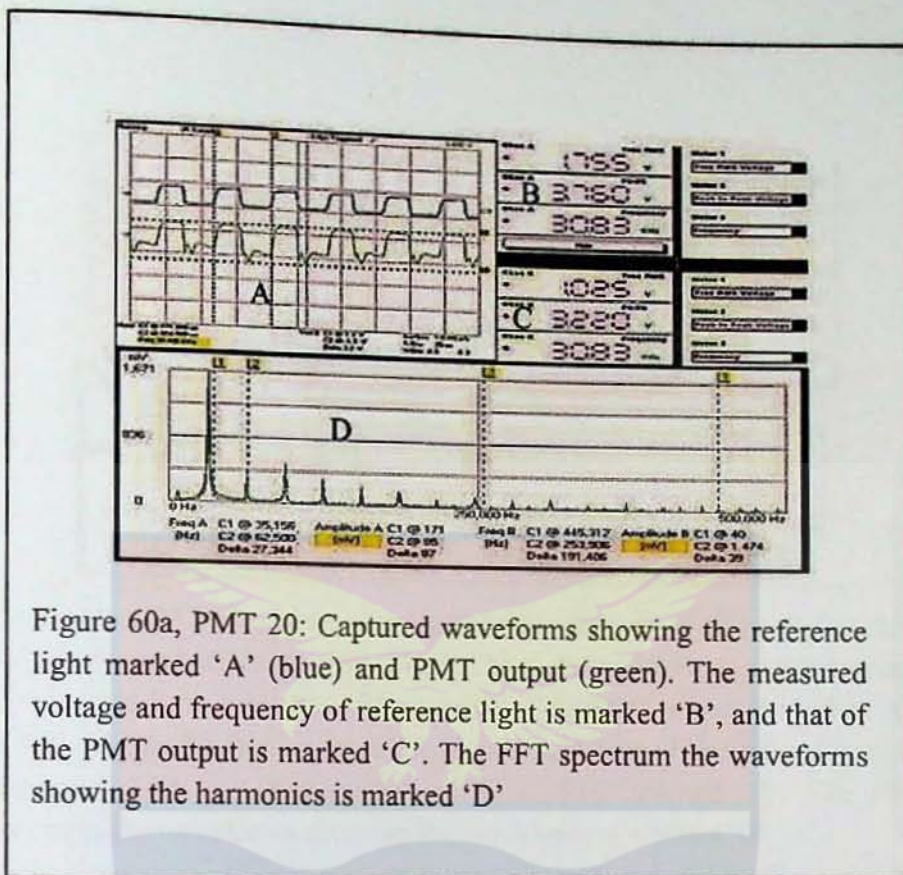


Figure 60a, PMT 20: Captured waveforms showing the reference light marked 'A' (blue) and PMT output (green). The measured voltage and frequency of reference light is marked 'B', and that of the PMT output is marked 'C'. The FFT spectrum the waveforms showing the harmonics is marked 'D'

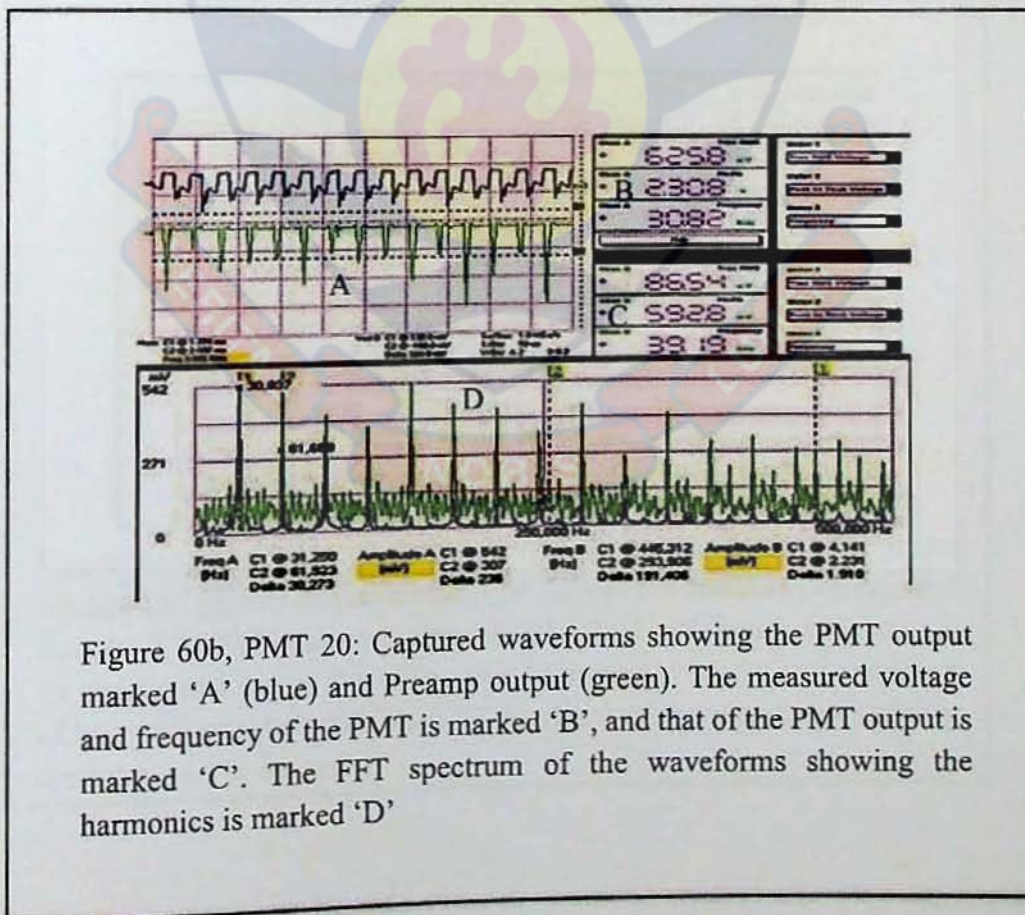


Figure 60b, PMT 20: Captured waveforms showing the PMT output marked 'A' (blue) and Preamp output (green). The measured voltage and frequency of the PMT is marked 'B', and that of the PMT output is marked 'C'. The FFT spectrum of the waveforms showing the harmonics is marked 'D'

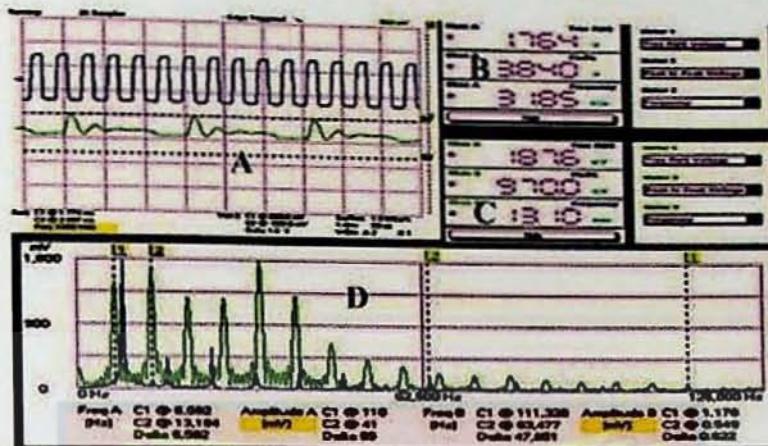


Figure 61a, PMT 21: Captured waveform showing the PMT output marked 'A' (green) and reference light (blue). The measured voltage and frequency of reference light is marked 'B', and that of the PMT output is marked 'C' is 970 mV, and a frequency of 13.10 kHz and that of the reference light measured 3.84 V and frequency of 31.85 kHz marked 'B'. The FFT spectrum the waveforms showing the harmonics is marked 'D'

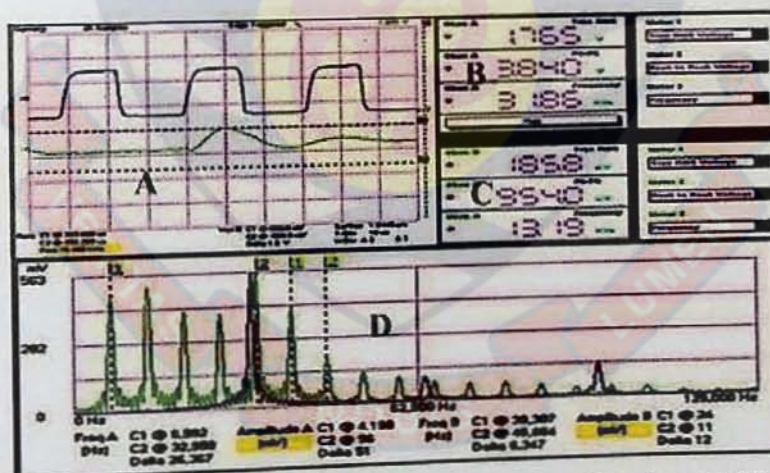


Figure 61b, PMT 21: Captured waveform showing the PMT output marked 'A' (green) and reference light (blue). The measured voltage and frequency of PMT output is marked 'C' is 954 mV, and a frequency of 13.19 kHz and that of the reference light measured 3.84 V and frequency of 31.86 kHz marked 'B'. The FFT spectrum of the waveforms showing the harmonics is marked 'D'

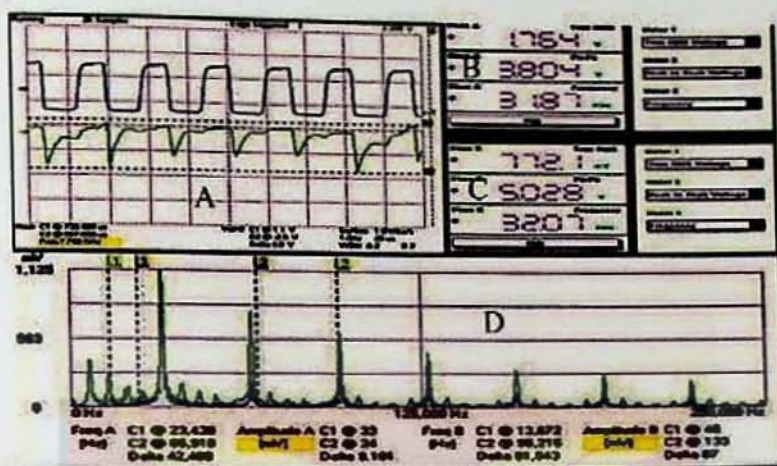


Figure 62a, PMT 22: Captured waveforms showing the reference light output marked 'A' (blue) PMT 22 (green). The measured voltage and frequency of reference light is marked 'B', and PMT output is marked 'C'. The FFT spectrum showing the harmonics is marked 'D'

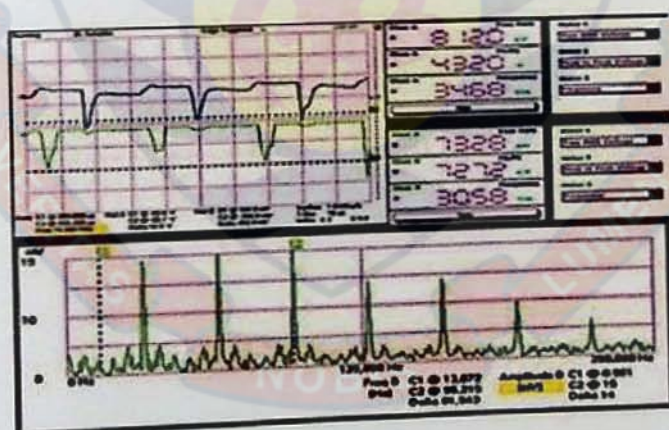


Figure 62b, PMT 22: Captured waveforms showing the PMT 22 output voltage marked 'A' (blue) and Preamp (green). The measured voltage and frequency of PMT is marked 'B' and Preamp output is marked 'C'. The FFT spectrum showing the harmonics is marked 'D'

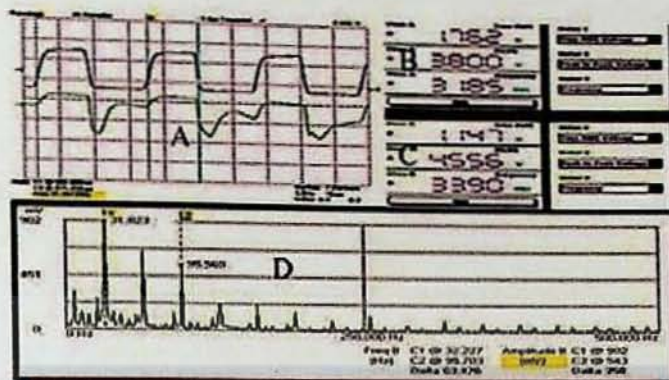


Figure 63a, PMT 23: Captured waveforms showing the reference light marked 'A' (blue) and the PMT 23 output (green). The measured voltage and frequency of reference light is marked 'B' and PMT output is marked 'C'. The FFT of the waveforms showing the harmonics is marked 'D'

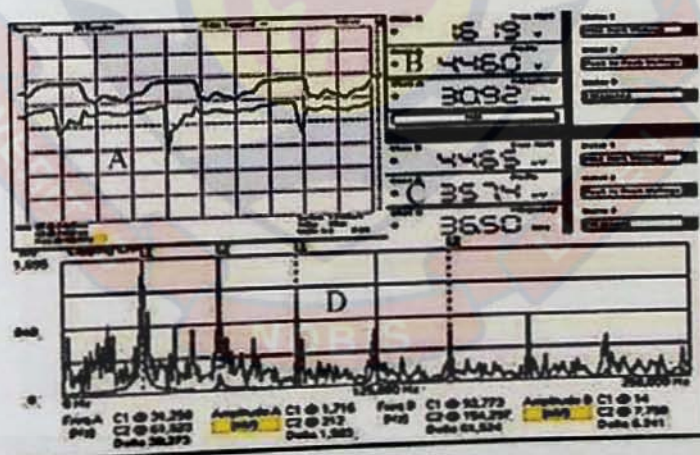


Figure 63b, PMT 23: Captured waveforms showing PMT 23 output voltage marked 'A' (blue) and Preamp output (green). The measured voltage and frequency of PMT 23 is marked 'B' and Preamp output is marked 'C'. The FFT spectrum showing the harmonics is marked 'D'

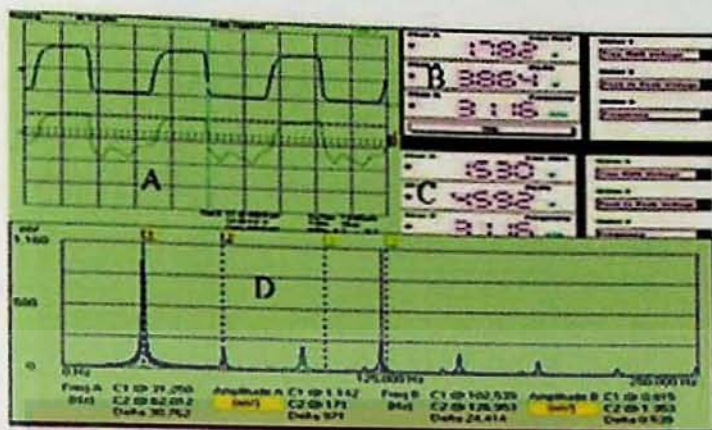


Figure 64a, PMT 24: Captured waveforms showing the reference light marked 'A' (blue) and the PMT 24 output (green). The measured voltage and frequency of reference light is marked 'B' and PMT output is marked 'C'. The FFT of the waveforms showing the harmonics is marked 'D'

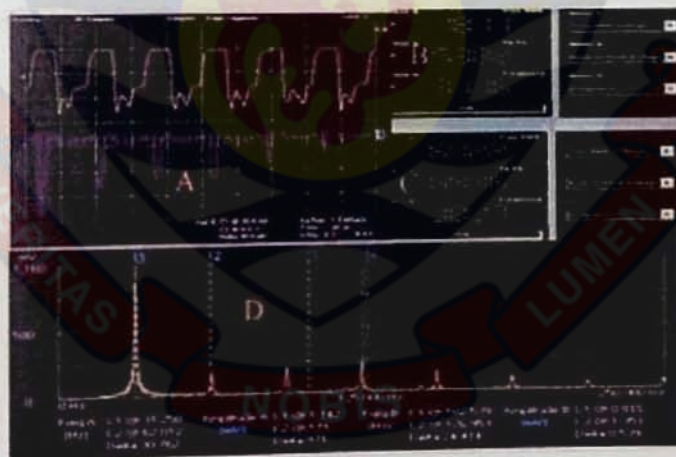


Figure 64b, PMT 24: Captured waveforms showing the PMT 24 output voltage marked 'A' (green) and Preamp (violet). The measured voltage and frequency of PMT 24 is marked 'B' and Preamp output is marked 'C'. The FFT spectrum showing the harmonics is marked 'D'

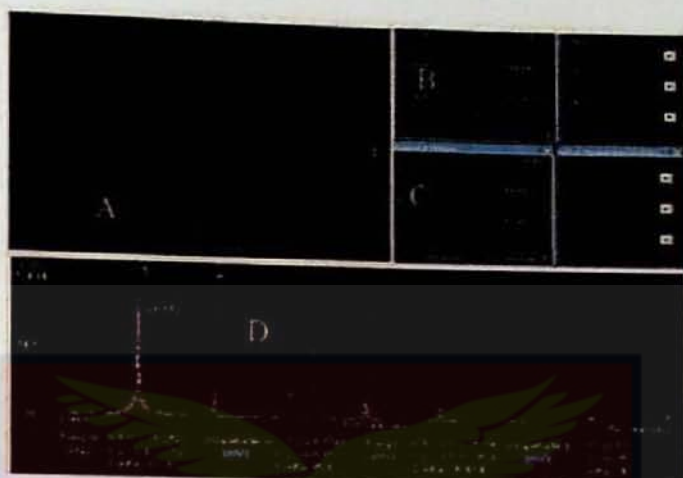


Figure 65a, PMT 25: Captured waveforms showing the reference light marked 'A' (green) and the PMT 25 output (violet). The measured voltage and frequency of reference light is marked 'B' and PMT output is marked 'C'. The FFT of the waveforms showing the harmonics is marked 'D'

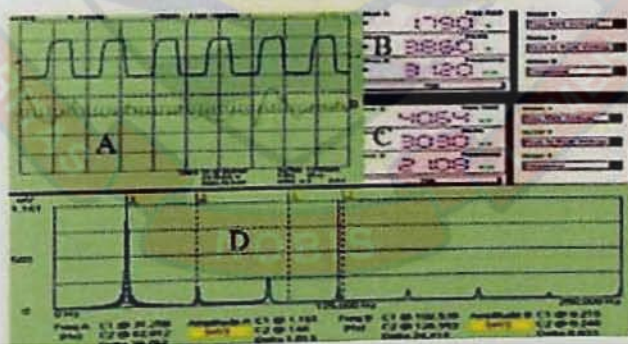


Figure 65b, PMT 25: Captured waveforms showing the reference light output voltage marked 'A' (blue) and Preamp output (green). The measured voltage and frequency of reference light is marked 'B' and Preamp output is marked 'C'. The FFT spectrum showing the harmonics is marked 'D'

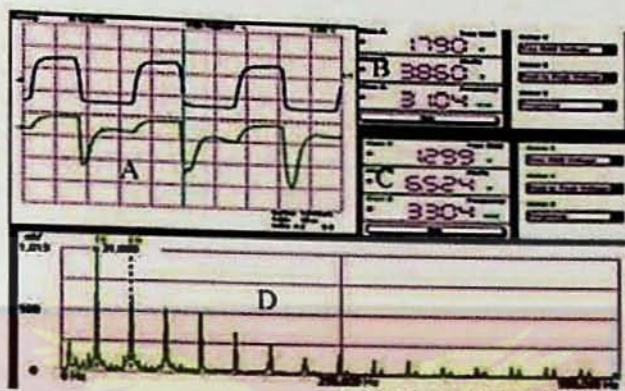


Figure 66a, PMT 26: Captured waveforms showing the reference light voltage marked 'A' (blue) and the PMT 26 output (green). The measured voltage and frequency of reference light is marked 'B' and PMT output is marked 'C'. The FFT of the waveforms showing the harmonics is marked 'D'.

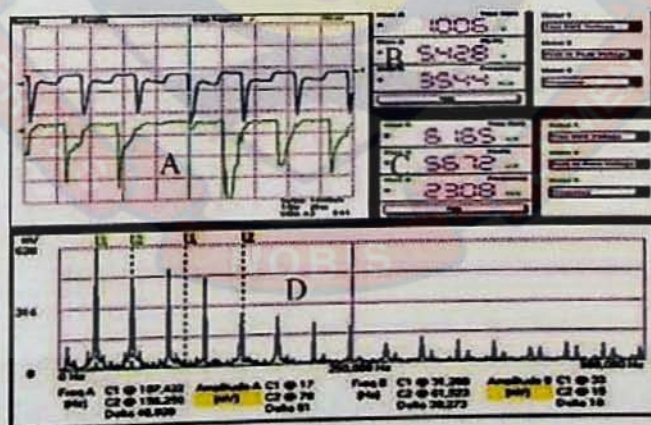


Figure 66b, PMT 26: Captured waveforms showing the PMT 26 output marked 'A' (blue) and Preamp output (green). The measured voltage and frequency of the PMT is marked 'B' and Preamp output is marked 'C'. The FFT spectrum showing the harmonics is marked 'D'

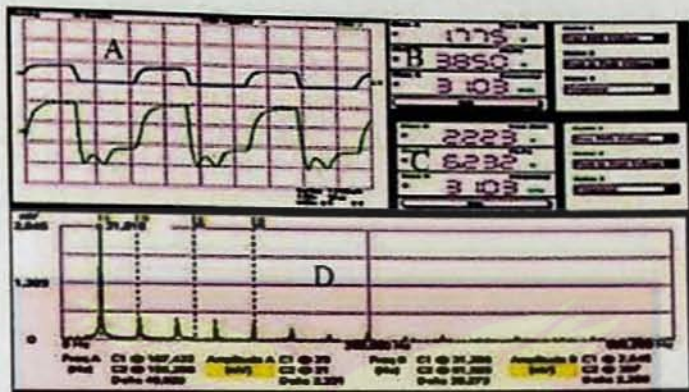


Figure 67a, PMT 27: Captured waveforms showing the reference light voltage marked 'A' (blue) and the PMT 27 output (green). The measured voltage and frequency of reference light is marked 'B' and PMT output is marked 'C'. The FFT of the waveforms showing the harmonics is marked 'D'.

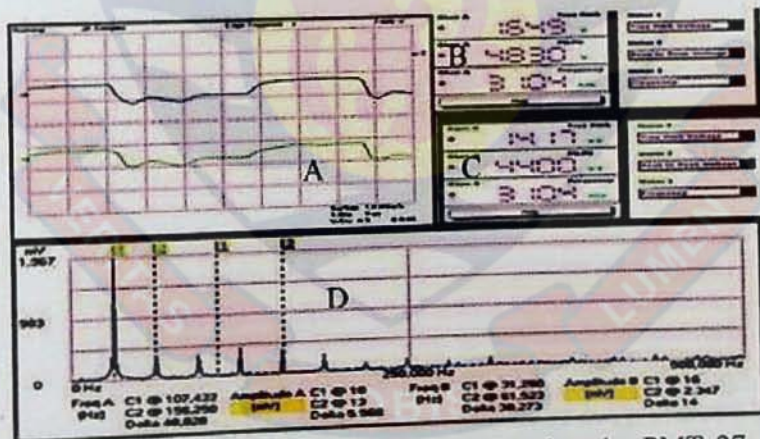


Figure 67b, PMT 27: Captured waveforms showing the PMT 27 output voltage marked 'A' (blue) and Preamp output (green). The measured voltage and frequency of PMT 27 is marked 'B' and Preamp output is marked 'C'. The FFT spectrum showing the harmonics is marked 'D'.

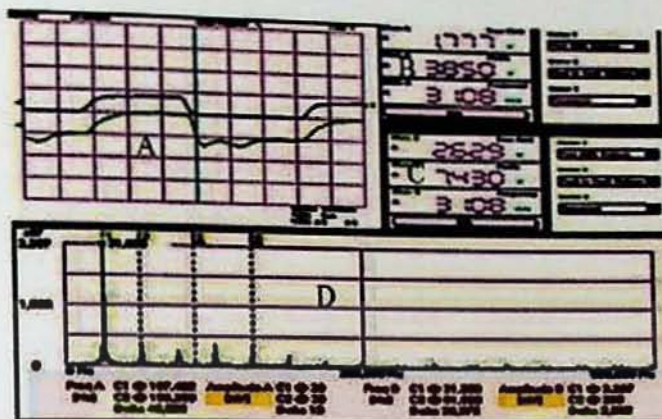


Figure 68a, PMT 28: Captured waveforms showing the reference light voltage marked 'A' (blue) and the PMT 28 output (green). The measured voltage and frequency of reference light is marked 'B' and PMT output is marked 'C'. The FFT of the waveforms showing the harmonics is marked 'D'.

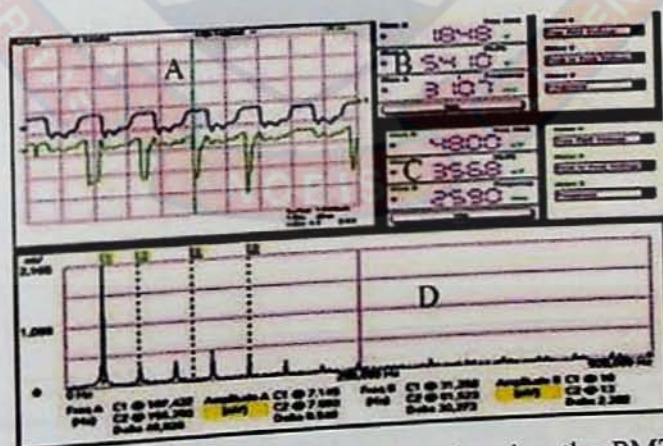


Figure 68b, PMT 28: Captured waveforms showing the PMT 28 output voltage marked 'A' (blue) and Preamp output (green). The measured voltage and frequency of PMT 28 is marked 'B' and Preamp output is marked 'C'. The FFT spectrum showing the harmonics is marked 'D'.

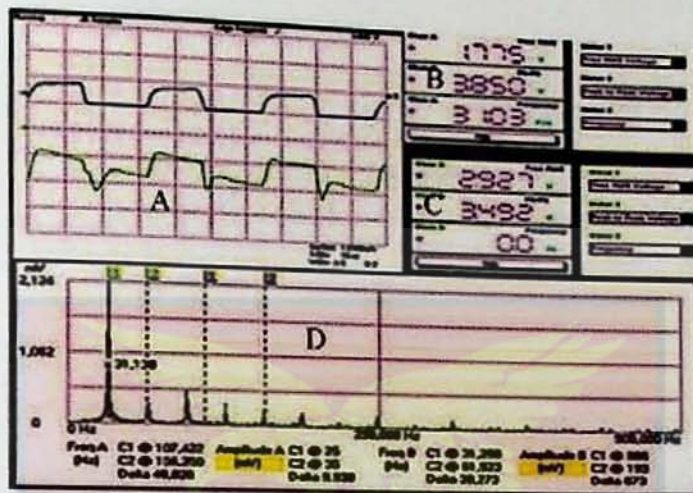


Figure 69a, PMT 29: Captured waveforms showing the reference light voltage marked 'A' (blue) and the PMT 29 output (green). The measured voltage and frequency of reference light is marked 'B' and PMT output is marked 'C'. The FFT of the waveforms showing the harmonics is marked 'D'.

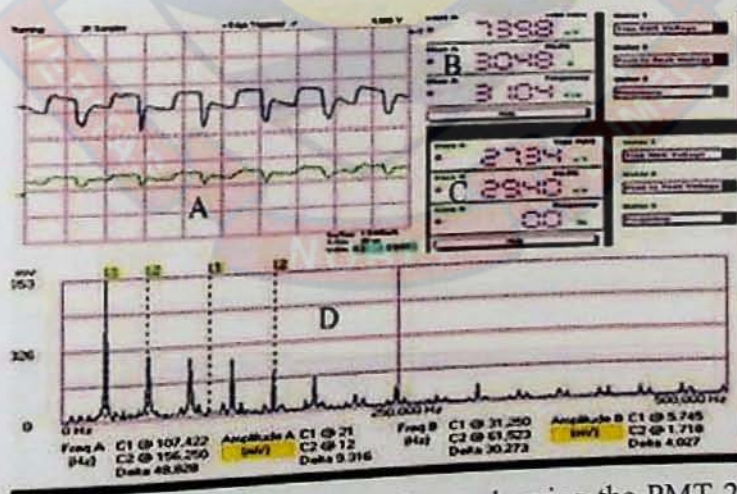


Figure 69b, PMT 29: Captured waveforms showing the PMT 29 output voltage marked 'A' (blue) and Preamp output (green). The measured voltage and frequency of PMT 29 is marked 'B' and Preamp output is marked 'C'. The FFT spectrum showing the harmonics is marked 'D'.

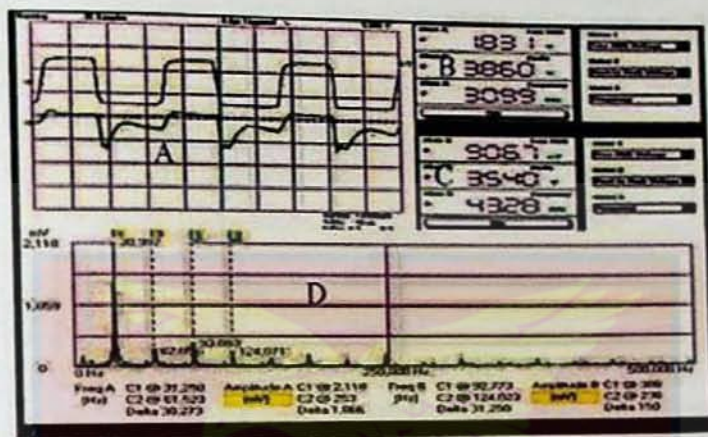


Figure 70a, PMT 29: Captured waveforms showing the reference light voltage marked 'A' (blue) and the PMT 30 output (green). The measured voltage and frequency of reference light is marked 'B' and PMT output is marked 'C'. The FFT of the waveforms showing the harmonics is marked 'D'.

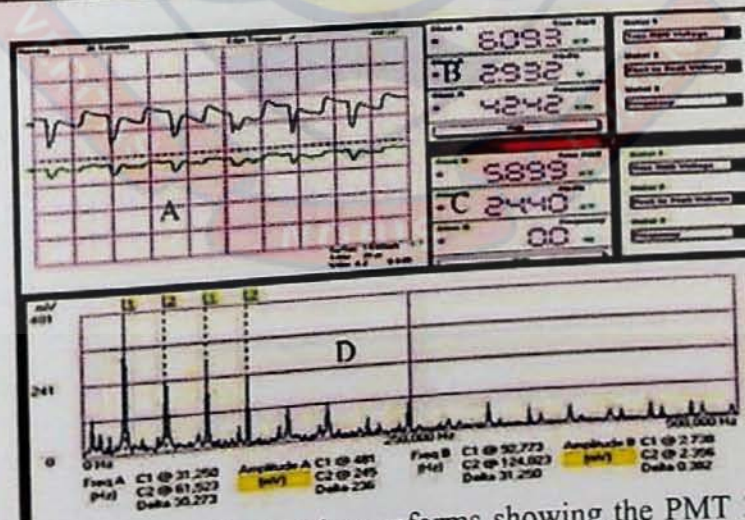


Figure 70b, PMT 29: Captured waveforms showing the PMT 30 output voltage marked 'A' (blue) and Preamp output (green). The measured voltage and frequency of PMT 30 is marked 'B' and Preamp output marked 'C'. The FFT spectrum showing the harmonics is marked 'D'.

Table 1: PMT Gain with and without Preamplifiers

HV set to -1200V

PMT No:	PMT Gain with No Preamp	PMT Gain with Preamp	PMT No:	PMT Gain with No Preamp	PMT Gain with Preamp
PMT1	2.4	9.00E-01	PMT21	0.097	—
PMT2	3.47	1.80E-01	PMT22	5.03	7.27E-01
PMT3	1.74	2.13	PMT23	4.56	3.57E-01
PMT4	4.28	5.94E-02	PMT24	4.59	6.45E-01
PMT5	3.32	5.18E-01	PMT25	6.512	3.98E-01
PMT6	3.22	3.01E-01	PMT26	6.52	5.67E-01
PMT7	2.95	3.56E-02	PMT27	6.23	4.40E-02
PMT8	21.72	—	PMT28	7.43	3.56E-01
PMT9	1.57	2.50E-02	PMT29	3.49	2.94E-02
PMT10	2.12	1.86E-02	PMT30	3.54	2.44E-02
PMT11	1.68	9.6E-02	PMT31	3.12	6.60E-02
PMT12	9.75	3.41E-01	PMT32	2.451	1.00E-01
PMT13	0.52	—	PMT33	1.841	2.50E-01
PMT14	5.87	3.35E-01	PMT34	4.37	3.60E-01
PMT15	2.96	4.00E-03	PMT35	3.88	1.65E-01
PMT16	3.23	4.80E-03	PMT36	4.91	4.00E-01
PMT17	6.08	2.57E-01	PMT37	2.942	3.30E-01
PMT18	5.81	4.10E-01	PMT38	3.102	3.30E-01
PMT19	3.64	2.16E-01	PMT39	1.52	1.96E-01
PMT20	3.22	5.93E-01	PMT40	3.58	3.50E-01

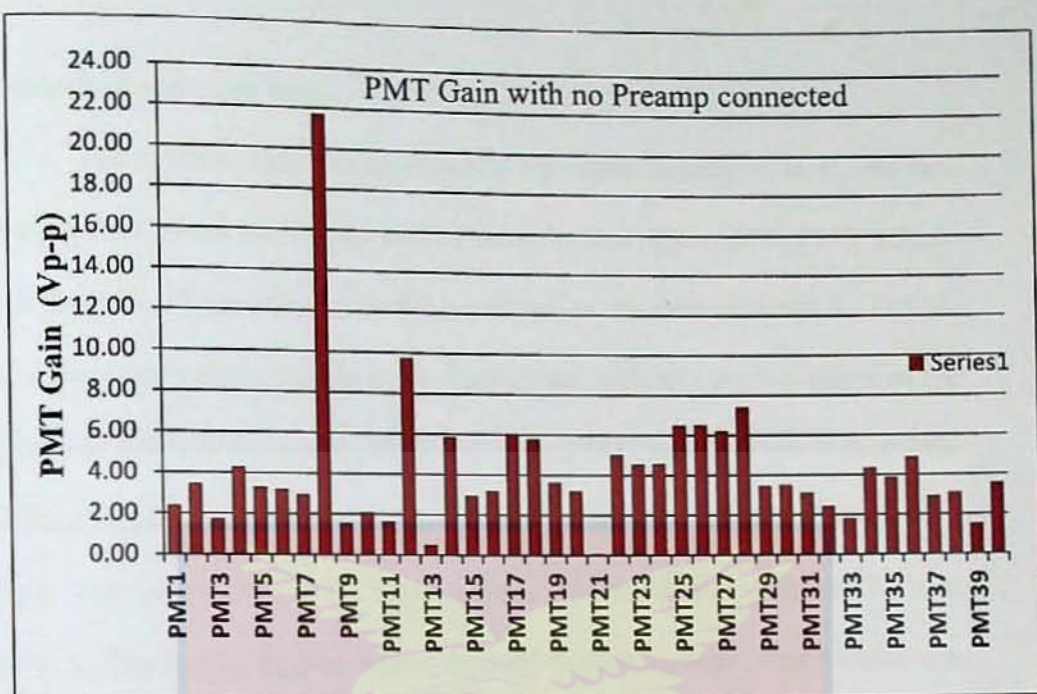


Figure 71: A bar chart showing the gain of PMTs with no preamp connected.

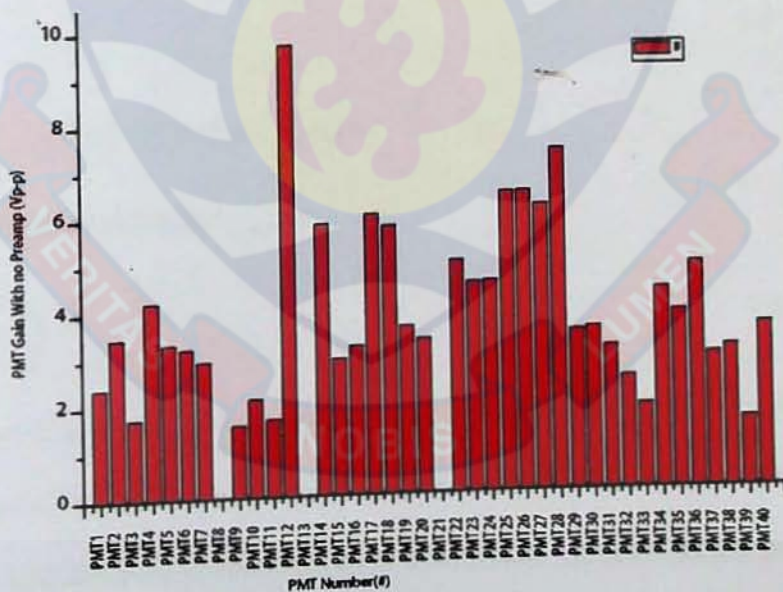


Figure 72: A bar chart showing the gains of PMTs with PMT8 output removed.

Analysis of captured data

The captured data was divided into four parts, namely A, B, C, and D. Part- A showed the waveforms part of the reference light and the PMT output. For example, Figure 42a shows the waveform of the data captured for PMT2, without preamp connected Part - A- blue colour indicates the waveform of the reference light and the green colour shows the PMT2 output. Part- B shows the voltage measured by the capture device during the acquisition for the reference light. The top reading is the RMS voltage and for PMT2 (Figure 42a) was 1.771V. The middle reading shows the peak to peak voltage (V_{p-p}) which was 3.850V for PMT2, and the bottom reading was the measured frequency of the reference light waveform, which for PMT2 was 31.16 kHz.

The Peak Voltage (V_p) is

$$V_p = \frac{V_{p-p}}{2} \quad 1.0$$

Where V_{p-p} is the Peak to Peak voltage.

The root mean square value V_{rms} is

$$V_{rms} = \frac{V_p}{2} \quad 2.0$$

Part-C shows the voltage measured by the data acquisition device during the capture of the PMT output waveform. The top reading shows the RMS voltage which for PMT2 was 998.2 mV. The middle reading was the peak to peak voltage (V_{p-p}) reading of PMT2 output which was 347.2 mV, and the bottom reading is the measured frequency of PMT2 output waveform which is 31.16 kHz and the same as the reference light frequency.

Part-D is the Fast Fourier Transform (FFT) which showed the spectrum of frequencies. Fundamental frequency, 1st harmonic, 2nd, 3rd etc, for the waveforms concerned.

Significance of the Graphic data

The significance of the graphical representation of the data was that, that it provided the observer the necessary waveforms for the observer to take a decision as to whether the PMT was good or bad. Decision on whether the PMT was good or bad could not be based on voltage reading on a voltmeter.

Identification of good PMTs

From the block diagram of the experimental setup in Figure 39, the LED which supplied the blue light to the PMT cathode under test was modulated with an oscillator frequency of 31 kHz. Therefore to identify a good PMT, the PMT waveforms were compared with the reference light waveforms in terms of shape (rectangular) and frequency (31 kHz). If the PMT under test output voltage has shape similar to rectangular and has frequency close to 31 kHz, then the PMT was regarded as good. The PMTs had some stabilization capacitors that were connected at the HV supply at the last stages of the PMT dynodes, so most of the PMTs outputs behaved as a differentiator. The Fast Fourier Transform (FFT) spectrum analysis as shown in part-D of the captured data was employed when it was difficult to interpret the result.

By using the above method, 25 PMTs were identified to be good for PMT with no preamp connected measurements. That is, without preamp

connected They included the followings PMTs, Figure 41a, Figure 42a, Figure 43a, Figure 45a, Figure 46a, and Figure 49a, others were Figure 50a, Figure 51a, Figure 52a, Figure 54a, Figure 55a, Figure 56a, Figure 57a, Figure 58a, and Figure 60a. The rest were Figure 62a, Figure 63a, Figure 64a, Figure 65a, Figure 66a, Figure 67a, Figure 68a, Figure 69a, and Figure 70a.

Identification of bad PMTs

Five PMTs were found to be malfunctioned or bad during the measurement. They were PMT 8, PMT 13 and PMT 21 and each is analysed in the following sections.

PMT 8 output voltage

PMT 8 gain was regarded, however as noise voltage since the voltage shape did not resemble the reference (oscillator) voltage and its frequency was also different from the reference (oscillator) frequency. Detailed information on PMT8 is discussed as below.

A voltage of 538.4 mV with a frequency of 6.81 kHz was measured at the output of PMT 8 even when there was no input reference light. This noise waveform is shown in Figure 48a, marked A, while the measured voltage and frequency is marked B on the graph.

When the blue light was switched on, a voltage of 21.72 V and a frequency of 15.25 kHz was measured at the output of the PMT 8. The highest voltage recorded during the experiment. While a voltage gain stated above was possible, the frequency and shape of the waveform did not resemble the blue

(reference) light waveform (Figure 48c). The blue light has a frequency of 31.78 kHz and rectangular waveform.

PMT 13 output voltage

Figure 53a shows the output waveform of PMT 13 (green colour) while that of the reference light is blue colour, marked A in the figure. The reference voltage was measured as 3.75V and a frequency 31.7 kHz, marked B. PMT 13 output voltage was measured as 519.8 mV and a frequency of 21.34 kHz.

This waveform does not resemble reference waveform because the frequency and shape of the waveform should have resembled the reference waveform.

PMT 21 output voltage

Figure 61a shows the waveform of PMT 21. The waveform of the reference light is blue colour, while the PMT output waveform is green colour marked 'A' in the figure. The measured voltage at the output was 970.0 mV and has a frequency of 13.10 kHz marked 'C' which is different from the reference frequency of 31.85 kHz marked 'B' in the figure. The fast Fourier transform (FFT), marked 'D' shows harmonics of the reference (blue colour) and the PMT output (green colour).

The two waveforms frequencies are seen in Part-D of the data in Figure 61a and Figure 61b, as the intervals are not the same for the two waveforms. The harmonics of the reference frequency are: 31.85 kHz, 62.7 kHz, and 94.55 kHz which are the 1st, 2nd and 3rd harmonics, respectively of the reference signal.

The PMT output has 6.592 kHz, 13.184 kHz, and 19.78 kHz which are 1st, 2nd and 3rd harmonics, respectively.

PMTs output gain with preamp connected

The results of the second experiment as shown in the bar chart of (Figure 73). The characteristics of the PMTs changed significantly when the preamplifiers were connected to the output of the PMTs, which was the situation found in the gamma camera.

The gains of the PMTs with no preamp connected. (Figure 71 and Figure 72) were far higher than the ones with preamps connected (Figure 73). With the preamp connected for example, PMT 3 and its preamp output was the highest gain (Figure 73), as compared to PMT 12 output (Figure 72), when the preamps were not connected.

The connection of the preamps to the PMTs outputs was vital to this work, because the preamp sat on top of the PMT, and the PMT output was directly coupled to the preamp input in the gamma camera detector assembly. The preamplifier determined the peak of the signal voltage from the PMT which was proportional to the photoelectrons energy amplified by the PMT. The preamp then sends the signal to the processing circuits in the gamma camera.

Some few preamps output did not produce any voltage at all or the shape of the waveform was different from expected. Among the PMTs which produced output voltage without the preamps connected (Figure 44a), but did not produce any output when the preamps were connected are PMT 4 (Figure 44b), PMT 7 (Figure 47b) PMT 15 (Figure 55b), PMT 16 (Figure 56b), and

PMT 27 (Figure 67b) others were very low as compared with the ones without the preamps connected.

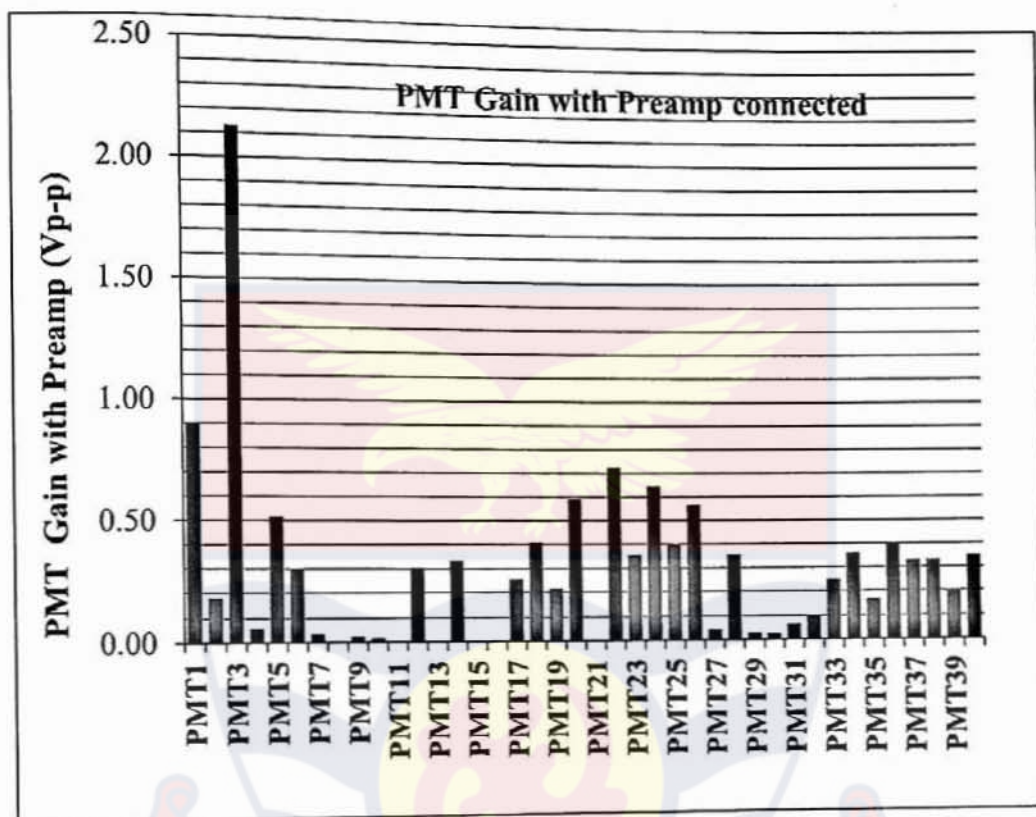


Figure 73: A bar chart showing the gains of PMTs with Preamp connected

Repair of faulty preamps

All the 40 preamps were repaired after it was found that some of the boards were found faulty. The improved PMTs output after repairs is found in Table 2, and the bar chart of Figure 74. The cause of the damage was the poor design, and construction of the components of the preamp boards. The components were not insulated (covered) therefore making them prone to short circuit with each other Plate 18.

In all 5 PMTs were declared bad in the experiment. The first three were PMT 8, PMT 13 and PMT 21 were found to be bad during testing. The other

three PMTs are PMT 21, PMT 24 and PMT 34 were found bad as a result of very high dark current.

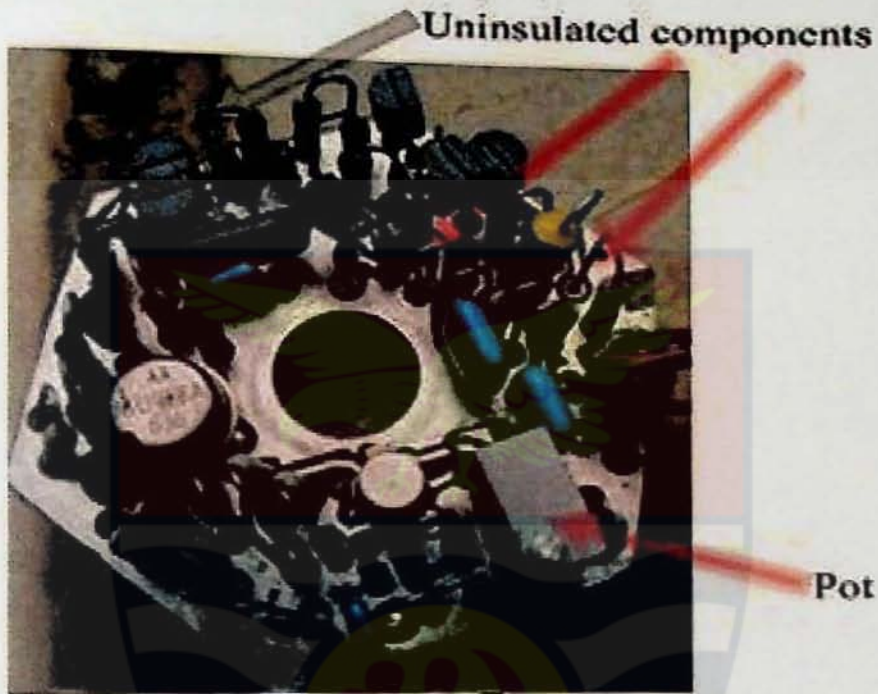


Plate 18: Gamma camera preamplifier that sits on top of the PMT. As seen from the figure above shows the Resistor and other components could easily touch each other to cause short circuit to the preamp.

The high dark current does affect the position (X or Y) stability of other PMTs that are grouped together with the one with high dark current.

Table 2: Preamplifier gain Vs. PMT numbers after the Preamps were repair

PMT #	GAIN (V)	PMT #	GAIN (V)
PMT1	1.20	PMT23	2.31
PMT2	2.4	PMT24	2.56
PMT3	2.13	PMT25	4.42
PMT4	2.84	PMT26	3.89
PMT5	1.95	PMT27	4.25
PMT6	1.92	PMT28	5.41
PMT7	1.62	PMT29	1.92
PMT8		PMT30	1.84
PMT9	0.98	PMT31	1.95
PMT10	1.22	PMT32	1.23
PMT11	0.95	PMT33	0.98
PMT12	5.88	PMT34	2.34
PMT13		PMT35	2.19
PMT14	3.25	PMT36	2.69
PMT15	1.78	PMT37	1.76
PMT16	1.93	PMT38	1.65
PMT17	3.12	PMT39	0.98
PMT18	2.82	PMT40	1.98
PMT19	1.83	PMT41	4.23
PMT20	2.11	PMT42	5.42
PMT21		PMT43	3.68
PMT22	2.11		

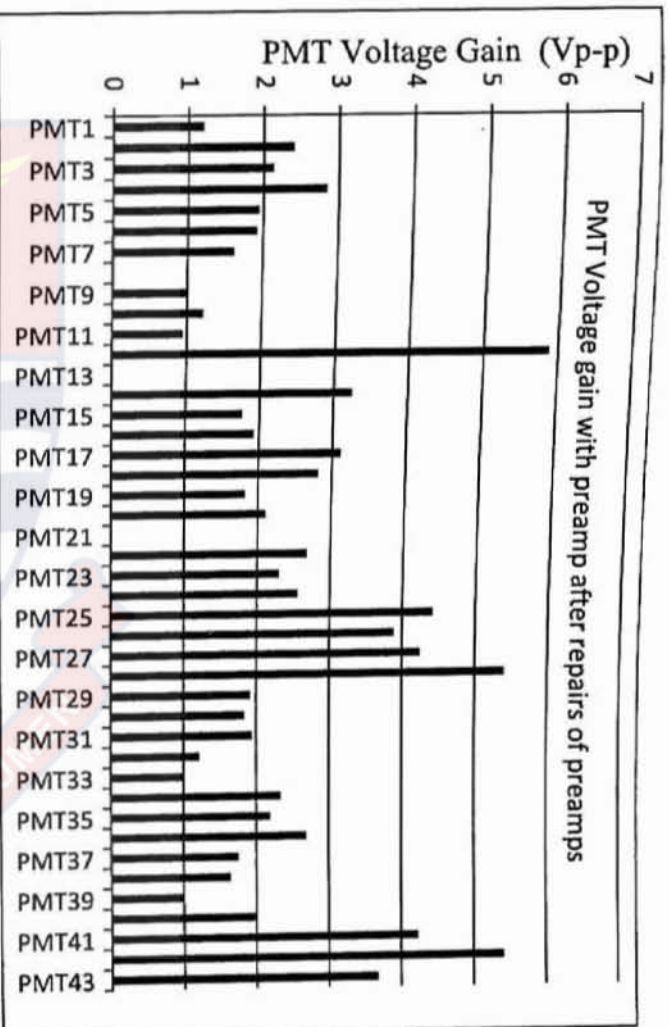


Figure 74: A bar chat of the PMT numbers vrs. gain of the PMTs after the damaged preamps were repaired



Table 3 (A): Effect of PMT Anode current on High Voltage

High Voltage (V)	PMT1 Anode Current (A)	PMT2 Anode Current (A)	PMT3 Anode Current (A)	PMT4 Anode Current (A)	PMT5 Anode Current (A)	PMT5 Anode Current (A)	PMT7 Anode Current (A)	PMT8 Anode Current (A)	PMT9 Anode Current (A)
300	2.00E-07	1.66E-06	1.10E-06	9.00E-07	5.60E-07	8.30E-07	8.90E-07	2.00E-07	6.00E-07
370	8.70E-07	3.34 E-6	1.34E-05	5.30E-06	6.90E-06	9.00E-06	5.90E-06	2.50E-06	1.02E-05
400	3.10E-06	9.80E-06	2.53E-05	1.16E-05	1.76E-05	2.11E-05	1.26E-05	8.10E-06	2.58E-05
500	4.54E-05	5.58E-05	1.35E-04	4.02E-05	1.23E-04	1.27E-04	5.48E-05	3.60E-05	3.00E-05
600	5.73E-05	7.36E-05	1.11E-04	4.80E-05	1.03E-04	1.06E-04	6.86E-05	3.00E-04	7.00E-05
900	9.57E-05	1.86E-04	3.89E-03	1.43E-04	2.10E-07	2.80E-07	1.82E-04	8.92E-05	1.00E-04
1000	1.24E-04	1.46E-04	4.90E-04	1.09E-04	2.30E-07	2.30E-07	1.51E-04	1.10E-04	1.25E-04
1300	1.35E-05	1.90E-04	3.80E-04	1.46E-04	6.90E-07	2.40E-07	1.82E-04	1.60E-04	1.50E-04

Table 3 (B): Effect of PMT Anode current on High Voltage

High Voltage (V)	PMT10 Anode Current (A)	PMT11 Anode Current (A)	PMT12 Anode Current (A)	PMT13 Anode Current (A)	PMT14 Anode Current (A)	PMT15 Anode Current (A)	PMT17 Anode Current (A)	PMT18 Anode Current (A)
300	1.20E-06	6.00E-07	1.62E-06	1.28E-06	8.96E-07	2.38E-06	1.04E-06	5.00E-07
370	1.01E-05	2.50E-05	1.95E-05	7.35E-06	6.58E-06	3.34E-06	2.66E-05	7.00E-06
400	2.56E-05	3.00E-05	3.15E-05	1.42E-05	1.28E-05	1.05E-05	1.08E-04	1.75E-05
500	1.01E-04	4.00E-05	1.43E-07	4.90E-05	4.59E-05	4.62E-05	1.20E-04	1.20E-04
600	1.80E-04	5.01E-05	9.34E-05	6.04E-05	5.41E-05	5.85E-05	9.16E-05	1.00E-04
900	2.50E-04	6.00E-05	1.13E-04	1.74E-04	1.86E-04	1.70E-04	1.22E-06	4.36E-06
1000	3.00E-04	1.00E-04	1.53E-07	1.29E-04	1.27E-04	2.09E-07	3.10E-08	2.33E-04
1300	2.60E-04	9.60E-05	5.90E-04	1.68E-04	1.82E-04	1.65E-04	7.90E-08	3.59E-04

Table 4: Dark current of PMTs

PMT No.	Dark Current (A)	PMT No.	Dark Current (A)
PMT1	5.66E-08	PMT21	3.03E-06
PMT2	1.20E-07	PMT22	4.36E-07
PMT3	2.27E-07	PMT23	1.75E-07
PMT4	8.70E-09	PMT24	3.30E-06
PMT5	5.60E-09	PMT25	2.86E-07
PMT6	4.00E-09	PMT26	1.09E-08
PMT7	1.91E-07	PMT27	4.24E-08
PMT8	4.60E-09	PMT28	1.03E-08
PMT9	3.86E-08	PMT29	6.70E-09
PMT10	1.48E-07	PMT30	2.42E-08
PMT11	7.79E-09	PMT31	4.82E-08
PMT12	5.74E-08	PMT32	3.56E-08
PMT13	2.28E-08	PMT33	1.00E-07
PMT14	2.10E-09	PMT34	2.50E-06
PMT15	2.90E-09	PMT35	1.30E-06
PMT16	2.50E-08	PMT36	5.00E-08
PMT17	5.26E-07	PMT37	1.65E-07
PMT18	3.00E-08	PMT38	3.64E-08
PMT19	8.00E-08	PMT39	2.24E-07
PMT20	1.06E-07	PMT40	-1.96E-08

HV set at -1200V

Effect of PMT anode current on high voltage

The graphs of Figure 75 and 76 show the effect of anode current on PMT high voltage.

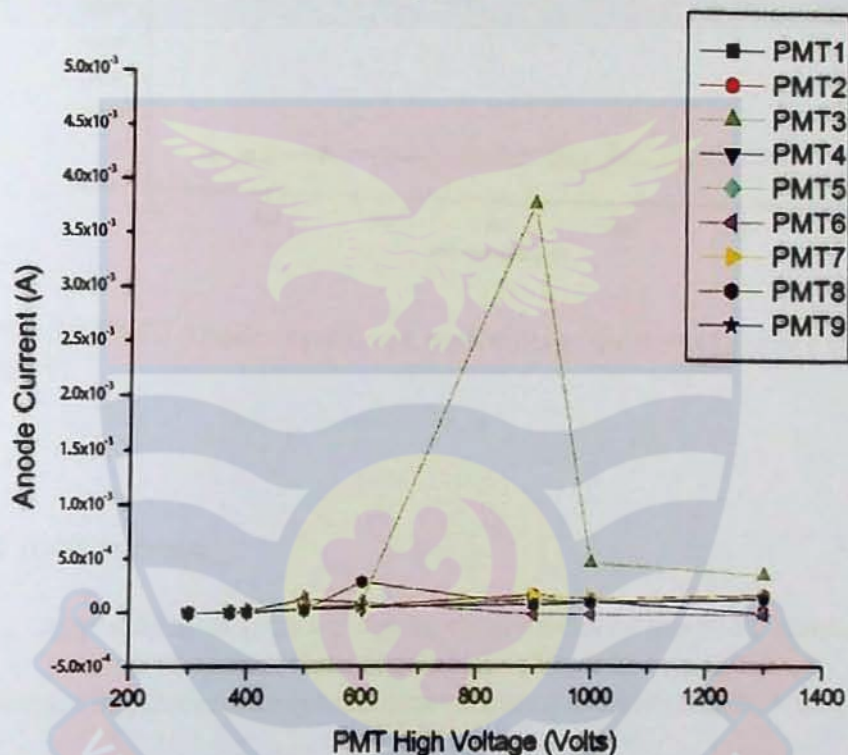


Figure 75: PMT anode current vrs. high voltage for 9 PMTs (PMT1-PMT9)

The two graphs show that there was some increase in anode current as the high voltage was increased. PMT3 has a sudden increase in anode current ($3.8 \times 10^{-3} \text{ A}$) at 900V (Figure 76) but decreases to $4.9 \times 10^{-4} \text{ A}$ at 1000 V. The increase in anode current as the HV was increased is not seem to be high is due to the range of high voltage plotted. If a range of 200V- 400V were plotted the increased in current would have been noticable.

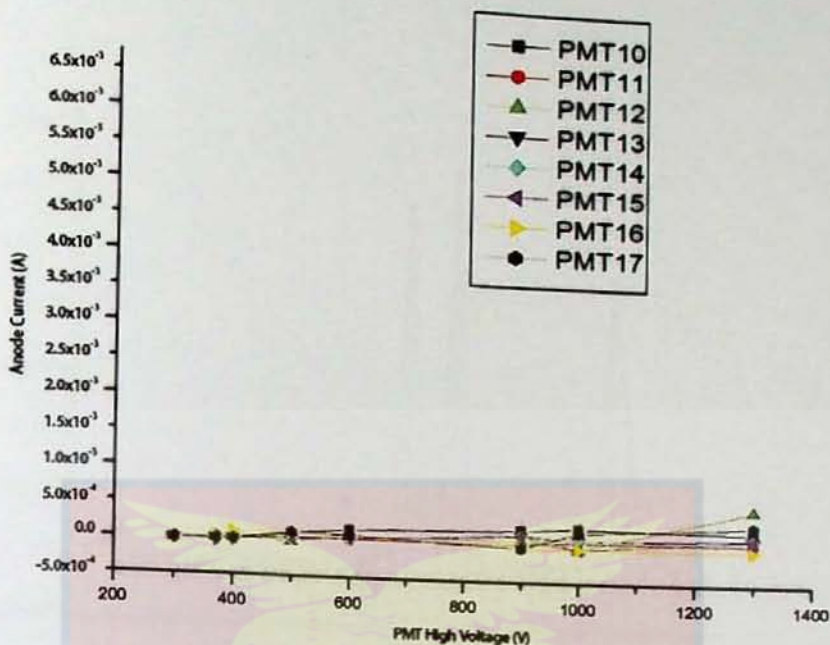


Figure 76: PMT Anode current vs. high voltage for 8 PMTs (PMT10-PMT17)

PMT dark current

Application of high voltage to the dynodes of the PMT results in both an increase in current gain (photoelectron multiplication) and dark current. This dark current can stem from a number of features including field emission, leakage current, and thermionic emission (IEC 60306-4, 1971), (Lung, K, *et al*; 2012). The results of the dark current measurements are shown in Figure 77. PMT 24 has the highest dark current (3.3×10^{-6} A) followed by PMT 21 (3.03×10^{-6} A) then PMT 34 (2.5×10^{-6} A). PMT 21 has already found to be bad during the measurement above (Figure 61). The 2 PMTs were rejected alongside PMT 21 and were not used in the work of the gamma camera. The PMT with the lowest dark current was PMT 14 (2.10×10^{-9} A), as shown in Figure 77.

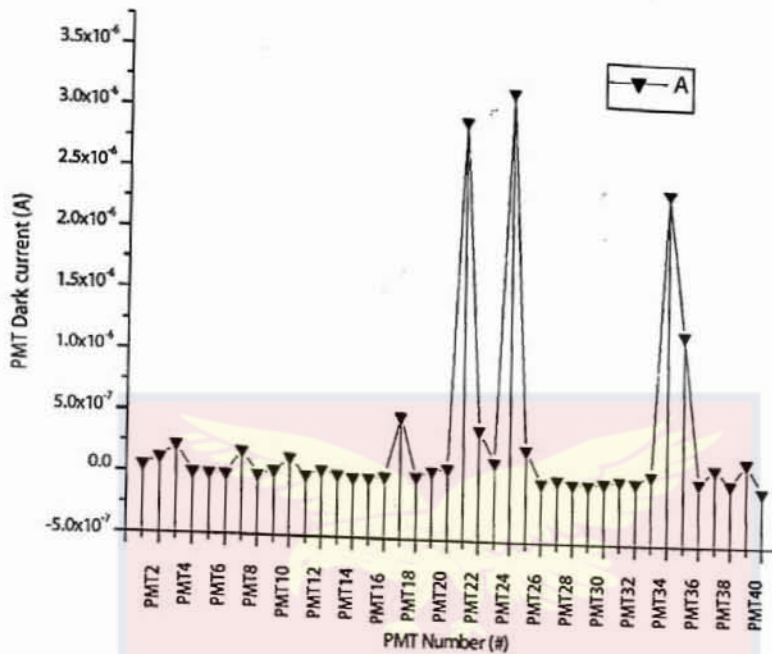


Figure 77: PMTs dark currents at a fixed HV (-1200V)

Ideally, the PMTs were expected to have very low dark current (Lung, K, *et al*; 2012), however, since the PMTs were old (manufactured in the 1980s), the measured dark currents apart from the two (excluding PMT 21) that were rejected, the result of the dark current measurement was expected. The dark current did not affect image quality (increase background radiation) because the single channel analyser in the analyser one board had the window level set to accommodate only the ^{99m}Tc energy of $140 \text{ keV} \pm 10\%$ which the isotope level was set (i.e. 140 keV) and voltage that was above and below this voltage was discriminated by the single channel analyser in the detector processor circuits.

Table 5: Rearrangement of Table 4, by their gains for placement on the detector

PMTs with Preamps connected sorted by their gains after repairs of preamps boards

PMT No	Gain (V_{p-p})	PMT No:	Gain (V_{p-p})
PMT 12	5.88	PMT 40	1.98
PMT 42	5.42	PMT 5	1.95
PMT 28	5.41	PMT 31	1.95
PMT 25	4.42	PMT 16	1.93
PMT 27	4.25	PMT 6	1.92
PMT 41	4.23	PMT 29	1.92
PMT 26	3.89	PMT 30	1.84
PMT 43	3.68	PMT 19	1.83
PMT 14	3.25	PMT 15	1.78
PMT 17	3.12	PMT 37	1.76
PMT 4	2.84	PMT 38	1.65
PMT18	2.82	PMT 7	1.62
PMT 36	2.69	PMT 32	1.23
PMT 22	2.68	PMT 10	1.22
PMT 2	2.40	PMT 1	1.20
PMT 23	2.31	PMT 9	0.98
PMT 35	2.19	PMT 33	0.98
PMT 3	2.13	PMT 39	0.98
PMT 20	2.11	PMT 11	0.95

HV set at 1200V

Characterization and Arrangement of PMTs on Sodium Iodide (NaI(Tl)) Detector

After sorting the PMTs by their gains, the PMTs were then placed on the sodium iodide (NaI(Tl)) detector, the PMT with the highest gain (PMT 12) was placed at the centre as shown in (B). After the PMTs preamps were repaired, the PMTs were then characterized (sorted by their gains (Figure 74) and were placed on the sodium iodide detector (Figure 74) and (Figure 75). The original PMTs arrangement on the detector of the gamma camera is indicated in Figure 78 (A), and the arrangement of PMTs as sorted out by the result in Figure 75 is shown in Figure 78 (B).

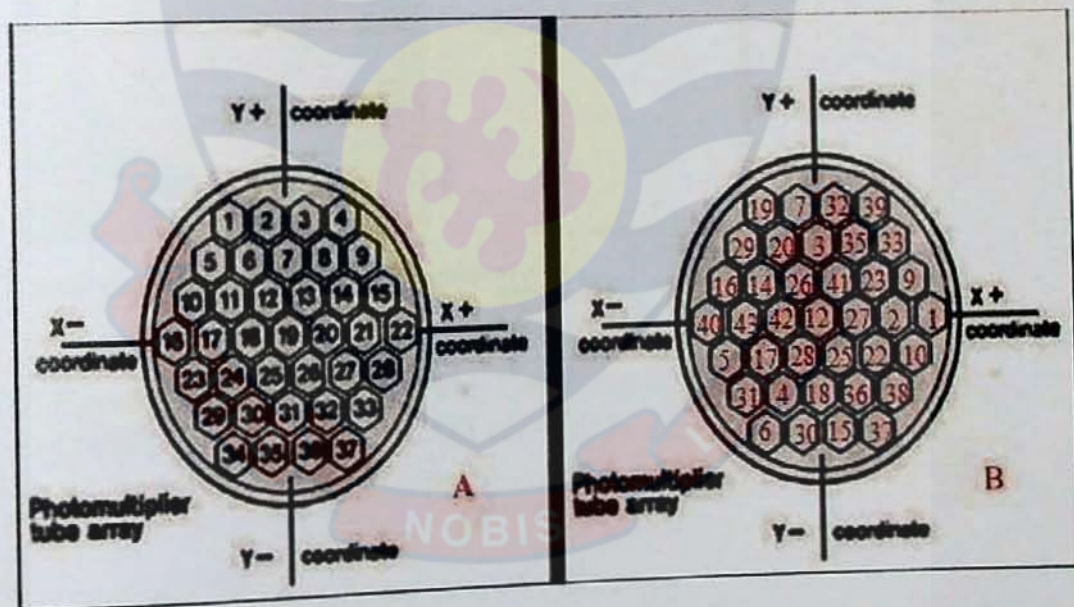


Figure 78: Arrangement of PMTs on the sodium iodide detector. On the left (A) shows the arrangement of PMTs on the detector by the manufacturer, the PMT with the highest (PMT 19) was placed at the centre by the manufacturer of the gamma camera.

Quality Control pictures taken after alignment and fine-tuning

After the gamma camera alignment was completed image acquisition of 16M counts was acquired with the Medic View software and Gamma PF Slovenian acquisition card for ^{99m}Tc radioisotope source. The Analyser 1 isotope level was set to 140 keV and the Analyser 1 window width was set to 20% or 140 keV ±10%. The same software was used to calculate the differential and integral uniformities of all the images shown in Figure 79- Figure 92.

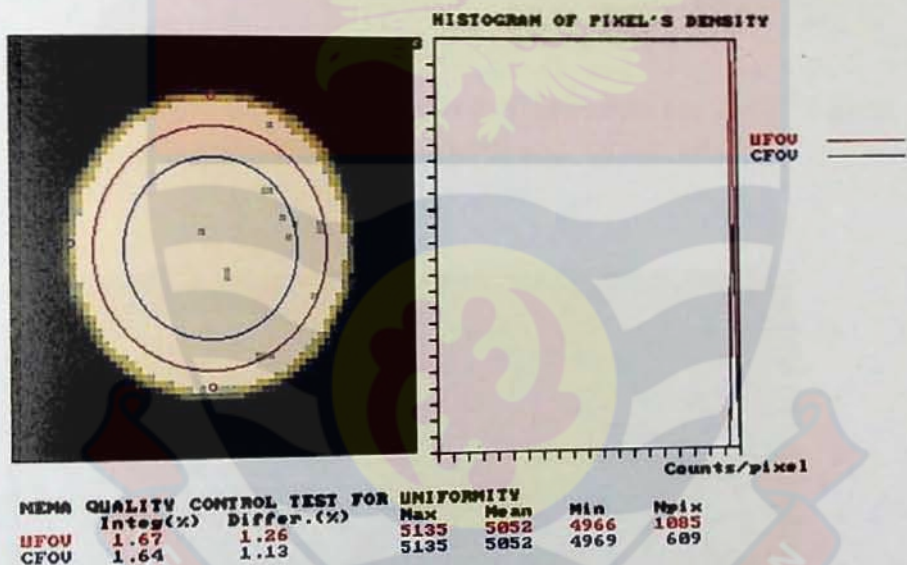


Figure 79: QC Picture No 1, This Picture has the highest uniformity. CFOV: Integ Unif=1.64%; Dif Unif.=1.13%

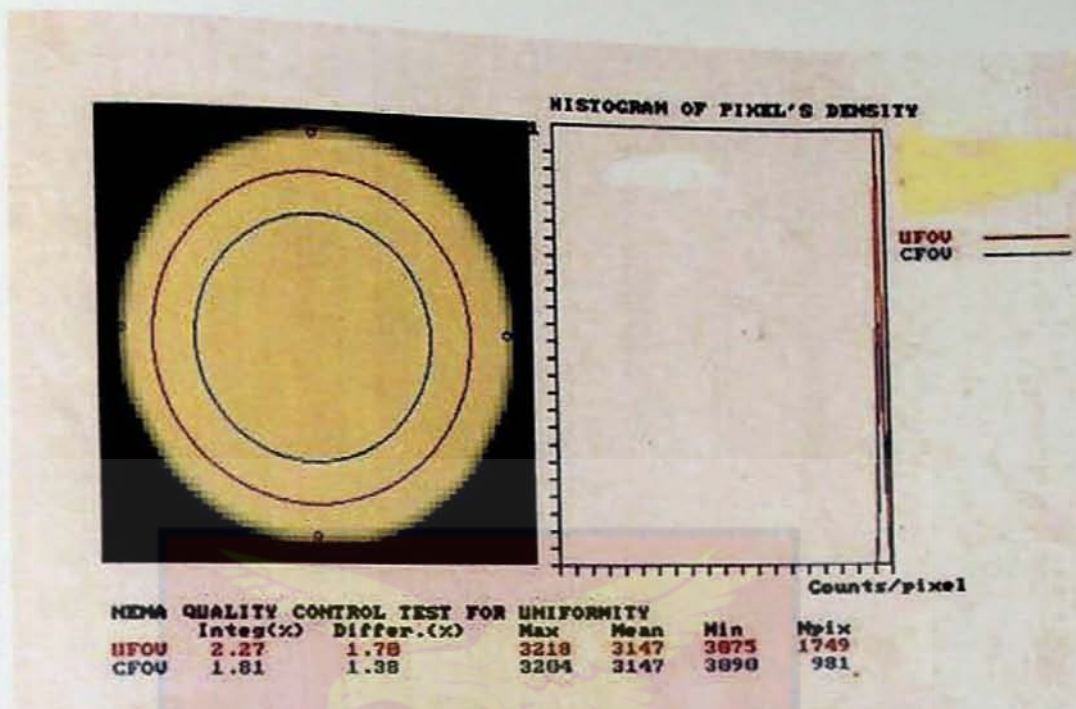


Figure 80: QC Picture No 2. This Picture has the 2nd highest uniformity CFOV IU=1.81%; and DU=1.38%



Figure 81: QC Picture No 3. This picture has the 3rd highest uniformity. CFOV: Integ.=2.01 %; Diff=1.38 %

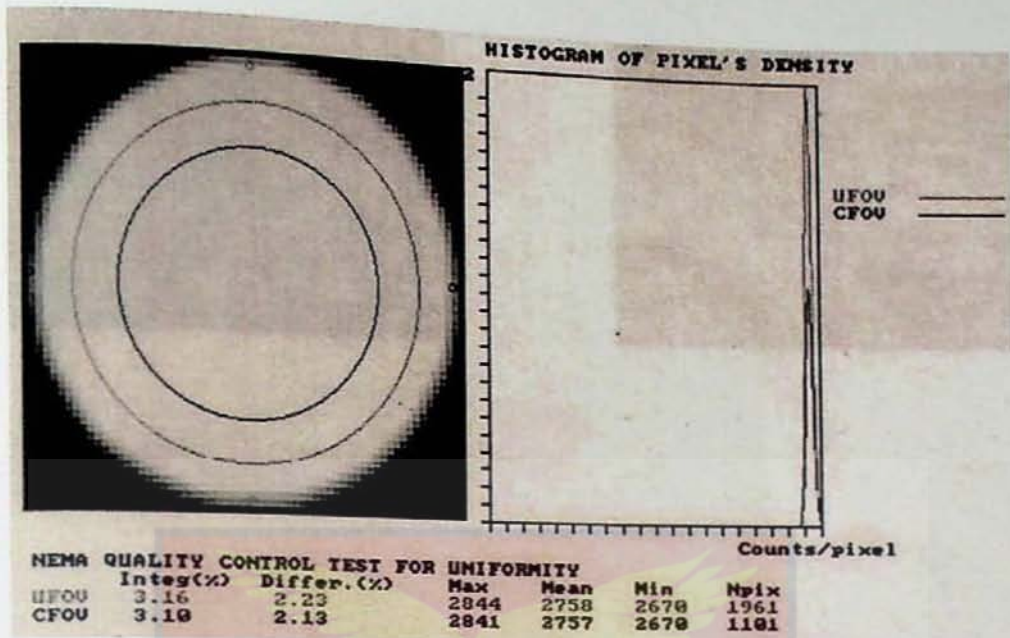


Figure 82: QC Picture No 4. This Picture has acceptable uniformity. The picture quality is good for clinical studies. CFOV, IU=3.01%; DU=2.13%

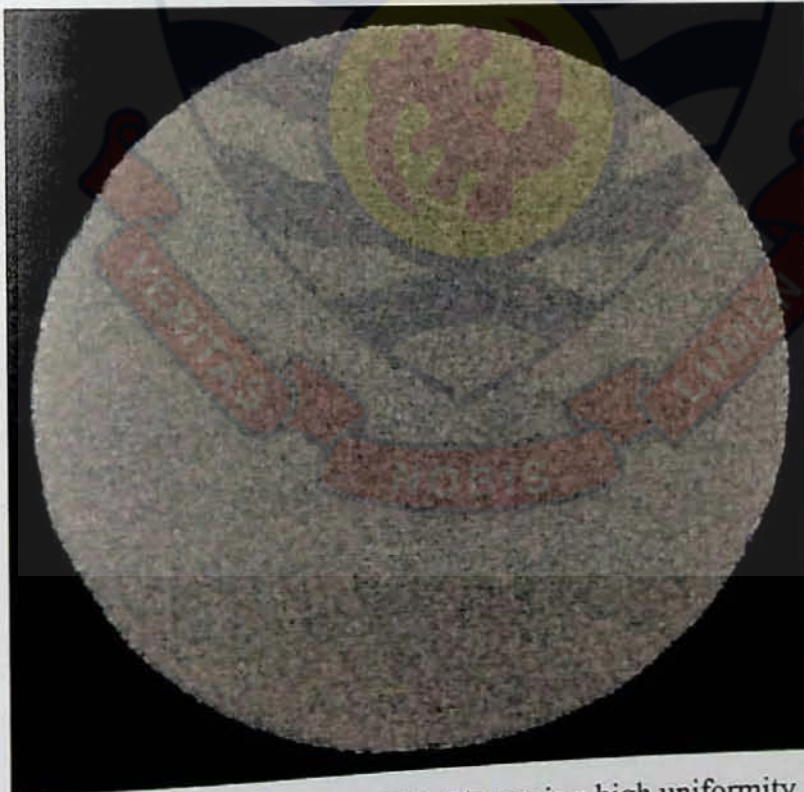


Figure 83: QC Picture No 5. This Picture is a high uniformity flood image. The entire surface of the flood is uniform.

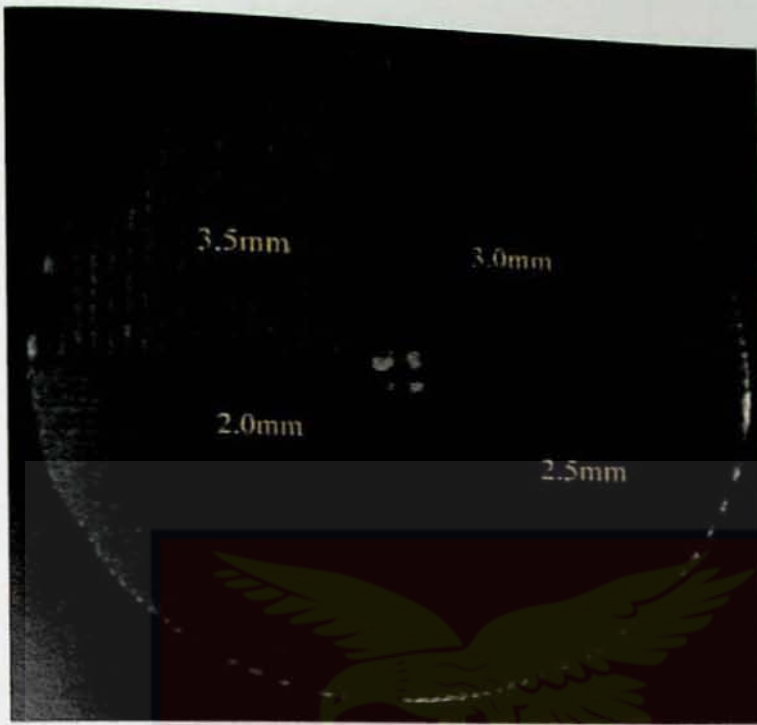


Figure 84: QC Picture No.6, This Picture has a quadrant Phantom bar, with different width. The picture defines the intrinsic resolution of flood image. When the smallest lines in the bars are seen, then the camera is said to have a high spatial resolution.

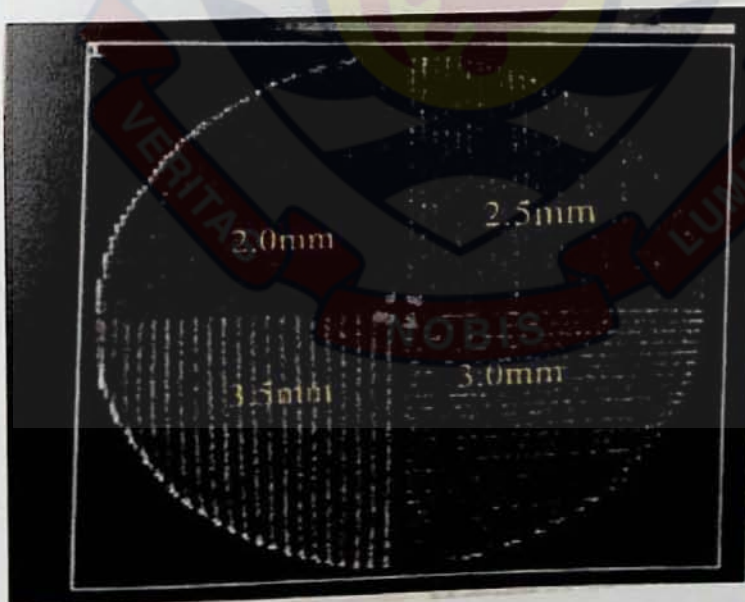


Figure 85: QC -Picture No 7. The phantom bar was rotated 90° . The Picture has a high spatial resolution, and sharp. The 2.5mm bars and spaces are seen

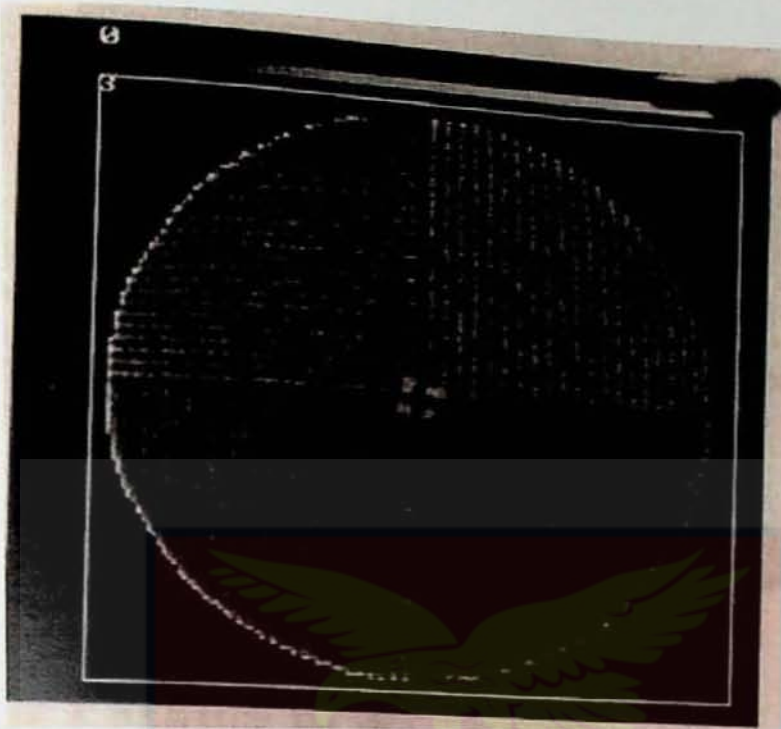


Figure 86, QC -Picture No 8. The phantom bar is rotated 90° . This Picture has a high spatial resolution, and sharp. The 2.5mm bars and spaces are seen

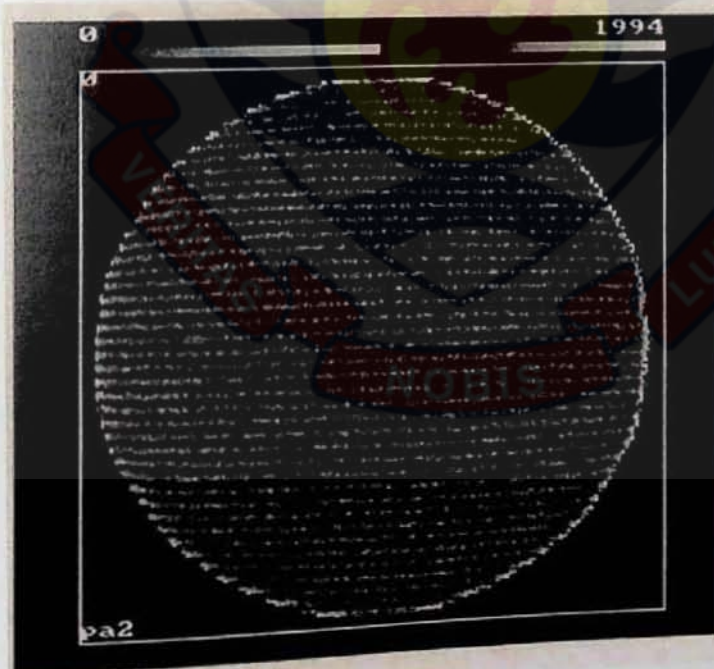


Figure 87, QC -Picture No 9. PLES phantom bar (Parallel to X-axis) is used to check linearity of the image This Picture has a high linearity, as the lines are almost straight.

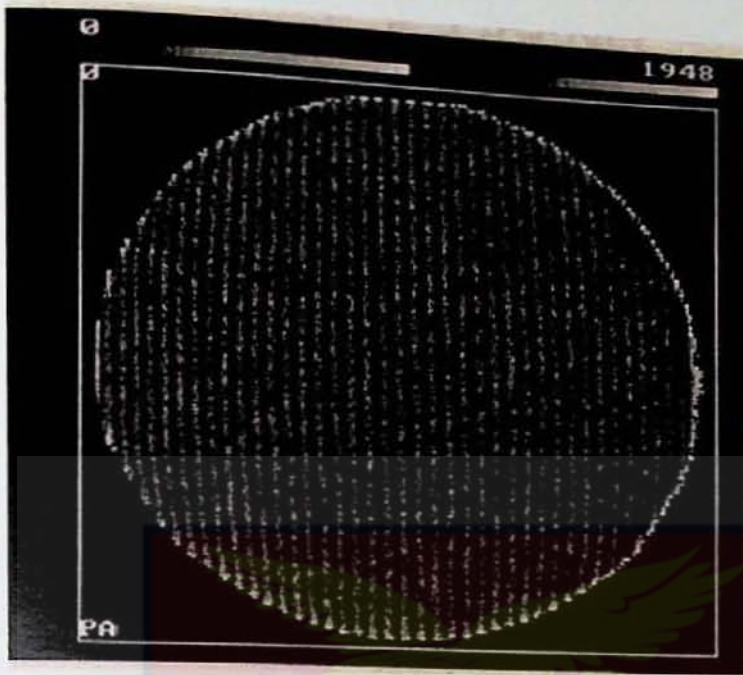


Figure 88, QC – Picture No. 10. PLES phantom bar (Parallel to Y-axis) is used to check linearity of the image. This Picture has a high linearity, as the lines are almost straight.

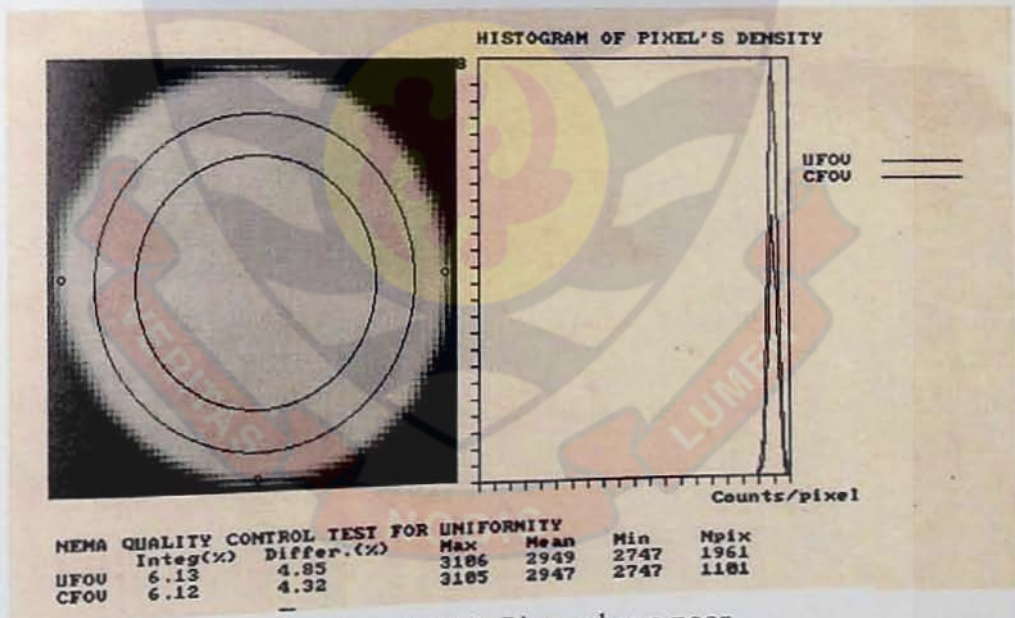


Figure 89: QC Picture No. 11. This Picture has a poor uniformity. The camera needs tuning. CFOV IU=6.12%; DU=4.32%

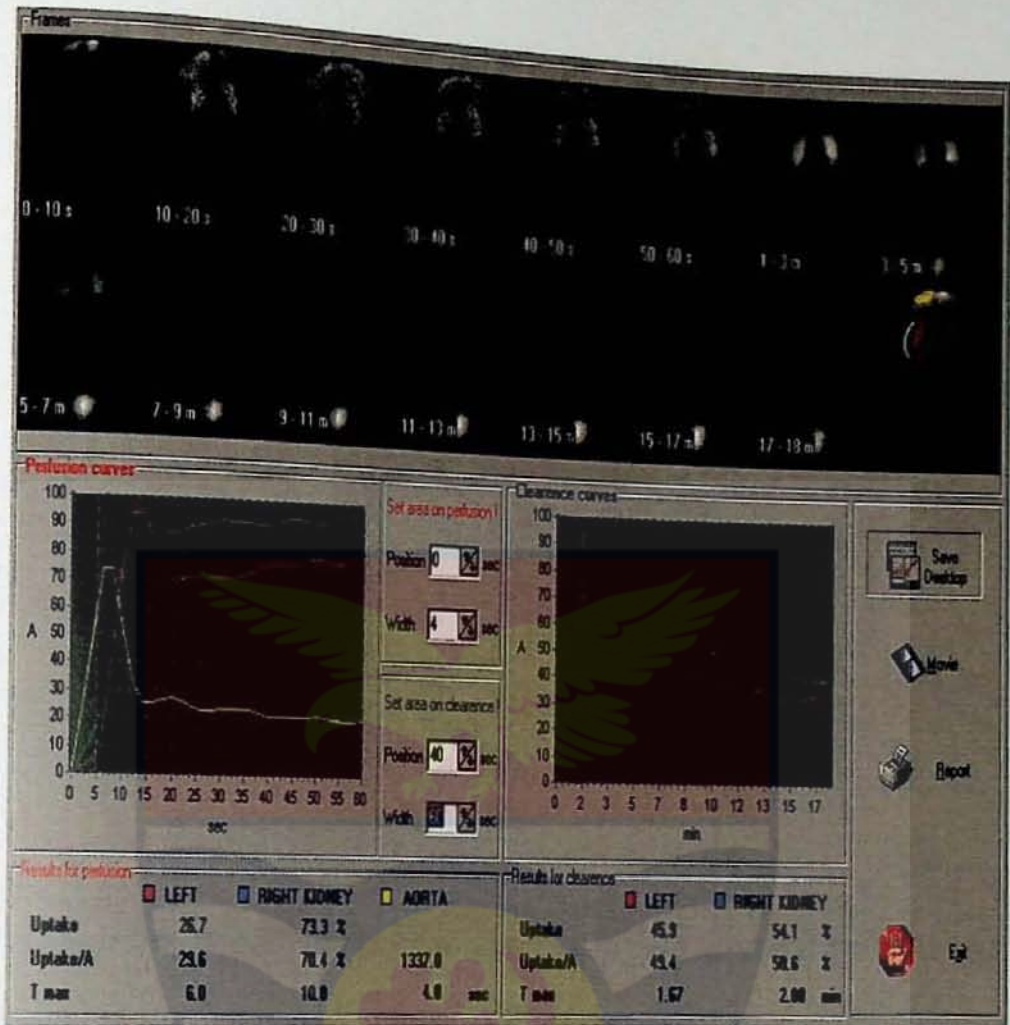


Figure 91: Report of one of the patients that was scanned with the Gamma camera after this work was completed. The picture shows a Kidney study report of one of the patients studied (Courtesy NMU, NCRNM, Korle Bu, 2009).

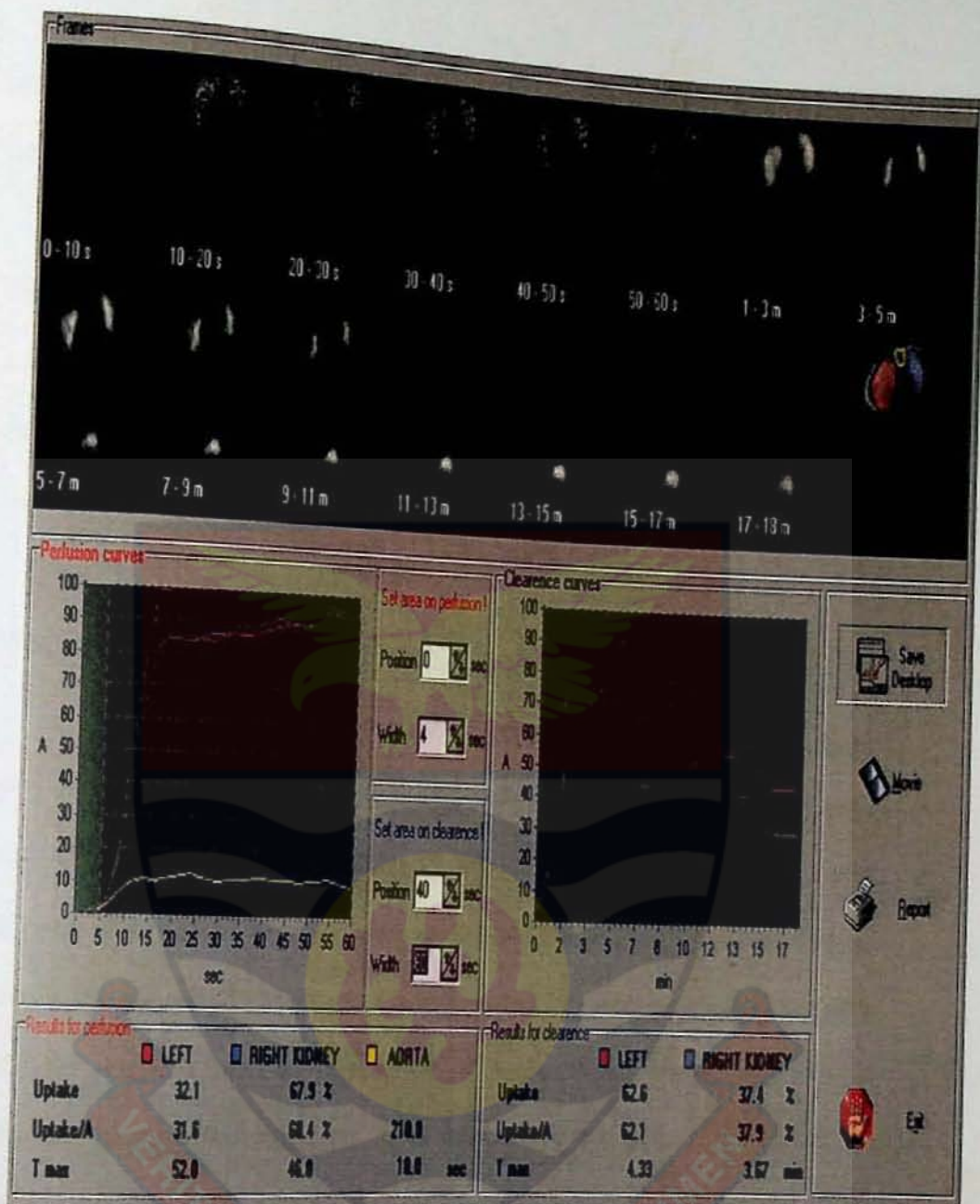


Figure 92: Another report of kidney studies after this work was completed. (Courtesy NMU, NCRNM, Korle Bu, 2009)

DISCUSSIONS

In all, 5 PMTs were rejected and 35 out of the 40 PMTs tested were found to be good. The LFOV (Large Field of View) Siemens gamma camera however requires 37 PMTs on its NaI(Tl) detector. so 3 additional PMTs were then measured for their gains and dark currents to make it possible to have the

required 37 PMTs for the continuation of the work. The PMTs were then placed on the detector by their gains.

After the characterization and placement of the PMTs on the detector, followed by the alignment and fine-tuning of the gamma camera, quality control pictures were then obtained (See Figures 79 – 92). The comparison of the pictures obtained with reported literature (NEMA standards) are also presented in this section.

Measurement of PMTs

In all, forty three (43) old PMTs were tested. 37 of the PMTs were sorted based on their gains, using the fabricated PMT (instrument) diagnostic tool, (Plate 4.4, Figure 71 and Figure 74). Bad PMTs were identified and rejected. The Results obtained after the measurements (testing) of the PMTs, justify the use of the PMT testing instrument as diagnostic tool to aid repairs of PMT related equipment in the field of medicine, nuclear or high energy physics, biology and chemistry. The device will be an important tool for technicians and engineers who work on gamma cameras, to reduce the down time of the gamma and SPECT cameras at Korle Bu teaching hospital.

Various researchers have conducted studies (for example, Barnhill *et al*, 2007; Becker, 2007; Akgun, 2005) on characterization of new PMTs for Cherenkov light detection. The present work on the other hand, aimed at extending the life span of existing instruments, i.e., gamma cameras by measuring, sorting and re-arrangement of PMTs on the detector to improve image quality. Whilst the 2000 tubes tested by Akgun *et al* (2005), for a CMS-

HF, forward calorimeter, 20 tubes were rejected mainly due to their high dark current which was $\approx 2\text{nA}$ at a gain of (10^4) . The present work detected and rejected three PMTs namely (PMT 21, PMT 24, and PMT34) because they measured high dark current (Figure 77). Incidentally, PMT 21 was already declared bad during the main measurement (Figure 61).

High dark current on Gamma camera performance

As previously stated under PMT dark current, high PMT dark current did not appear as background noise (radiation) during gamma camera image acquisition. It did however affect the stability of the tubes around it. The single channel Analyzer in the gamma camera ensures that all signals that were above all below the radio isotope energy (140 keV for $^{99\text{m}}\text{Tc}$) which was used in the investigation were all rejected and only the 140 keV signals were amplified by the analyser. As the tube becomes unstable, it disturbs the image surrounding PMTs to produce the photopeak energy also called the unblank signal and X, Y positions signals.

Background radiation occurs when there is no radionuclide point source placed near or under the gamma camera and yet some activity like low flood in region of 3-6 kc/s is observed on the scope or screen of the computer or the oscilloscope. Background radiation is often attributed to hand or body contamination during eluting of radionuclide from the $^{99\text{m}}\text{Tc}$ generator or handling of contaminated syringes or materials.

PMT output with preamp connected

When the preamplifier (Figure 74) was connected to the PMT output as was the situation in the detector assembly of the gamma cameras, the behaviour of the PMT output changed completely as is evident in Figure 73 and Figure 74. For example measurement of PMTs gain with preamplifier discounted from the PMT output, saw PMT 12 to have the highest gain 9.75 Vp-p as shown in (Figure 72), but when the preamplifier was connected, the gain was just over (0.341 Vp-p) (Figure 73) for PMT 12. PMT 3 output had the highest gain as shown in the graph of Figure 73 (i.e., when the preamp was connected to the PMT output).

The sharp contrast between the results obtained for the measurement of PMTs with and without preamps connected revealed the faulty preamps which prompted their repairs and subsequent increased in their output voltage. The revelation of faulty preamps also attest to the fact that the PMT instrument as an important tool to aid repairs of PMT based scientific and medical equipment.

Effect of characterization and sorting of PMTs

The characterization and sorting of PMTs were very important to achieve the required uniformity and resolution of the camera. Tuning the PMTs to the radionuclide energy (140 keV) used for studies required the knowledge of the gain of the PMT concerned for proper positioning of the PMT on the surface of the detector, as it would be extremely difficult to tune the camera

when the PMTs with highest gains were placed edges of the camera and the weak PMTs were placed at the centre of the detector.

Quality control pictures obtained

Modern gamma camera systems typically have integral and differential uniformities between 4-7%. Non-uniformities of this magnitude can generate ring artefacts in (planer) tomographic data, hence all planer (tomographic) systems apply an additional correction to the raw image data, called uniformity (flood) or (sensitivity correction before reconstruction.

Following uniformity correction, a planer (tomographic) system in good working order will have values of differential uniformity in the range of 1.0-2.5%, with values of integral uniformity a little higher at 1.5 – 3.5%. (O'Conner, ND,)

Quality control pictures obtained after boards' alignment and PMT fine-tuning are shown in Figure 79 to Figure 92. Before the best picture (image) shown in Figure 82, with CFOV – IU=1.164%; and DU=1.13%; was obtained, fine-tuning and image acquisition was continuously performed, which gave the pictures in Figure 83, Figure 84, and Figure 85.

After the best flood image of Figure 79 and Figure 82, was obtained, there was a need to find the intrinsic (without the collimator installed) spatial resolution of the camera. So a quadrant phantom bar with lead bar sizes of 2.0 mm, 2.5 mm, 3.0 mm. and 3.5 mm was installed and pictures were taken. The pictures produced are shown in Figure 84 to Figure 86. From Figure 85, the bars that were well resolved by the camera are 3.5 mm, 3.0 mm and 2.5 mm.

The 2.0 mm bars were not resolved. Therefore this camera has 2.5 mm spatial resolution. <https://ir.ucc.edu.gh/xmlui>

The next assignment was to find the linearity of the camera. A parallel lines equal space (PLES) phantom bar was used to check for the linearity of the camera. The phantom bar was installed and acquisition as described below was performed. The pictures obtained after acquisition are shown in Figure 87 (parallel to y-axis) and Figure 88 (parallel to x-axis).

From the pictures, it is seen that the camera has very good linearity as the lines are straight with little bending in both x and y axis. Pictures in Figure 89 and Figure 90 have very poor uniformity, and camera with such pictures requires repairs and tuning. These two images were included to show images with poor uniformities, or good pictures from bad ones.

Comparison of images between this work and NEMA standards (1994)

NEMA

Example 1: Symmetric 20% energy window



Figure 93 NEMA Flood Uniformity Image, ^{99m}Tc 3 million counts, 20% windows

Routine intrinsic uniformity image, ^{99m}Tc , 3 million counts, 20% energy window set symmetrically over the 140 keV photopeak of ^{99m}Tc .

Results: The image shows good uniformity.

Comments: The most basic and sensitive routine QC test of a gamma camera is that of uniformity. This must be performed carefully (preferably daily before using the camera for clinical studies), it must be critically evaluated and any necessary action must be undertaken before further imaging takes place.



Figure 94: This work flood uniformity image after fine tuning is compared with the NEMA standard image example 1. A careful at the two images show that this work result has better flood uniformity than the NEMA standard

Example 2: Poor spatial linearity and spatial resolution — ^{99m}Tc and ^{67}Ga

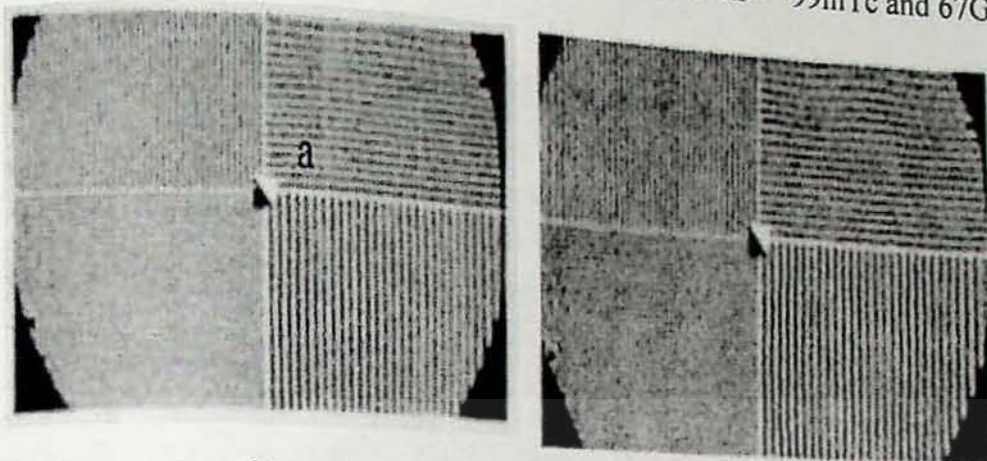


Figure 95 A): ^{99m}Tc (20% energy window)

Figure 95 B): ^{67}Ga (sum of three photopeaks — 20% over 93, 184 and 300 keV)

Figure 95 shows NEMA standard showing examples of images with poor spatial linearity and resolution for ^{99m}Tc and ^{67}Ga radioisotopes. The wavy lines marked (a) of Figure 95 B), shows very poor spatial linearity for ^{99}Tc . Intrinsic spatial resolution images obtained using a four quadrant bar pattern. This was a new, modern camera system.

Results: The wavy lines show very poor spatial linearity for ^{99m}Tc , and even worse for ^{67}Ga . There is also a loss of spatial resolution in the vicinity of the PMTs.

Comments: This example demonstrates the usefulness of obtaining intrinsic spatial resolution/linearity images for radionuclides other than ^{99m}Tc , although the poor performance with ^{99m}Tc is indication enough that there is a problem. This test with ^{67}Ga is also very sensitive to multiple window spatial registration errors (see also Section 2.4). If the images for the three energy windows are

not registered accurately, then misalignment will result in blurring of the line pattern.



Figure 96: This work result showing Phantom bar with good linearity and spatial resolution as compared with the NEMA example of 2.3.1.12 above.

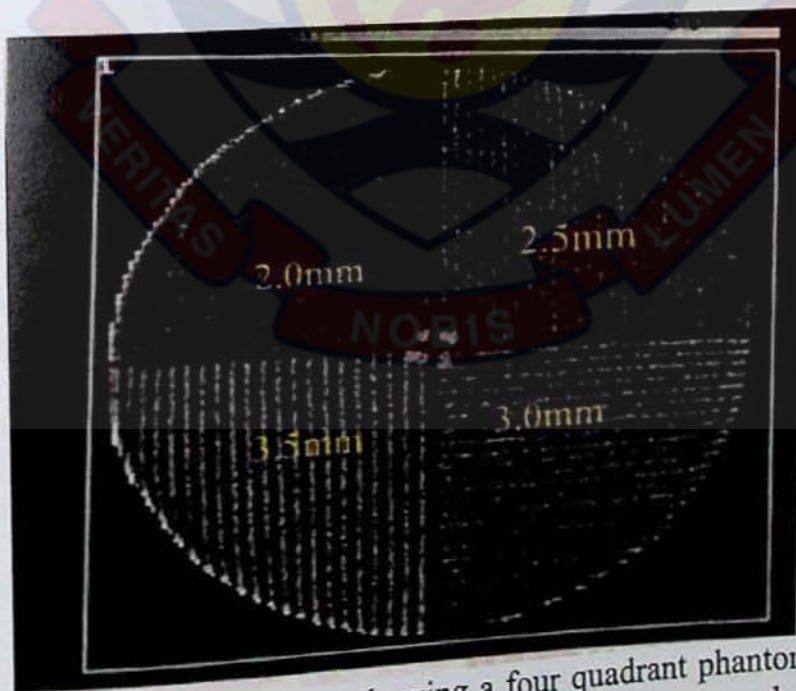


Figure 97: This work's result showing a four quadrant phantom bar pattern. From the image the bars and spaces up to the 2.5mm can be seen clearly (intrinsic spatial resolution). The bars are also straight not curving (linearity). This image is compared with NEMA example image of 2.3.1.5 below.

Example 3: Qualitative spatial resolution/linearity — four quadrant bar pattern

Two intrinsic resolution/linearity images obtained with a four quadrant bar pattern on two different scintillation cameras. ^{99m}Tc point source at 5 FOV distance, 15% energy window, 3 million counts each image.

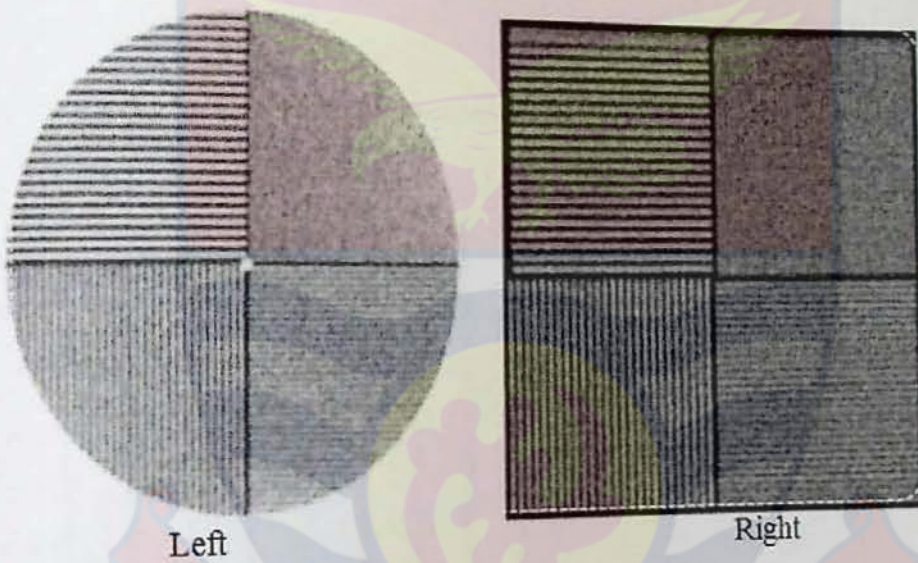


Figure 98: NEMA qualitative spatial resolution and Linearity
 Left: Older camera, 9.5 mm (3/8 inch) thick crystal
 Right: New camera, 15.8 mm (5/8 inch) thick crystal

Results: The four quadrant bar pattern is suitable for checking both linearity and spatial resolution, since one quadrant is barely resolvable (upper right quadrant in these images). The linearity is satisfactory. The spatial resolution does not show any specific problems, although in the upper right quadrant of the left image it appears to decrease slightly towards the edge of the FOV. Note that in the thicker crystal the changes in spatial resolution are quite obvious compared with the thinner crystal.

Comments: In order to check all quadrants of the FOV in both x and y directions with the smallest recognizable bar spacing, one needs to image the phantom in eight positions: four positions are imaged with the phantom rotated through 90° , and then the phantom is turned over and the procedure is repeated.

The bar spacing should be matched to the scintillation camera spatial resolution such that the bar spacing of one quadrant is just barely resolvable. Note any loss of spatial resolution related to the PM tube position.

Example 4: NEMA slit pattern — non-linearity

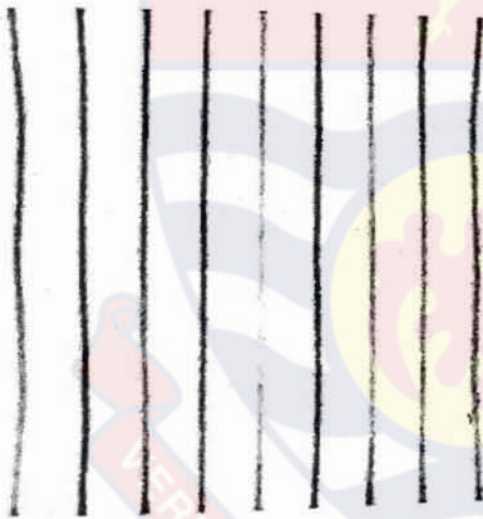


Figure 99: Intrinsic image of the NEMA slit phantom pattern (1 mm wide slits in a sheet of lead with separations of 30 mm) using a distance point source of ^{99m}Tc .

Results: Image shows distinct non-linearity of the lines. Also, the lines have different intensities.

Comments: The slits in the NEMA slit phantom must have uniform width in order to assess the uniformity of the lines imaged. The largest available matrix size must be used in order to ensure that one has several pixels over each line for purposes of quantification of the spatial resolution.

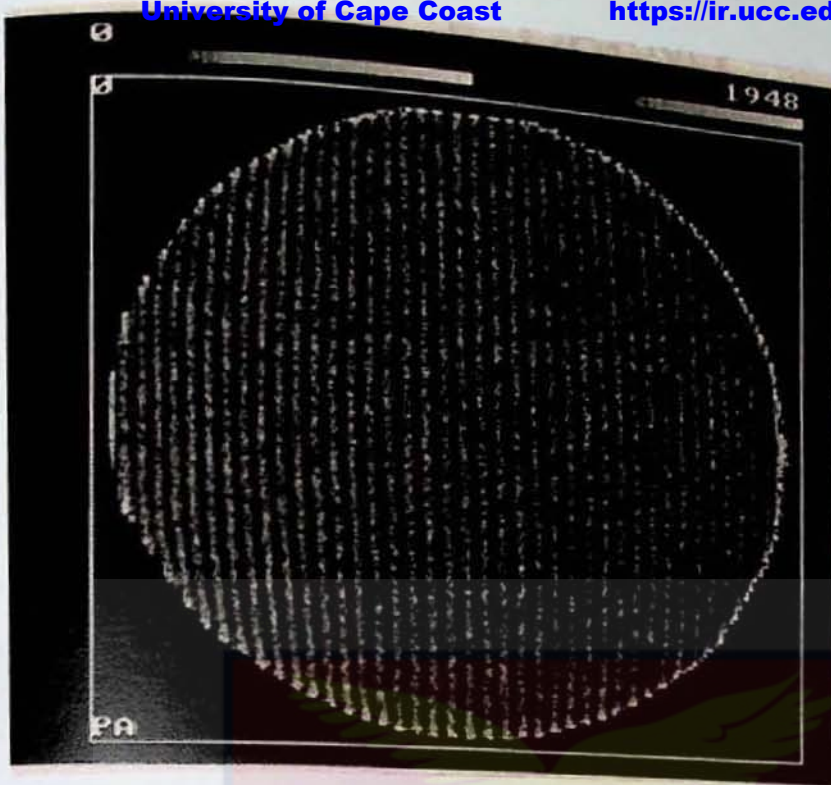


Figure 100: (This work) Parallel lines Equal Spaces (PLES) phantom bar was used to check linearity of the image, and is compared with the NEMA example 2.3.1.2 (Figure 99) above which has no linearity because the lines are curvy and the lines width are not the same. This work image has good linearity (the lines are straight even at the edges of the image).

Image Acquisition

Whenever a picture is taken in this work, it implies that an image acquisition has taken place. To perform image acquisition, the analyser isotope level was set to the radioisotope energy concerned, which in this work was technetium-99m (^{99m}Tc) energy of 140 keV, and the analyser window was set to 20 %. A 100 μCi (3.7 MBq) activity is placed on top of the camera as indicated in Figure 81. The acquisition software is then run for a 16 million counts at a count rate of (20-30 kc/s), to be acquired and stored into the computer. The picture was then printed to produce the pictures in Figure 82 to Figure 91.

Calculation of gamma camera integral and differential uniformity on quality control picture No.1

The (QC) pictures taken after sorting and arranging the PMTs (Figure 78), boards' alignment and fine-tuning resulted in a significant improvement in the image quality of the gamma camera. The pictures are shown in Figure 82- Figure 90 for this work. Figure 91 and Figure 92 were added to show poor pictures (high uniformity values). The highest uniformity achieved by the first picture (Figure 82). Integral Uniformity formula is given by NEMA (2007), as:

$$\text{Integral Uniformity} = {}^{99m}\text{Tc} = \frac{\text{Max} - \text{Min}}{\text{Max} + \text{Min}} \times 100\% \quad 6.1$$

Where Max – Maximum count per pixel

Min – Minimum count per pixel

$$\text{CFOV, Integral Uniformity (IU)} = \frac{5135 - 4969}{5135 + 4969} = 0.0164 \times 100\% = 1.64\% \\ = 1.64\%$$

as stated in Figure 82.

$$\text{CFOV Differential Uniformity (DU)} = \frac{\text{high} - \text{low}}{\text{high} + \text{low}} \times 100\% \quad 6.2$$

(NEMA, 2007).

Where *high* and *low* refer to the highest and lowest count /pixel values respectively, within a five – pixel segment in a row or column.

Since the high and low counts are not indicated in the picture of Figure 82. Therefore there is a need to find the values to give us the DU of 1.13%.

From equation (6.2),

$$DU = \frac{y-x}{y+x} \times 100\%$$

where $y = \text{high}$; $x = \text{low}$, and better still, if $y-x = k$ and $y = k+x$, $DU =$

$$\frac{k}{(k+x)+x} \times 100\% = 1.13\% = \frac{k}{k+2x} = 0.0113$$

Let $0.0113 = \delta$

$$x = \left(\frac{k}{\delta} - k \right) / 2$$

Suppose the count difference between the high and low for the CFOV is =50, then

$$x = \left(\frac{50}{0.0113} - 50 \right) / 2 = 2187.4;$$

$$x = 2187.4 \text{ and } y = x + k = 2187.4 + 50 = 2237.4$$

$$DU (\text{CFOV}) = \frac{2237.4 - 2187.4}{2237.4 + 2187.4} \times 100\% = \frac{50}{4424.4} = 0.0113 \times 100\% = 1.13\%$$

$$\text{UFOV, Integral Uniformity} = \frac{5135 - 4966}{5135 + 4966} = 0.0167 \times 100\% = 1.67\%$$

The same method could be used to find the low and high values to give DU for the Useful Field of View (UFOV) which was $DU = 1.26\%$,

Comparison of images uniformities obtained in this work with modern gamma cameras

Sanchez *et al*, (2004), designed and tested a portable gamma camera and obtained a differential uniformity of 8.1% for both UFOV and CFOV and obtained 14.1 % and 4.7 % UFOV and CFOV, respectively for integral

uniformity. To this end, Sanchez *et al* (2004), further compared his values obtained with those reported for small field of view gamma cameras. Values of 25% by Williams *et al*, (2000), 29% by Mathews, (1997) and 18%, by Maini *et al*, (1999) were reported for the UFOV integral uniformity, while 23%, by Mathews, (1997) and Williams, *et al*, (2000) and 13.5%, by Maini, (1999) values were obtained for the differential uniformity. In the work of Sanchez *et al* (2004) they stated that their gamma camera showed better uniformity behaviour when compared with other developed gamma cameras.

One clinical system, the Siemens Multi-SPECT3, an older scintillator based system, requires integral uniformity in the central field of view (CFOV) to be lower than 3.5% or re-calibration must be done (Kuikka *et al*, 1993). Other newer system, such as CZT system intended for use in clinical scintimammography, reported integral uniformity in the useful field of view to UFOV to be 2 to 3% by Mueller *et al*, (2003).

On the other hand, a newly developed preclinical SPECT system using a CdTe detector was found to have integral and differential uniformities of 28.5 % and 26.3 % respectively by Ogawa *et al*, (2009). Johnson *et al*, (2011) using position sensitive strip HPGe, with uniformity <1 %, precise integral uniformity = 0.35 % for both UFOV and CFOV; and differential uniformity = 0.27 % for both UFOV and CFOV.

As seen from above, Kuikka *et al*, (1993) work on an old Siemens Multi-SPECT which was similar to old old Siemens gamma camera used in the present study, stated that an integral uniformity in the central field of view should be less than 3.5%, else a re-calibration (PMT alignment) must be done.

The result for the central field of view was 1.64 %, which is far below the 3.5% by Kuikka *et al*, (1993), noting that (the lower the value the better the uniformity).

Apart from Johnson *et al* (2011) who measured uniformity for both CFOV and UFOV <1 %, using a High purity germanium detector (HPGe), none of the new small cameras intended for scinti-mammography reported above got near the values obtained in the present work. Mueller *et al* (2003), CZT camera -2 to 3 %, and Ogawa *et al* (2009) 28.5 % and 26.3 % for integral and differential uniformity, respectively.

Clinical studies Image (Picture) of a patient (Courtesy of NMU, NCRNM, Korle Bu, 2009)



Figure 101: A typical Kidney study analysis of the Gamma camera after this work was completed at the NMU, Korle Bu Teaching Hospital, 2009).

After this work was completed in 2009, the camera was used for Clinical studies of patients that visited the Nuclear Medicine Unit (NMU). Among the studies were two patients that reported for Kidney (Renal) studies (Figure 91 and Figure 92) one of which is re-produced here Figure 101. The perfusion and clearance curves for both left (Red) and right (blue) are shown.



CHAPTER SIX

SUMMARY, CONCLUSIONS AND RECOMMENDATIONS

Overview

This chapter presents the summary of the work, conclusions and recommendations

Summary of key Points

1. Design and fabrication of PMT testing instrument and its accessories
 - I. PMT instruments' casing was designed and fabricated
 - II. Low and HV supplies were designed and constructed
 - III. The oscilloscope circuit that was used to generate the 31 kHz rectangular pulses was also designed and constructed
2. Forty PMTs were characterized by their
 - I. Quantum efficiencies (voltage gain)
 - II. Dark currents
3. Forty preamplifiers for the PMTs were tested and the faulty ones repaired.
4. The sorted PMTs were placed on the NaI (Tl) detector. The PMT was placed at the centre.
5. The Gamma camera processor boards were all aligned and the PMTs were finely tuned to bring their energy to the photopeak (140 keV) of the ^{99m}Tc radio isotope.

6. The quality control pictures were taken and compared with NEMA standards, which showed an appreciable increase in picture quality.
7. The gamma camera was then used for clinical studies. Figures 91 and 92 show kidney study reports for two patients after the gamma camera alignment and fine tuning. The pictures were produced with a kind courtesy of NMU, NCRNM, Korle Bu (2009).

PMT diagnostic tool

- 1 The PMT testing instrument can be used as a diagnostic tool to aid repair of PMT related instruments or equipment. In research and scientific institutions
- 2 The PMT instrument can also be used to extend the life span of gamma cameras, spectrophotometers, and other PMT related instruments in hospitals. Once the characteristics of a PMT are known (QE, maximum High Voltage, Dark current, etc) a PMT with the same characteristics can be bought from any company not necessarily the manufacturer, to service the gamma camera.

CONCLUSIONS

The study has significantly shown for the first time, an enhanced improvement of image quality which compares very with NEMA standards (NEMA, 1994), in terms of image uniformity, spatial resolution and linearity was achieved. Bad PMTs were identified during the measurements and dark currents of the PMTs were also measured and those with high dark currents were also rejected. Therefore, we posit that the PMT instrument can be used to

test any Scientific or Medical equipment that uses PMT as its light detector. To this end, we are able to substantiate that, the aims and objectives of the thesis work have been fully achieved.

RECOMMENDATIONS

With the fast changing technology, manufacturers of medical and scientific equipment are regularly updating and upgrading their equipment. Some of the upgrading may require the user to buy additional software and (or) hardware to use with their equipment. Some of these software and hardware are very expensive and not all developing countries can afford to buy.

Frequent power fluctuations causes the equipment to breakdown often in Africa and getting the service engineer to come to Africa to repair the equipment is a big problem. Also the manufacture stops supplying of spare parts after few years of usage and will be asked to buy the latest model of the equipment, as such the equipment becomes a "white elephant" after few years of usage.

It is therefore, recommended for developing countries:

1. to train new generation of technicians who can design and upgrade their equipment without relying on the manufacturer.
2. should encourage their technicians and engineers to design and build gadgets that will enable old equipment meet the present research needs of scientists.

REFERENCES

- Aintablian, H. O. and Hill, H.W., (1994). A new single phase AC to DC harmonic reduction converter based on the voltage –doubler circuit. *IEEE, 1*, 452 – 457.
- Akgun, U., Ayan, A. S., Brueckun, P., Duru, F., Gulmez, E., Mestvirishvilli, A., Miller, M., Olson, J., Onel, Y., and Schmidt, I. (2005). Complete tests of 2000 Hamamastu R7525HA phototubes for the CMC-HF forward collider. *Nuclear Instruments and Methods in Physics Research, A*. 550, 145-156.
- Allen, J. S. (1947). An improved electron multiplier particle counter. *Review of Science Instrumentation*, 18 (10), 739–749.
- American Association of Physicists in Medicine. (1980). *Scintillation Camera Acceptance Testing & Performance Evaluation (Report No. 6)*. Chicago, USA.:AAPM
- American Association of Physicists in Medicine. (1981). *Computer Aided Scintillation Camera Acceptance Testing (Report No. 9)*. New York, USA.:AAPM
- American Association of Physicists in Medicine. (1987). *Rotating Scintillation Camera SPECT Acceptance Testing and Quality Control (Report No. 22)*. New York, USA.:AAPM
- Anger, H. O. (1958). Scintillation camera. *Review of Science Instrumentation*, 29, 27 – 33.

- Anger, H. O. (1964). Scintillation camera with multi-channel collimators. *Journal of Nuclear Medicine*, 5, 515 – 531.
- Anger, H. O. (1966). Survey of radioisotope cameras. *Journal of Nuclear Medicine*, 5, 311 – 334.
- Apker, L., Taft, E., and Dickey, J. (1948). Photoelectric emission and contact potentials of semiconductors. *Physic Review*, 74, 1462-1474.
- Arisaka, K., (2000). New trends in vacuum-based photon detectors. *Nuclear Instrument and Methods A (442)*, 80.
- Avset, B. S., Ellison, J., Evensen, L., Hansen, T. E., Roe, S., and Wheadon, R. (1990). Silicon drift photodiodes. *Nuclear Instruments & Methods in Physics Research, A (288)*, 131 – 136.
- Barnhill, D., Suarez, F., Arisaka, K., Garcia, B., Gongora, J.P., Lucero, A., Navarro, I., Ohnuki, T., Risi, A., and Tripathi, A. (2007). Testing of photomultiplier tubes for use in the surface detector of the Pierre Auger observatory. Retrieved from www.sciencedirect.com.
- Bates, C. W., and Clayton, W. (1981). Photoemission from Ag-O-Cs. *Physical Review Letters*, 47 (3), 204-208.
- Beekman, F. J., Van der Have, F., Vastenhouw, B., Annemarie, J. A., Van der Linden, Van Rijk, P. P. (2005). U-SPECT-I: A novel system for submillimeter-resolution tomography with radiolabeled molecules in mice. *Journal of Nuclear Medicine*, 46, 1194–1200.
- Beekman, F. J., and Vastenhouw, B. (2004). Design and simulation of a high-resolution stationary SPECT system for small animals. *Phys. Med. Biology*, 49, 4579-4592.

- Berglund, C. N. and Spicer, W. E. (1964). Photoemission studies of copper and silver: theory. *Physical Review*, 136 (4A).
- Blackett, P. M. S. and Occhialini, G.P.S. (1933). Some photographs of tracks penetrating radiation. *Proc. Roy Soc. London, ser A*, 139 (839), 699-726.
- Boylestad, R. L. and Nashelsky, L. (1999). *Electronic devices and circuit theory (7th ed.)*. Columbus, Ohio: Prentice Hall.
- Bradbury, S. M., Mirzoyan, R., Gebauer, J., Feigl, E., and Lorenz, E. (1997). Test of the new hybrid INTEVAC intensified photocell for the use in air Cherenkov telescopes. *Nuclear Instruments and Methods A*, 387, 45.
- Brownell, G. L., Burnham, C. A., Wilensky, S., Manonow, S., Kaemi, H. and Strieder, D. (1969). *New development in positron scintigraphy and the application of cyclotron-produced positron emitter Medical Radioisotope Scintigraphy*. IAEA Proceedings of symposium station Salzburg, Austria, (1968) Vienna, IAEA, 163-176.
- Brice, S. J., Bugel, L., Conrad, J. M., Fleming, B., Gladstone, L., Hawker, E., Killewald, P., May, J., and McKenney, S. (2006). Photomultiplier tubes in the MiniBooNE experiment. *Nuclear Instruments and Methods in Physics Research, A* (562), 97-109.
- Bruining, J. H. (1954). *Physics and applications of secondary electron emission*. USA.: McGraw-Hill Book Co., Inc.
- Bumham, C. A., Bradshaw, J., Kaufmann, D., Chesler, D., and Brownell, G. L. (1983). A positron tomograph employing a one dimension BGO scintillation camera. *IEEE Transactions on Nuclear Science*, 30, 661-664.

- Bumham, C. A., Bradshaw, J., Kaufmann, D., Chesler, D. A., Stearns, C. W., and Brownell, G. L. (1985). Design of a cylindrical shaped scintillation camera for positron tomography. *IEEE Transactions on Nuclear Science*, 32, 889-893.
- Burle Industries, Inc. (1980). *Photomultiplier Handbook*. Maracas, USA.: Burle Technologies Inc.
- Burle Industries, Inc. (1980). *Photomultiplier Handbook*. Retrieved from <http://www.burle.com/cgi-bin/byteserver.pl/pdf/Photo.pdf>.
- Bushberg, J. T., Seibert, J. A., Leidholdt, J. R., Edwin M., and Boone, J. M. (1994). *The Essential Physics of Medical Imaging*. USA.: Williams & Wilkins.
- Campbell, N. R. (1931). The photoelectric emission of thin films. *Philos Mag.*, 12 (75), 173-185.
- Caroli, C., Lederer-Rozenblatt, D., Roulet, B., and Saint-James, D. (1973). Inelastic in photoemission: Microscopic formulation and qualitative discussion. *Physical Review*, 8, 4552-4569.
- Cassen, B., Curtis L., Reed C., and Libby, R. (1951). Instrumentation for ^{131}I use in the studies. *Nucleonics*, 9, 46-50.
- Cassen, B., Curtis, L., and Reed, C. W., (1950). A sensitive direction gamma ray detector. *Nucleonics*, 6, 78-80.
- Causser, D. A. (1975). The design of parallel hole gamma camera collimators. *International Journal of Applied Radiation and Isotopes*, 26, 355-462.
- Chapman, D., Newcomer, K., Berman, D., and Waxman, A. (1979). Half-inch versus quarter-inch Anger camera technology: resolution and

- sensitivity differences at low photopeak energies. *Journal of Nuclear Medicine*, 20, 610-611.
- Cherry, S. R., Sorenson, J. A. and Phelps, M. E. (2003). *Physics in nuclear medicine (3rd ed)*. USA.: Saunders, Elsevier Science.
- Compton, A. H. (1923). The spectrum of scattered X-rays. *Physical Rev*, 2, 409.
- D'Ambrosio, C., and Leutz, H. (2003). Hybrid photon detector. *Nuclear Instruments and Methods in Physics Research, A (501)*, 463-498.
- Dwivedi, C. K., and Daigavane, M. B. (2011). Multi-purpose low cost DC high voltage generator (60 kV output), using Cockcroft-walton voltage multiplier circuit.
- Early, P. J. and Sodee, D. B. (1985). *Principles and practice of nuclear medicine*. USA.: C. V. Mosby Company.
- Ehrenreich, H. and Philipp, H. R. (1962). Optical properties of Ag and Cu. *Physical Review*, 128, 1622-1629.
- Einstein, A. (1905). On a heuristic point of view concerning the production and transformation of light. *Ann Phys*, 17, 132-148.
- Engstrom, O. (1977). Properties of Crystalline Silicon. *Applied Physics*, 48, 1806.
- Engstrom, R. (1980). *RCA Photomultiplier Handbook*. USA.: RCA Corporation.
- Farr, R. F., and Allisy-Roberts, P. J. (1999). *Physics for Medical Imaging*. USA.: WB Saunders.

- Flower, M. A., Adam, I., Masoomi, A. M., and Schlesinger, T. (1986). Special collimators for quantitative imaging of high activity levels of Iodine-131. *Br. J. Radiol*, 59, 836-837.
- Fowler, R. H. (1931). The Analysis of photoelectric sensitivity curves for clean metals at various temperatures. *Physical Review*, 38, 45-56.
- Flyckt, S. O. and Marmonier, C. (2002). *Photomultiplier tubes: Principles and applications*. Brive, France.: Philip Photonics.
- Funk, T., Parnham, K. B., Patt, B. E., Li, J., Iwanczyk, J. S., Iwata, K., and Hwang, A. B. (2003). A new CdZnTe-based gamma camera for high resolution pinhole SPECT. *IEEE Nuclear Science Symposium Conf Rec.* 4, 2320-2324.
- Geiger, H., and Marsden, E. (1913). Deflection of α particles through large angles. *Philos, Mag.* 25 (148), 604.
- Ghosh, C., and Varma, B. P. (1978). Secondary emission from multi-alkali photocathodes. *Journal of Applied Physics*, 49, 4554-4555.
- Gobeli, G. W. and Allen, F. G. (1962). Direct and Indirect excitation processes in photoelectric emission from silicon. *Physical Review*, 127, 141-149.
- Gorlich, P. (1936). About composite transparent photocathodes. *Z Physics*, 101, (5-6), 335-342.
- Gramsch, E., Gullikson, E., Moses, W. W., and Avila, R. (1996). Operating characteristics of avalanche photodiodes for PET systems. *IEEE Nuclear Science Symposium Conference Record*, 2, 768-772.
- Gruber, G. L., Choon, W. S., Moses, W. W., Derenzo, S. E., Holland, S. E., Pedrali-Noy, M., Krieger, B., Mandelli, E. Meddeler, G., and Wang, N.

- W. (2001). A compact 64-Pixel CsI(Tl)/Si PIN photodiode imaging module with IC readout. *IEEE Transactions on Nuclear Science*, (submitted for publication) 2001.
- Guru, S. V., Valentine, J.D., Wehe, D.K., and Knoll, G.F. (1994). Monte Carlo modeling of multiple-hole collimator for high energy gamma ray imaging. *IEEE Transactions on Nuclear Science*, 41 (4), 898-902.
- Hall, L. H., Bardeen, J., and Blatt, F. J. (1954). Infrared absorption spectrum of germanium. *Physical Review*, 559-560.
- Hallensleben, S., Harmer, S. W., and Townsend, P. D. (1999). Limitations on the enhancement of photomultiplier quantum efficiency through multiple total internal reflection. *Journal of Applied Physics*, 32, 623-628.
- Hallwachs, W. (1888). Uber den Einfluss des Lichtes auf elektrostatisch geladene Korper. *Ann Phys Chem*, 269, 301-312.
- Hamamatsu Photonics. (1999). Photomultiplier tubes: Basics and applications. *Editorial Committee*, Japan.
- Hamamatsu Photonics. (2005). Photomultiplier tubes and assemblies for scintillation Counter and High Energy Physics. Japan.
- Hamamatsu Photonics. (2006). Photomultiplier tubes basics and application (3rd ed.). Japan.
- Hertz, H. (1887). Ueber einen Einfluss des ultravioletten Lichtes auf die electrische Ent-ladung, *Annalen der Physik*, 267, 983.
- Hine, G. J. (1967). *Instrumentation in Nuclear Medicine*. Academic Press

- Hoffer, R. (1964), Construction of a high-efficiency, low-energy collimator. *Medical Radioisotope Scanning*, 1, 233-241.
- Holland, S. E., Wang, N., and Moses, W. W. (1997). Development of noise, back-side illumination silicon photodiode arrays. *IEEE Transactions on Nuclear Science*, 44, 443-447.
- Husak, V. and Pernova, V. (1969). The design of collimators for radioisotope scanning. *Physics in Medicine and Biology*, 14 (2), 233-244.
- Iams, H. E., and Salzberg, B. (1935). The Secondary Emission Phototube, Proc. *IRE*, 23, 55-64.
- IAEA Human Health Series No. 6. (2009). Quality Assurance for SPECT systems. Vienna, Austria.
- IAEA Human Health Series (2003). Quality control Atlas for scintillation camera systems. *IAEA Library Catalogue Pub.*, Vienna, Austria.
- Institute of Physics and Engineering in Medicine. (2003). *Quality Assurance in Gamma Camera Systems. Rep. 86*. York: IPEM.
- International Electrotechnical Commission. (1971). *Measurement of Photosensitive devices, part4: methods of measurement of photo-multipliers*, (IEC 60306-4th ed.). 1.0b
- International Electrotechnical Commission (1998). *Radionuclide Imaging Devices: Characteristics and Test Conditions — Part 2: Single Photon Emission Computed Tomographs. Rep. IEC 60789-2*. Geneva: IEC
- International Electrotechnical Commission (1998). *Radionuclide Imaging Devices: Characteristics and Test Conditions — Part 3: Gamma*

- Camera Based Wholebody Imaging Systems. Rep. IEC 61675-3.*
Geneva: IEC
- International Electrotechnical Commission (2004). *Radionuclide Imaging Devices — Characteristics and Test Conditions — Part 2: Single Photon Emission Computed Tomographs, Amendment 1. Rep. IEC 60789-2-am1.* Geneva: IEC
- International Electrotechnical Commission (2005). *Medical Electrical Equipment — Characteristics and Test Conditions of Radionuclide Imaging Devices — Anger Type Gamma Cameras. Rep. IEC 60789, (3rd ed.).* Geneva: IEC
- Izaguirre, W. E., Sun, M., Vandehei, T., Despres, P., Huang, Y., and Funk, T. (2006). Evaluation of a large pixellated cadmium zinc telluride detector for small animal radionuclide imaging. *IEEE Nuclear Science Symposium Conference Records*, 6, 3817–3820.
- John, C. S. (1993). Circuit topologies for single phase, Voltage–doublers Boost rectifiers. *IEEE Trans. Power Elect.*, 8 (4).
- Johnson, L. C., Campbell, D. L., Hull, E. L. and Peterson, T. E. (2011). *Characterization of high purity germanium detector for small animal animal, SPECT.9*
- Joseph, M. B. (2001). Using rectifiers in voltage multipliers circuits, General Semiconductor. Retrieved from www.eettaiwan.com/ARTICLES/.../2001JUN14_AMD_AN2009.PDF
- Kane, E. O. (1962). Theory of Photoelectric emission from semiconductors. *Physical Review*, 127, 131-141.

- Kastis, G. A., Barber, H. B., Barrett, H. H., Balzer, S. J., Lu, D., Marks, D. G., Stevenson, G., Woolfenden, J. M., Appleby, M. and Tueller, J. (2000). Gamma-ray imaging using a CdZnTe pixel array and a high-resolution, parallel-hole collimator. *IEEE Transactions on Nuclear Science*, 47, 1923-1927.
- Kastis, G. A., Wu, M. C., Balzer, S. J., Wilson, D. W., Furenlid, L. R., Stevenson, G., Barber, H. B., Barrett, H. H., Woolfenden, J. M., Kelly, P, and Appleby, M. (2006). Tomographic small-animal imaging using a high-resolution semiconductor camera. *IEEE Transactions on Nuclear Science*, 49, 172-175.
- Kastis, G. A., Wu M., Balzer, S. J., Wilson, D. W., Furenlid, L. R., Stevenson, G., Barber, H. B., Barrett, H. H., Woolfenden, J. M., Kelly, P. and Appleby, M. (2002). Tomographic small animal imaging using a high-resolution semiconductor camera. *IEEE Transactions on Nuclear Science*, 49, 172-175.
- Keller, E. L. (1967). Optimum dimensions of a parallel hole multi-aperture collimators for gamma-ray cameras. *Journal of Nuclear Medicine*, 9, 233-235.
- Kim, H., Furenlid, L. R., Crawford, M. J., Wilson, D. W., Barber, H. B., Perterson, T. E., Hunter, W. C. J., Liu, Z., Woolfenden, J. M., and Barrett, H .H. (2006). SemiSPECT: a small-animal single-photon emission computed tomography (SPECT) imager based on eight cadmium zinc telluride (CZT) detector arrays. *Medical Physics*, 33, 465-476.

- Kittel, C. (1960). *Introduction to Solid State Physics*. New York: John Willey & Sons Inc.
- Kittel, C. (1962). *Elementary solid State Physics*. New York: John Willey & Sons Inc.
- Knoll, G. F. (2000). *Radiation Detection and Measurement (2nd Ed.)*. USA: John Wiley & Sons.
- Koller, L. R. (1930). Photoelectric emission from the films of Cesium. *Physical Review*, 36 (11), 1639-1653.
- Kowalski, E. (1970). *Nuclear Electronics*. Springer-Verlag
- Kubetsky, L. A. (1937). Multiple Amplifier. *Proc. Inst. Radio Eng.*, 25, 421-433.
- Kubo, N., Zhao, S., Fujiki, Y., Kinda, A., Motomura, N., Katoh, C., Shiga T., Kawashima H., Kuge, Y., and Tamaki, N. (2005). Evaluating performance of a pixel array semiconductor SPECT system for small animal imaging. *Ann Nucl Med.*, 19, 633-639.
- Kuffel, E., Zaengl, W. S., and Kuffel, J. (2000). *High Voltage Engineering Fundamental (2nd ed.)*. Butterworth: Oxford Ltd.
- Kuikka, J. T., Tenhunen-Eskelinen, M., Jurvelin, J., and Kiilianen, H. (1993). Physical performance of the Siemens MultiSPECT 3 gamma camera. *Nuclear medicine communications*, 14, 490-497.
- Lackas, C., Schramm, N. U., Hoppin, J. W., Engeland, U., Wirrwar, A., and Halling, H. (2005). T-SPECT: A novel imaging technique for small animal research. *IEEE Transactions on Nuclear Science*, 52, 181-187.

- Lage, E., Vaquero, J. J., Villena, J., de-Carlos, A., Tapias, G., Sisniega, A., and Desco, M. (2007). Performance evaluation of a new gamma imager for small animal SPECT applications. *IEEE Nuclear Science Symposium and Conference*, 5, 3355-3360.
- Leo, W. R. (1987). *Techniques for nuclear and particle physics Experiments-a how-to approach*. New York: Springer-Verlag.
- Lewellen, T. K., Pollard, K. R., Bice, A. N., and Zhu, J. B. (1990). A new clinical scintillation camera with pulse tail extrapolation electronics. *IEEE Transactions on Nuclear Science*, 37, 702-706.
- Lopes, M. I., and Chepel, V. (2004). Detectors for medical radioisotope imaging: demands and perspectives. *Elsevier, Radiation Physics and Chemistry*, 71, 683-692.
- Lyashenko, A. (2009). Development of gas avalanche PMTs, sensitive in the visible spectral range. PhD Thesis Submitted to Weizmann Inst., of Scien. Rehovot, Isreal.
- MacDonald, L. R., Patt, B. E., Iwanczy, J. S., Tsui, B. M. W., Wang, Y., Frey, E. C., Acton, P. D., and Kung, H. F. (2001). Pinhole SPECT of mice using the LumaGEM gamma camera. *IEEE Transactions on Nuclear Science*, 48, 830-836.
- Madson, M. T. (2007). Recent advances in SPECT imaging. *Journal of Nuclear Medicine*, 48, 661-673.
- Maini, C. L., Notaristefani, F. D. E., Tofani, A., Iacopi, F., Sciuto, R., Semprebene, A., Malatesta, T., Frezza, F., Botti C., Giunta, S., and Natali, P. G. (1999). ^{99m}Tc -MIBI scintimammography using a

- dedicated nuclear mammograph. *Journal of Nuclear Medicine*, 40, 46-51.
- Mallard, J. R., and Peachey C. J. (1959). A quantitative automatic body scanner for the localization of radioisotope, in in-vivo Br. *Journal of Radiology*, 32, 652-657.
- Marcel, R. (2004). Imaging of gamma emitters using scintillation cameras. *Nuclear Instruments and Methods in Physics Research, A (527)*, 124-129.
- Matthews, K. L. (1997). Development and application of a small gamma camera. *Medical Physics*, 24, 1802.
- Mayneord, W. V., and Newbery, S. P. (1952). An Automatic method of studying the distribution of activity in a source of ionizing radiation Br. *Journal of Radiology*, 25, 589-596.
- Mazen, A. S., and Radwan, R. (2000). *High Voltage Engineering Theory and Practice. (2ndEd.)*. Revised and Expanded, Marcel Dekker, Inc.
- American Journal of Applied Science*, 3 (12), 2178-2183, 2006 - 2183.
- McElroy, D. P., MacDonald, L. R., Beekman, F. J., Wang, Y., Patt, B. E., and Iwanczyk, J. S. (2005). Performance evaluation of A-SPECT: a high resolution desktop pinhole SPECT system for imaging small animals. *IEEE Transactions on Nuclear Science*, 49, 2139-2147.
- MediaWiki.Org. (2014). Communication: Landing. Retrieved from <http://www.mediawiki.org/wiki/Communication>

- Mirzoyan, R., Ferenc, D., and Lorenz, E. (2000). An evaluation of the new compact hybrid photodiodes R7110U-07/40 from Hamamatsu in high-speed light detection mode. *Nuclear Instrumentation and Methodology A* (442), 140.
- Mori, I., Takayama, T., and Motomura, N. (2001). The detector module and its imaging performance. *Ann Nucl Med.*, 15, 487-494.
- Mormann, D. (2005). Study of novel gaseous PMTs for UV and visible light. PhD Thesis Submitted to the Weizmann Institute of Science, Rehovot, Isreal.
- Morton, G. A. (1968). Photon Counting. *Applied Optics*, 7 (1), 1-10.
- Moses, W. W., Pedrali-Noy, M., Gruber, G. J., and Krieger, B. (2001). PETRIC-A positron emission tomography readout integrated circuit. Submitted for Publication to *IEEE Transactions on Nuclear Science*, NS (48).
- Mostovskii, A. A., Vorobeva, G. B., and Struchinskii, G. B. (1964). Soviet Physics. *Solid State*, 5, 2436.
- Motizuki, K., and Sparks, M. L. R. (1963). No. 1032, Contract SD-87 (ARPA). Stanford University, California: W. W. Hansen Labs., of Physics.
- Mueller, B., O'Connor, M. K., Blevis, I., Rhodes, D. J., Smith, R., Collins, D. A., and Phillips, S. W. (2003). Evaluation of a small Cadmium Zinc Telluride detector for scintimammography. *Journal of Nuclear Medicine*, 44, 602-9.
- Muehllehner, G. (1969). A diverging collimator for gamma-ray imaging cameras. *Journal of Nuclear Medicine*, 10, 197-201.

- Muehllehner, G. (1979). Effect of crystal thickness on scintillation camera performance. *Journal of Nuclear Medicine*, 20 (9), 992-993.
- Muehllehner, G., and Karp, J. S. (1986). A positron camera using positive-sensitive detectors: PENN-PET. *Journal of Nuclear Medicine*, 27, 90-98.
- Muehllehner, G., and Wetzel, R. A. (1971). Section imaging by computer calculation. *Journal of Nuclear Medicine*, 12, 76-85.
- Naidu, M. S., and Kamaraju, V. (2004). *High Voltage Engineering* (3rd Ed.). McGraw- Hill Company Ltd.
- National Electrical Manufacturers Association. (1994). *Performance Measurements of Scintillation Cameras*. NUI, Washington, DC.: NEMA Standards Publication.
- National Electrical Manufacturers Association. (2001). *Performance Measurements of Scintillation Cameras*. Rosslyn, VA.: NEMA Standards Publication.
- National Electrical Manufacturers Association. (2007). *Performance Measurements of Gamma Cameras*. Rosslyn VA.: NEMA.
- Nicholson, P. W. (1974). *Nuclear electronics*. London: John Wiley & Sons.
- Nutt, R. (2002). The history of positron emission tomography. *Mol. Imaging Biol.*, 411-426.
- Obeng, P. K. (2000). *End of mission report to IAEA: On the repair of MEDX (Siemens) gamma camera, Mulago Hospital*. Kampala, Uganda.
- Obeng, P. K. (2000). *End of mission report to IAEA: On repair of gamma camera at the Black lion hospital*. Addis Ababa, Ethiopia.

- Obeng, P. K. (1996). *End of mission report to IAEA: On maintenance and repairs of the gamma camera at Mulago Teaching Hospital*. Kampala, Uganda.
- O'Connor, M. K. (n.d.). *Quality control of scintillation cameras (Planar and SPECT)*, Mayo Clinic. Rochester, Minnesota, USA. Published on the website of the American Association of Physicists in Medicine. Retrieved from www.aapm.org/meetings/99AM/pdf/2741-6067.pdf
- Ogawa, K., Ohmura, N., Iida, H., Nakamura, K., Nakahara, T., and Kubo, A. (2009). Development of an ultra-high resolution SPECT system with a CdTe semiconductor detector. *Annals of nuclear medicine*, 23, 763-770.
- Ogawa, K., Ohta, A., Shuto, K., Motomura, N., Kobayashi, H., Makino, S., Nakahara, T., and Kubo, A. (2006). Development of semiconductor gamma-camera system with CdZnTe detectors. *IEEE Nucl Sci Symp Conf Rec.*, 4, 2426-2429.
- Ogawa, K., Ohta, A., Saito, Y., Syuto, K., Motomura, N., Kobayashi, H., Makino, S., Nakahara, T., and Kubo, A. (2007). Prototype gamma camera system with CdZnTe semiconductor detectors. *Med Imaging Tech.*, 25, 296-302.
- Ogawa, K., Ohmura, N., Iida, H., Nakamura, K., Nakahara, T., and Kubo, A. (2009). Development of an Ultra-high resolution SPECT system with a CdTe semiconductor detector. *Ann Nucl. Med*, 23, 763-770.
- Olschner, F., Shah, K., Lund, J. C., Zhang, J., Daley, K., Medrick, S., and Squillante, m. R. (1992). Thallium bromide semiconductor x-ray and

- gamma-ray detectors. *Nuclear Instruments & Methods in Physics Research, A* (322), 504-508.
- Pendry, J. B., and Hopkinson, J. F. L. (1978). *Journal de Physique, Colloque C4*, supplement au no. 7, Tome 39. Retrieved from <http://dx.doi.org/10.1051/jphyscoi:19/8418>
- Perkins, A. E., Muehllehenr, G., Surti, S., and Karp, J. S. (2003). Performance measurements of a pixelated NaI(Tl) pet scanner. *IEEE Transactions on Nuclear Science*, 50, 373-377.
- Persyk, D. E., and Moi, T. (1978). State-of-the-art photomultipliers for anger cameras. *IEEE Transactions on Nuclear Science*, 25, 615.
- Phelps, M. E., Hoffman, E. J., Mullani, N. A., Higgins, C. S., and Ter-Pogossian, M. M. (1976). Design Considerations for a positron emission transaxial tomography. *PETT (III) IEEE Transactions on Nuclear Science*, 23, 516-522.
- Photonics. (2007). *Photomultiplier tubes: Principles and applications*. France.
- Prekeges, G. (2011). *Nuclear Medicine Instrumentations*. USA.: Jones and Bartlett Pub.
- Rappaport, P. (1954). Methods of processing silver-magnesium secondary emitters for electron tubes. *Journal of Applied Physics*, 25, 288-292.
- Rollo, F. D. (1977). *Nuclear Medicine Physics, Instrumentation, and Agents*. St. Louis: C. V. Mosby.
- Rowland, D. J. and Cherry, S. R. (2008). Small-animal preclinical nuclear medicine instrumentation and methodology. *Semin Nucl Med.*, 38, 209-222.

- Sanches, F., Benlloch, J. M., Escat, B., Pavon, N., Porras, E., Kadi-Hanifi, D., and Ruiz, J. A. (2004). *Medical Physics*, 31 (6), 1394-1396.
- Schramm, N. U., Ebel, G., Engeland, U., Schurrat, T., Behe, M., and Behr, T. (2003). High-resolution SPECT using multipinhole collimation. *IEEE Transactions on Nuclear Science*, 50, 315-320.
- Shung, K., Smith, K., Michael, B., and Tsui, B. (1992). *Principles of Medical Imaging*. USA.: Academic Press.
- Simon, R. C., Blowey, R. W., and Phelps, M. E. (2003). *Physics in Nuclear Medicine (3rd ed.)*. USA.: W. B. Saunders.
- Singh, M., and Mumcuoglu, E. (1998). Design of a CZT based breast SPECT system, *IEEE Transactions on Nuclear Science*, 45, 187-194.
- Sommer, A. H. (1958). Activation of silver-magnesium and copper-beryllium dynodes, *Journal of Applied Physics*, 29, 598-599.
- Sommer, A. H. (1968). *Photoemission Materials*. New York, USA.: John Wiley and Sons.
- Sommer, A. (1983). The Element of Luck in Research – Photocathodes 1930 to 1980. *Journal of Vac. Science Technology A*, 1(2), 119-124.
- Spencer, D. F., Aryaeinejad, R., and Reber, E. L. (2001). Using the Cockcroft-Walton Voltage Multiplier Design in Hand held Devices. *Idaho National Engineering and Environmental Laboratory*, Idaho Falls, ID 83415.
- Spicer, W. E. (1958). Photoemissive, photoconductive, and optical absorption studies of alkali-antimony compounds. *Physical Review*, 112, 114-122.

- Spicer, W. E. (1960). Photoemission and related properties of alkali-antimonides. *Journal of Appl. Physics*, 31, 2077.
- Spicer, W. E. (1963). Optical transition in which crystal momentum is not conserved. *Physical Review Letters*, 11, 243-245.
- Spicer, W. and Herrera-Gomez, A. (1993). Modern theory and applications of photocathodes, *SLAC-PUB-6306*. Presented at SPIE's 1993 International Symposium on Optics, Imaging and Instrumentation, San Diego, CA.
- Staurt, R. N., Wooten, F., and Spicer, W. E. (1963). Mean free Path of Hot Electrons. *Physical Review Letters*, 10, 119.
- Staurt, R. N., Wooten, F., and Spicer, W. E. (1964). Monte Carlo calculations pertaining to the transport of hot electrons. *Physical Review*, 135, 495.
- Sun, M., Izaguirre, E. W., Funk, T., Hwang, A. B., Carver, J., Thompson, S., and Patt, B. E. (2005). A small animal helical SPECT scanner. *IEEE Nucl Sci Symp Conf Rec.* 4, 2066–2069.
- Sun, X., Wang, S., Ma, T., Zhou, R., Li, X., Zhang, Z. (2007). A high resolution and high sensitivity small animal SPECT system based on H8500. *IEEE Nucl Sci Symp Conf Rec.*, 4, 2941-2943.
- Tait, W. H. (1980). *Radiation Detection*. Butterworth.
- Ter-Pogossian, M. M., Mullani, N. A., Hood, J. T., Higgins, C. S., and Ficke, D. C. (1978). Design considerations for a positron emission transverse tomography (PETT V), *Journal of Comput. Assist. Tomogr*, 2, 539- 544.
- The Free Encyclopedia. (1996). Photomultiplier tube: Design. Retrieved from <http://elchem.kaist.ac.kr/vt/chem-ed/optics/detector/pmt.htm>

- The Free Encyclopedia. (2014). Photomultiplier: Structure and operating principles. Retrieved from <http://en.wikipedia.org/wiki/Photomultiplier>.
- Thomas, J. (2003). *Revival of Gamma camera (Adaptation of new electronics and conversion of the camera to a demonstrator in medical imaging)*. MSc. Thesis Submitted to Physics Department, Royal Institute of Technology, Stockholm.
- Thompson, C. J., Yamamoto, Y. L., and Myer, E. (1979). Positron II: A high efficiency positron imaging device for dynamic brain studies. *IEEE Transactions on Nuclear Science*, 26, 583-589.
- Tyutikov, A. M. (1963). Structure and secondary emission of emitters of activated beryllium bronze. *Radio Engineering and Electronic Physics* (Translated from the Russian and published by the IEEE), 8 (4), 725-734.
- Webb, S. (2000). *The Physics of Medical Imaging*. Bristol Institute of Physics Publishing.
- Weisenberger, A. G., Wojcik, R., Bradley, E.L., Brewer, B. P., Majewski, S., Qian, J., Ranck, A., Saha, M.S., Smith, K., Smith, M.F., and Welsh, R. E. (2003). SPECT-CT system for small animal imaging. *IEEE Transactions on Nuclear Science*, 52, 181-189.
- Williams, M. B., Goode, A. R., Galbis-Reig, V., Majewski, S., Weisenberger, A. G., and Wojcik, R. (2000). Performance of a PSPMT based detector for scinti-mammography. *Phys. Med. Biol*, 45, 781-800.

Zeniya, T., Watabe, H., Aoi, T., Kim, K. M., Teramoto, N., Takeno, T., Ohta Y., Hayashi T., Mashino H., Ota T., Yamamoto, S., and Iida, H. (2006). Use of a compact pixellated gamma camera for small animal pinhole SPECT imaging. *Ann Nucl Med.*, 20, 409–416.

Zworykin, V. K., Morton, G. A. and Malter, L. (1936). The secondary emission multiplier: A new electronic device. *Proc. IRE*, 24, 351 – 375.

Zworykin, V. K., Ruedy, J. E., and Pike, E. W. (1941). Silver-magnesium alloy as a secondary emitting material. *Journal of Applied Physics*, 12.

